

General Disclaimer

One or more of the Following Statements may affect this Document

- This document has been reproduced from the best copy furnished by the organizational source. It is being released in the interest of making available as much information as possible.
- This document may contain data, which exceeds the sheet parameters. It was furnished in this condition by the organizational source and is the best copy available.
- This document may contain tone-on-tone or color graphs, charts and/or pictures, which have been reproduced in black and white.
- This document is paginated as submitted by the original source.
- Portions of this document are not fully legible due to the historical nature of some of the material. However, it is the best reproduction available from the original submission.

(NASA-CR-158706) DEVELOPMENT OF PULSED
PROCESSES FOR THE MANUFACTURE OF SOLAR CELLS
Interim Report (Spire Corp., Bedford, Mass.)
215 p HC A10/MF A01 CSCL 10A

N79-25484

Unclas

G3/44 22161

**DEVELOPMENT OF PULSED PROCESSES
FOR THE MANUFACTURE OF SOLAR CELLS**

**INTERIM REPORT NO. 1
DECEMBER 1978**

"THE JPL LOW-COST SILICON SOLAR ARRAY PROJECT IS SPONSORED BY THE U.S. DEPARTMENT OF ENERGY AND FORMS PART OF THE SOLAR PHOTOVOLTAIC CONVERSION PROGRAM TO INITIATE A MAJOR EFFORT TOWARD THE DEVELOPMENT OF LOW-COST SOLAR ARRAYS. THIS WORK WAS PERFORMED FOR THE JET PROPULSION LABORATORY, CALIFORNIA INSTITUTE OF TECHNOLOGY BY AGREEMENT BETWEEN NASA AND DOE."



PREPARED UNDER CONTRACT NO. 954786 FOR:
**JET PROPULSION LABORATORY
CALIFORNIA INSTITUTE OF TECHNOLOGY
PASADENA, CA 91103**



DEVELOPMENT OF PULSED PROCESSES
FOR THE MANUFACTURE OF SOLAR CELLS

Interim Report No. 1
December 1978

Contract 954786

Submitted to
JET PROPULSION LABORATORY
California Institute of Technology
Pasadena, CA 91103

Prepared by:

Principal Investigator

Approved by:

Program Manager

SPIRE CORPORATION
Patriots Park
Bedford, MA 01730

TABLE OF CONTENTS

<u>Section</u>	<u>Page</u>
ACKNOWLEDGMENT	xi
ABSTRACT	xiii
1 INTRODUCTION	1-1
2 TECHNICAL DISCUSSION	2-1
2.1 Ion Implantation Facilities For Solar Cell Production	2-1
2.1.1 General Considerations	2-1
2.1.2 High-Current Solar Cell Implanter	2-8
2.1.3 Design of an Automated Production Implanter	2-16
2.1.4 Manufacturing Cost	2-31
2.2 Solar Cell Development	2-33
2.2.1 Advantages of Ion Implantation Processing	2-33
2.2.2 Ion Implantation Parameter Selection	2-35
2.2.3 Ion Implantation Damage Annealing	2-38
2.2.4 Annealing Optimization for Solar Cell Implant Parameters	2-44
2.2.5 Contact Design	2-49
2.2.6 Process Development	2-54
2.3 Solar Cell Performance Status	2-59
2.3.1 Single-Crystal Starting Material	2-59
2.3.2 Cast Polycrystalline Silicon Solar Cells	2-66
2.3.3 Cell Process Comparisons: 1-ohm-cm Silicon	2-78
2.3.4 Cell Process Comparisons: 10-ohm-cm Silicon	2-79
2.3.5 Cell Process Comparisons: Pulsed Laser and Electron Beam Annealing	2-81
2.4 Advanced Production Technology	2-81
2.4.1 Ion Implanted/Pulse Annealed Solar Cells	2-81
2.4.2 Automated Production Process Concept	2-82
2.5 Pulsed Energy Processing Studies	2-90
2.5.1 Advantages of Pulsed Energy Processing	2-90
2.5.2 Advantages of the Pulsed Energy Product	2-93
2.5.3 Theoretical Models for the Pulsed Energy Processes	2-99
2.5.4 Stress Analysis	2-112
2.5.5 Pulse Sintering of Contact Metals	2-122
2.5.6 Functional Requirements for Pulsed Electron Beam Processor	2-129

TABLE OF CONTENTS (Concluded)

<u>Section</u>	<u>Page</u>
2.6 Economic Analysis	2-135
2.6.1 Ion Implantation	2-135
2.6.2 Pulse Annealing	2-151
2.6.3 Cost Analysis and Production Schedule for Machine Fabrication	2-151
3 CONCLUSIONS	3-1
4 NEW TECHNOLOGY	4-1
REFERENCES	R-1
APPENDIX A System Detail Drawings for Automated Implanter with 500 cm ² /sec Throughput	A-1
APPENDIX B Tabular Data for (500) Cells Delivered to JPL with Ion Implanted n ⁺ /pp ⁺ Structures	B-1
APPENDIX C Tabular Data for Cell Manufacturing Process Comparison with 1 ohm-cm Silicon	C-1
APPENDIX D Tabular Data for Cell Manufacturing Process Comparison with 10 ohm-cm Silicon	D-1

LIST OF FIGURES

<u>Figure</u>		<u>Page</u>
2-1	Typical Ion Implanter Configuration	2-2
2-2	Phosphorus Ion Profiles in Silicon	2-4
2-3	Arsenic Ion Profiles in Silicon	2-5
2-4	Standard, Medium-Current Ion Implanter	2-7
2-5	High-Current Solar Cell Implanter	2-9
2-6	Wafer Holder/Rotator for Solar Cell Implants	2-11
2-7	Sheet Resistance Contour Map for Standard Boron Implants After Annealing	2-14
2-8	Sheet Resistance Contour Map for Standard Phosphorus Implants After Annealing	2-15
2-9	Conceptual Drawing of a 100 mA Automated Production Implanter	2-18
2-10	High-Current Ion Source Cross Section	2-20
2-11	Schematic Diagram of the Beam Trajectory Through the Analyzing and Scanning System	2-22
2-12	Material Transport System	2-24
2-13	Two-Level Material Transport Sequence	2-25
2-14	Implanter Control System Block Diagram	2-30
2-15	Facility Requirements and Overall Dimensions for an Automated Production Implanter	2-32
2-16	Measured Junction Implant Profile for n^+/pp^+ Cell Structure	2-36
2-17	Highly Channeled Implant Junction Profile	2-37
2-18	Back Surface Implant Profile for n^+/pp^+ Cell	2-39
2-19	Typical Implant Damage for Various Implant Doses	2-41
2-20	Helium Ion Backscattering and Channeling Analysis of Implanted and Annealed Layer(s)	2-43

LIST OF FIGURES (Continued)

<u>Figure</u>		<u>Page</u>
2-21	Epitaxial Regrowth Behavior for Implanted Layers at 550°C	2-44
2-22	Isochronal Annealing of 10-ohm-cm CZ Silicon	2-45
2-23	Isochronal Annealing of 1-ohm-cm CZ Silicon	2-46
2-24	Junction Depth as a Function of Temperature for Single- and Two-Step Anneals of 10-ohm-cm CZ	2-47
2-25	Junction Depth as a Function of Temperature for Single- and Two-Step Anneals of 1-ohm-cm CZ	2-48
2-26	Generalized Rectangular Geometry Unit Cell	2-50
2-27	Percent of Total Cell Power Lost by Resistance and Shadowing Versus Line Width for Several Sheet Resistances	2-53
2-28	Optimized Front Contact Metallization Pattern for 7.6-cm (3-Inch) Cells	2-55
2-29	Schematic of Baseline, High-Efficiency, Implanted Cell Process	2-58
2-30	Distribution of Short-Circuit Current for n ⁺ /pp ⁺ Implanted, Furnace Annealed Solar Cells with 7.6-cm Diameters	2-61
2-31	Distribution of Open-Circuit Voltage for n ⁺ /pp ⁺ Implanted, Furnace Annealed Solar Cells with 7.6-cm Diameters	2-62
2-32	Distribution of Current at 490 mV for n ⁺ /pp ⁺ Implanted, Furnace Annealed Solar Cells with 7.6-cm Diameters	2-63
2-33	Distribution of AM0 Conversion Efficiency for n ⁺ /pp ⁺ Ion Implanted/Furnace Annealed Solar Cells with 7.6-cm Diameters	2-64
2-34	AM0 I-V Characteristics for AM0-25°C, 7.62-cm Diameter, n ⁺ /pp ⁺ Implanted Solar Cell of 10-ohm-cm Czochralski Silicon	2-65
2-35	Typical Grain Configuration of Polycrystalline SILSO Wafer	2-67
2-36	Polycrystalline Sheet Silicon (SILSO) Solar Cell	2-68
2-37	Distribution of Open-Circuit Voltage for n ⁺ /pp ⁺ Implanted Polycrystalline Solar Cells	2-70

LIST OF FIGURES (Continued)

<u>Figure</u>		<u>Page</u>
2-38	Distribution of Short-Circuit Current for n^+/pp^+ Implanted Polycrystalline Solar Cells	2-71
2-39	Distribution of Current at 450 mV for n^+/pp^+ Implanted Polycrystalline Solar Cells	2-72
2-40	I-V Characteristics for 5x5 cm Ion Implanted n^+/pp^+ Polycrystalline Solar Cell	2-73
2-41	Concept for Total Automated Production - 100 mW _e of Solar Cells per Year	2-83
2-42	I-V Characteristics for Cells Processed Using Pulsed Electron Beam Annealing of Both Phosphorus Junction and Boron BSF Implanted Layers	2-87
2-43	I-V Characteristics for Pulse Annealed Ion Implanted Polycrystalline Solar Cells	2-88
2-44	I-V Characteristics for Cells Processed Using Laser-Annealed Implanted Junctions and Alloyed p^+ Layers	2-91
2-45	Dislocation Density as a Function of Depth Into Crystal Revealed by Layer Stripping	2-94
2-46	Helium Ion Backscattering from Furnace and Electron Beam Annealed Implanted Wafers	2-95
2-47	Transmission Electron Microscope Photos of Furnace-Annealed and Electron Beam Annealed Layers on (100) Silicon	2-97
2-48	Measured Arsenic Impurity Profiles for (1) As-Implanted and (2) After Pulse Annealing	2-98
2-49	Flow Chart for VXTEMP	2-101
2-50	Electron Beam Energy Spectrum	2-102
2-51	Energy Deposition versus Depth Profile in Silicon for Pulsed Electron Beam	2-103
2-52	Voltage (Corrected for di/dt) and Current Across Cathode-Anode Gap	2-104
2-53	Variation of Thermal Conductivity with Temperature for Amorphous and Crystalline Silicon	2-105
2-54	Front Surface Temperature as a Function of Time Following Deposition of Pulsed Electron Beam	2-106

LIST OF FIGURES (Continued)

<u>Section</u>	<u>Page</u>
2-55 Calculated Temperature Profile During Pulsed Electron Beam Annealing from VXTEMP Output	2-107
2-56 Regrowth Rates for α -Si to Recrystallize With and Without Single Crystal Substrate	2-110
2-57 Diffusion Coefficients for Arsenic and Phosphorus in Solid and Liquid Silicon	2-111
2-58 Shock Wave Propagation Induced by Electron Beam Pulse	2-119
2-59 Pressure as a Function of Depth at Various Times After Beginning of Pulse	2-121
2-60 Auger Analysis of Pulse-Sintered, Thin-Film Molybdenum on Silicon	2-124
2-61 Auger Analysis of Furnace-Sintered, Thin-Film Molybdenum on Silicon	2-125
2-62 Calculated Spatial Temperature Profiles for Thin-Film Molybdenum on Silicon Following Pulsed Electron Beam Deposition	2-127
2-63 Calculated Front Surface Temperature Rise for 500A Molybdenum Thin Film on Silicon Following 0.2 cal/cm ² Pulsed Electron Beam Deposition	2-128
2-64 Components of Automated Production Processor	2-131
2-65 Electron Beam Processor System Elements	2-132
2-66 Format A Statement: Process Description for 0.3 mA, Medium-Current Ion Implantation	2-136
2-67 Format A Statement: Process Description for 3-mA, High-Current Ion Implantation	2-138
2-68 Format A Statement: Process Description for 100-mA, Automated Ion Implantation	2-140
2-69 Format B Statement: Company Description for Manufacturer of Ion-Implanted Silicon Wafers	2-142
2-70 Format C Statement: 1978 Standard Industry Description	2-143
2-71 SAMICS Input Data	2-144

LIST OF FIGURES (Concluded)

<u>Figure</u>		<u>Page</u>
2-72	SAMICS Process Cost Forecast for Ion Implantation with 0.3-mA Ion Implanters in 1978	2-145
2-73	SAMICS Process Cost Forecast for Ion Implantation with 3-mA Ion Implanters in 1978	2-146
2-74	SAMICS Process Cost Forecast for Ion Implantation with 3-mA Ion Implanters in 1982	2-147
2-75	SAMICS Process Cost Forecast for Ion Implantation with 3-mA Ion Implanters in 1986	2-148
2-76	SAMICS Process Cost Forecast for Ion Implantation with 100-mA Ion Implanters in 1982	2-149
2-77	SAMICS Process Cost Forecast for Ion Implantation with 100-mA Ion Implanters in 1986	2-150
2-78	Production Schedule of Prototype Solar Cell Implanter	2-154

LIST OF TABLES

<u>Table</u>	<u>Page</u>
2-1 Minimum Beam Currents Required for Implanting at End Station Limited Operation of 300 Wafers Per Hour	2-12
2-2 Measured Beam Currents for the High-Current Implanter as a Function of Beam Energy	2-12
2-3 High-Current Implanter Setup Parameters	2-13
2-4 Comparison of Ion Implantation Equipment for Solar Cell Junction Implants	2-16
2-5 Solar Cell Production Implanter Performance Specifications . .	2-17
2-6 Facility Requirements for Prototype Solar Cell Production Implanter	2-31
2-7 Estimated Manufacturing Costs of Solar Cell Production Implanters	2-33
2-8 Baseline Process Specification for Ion-Implanted, n^+/pp^+ , High-Efficiency Solar Cells	2-57
2-9 Summary of Performance Characteristics for 500 Ion-Implanted, Furnace Annealed Cells	2-60
2-10 Polycrystalline Solar Cell Performance Data	2-74
2-11 Summary of First Performance Comparison of Cell Junction Formation Techniques	2-79
2-12 Summary of Second Performance Comparison of Cell Junction and Back Surface Field Formation	2-80
2-13 Outline for All-Vacuum, In-Line Processing	2-85
2-14 Summary of Measured Fracture Thresholds for Pulsed Electron Beam Heating as a Function of Silicon Crystallographic Orientation	2-116
2-15 Functional Requirements for Prototype Pulsed Electron Beam Processor	2-130
2-16 Summary of Samics Analysis for Ion Implanted Junctions	2-151
2-17 Summary of Samics Analysis for Pulsed Electron Beam Annealing	2-152
2-18 Estimated Manufacturing Cost of High Volume Solar Cell Implanter	2-153

ACKNOWLEDGMENT

Contributions to this program have been made by many individuals at Spire Corporation. The program manager was A. R. Kirkpatrick, and the principal investigator was J. A. Minnucci. The project team was staffed as follows:

P.H. Rose, Ion Implanter Design

A.C. Greenwald, Electron Beam Processing

R.C. Thomas, Solar Cell Processing

The considerable contributions by other technical staff and support personnel at Spire and at Jet Propulsion Laboratory, particularly R. H. Josephs, the Technical Manager, are gratefully acknowledged.

ABSTRACT

This report describes the results of a 1-year program to develop the processes required for low-energy ion implantation for the automated production of silicon solar cells.

The program included (1) demonstrating state-of-the-art ion implantation equipment and designing an automated ion implanter, (2) making efforts to improve the performance of ion-implanted solar cells to 16.5 percent AM1, (3) developing a model of the pulse annealing process used in solar cell production, and (4) preparing an economic analysis of the process costs of ion implantation.

During the program, phosphorus ions at an energy of 10 keV and dose of $2 \times 10^{15} \text{ cm}^{-2}$ were implanted in silicon solar cells to produce junctions, while boron ions at 25 keV and $5 \times 10^{15} \text{ cm}^{-2}$ were implanted in the cells to produce effective back surface fields. An ion implantation facility with a beam current up to 4 mA and a production throughput of 300 wafers per hour was designed and installed. A design was prepared for a 100-mA, automated implanter with a production capacity of 100 MW_e per year. A Solar Array Manufacturing Industry Costing Standards (SAMICS) economic analysis of the automated process steps of ion implantation and pulse annealing indicated that junctions can be formed and annealed at a cost of less than 3 cents per watt.

The efforts during this program represent a major advancement in developing the automated production of silicon solar cells with efficiencies greater than 16 percent AM1.

SECTION 1

INTRODUCTION

This is an interim report under Contract Number 954786, "Development of Processes for the Manufacture of Solar Cells", being performed under the Automated Array Assembly Task of the LSA project. Development over the long term is directed towards an extremely abbreviated production scheme for the manufacture of solar cells, which precludes the use of thermal operations and wet chemistry. Emphasis during the past year has been on the major element of the production concept: ion implantation. Ion implantation equipment, ion implantation processes, and advanced procedures for annealing ion implantation damage have been developed.

Under a previous Spire contract⁽¹⁾, it was demonstrated that silicon solar cells can be fabricated very rapidly without heat treatment in a furnace, wet chemistry, or operations in a gas atmosphere if ion implantation is employed in conjunction with pulsed energy techniques. Studies by other contractors^(2,3,4) have shown that ion implantation will be economically advantageous for automated production if practical, large-throughput ion implanters can be constructed. Further economic advantages are realized if equivalent-throughput pulse processors are constructed for annealing the ion implantation damage.

Conventional ion implantation facilities, up to now, have been technically inadequate for the simple preparation of high-efficiency cells; even the larger machines have had very low solar cell throughput capacities. Performance optimization of ion implanted solar cells had received little attention until this effort, so that implanted cell efficiencies had fallen behind those associated with the best diffused junction cell technology. The program at Spire has emphasized resolving the questions regarding the hardware and economics of ion implantation for automated production. It has also involved introducing cost-effectively to the solar cell structure by implantation, such high-efficiency characteristics as back surface fields and shallow junctions. To support this effort, the first high-throughput implanter yet produced, dedicated to solar cell production, has been installed and employed to fabricate solar cells with AM1 efficiencies greater than 16 percent. This 3-mA ion implanter, operational for the last 9 months, has a throughput of 1 MW of solar cell product per year.

A 100-mA, automated ion implanaton system has been designed to process 100 MW of solar cells per year. The most important step in a production process which includes ion implantation is annealing the damage in the crystal lattice caused by the implantation. The most promising production concept involves applying directed energy pulses of submicrosecond duration to replace the thermal annealing operations to correct the crystal damage. Pulse annealing, which has been shown to produce the necessary recrystallization effect, is being studied under this program to establish the optimum process parameters and identify the physical mechanisms involved. In summary, the major elements of the program have included:

- Development of processes for high-efficiency, ion implanted cell fabrication,
- Installation and operation of a dedicated solar cell ion implanter,
- Conceptual design of a next-generation solar cell implanter for automated production, and
- Development and analysis of pulsed energy solar cell processing techniques.

SECTION 2

TECHNICAL DISCUSSION

2.1 ION IMPLANTATION FACILITIES FOR SOLAR CELL PRODUCTION

2.1.1 General Considerations

Ion implantation machines are presently versatile, sophisticated, and expensive. A typical machine for semiconductor industry production will provide spectroscopically pure ion beams of most of the elements on the periodic table at any energy from 25 to 200 or more keV. Ion doses between 10^{11} and 10^{17} ions/cm² are delivered accurately and with virtually complete uniformity and reproducibility. In spite of, and partly because of, their versatility, these implanters are not suitable for solar cell production purposes, not even at 1978 levels. However, the limitations are associated with the available machines and not with the process of ion implantation. The correction of implantation machine inadequacies has been addressed in this program.

The general configuration of an ion implanter is shown in Figure 2-1. Among the factors which must be considered in the design of ion implantation equipment specifically for solar cells are the following:

1. Ion species requirements
2. Ion purity requirements
3. Ion energy requirements
4. Ion dose requirements
5. Dose uniformity/reproducibility requirements
6. Ion beam/substrate geometry

Both n- and p-type dopants have been implanted to form a high-performance n⁺/pp⁺ (or p⁺/nn⁺) silicon solar cell structure. The use of phosphorus (P) and boron (B) ions is adequate. It is possible that certain advantages may be realized if arsenic (As) is used in place of, or in combination with, phosphorus, or if aluminum (Al) is substituted for boron. Ions other than P, As, B, and Al, however, are not needed from ion implanters for processing silicon solar cells.

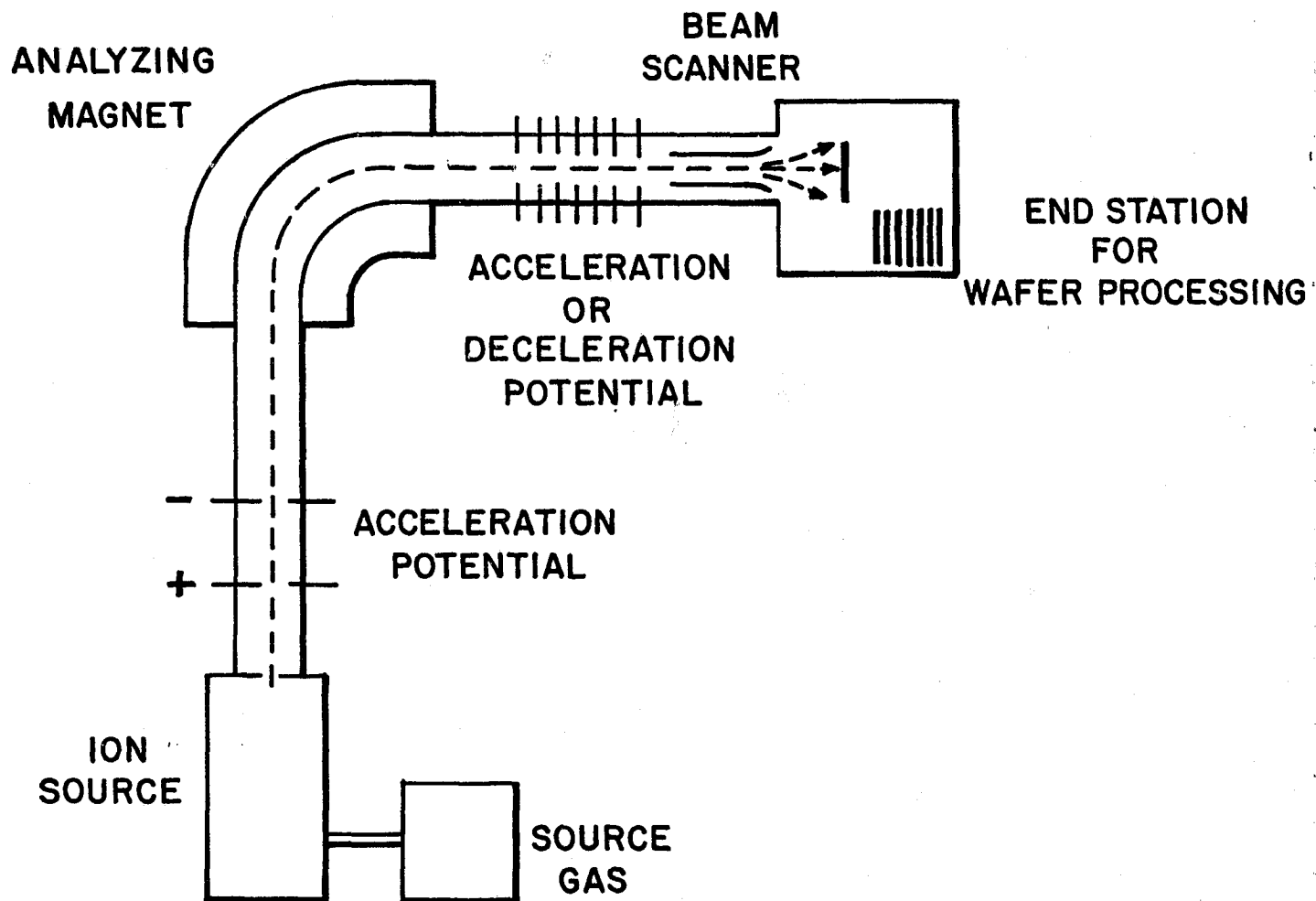


FIGURE 2-1. TYPICAL ION IMPLANTER CONFIGURATION

In general, and as presently performed, ion implantation introduces spectroscopically pure dopant. Before being directed onto the material being processed, the ion beam undergoes mass separation, so that only a particular isotope of the desired element is actually implanted. Major simplification of implanter design would result if mass separation were not required, in which case small amounts of unavoidable impurities in the beam would also be implanted. A degree of control might be established over the choice of the major impurity components, so if the effect upon performance of the solar cell device could be made benign, implantation without beam analysis might be used in production. Consideration of this possibility in detail is beyond the scope of this program.

The depth to which a dopant is implanted depends upon ion energy and target lattice structure. Calculated profiles for representative $^{31}\text{P}^+$ and $^{75}\text{As}^+$ implants into silicon are shown in Figures 2-2 and 2-3. Actual profiles can extend somewhat deeper because of ion "channeling" effects. Most ion implantation equipment now in use operates inefficiently or not at all at ion energies below roughly 25 keV, yet lower energies are desirable for very shallow junction solar cells. If necessary, shallow junctions can be produced even with higher energy ions — for example, by implanting through a surface coating — but complications result which can be avoided by the selection of implanter design.

Ion doses for optimized junction and back surface field implants in the silicon solar cell depend upon the particular cell structure involved. Doses between 3×10^{14} and 3×10^{15} ions/cm² are typical for both layers. These levels are much higher than the 10^{12} to 10^{14} ions/cm² doses which have been used in most semiconductor device applications to date. Until recently implanters for low-dose applications have had low beam currents, a few hundred microamperes maximum or less, and were capable of processing solar cell material only slowly because of the beam limitations. Machines with higher currents in the milliampere range now exist, but to achieve good uniformity and avoid excessive wafer heating at high ion energies, these machines have not been designed to utilize the available beam current efficiently.

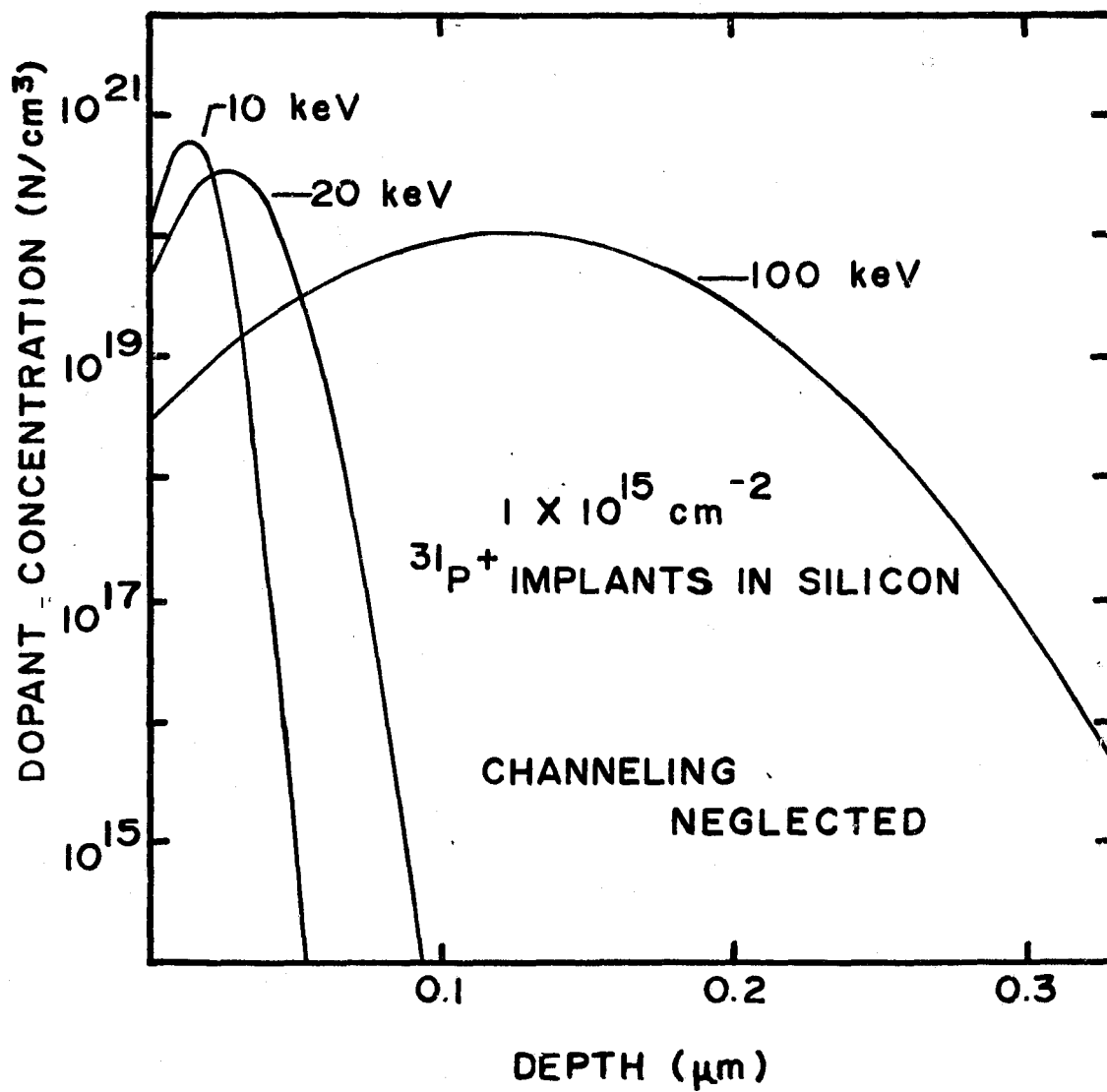


FIGURE 2-2. PHOSPHORUS ION PROFILES IN SILICON

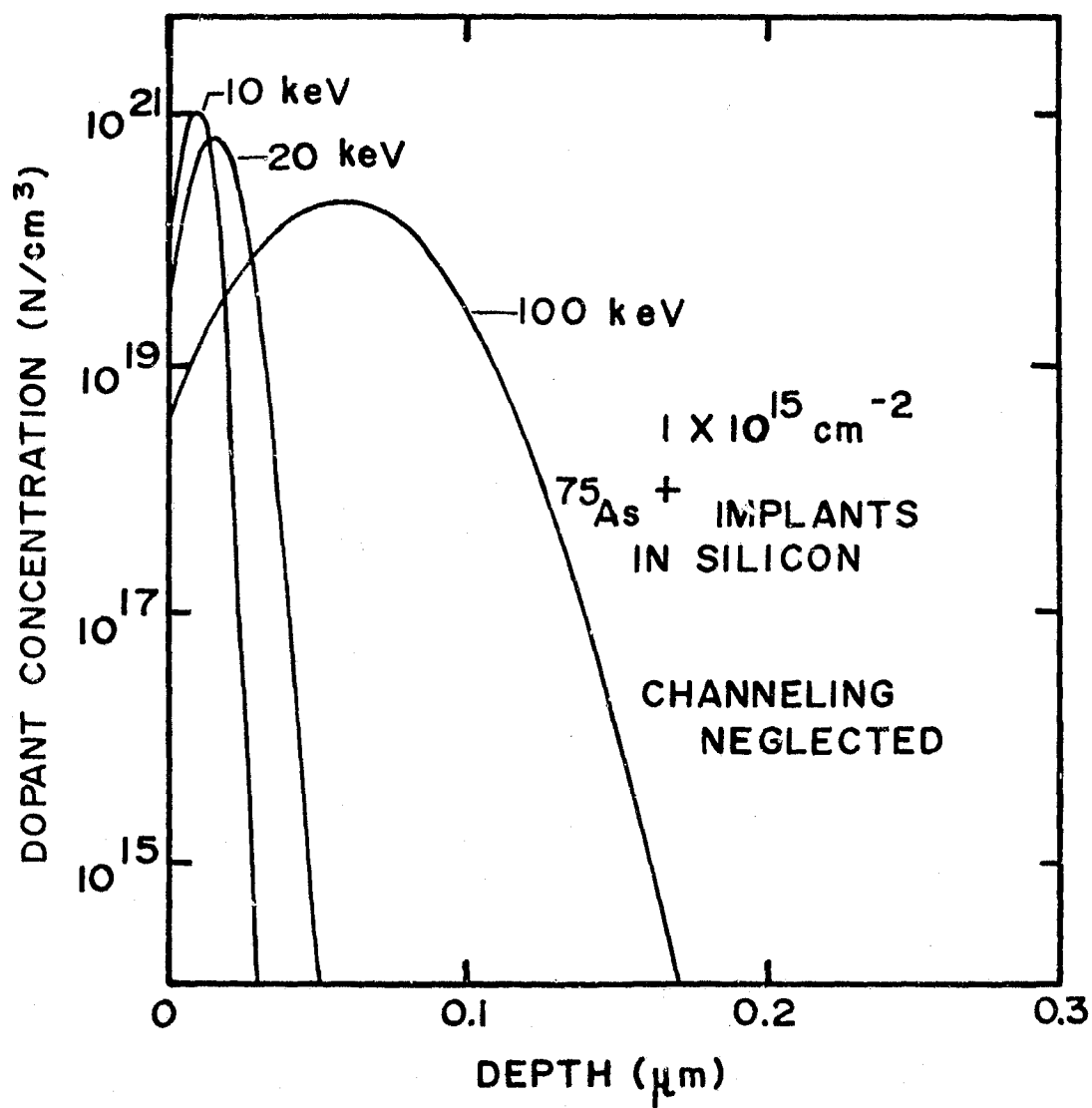


FIGURE 2-3. ARSENIC ION PROFILES IN SILICON

Among the major advantages of implantation for applications to devices other than solar cells has been the ability to introduce dopants controllably and reproducibly at very low dose levels. Much of the design of existing machines has been selected to provide these characteristics. Dose uniformity over wafers processed and reproducibility from wafer to wafer of better than ± 1 percent are typical of existing equipment, although not necessary for solar cells. The minimum uniformity and reproducibility requirements for solar cells are yet to be established, but it is known that ± 10 percent can be tolerated, as discussed in Section 2.3.3.

Ion implantation is a line-of-sight process, in which ions are deposited only in those regions exposed to the beam. The high-quality surfaces characteristic of the materials used in the fabrication of most semiconductor devices can be implanted directly. Usually, the material is tilted by a few degrees to misalign the ion beam and the major crystal axis, to avoid ion channeling through the open structure of the aligned crystal.

While the problem of the shadowing of certain regions of the material's surface from the ion beam does not occur with high quality surfaces, the low-grade surfaces on simply processed silicon wafers or sheets or on as-grown web or ribbon will contain features causing shadowing if implantation at a fixed angle is employed. Texturized surfaces present even more obvious problems in this respect. Since gaps in the doped layers of the cell device cannot be tolerated, solar cell implantation must take place so as to avoid any directional shadowing by varying the alignment between the ion beam and an irregularly featured surface during the implant. Consideration must also be given to surface shadowing by the mechanism used to hold the material during implant. Fixed holders with impediments like slotted rails or clips cannot be used.

Figure 2-4 shows an ion implanter at Spire which was not designed for solar cell purposes and is typical of existing production equipment. Such a machine can deliver ions of most elements on the periodic table at a desired energy between 25 and 200 keV. The ion beam is electrostatically scanned to produce dose uniformity better than ± 1.5 percent over a 3-inch square implant target. Sample-to-sample dose reproducibility is better than ± 1 percent. The beam current varies with the ion being implanted, but the machine shown can deliver up to a maximum of 200 microamperes of $^{31}\text{P}^+$ ions and less of most other ion species. Under normal operation, this machine will introduce junctions at a dose of 10^{15} ions/cm² into roughly 25 three-inch solar cell wafers per hour. At the beginning of this program, implanters existed which could deliver higher beam

ORIGINAL PAGE IS
OF POOR QUALITY

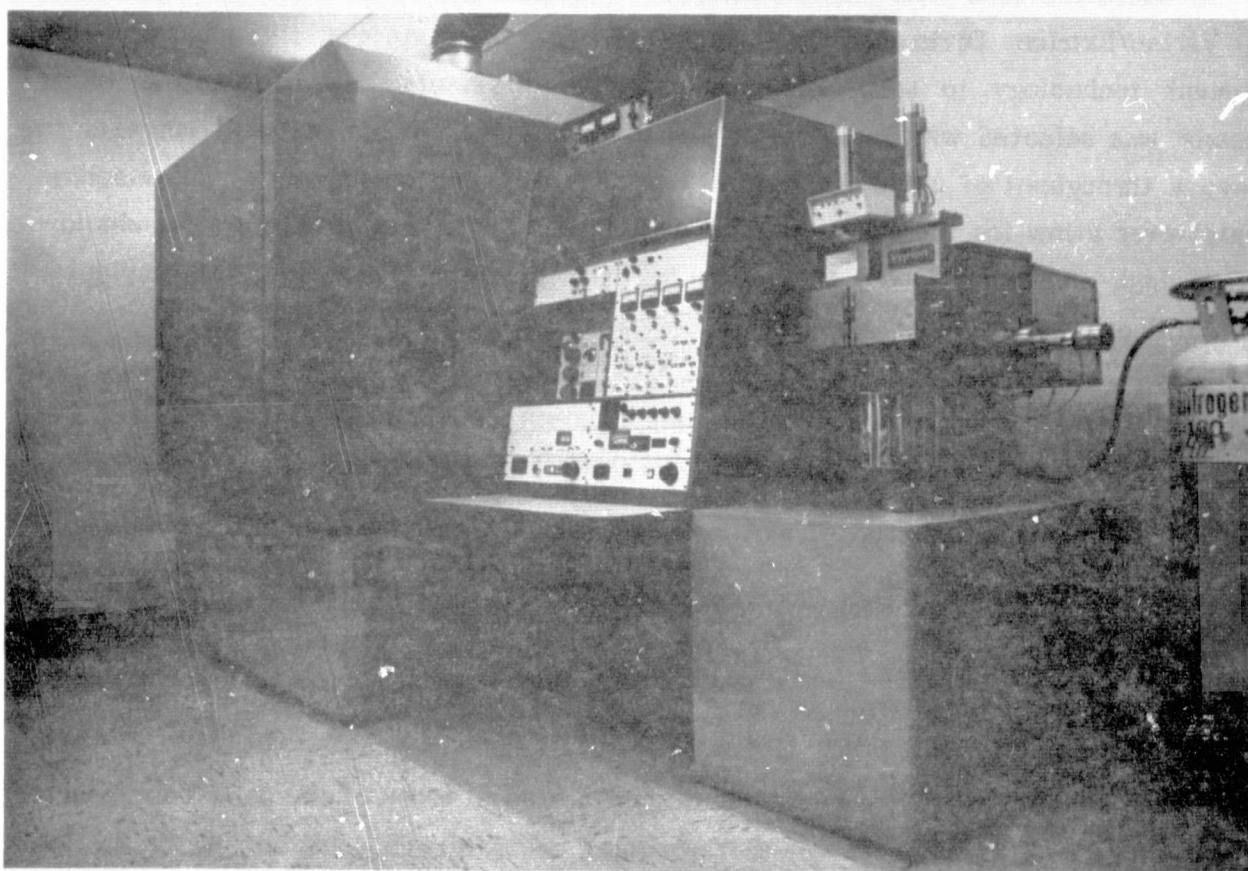


FIGURE 2-4. STANDARD, MEDIUM-CURRENT ION IMPLANTER

currents, up to a few milliamperes of $^{31}\text{P}^+$; however, such machines had batch-loaded wafer stations and incorporated mechanical scanning to achieve tight dose uniformity and minimize wafer heating at high ion energies. Most of these machines used the available ion beam inefficiently, particularly for implant doses not considerably greater than 10^{15} cm^{-2} , and throughput for solar cell purposes was not necessarily appreciably greater than that of the implanter shown in Figure 2-4.

2.1.2 High-Current Solar Cell Implanter

A dedicated solar cell implanter has been designed and fabricated in conjunction with Varian/Extrion Division. The design has adapted state-of-the-art implanter equipment technology to solar cell production requirements. An end station wafer processor was selected which utilizes a high percentage of available beam currents to achieve a throughput of up to 300 wafers per hour for junction implants. The machine operates over a low ion energy range from 5 to 50 keV, which is of interest for shallow junction, high-efficiency solar cell processing. Other unique features of this implanter (shown in Figure 2-5) include:

- Rotation of the wafer during implantation at the rate of one rotation per second to produce uniform doping of texturized surfaces,
- Elimination of fixture shadowing because of the absence of holding devices,
- Continuous wafer processing rather than batch loading, and
- Magnetic field oscillation of the ion beam to provide the necessary implant dose uniformity.

Other implanters with beam currents comparable to those of the solar cell process machine in general have much lower throughput capability because of wafer station design. For example, a high-current implanter capable of processing at 200 keV would not be designed to implant individual wafers in a few seconds; yet at 200 keV, a 10^{15} ion/cm^2 implant carries sufficient energy to raise the temperature of a silicon wafer 250 micrometers thick by approximately 750°C . Aside from the problems encountered in trying to anneal the radiation damage remaining after implant, the transport and handling of high-temperature wafers would be impractical. To speed

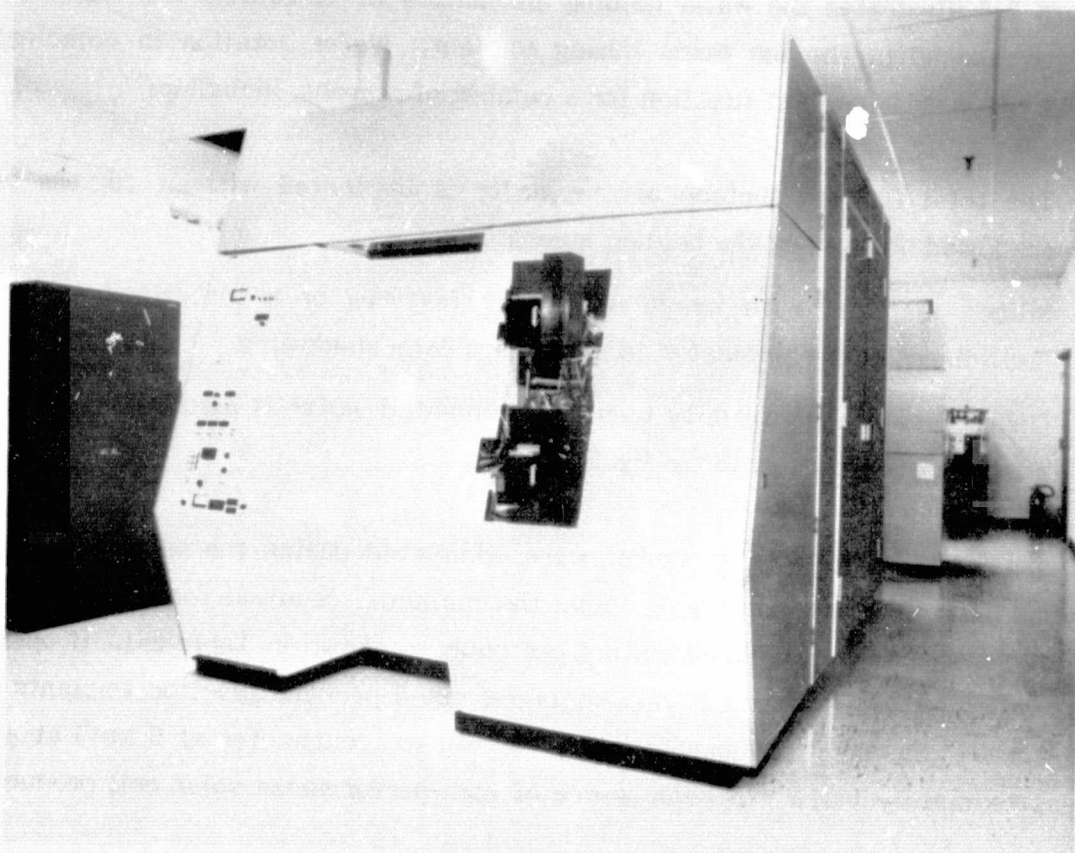


FIGURE 2-5. HIGH-CURRENT SOLAR CELL IMPLANTER

processing with the high-current machine, many wafers usually are implanted over a relatively long period of time through batch loading. However, the solar cell implanter is designed for low ion energies, and at 10 keV, a 10^{15} ion/cm² implant increases the temperature of a wafer 250 micrometers thick by only 37°C.

Figure 2-6 illustrates the wafer holding mechanism which rotates the wafer at one revolution per second in the ion beam during implant. Wafer rotation in combination with off-axis tilt is an important function for a number of reasons, including:

1. The total forward surface of the wafer is implanted without regions being shadowed because of the holding mechanism.
2. Silicon material with irregular surface features or a texturized surface is multidirectionally implanted to avoid gaps from shadowing.
3. Circumferential uniformity over the implanted wafer is assured regardless of any lack of symmetry in the ion beam, itself.

Acceptance tests for the implanter were completed during the second quarter of the program. Beam currents were well above the minimum required for the end station limited throughput of 300 three-inch wafers per hour, as shown in Table 2-1. If operated to capacity on a multiple-shift basis, this implanter could produce junction implants (at a density of 1×10^{15} to 2×10^{15} phosphorus ions per square centimeter at 5 keV) at a rate equal to approximately 1 MW_e of peak power of high-performance solar cell product per year.

The normal operating range for the standard Varian/Extrion high-current implanter is from 25 to 200 keV. Standard machine beam currents typically fall off when beam energy is decreased below 25 keV. Low-energy ions are desirable because shallow junction solar cells can be achieved without oxide or nitride other surface coatings. The beam focusing and magnetic field scanning systems were specially designed for this implanter for efficient transport of low-energy ion beams within the range of 5 to 25 keV. Performance data for the implanter at low energy is shown in Table 2-2. The facility has been used in this mode to address critical questions on the application of high-current ion implantation to automated solar cell production. Many of these questions could not be previously answered because of low beam currents and excessively long implant times per wafer.

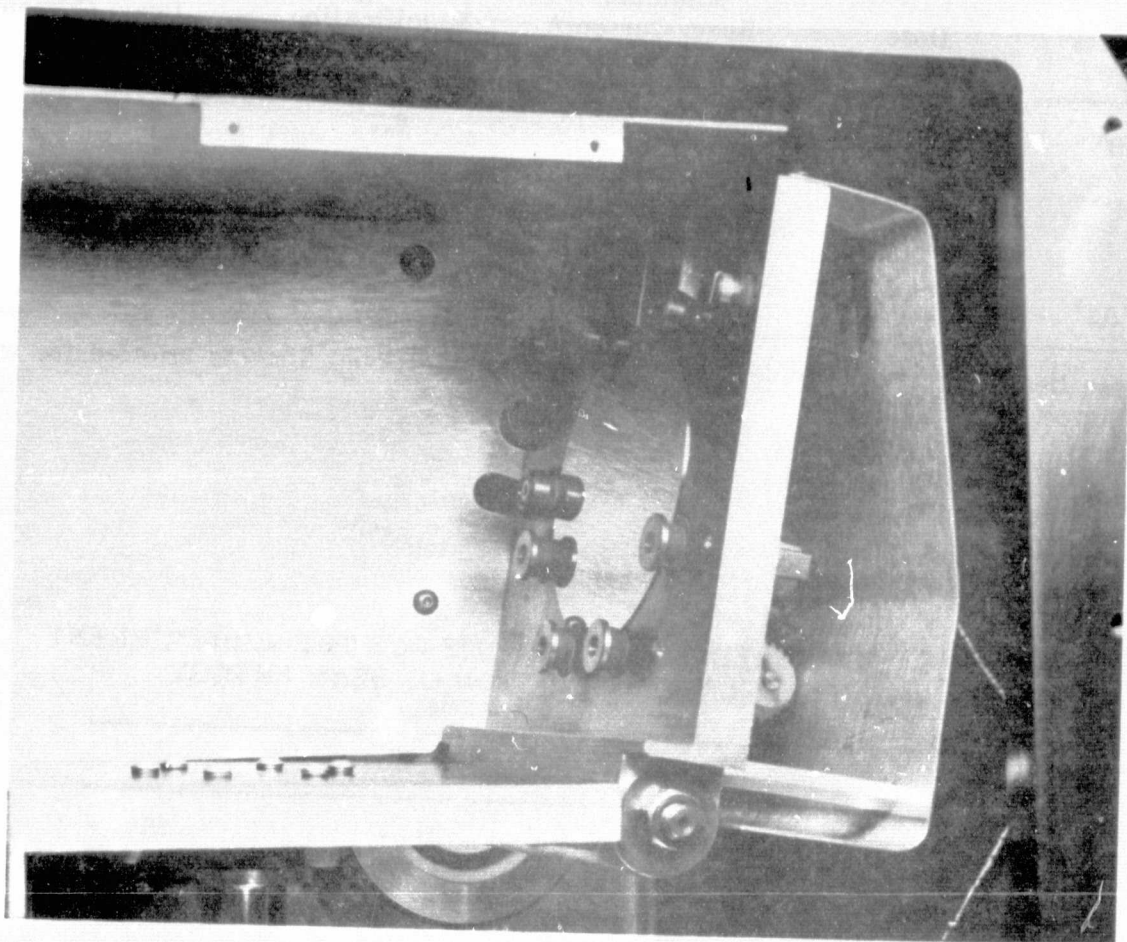


FIGURE 2-6. WAFER HOLDER/ROTATOR FOR
SOLAR CELL IMPLANTS

TABLE 2-1. MINIMUM BEAM CURRENTS REQUIRED FOR IMPLANTING AT
END STATION LIMITED OPERATION OF 300 WAFERS PER HOUR

Species	Dose (ions/cm ²)	Required Minimum Beam Current* (mA)	Machine Design Specification (mA)	Demonstrated Beam Current (mA)
¹¹ B ⁺	1 x 10 ¹⁵	1.0	0.7	0.9
³¹ P ⁺	1 x 10 ¹⁵	1.0	1.0	4.2
	2 x 10 ¹⁵	2.1	1.0	4.2
⁷⁵ As ⁺	1 x 10 ¹⁵	1.0	1.0	2.5

* These beam currents provide 7-sec implants; an additional 5 sec is allowed for wafer transport.

TABLE 2-2. MEASURED BEAM CURRENTS FOR THE HIGH-CURRENT
IMPLANTER AS A FUNCTION OF BEAM ENERGY

Beam Energy (keV)	Beam Current (mA)		
	¹¹ B ⁺	³¹ P ⁺	⁷⁵ As ⁺
5	0.89	-	-
10	0.89	4.2	2.5
15	0.95	2.4	1.6
20	0.95	2.2	1.2
25	0.96	2.0	1.1
30	0.96	2.0	1.1
35	0.96	2.0	1.1
40	0.96	2.1	1.1
45	0.96	2.2	1.2
50	0.95	2.3	1.2

An example of an implant requirement previously impractical because of low beam currents is effective back surface fields. Back surface fields processed with a 50-microampere beam and a dose of $5 \times 10^{15} \text{ }^{11}\text{B}^+ \text{ cm}^{-2}$ needed approximately 16 min for a 3-inch wafer. The high-current machine, however, with 1-mA beam of $^{11}\text{B}^+$ ions, can complete the implant in 40 sec. Implant parameters which effectively replace conventional aluminum thick-film back surface fields have been produced. The advantages of boron implantation over the aluminum alloy will become critical for polycrystalline-silicon material processing where intergranular alloying is to be avoided.

It has been necessary to develop operational parameters for the high-current solar cell implanter to provide adequate implant dose uniformity. A target uniformity variation was specified to be ± 10 percent across the wafers with diameters of 7.6 cm. The requirement of ± 10 percent uniformity was placed on both the phosphorus ($^{31}\text{P}^+$) junction implants and the boron ($^{11}\text{B}^+$) back surface field implants. Implant dose levels and ion energies were optimized for maximum cell efficiency using a Varian/Extrion model 200-20A implanter.

The final implanter setup parameters were determined by considering the dose uniformity variables of ion energy, ion species, degree of overscan, and scan frequency. Table 2-3 shows the specified implant parameters necessary to manufacture 500 deliverable cells for JPL. Figure 2-7 shows the resultant implant dose uniformity achieved for boron implants, and Figure 2-8 shows the uniformity for phosphorus junction implants. Both sets of implant parameters result in dose variations within the uniformity goal of ± 10 percent. Quantitative measurements of the neutral beam component have shown this nonscanned component to be the major contributor in the uniformities of ± 10 percent.

TABLE 2-3. HIGH-CURRENT IMPLANTER SETUP PARAMETERS

Ion	Energy (keV)	Dose (cm^{-2})	Scanning External Magnetic Field Frequency (Hz)*		Overscan (%)
			X	Y	
$^{11}\text{B}^+$	25	5×10^{15}	8	6	30
$^{31}\text{P}^+$	10	2.5×10^{15}	8	6	20

* All electromagnets are driven by a sine-wave modulated power supply.

SHEET RESISTANCE MAP

Signetics Corp., June 5, 1978, 21:24
U3385, Spire's Boron Implant Wafer #1184-11

<u>Parameters</u>	
CF	= 4.500
FPP Spacing	= 0.025 in.
Current	= 1050.0 microamperes
Contour Integral	= 1 percent
Wafer Diameter	= 3 in.
Measured Uniformity	= 96.82 ohms/sq + 7.50 percent
Implant	= 5×10^{15} 11B^+ cm^{-2} , 25 keV (100) Si

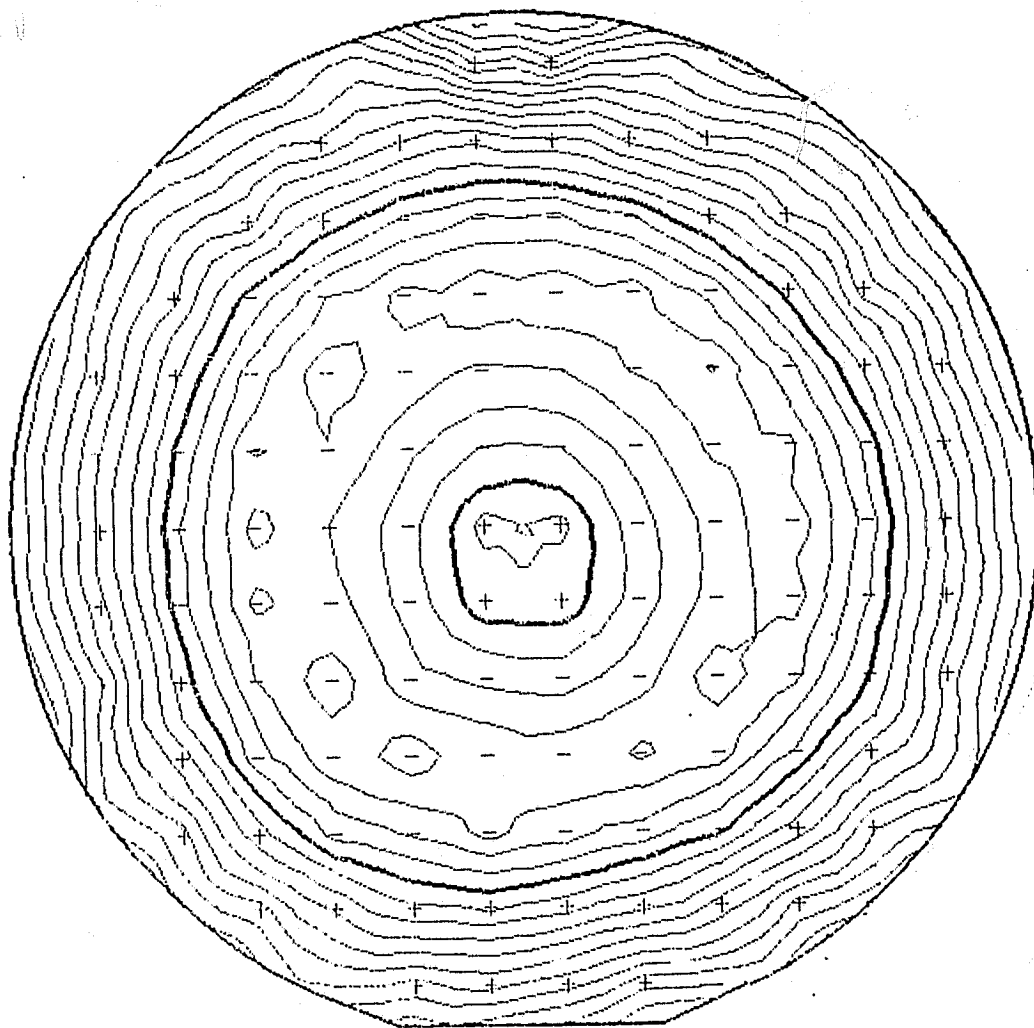


FIGURE 2-7. SHEET RESISTANCE CONTOUR MAP FOR STANDARD BORON IMPLANTS AFTER ANNEALING

SHEET RESISTANCE MAP

Signetics Corp., July 12, 1978, 19:40
U3421, Spire's Phosphorus Implant Wafer #1184-8

Parameters	
CF	= 4.5
FPP Spacing	= 0.250 in.
Current	= 3000 UA
Contour Integral	= 1 percent
Wafer Diameter	= 3 in.
Measured Uniformity	= 45.71 ohms/sq + 7.81 percent
Implant	= 2×10^{15} 31P^+ cm^{-2} , 10 keV (100) Si

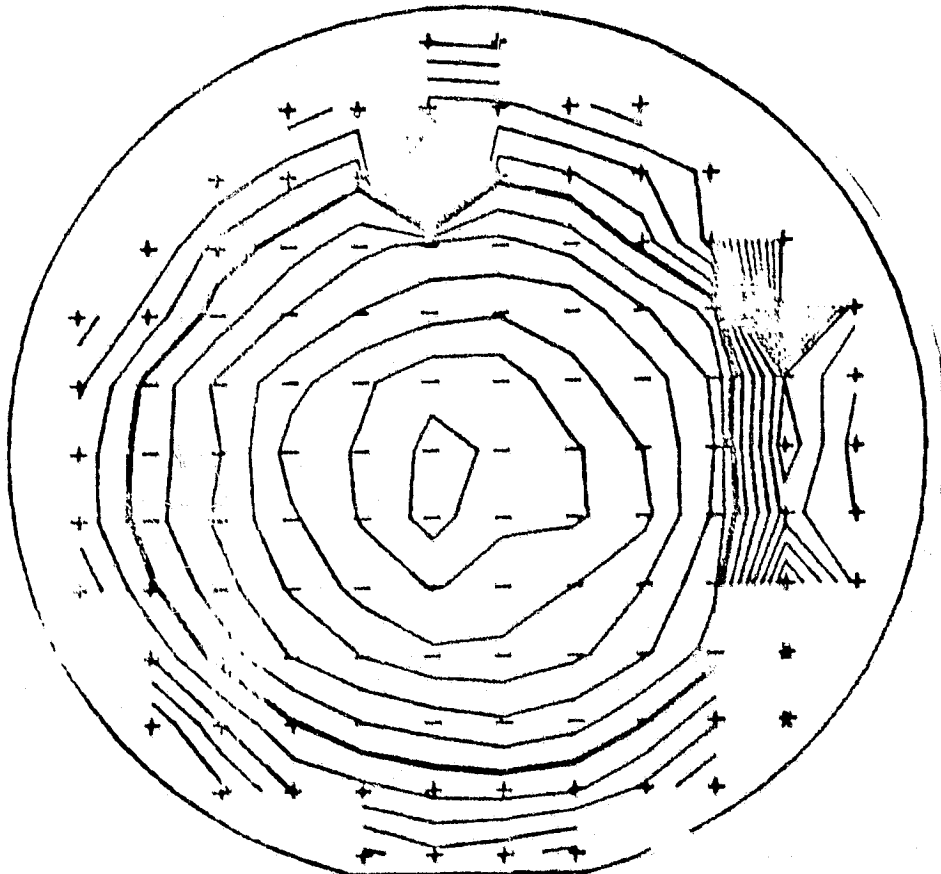


FIGURE 2-8. SHEET RESISTANCE CONTOUR MAP FOR STANDARD PHOSPHORUS IMPLANTS AFTER ANNEALING

2.1.3 Design of an Automated Production Implanter

The implanter described in Section 2.1.2 can serve immediate needs for implanted solar cell process development. But if implantation is to be practical for use as the central element for automated production to meet the mid-1980 objectives, dedicated machines with higher beam currents and faster throughput characteristics must be developed. The basic engineering design of such a solar cell production implanter has been completed. The production implanter will operate continuously at delivered beam current levels of not less than 100 mA. (The operational characteristics of a conventional high-current implanter, the dedicated solar cell implanter and an automated production implanter are compared in Table 2-4.) As shown in Table 2-4, solar cell product throughput of one automated production implanter machine in full operation will be approximately 100 MW_e peak output per year. To conduct this design study, Spire employed Dr. Peter H. Rose, generally recognized as one of the world authorities on ion implanter design and construction.

TABLE 2-4. COMPARISON OF ION IMPLANTATION EQUIPMENT FOR SOLAR CELL JUNCTION IMPLANTS

Specification	Conventional High Current Implanter (Extrion 200-1000)	State-of-the-Art Solar Cell Process Implanter	Advanced Solar Cell Automated Production Implanter
Process Mode	Batch	Continuous	Continuous
Carrier	None	Cassette	Platen
Phosphorus Beam Current	2 mA @ 25 keV	4 mA @ 10 keV	100 ma @ 10 keV
Beam Utilization Efficiency	3%	15%	83%
Throughput	0.14 m ² /hr	1.4 m ² /hr	180 m ² /hr
Solar Cell Product Per Year	100 kW _e	1 MW _e	100 MW _e

A set of functional requirements for the automated production implanter has been defined to meet minimum performance objectives (as shown in Table 2-5). The implanter must provide continuous, uniform, reproducible, high-volume throughput. The design is conservative, with high assurance of meeting all objectives. The general design requirements are described below, with system drawings included in Appendix A. An artist's conception of the facility is shown in Figure 2-9.

The automated production implanter system includes multiple ion sources (10), a beam extraction and acceleration stage, an ion-beam mass analysis system, a magnetic beam-scanning system with a material processing chamber complete with load/unload systems, and conveyors and vacuum locks to allow for the continuous flow of material through the system.

TABLE 2-5. SOLAR CELL PRODUCTION IMPLANTER PERFORMANCE SPECIFICATIONS

Ion Species:	$^{31}\text{P}^+$, $^{75}\text{As}^+$, $^{11}\text{B}^+$ (Single machine may be dedicated to only one ion)
Ion Energy:	Fixed within the range 10 - 30 keV
Beam Current:	Minimum 100 mA of $^{31}\text{P}^+$
Analyzed Beam Purity:	Resolution of 0.5 amu at mass 31
Beam Uniformity/Reproducibility:	Not worse than $\pm 10\%$ over all material area processed
Substrate Throughput:	Variable - minimum of 500 cm^2/sec at 1×10^{15} ions/ cm^2
Materials to Be Processed:	Silicon wafers, ribbon, or sheet to maximum individual-item dimensions of 20 x 20 cm
Surfaces to Be Implanted:	Planar and texturized
Processing Mode:	Continuous flow
Operational Mode:	Continuous throughout routine and predictable component failure maintenance

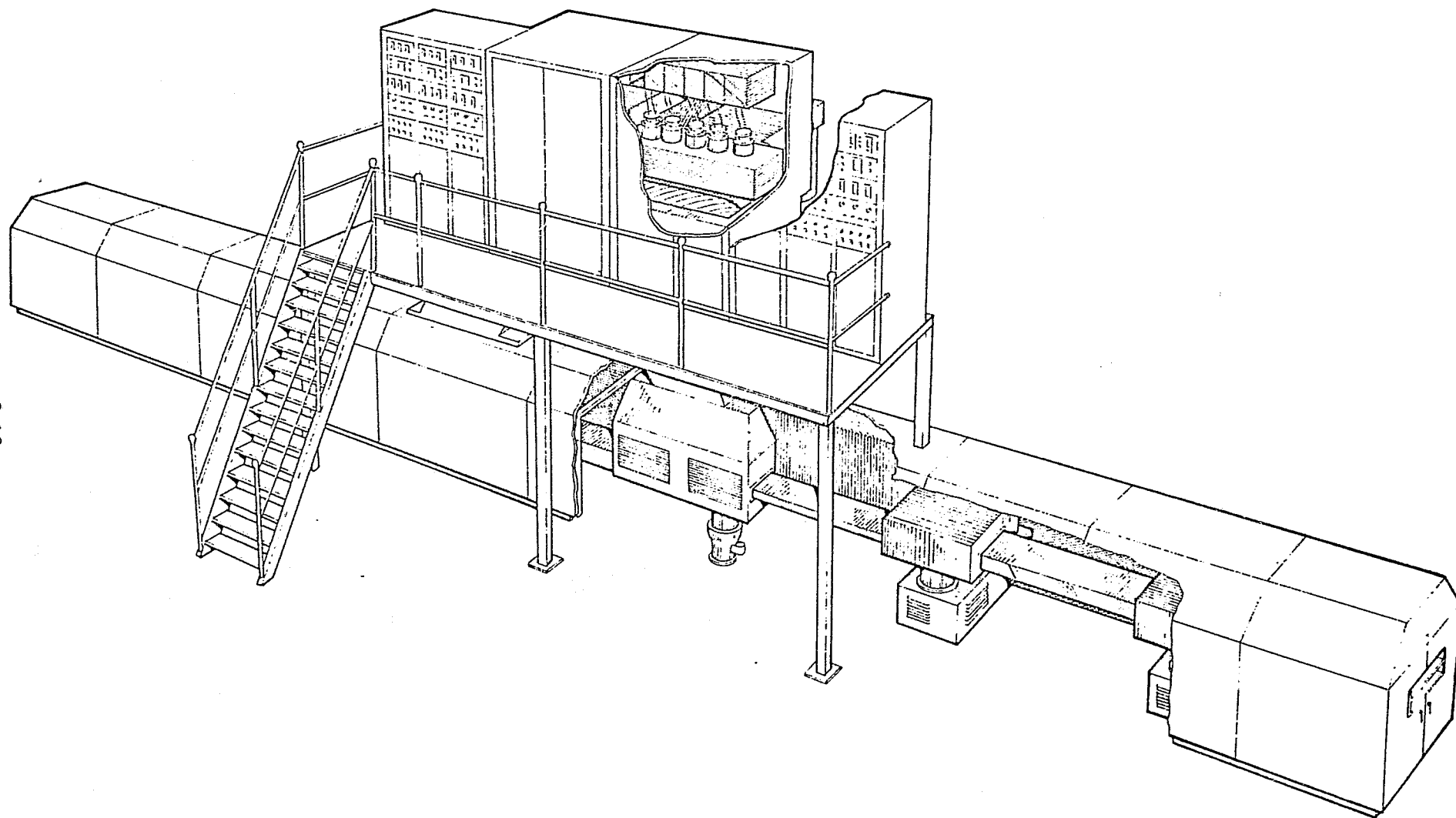


FIGURE 2-9. CONCEPTUAL DRAWING OF A 100 mA AUTOMATED PRODUCTION IMPLANTER

The material to be processed must be of a size to fit inside the boundaries of the 21-centimeter-by-21-centimeter carriers which will be used to transport substrates through the system. Vacuum systems using diffusion pumps will be provided to pump the gas from the ion sources and to pump the gases and vapors evolved by the substrate during its passage through the target chamber. Additional pumping — in this case, mechanical pumping — is to be provided to reduce the atmospheric pressure to the operating pressure in the entrance and exit sections of the machine. Fast-operating locks will be used to prevent continuous gas flow into the system.

The implanter will include power supply systems for the ion sources, analyzing magnet, and scanner system. These units will be linked together by the signals from the instrumentation for beam current measuring, which will include Faraday cages and multichannel current metering. The dose monitoring system will be capable of measuring the uniformity of the dose provided by each ion source system. The dose may be preset, with the dose controller then automatically keeping the dose within specification of ± 10 percent.

The machine is to be fully automated; i.e., only one control is to be needed to start or stop the implanter once the setup conditions have been satisfied. A minicomputer will be used to link together the various subsystems and to provide controls, displays, and data logging.

Ion Sources

The ion sources (Figure 2-10 shows one such source) are to be arc discharge sources with an exit aperture 75 mm long by 2 mm wide. The arc chamber is to be made of molybdenum shaped to focus the beam from the ion source into the magnet gap with very little loss of beam. The ion sources are designed to operate on gases such as hydrogen-diluted PH_3 (or, in the case of boron, BF_3). The design of the source and the source power supplies does not exclude the later provision of vaporizer sources. It will be possible safely to remove an ion source from the system for maintenance and replacement while the machine is running. The source gas feeds, roughing system, and power supplies are to be independent of each other. Each source module is to be completely interlocked to prevent accidental operational errors or dangerous situations. The sources are designed to operate for 24 hours with a probability of failure of less than 1 percent. The sources are to be removed for filament replacement and maintenance

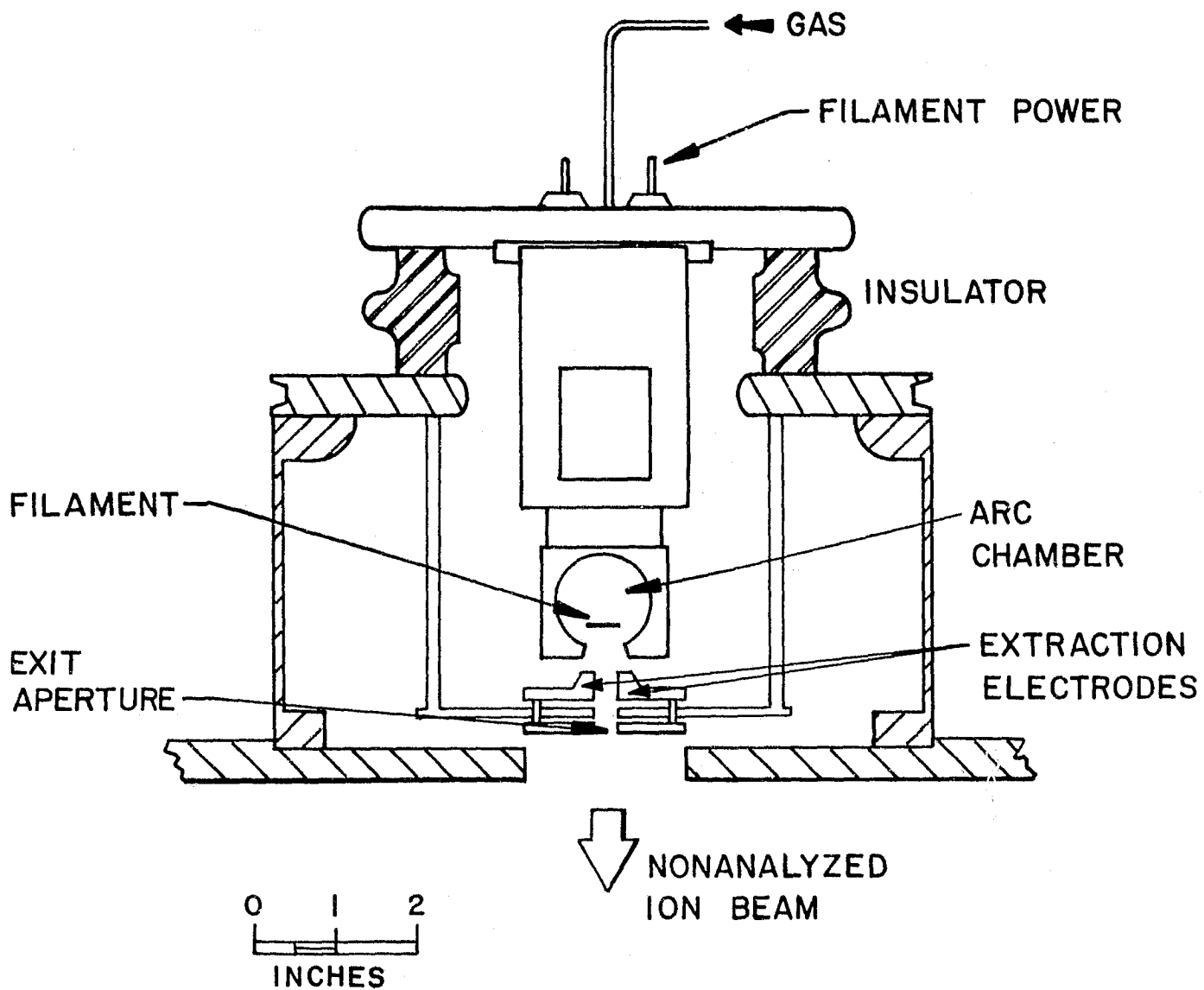


FIGURE 2-10. HIGH-CURRENT ION SOURCE CROSS SECTION

within this 24-hour period. Each source is to be controlled by its own servo-loop with monitoring instructions from the main control computer. All control signals and displays will be optically isolated.

Each ion source is designed to provide 20 mA of analyzed $^{31}\text{P}^+$ beam. To process texturized or low-grade surface substrates, five sources will implant at an angle of $+15^\circ$ to normal and five at -15° to normal. During machine operation with a total beam current of 100 mA, three sources will operate at 16 mA each and at $+15^\circ$, while three others will operate at the same current level at -15° . The additional 4 mA will be made up by a seventh source, which will provide the fine-dose control. The remaining three sources will be in various stages of programmed maintenance. At any given time the combination of the 16-mA sources and one 4-mA source will be providing the total of 100 mA of analyzed beam.

Acceleration System

The extraction or acceleration system involves a single-gap geometry with a negatively biased electrode to trap electrons. The extraction power supply for each of the 10 ion sources is to be rated at 50 mA of continuous current. The supplies for each source will be independently controlled and may be varied ± 2 percent about the predetermined value, so that the position of the beam in the analyzing slit region can be optimized. To minimize neutral beam formation, a series of restrictions or apertures, one for each source, is to be placed ahead of the analyzer entrance pole face. After initial adjustment, the mechanical components can be removed for changing or cleaning and returned to the original position with a jig.

Mass Analyzing System

The ion beam will enter the analyzer pole face perpendicularly (see Figure 2-11). The magnet pole deflection angles (there are two poles, one deflecting at $+45^\circ$ and the other at $+30^\circ$) and pole face angles will be chosen to focus the beam on the target at an angle of $+15^\circ$. The focusing system is to be such that the beam will focus in the analyzing slits and in an orthogonal direction on the target. The radius of curvature of the beam trajectory in the magnetic field will be 30 cm.

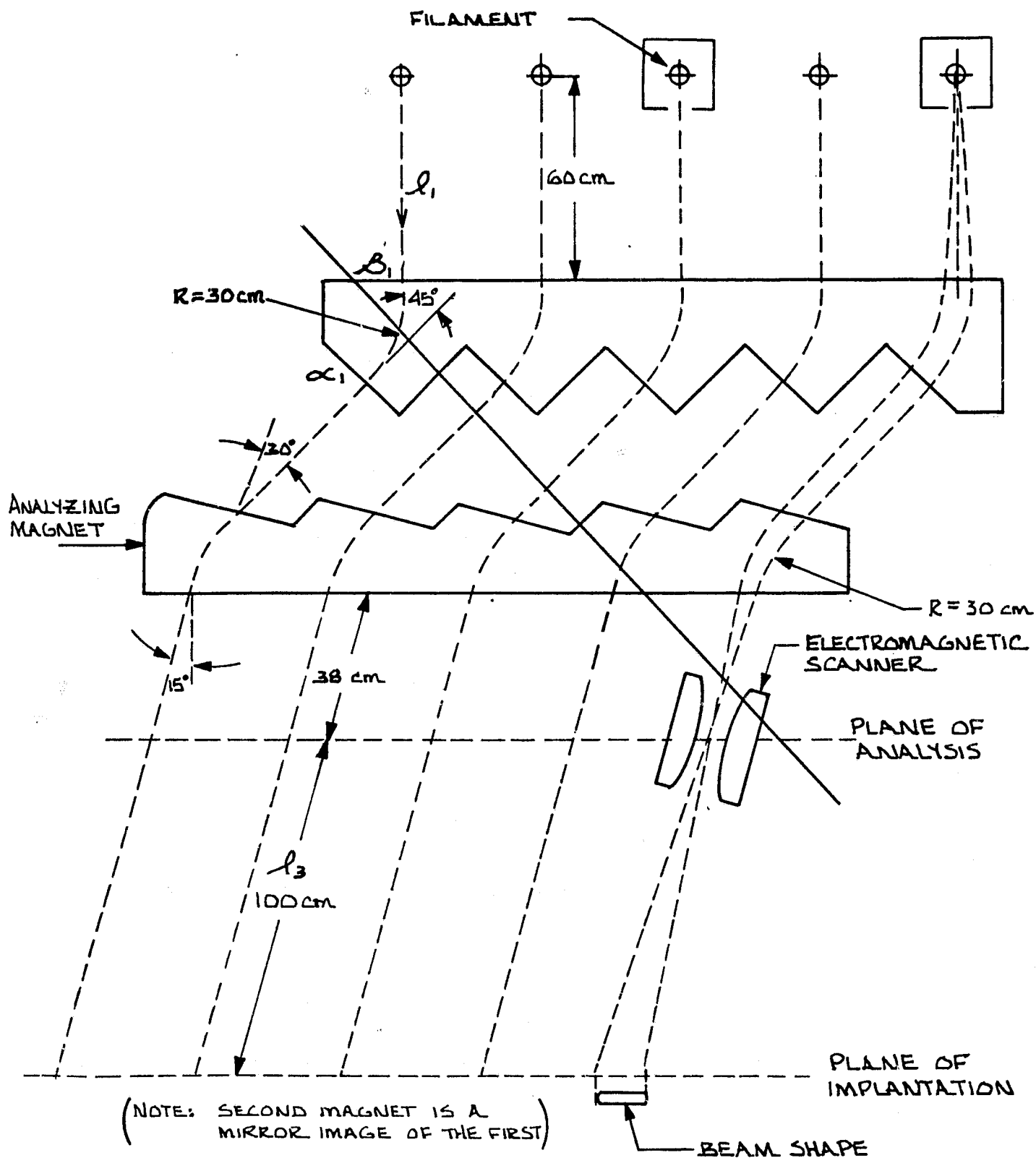


FIGURE 2-11. SCHEMATIC DIAGRAM OF THE BEAM TRAJECTORY THROUGH THE ANALYZING AND SCANNING SYSTEM

Ion-Beam Scanning System

A magnetic ion-beam scanning system with a laminated core will be utilized and, to minimize the power required to scan the ion beam, the magnetic field gap will be located in the region of the crossover. The minimum gap between the poles of the scanning magnet will be 10 mm and the deflection angle will be $\pm 5^\circ$. The magnet iron and drive coils will be shielded from the ion beam and located in the vacuum of the analyzer tank. A scan generator is to be provided which can be adjusted to produce the correct waveform to satisfy uniformity requirements. This part of the system will provide a ± 5 percent uniformity of dose. A wide-band amplifier will be employed to drive the system. The mean position of the scanning magnet is to be 1,200 mm below the exit of the analyzing magnet. Each scanner coil and magnet will be removable for repair, and will be coded and pinned to prevent replacement into an incorrect location. To change a scanner magnet the main vacuum system will have to be vented to atmospheric pressure.

Process Chamber

The implant process chamber is to be provided with a chain drive substrate carrier system. Carriers are to be fed onto this chain at two levels from the entrance lock, one 15 mm below the other (see Figure 2-12). Three carriers at a time will pass through each level with a gap of 45 mm between the groups of three on the same level. The chamber is to be provided with a series of mechanical beam gates provided with Faraday cages. A set of eight slits is to be used for beam dose uniformity measurement and for scan adjustment. The beam gates are to be driven by stepping motors under control of the central computer. Cooling is to be provided for all parts of the system where necessary.

Material Transport

The three-carrier groups will be fed in sequence into the machine at the alternate levels, spaced vertically by 24 mm at the entrance and exit. This sequence is shown diagrammatically in Figure 2-13. The spacing between the sets of three in the longitudinal direction of 45 mm will provide time for valve sequencing. The vacuum locks are to be closely synchronized, to maintain the relative spacing of the carriers to prevent jamming and vacuum failure. The speed of the system is to be nominally 30 cm/sec, but will be variable between a maximum speed of 40 cm/sec and a minimum

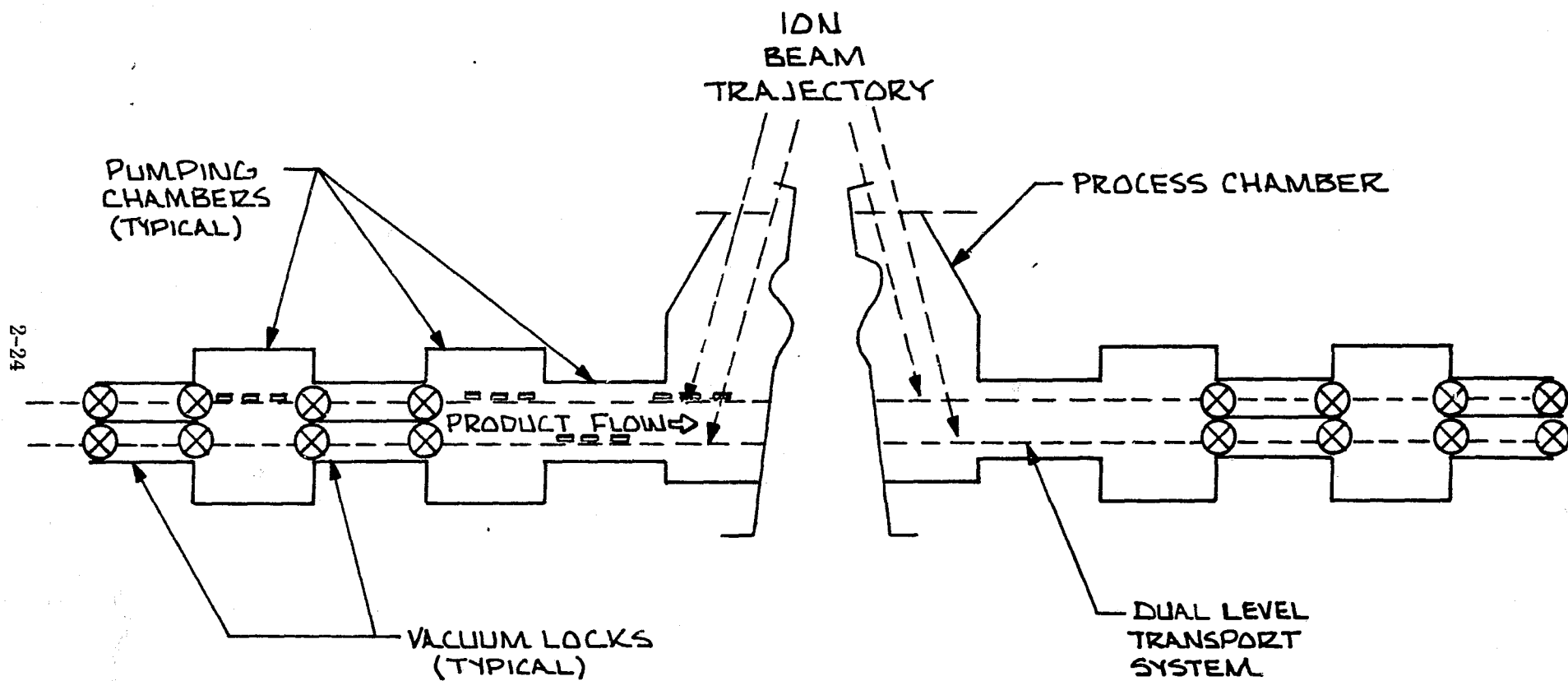


FIGURE 12. MATERIAL TRANSPORT SYSTEM

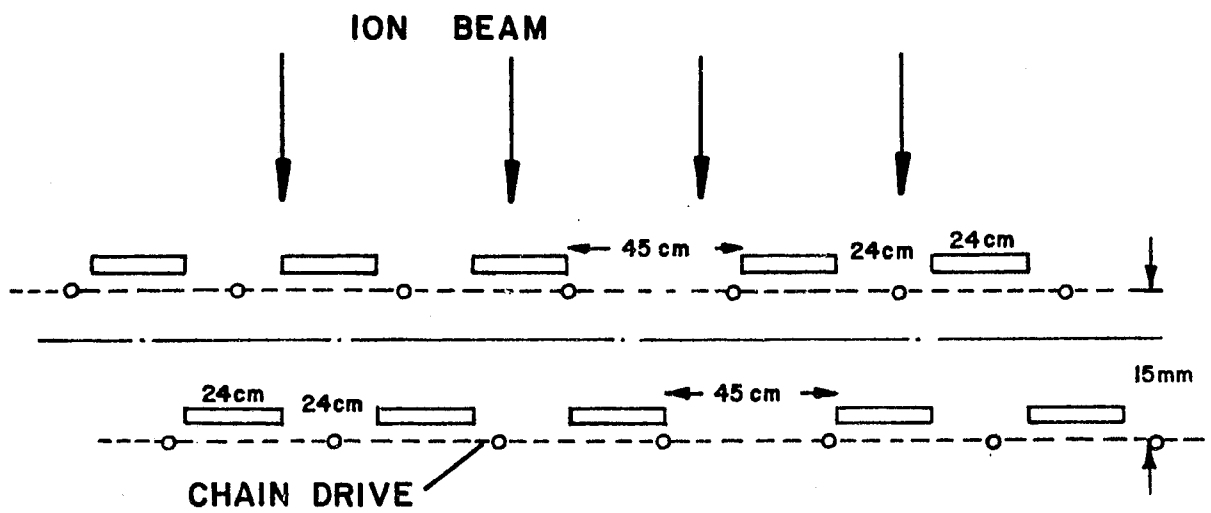


FIGURE 2-13. TWO-LEVEL MATERIAL TRANSPORT SEQUENCE

of 5 cm/sec by adjusting the speed of the drive motor. The carrier system will be constructed to be operated from this single motor, using a mechanical means to provide the belt or carrier drive along the length of the machine. The lock valves will open and close within 0.1 sec, and will be constructed to be individually and quickly serviced. The pumping is to be provided by 1,000-l/sec blowers pumping a plenum after each of the two vacuum lock systems. Between the second lock system and the process chamber there is to be a gas restriction channel. This channel will be provided with a port to enable an extra stage of differential pumping to be employed if necessary. The lock system will reduce the influx of dry nitrogen into the process chamber to less than 500 l/sec at the operating pressure of 5×10^{-6} torr. Moist air will be prevented from entrainment into the implanter by a filtered hood system at the entrance and exit, continuously purged with dry nitrogen. The class of cleanliness in this entrance region is to be 100 or better.

Vacuum System

General - The vacuum system is to be divided into different subsystems (1), (2), (3), and (4), which depend on the degree of vacuum required and the function to be performed.

- (1) The high-vacuum subsystem — comprising the ion source chambers, analyzing section, and process chamber — will, when sealed from the rest of the system, be capable of reaching a base pressure of 5×10^{-7} torr. To make this possible, the major parts of the vacuum system are to be constructed of stainless steel, cleaned by the Diversy process or some equivalent technique. The mild steel electromagnetic poles in the analyzing vacuum system will also be carefully cleaned and free from inclusions or virtual leaks. It may be necessary to ion plate or coat the poles with a corrosion resistant material such as nickel to prevent outgassing. Viton gaskets are to be used as a vacuum seal in this and all other parts of the system. The analyzer and process chamber will be pumped by large diffusion pumps.

The ion-source vacuum subsystem must provide adequate pumping speed to accommodate source gas introduction while maintaining the operating vacuum level.

- (2) The source gas system is to be of stainless steel and other corrosion resistant materials such as ceramic. The gas lines are to be designed to minimize the hazard associated with toxic gas feeds. A special, protective gas venting system is to be provided. The source roughing system is to be fabricated from brazed copper pipe, with brass or stainless steel bellow valves being employed. Flanged couplings are to be provided where necessary to enable the system to be disassembled for cleaning. Stainless steel bellows are to be provided between each source chamber and the roughing valve, and also for isolating the vibration of the mechanical pumps.
- (3) The lock chambers are to be fabricated from stainless steel, cleaned by an electrochemical means. The chains and chain drives are to be of ordinary steel, with some lubrication with low-vapor-pressure grease allowed in this transport area. The moving mechanical parts inside the vacuum are to be designed to operate without maintenance for at least 2,000 hours. The blowers are to be coupled directly to the pumping plenums without vibration isolation. Viewing ports are to be provided for inspection of the system during operation. The entrance and exit systems are to be identical, except for changes due to the different directions of product flow.
- (4) A roughing and dry-nitrogen bleed subsystem is to be provided for system maintenance. The rough-down time of the main chamber to a pressure of 10 micrometers is expected to be 20 minutes.

Controls - The vacuum system will cycle from the atmosphere pressure level to the operating condition automatically under control of the main computer. Necessary readouts and interlocks are to be provided to make this possible. Certain valves will have positive indication of closure to prevent accidents due to the accidental presence of a carrier or substrate material. In addition, because of the continuous and rapid flow of material through the system, clutches and other devices will be provided to stop the system and prevent a catastrophic vacuum failure. It will be possible to bring the carrier system to rest in 3 seconds.

Maintenance - Routine vacuum maintenance will be provided based on the vacuum equipment manufacturers' regular requirements. Forepump fluid can be changeable without shutting the machine down. Changing diffusion pump oils and cleaning the analyzer and process chamber will take 24 hours.

Pumps required for the system are:

- Twenty-inch oil diffusion pumps with halo baffles giving an effective pumping speed for air of 11,000 l/sec.
- Six-inch oil diffusion pumps unbaffled with a speed of 24,000 l/sec.
- Two-stage, direct-drive mechanical pumps (14.6 cfm).
- Two-stage, direct-drive mechanical pumps (37.6 cfm).
- Roots-type blower pumps with internal motors (no shaft seal) and a speed of 1,000 l/sec.

Valves for the system are available commercially, for the most part. The lock valves and the valves above the 20-inch diffusion pumps will have to be engineered specially for this machine.

Carriers

The carriers are to be made of aluminum plate, with the following dimensions: 210 mm by 210 mm by 6 mm (8.375 in. by 8.375 in. by 0.25 in.). The plate will be selected for minimum outgassing. After manufacture, the surfaces will be polished and cleaned.

Control Console

The implanter control console will be connected to the implanter by armored cables. The console will consist of three 6-foot-high cabinets connected together and provided with a desk. The console will provide a main operator control panel to enable an operator to start up, process, and shut down the machine without any other actions. Two display panels will indicate the status of the ion sources and of the vacuum system. The display will be such that a fault condition is indicated by both a red light and an audible alarm. The computer system is expected to be a Digital Equipment Corporation PDP/11. The unit selected for the prototype implanter system will be suitable for software development and will include:

- 11/34A CPU (32 KW of memory)
- Serial line unit
- Real-time clock

- RL11 - AK disk control/drive (5 megabytes)
- RL01 - AK drive (5 megabytes)
- LA11 - PA printer

All communication from the implanter subsystems to the computer will be via optical isolators, as shown in Figure 2-14.

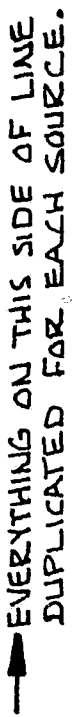
Software

The system is to be designed to minimize the initial software requirements. The control circuitry will be designed so that the servo-loops are at the lowest level. Software programs will be written initially for:

- Uniformity measurement (but not to adjust the scanner waveform automatically)
- Dose calculation and adjustment of the scanned source current to give the correct dose
- Vacuum system control
- Transport system control and synchronization
- Monitoring variables such as the status of locks, temperature levels, and carrier speeds
- Data logging
- Displays for the CRT system for use in diagnostics
- Troubleshooting routines
- Start-implant and stop-implant programs.

Facility Requirements

Based upon the present design, the facility requirements for installation and operation of the prototype solar cell production implanter are as listed in Table 2-6. The size and weight of the solar cell implanter will be compatible with a typical semiconductor production area. The power, cooling, and other requirements will be met by standard industrial facilities. Overall dimensions are given in Figure 2-15.



2-30

TABLE 2-6. FACILITY REQUIREMENTS FOR PROTOTYPE
SOLAR CELL PRODUCTION IMPLANTER

Item	Requirement
Power	200 kVA, three-phase, four-wire, grounded neutral plus equipment ground
Water	5 kg/cm ² (75 psig) maximum inlet pressure; 2.8 kg/cm ² (40 psig) minimum differential pressure between inlet and outlet; flow rate 140 l/sec (35 gpm); Maximum inlet temperature 27°C (80°F)
Compressed Air	4.7 - 7 kg/cm ² (60-100 psig) for pneumatic valves
Dry Nitrogen	1.9 l/sec (4 cfm) continuous flow at transport system entrance and exit
Ventilation	565 l/sec (1,200 cfm) exhaust
Site Preparation	For unit shown in Figure 2-15.

2.1.4 Manufacturing Cost

Estimated costs to manufacture the solar cell production implanter are summarized in Table 2-7. Costing is based upon experience with present generation implanters which are much smaller, but more versatile and complex. Profit to be expected by the machine manufacturer is not indicated. Costs for units subsequent to the prototype model assume that at least 10 machines will be constructed over a period of several years, and engineering changes will be incorporated as a result of operational experience.

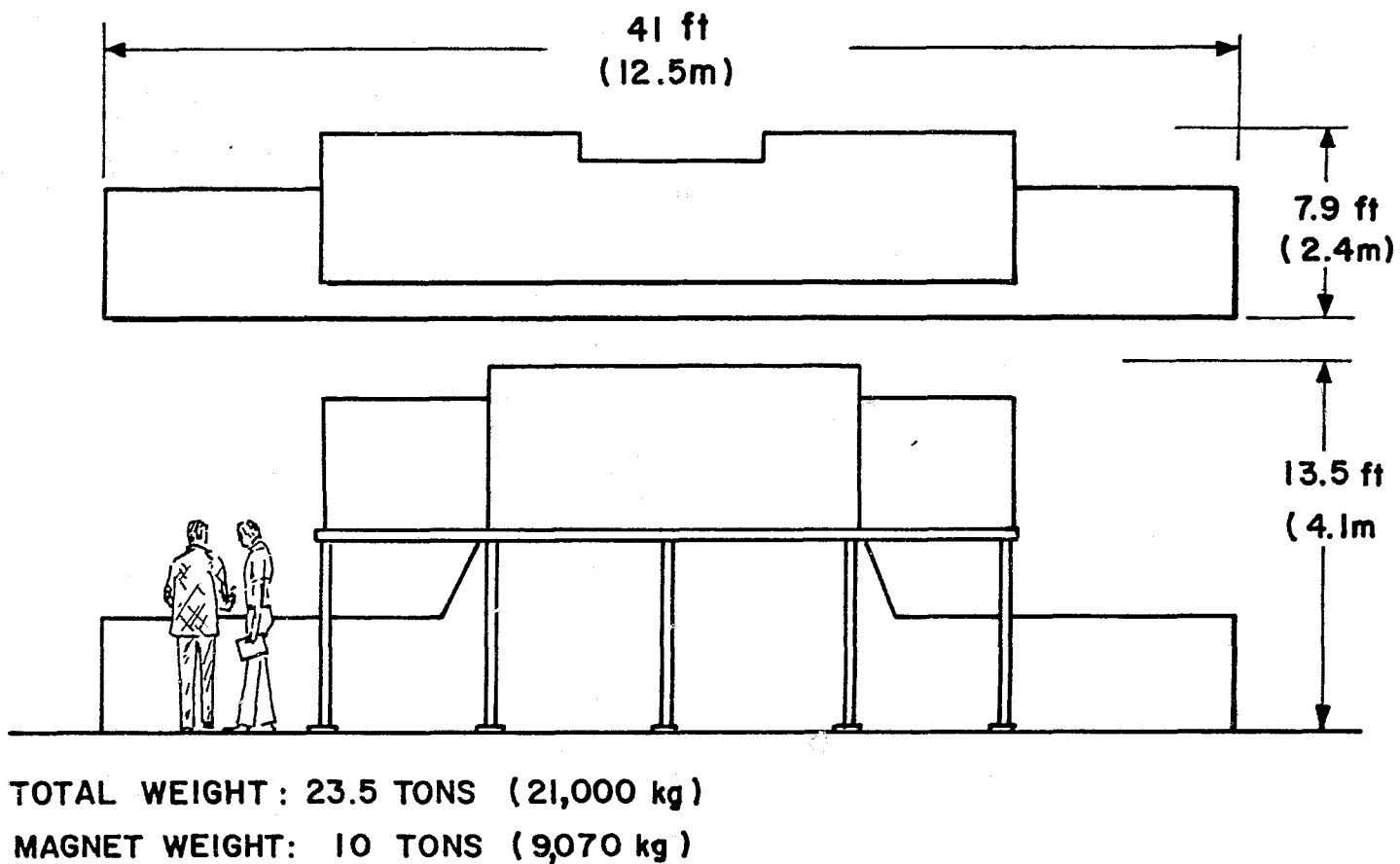


FIGURE 2-15. FACILITY REQUIREMENTS AND OVERALL DIMENSIONS FOR AN AUTOMATED PRODUCTION IMPLANTER

TABLE 2-7. ESTIMATED MANUFACTURING COSTS OF SOLAR CELL PRODUCTION IMPLANTERS

Item	Cost	
	Prototype Unit	Subsequent Units
1. Construction Management	\$ 100,000	\$ 10,000
2. Engineering	400,000	38,000
3. Documentation	(Included in item 2)	14,000
4. Material and Subassembly Labor		
- Control Console	18,000	
- Entrance and Exit Vacuum Assembly	197,000	
- Analyzing Magnet	78,000	
- Magnet Power Supply	129,000	
- Ion Sources	20,000	
- Implanter Vacuum Chamber	107,000	
- Diffusion Pumps	15,000	
- Mechanical Pumps	8,000	
- Miscellaneous	18,000	
Subtotal	590,000	400,000
5. Other Manufacturing Costs	59,000	40,000
6. Assembly on Site	32,000	20,000
7. Test and Qualification	40,000	20,000
8. Software Development	60,000	10,000
Totals	\$1,281,000	\$552,000

2.2 SOLAR CELL DEVELOPMENT

2.2.1 Advantages of Ion Implantation Processing

It has become apparent that ion implantation will have a major role in high-volume, automated production of terrestrial solar cells. The inherent purity, control, and reproducibility traditionally associated with implantation are important to any automated manufacturing process. However, implantation, when properly utilized for solar cells, can involve many other significant advantages.

Implantation is an ambient temperature, line-of-sight process, carried out in a vacuum environment, which deposits no residues and produces no surface layers requiring subsequent removal. As a result, implantation can be incorporated into drastically abbreviated production concepts. Even in simplified processing schemes, implantation allows versatility in the preparation of advanced solar cell structures to yield high performance.

For integration into production lines with massive throughput, ion implantation offers genuine ease of automation, can be scaled to satisfy virtually any line rate and throughput required, and can be utilized with simple redundancy to insure process continuity even throughout routine maintenance and component failure correction. Dopant introduction by implantation is efficient and involves minimal waste of often toxic, always costly dopant source materials. Elimination of postdoping, wet chemistry operations for residue or surface layer removal not only reduces processing complexity, but also substantially decreases processing wastes. Implantation is performed at room temperature and requires only modest expenditure of energy. Finally, for massive scale production, the unit item expense of ion implantation will be very small, with implantation allowing the production of the highest possible efficiency solar cells at the lowest possible cost.

To assess and advance the technical status of ion implantation for silicon solar cells and to integrate implantation processing into a simplified, automated production process for the highest efficiency cells, the following tasks were performed under this program:

1. Improvement of cell design, structure, and performance using implantation for n^+ and p^+ dopant introduction
2. Assessment of the relative performance of otherwise identical cells with diffused and ion implanted junctions
3. Integration of high-performance cell structures into an abbreviated implantation/pulse energy processing sequence being developed for low-cost, automated production.

2.2.2 Ion Implantation Parameter Selection

To utilize ion implantation in manufacturing solar cells, process parameters must be selected for both junction and back surface field layers. These parameters include ion species, ion dose, ion energy, beam current, angle of incidence, substrate temperature, and dose uniformity both wafer to wafer and within the wafer.

Junction Layer for n^+/pp^+ Structures

Selection of implant parameters for junction introduction is one of the critical design elements for high efficiency solar cells. The parameters are interdependent with subsequent annealing processes and contact grid design. Because implant parameters are flexible, both concentration and dopant location can be easily controlled; however, implanted dopant profiles are quite different from the theoretical predictions for low-energy ions in crystalline materials.

Desirable characteristics of a solar cell junction layer are quite well known. These are summarized below and in Figure 2-16.

1. A relatively shallow junction is necessary for good blue response. Typically, the desired junction depth is from 0.1 to 0.3 micrometers for highest efficiency. Either phosphorus ($^{31}\text{P}^+$) or arsenic ($^{75}\text{As}^+$) can be used as an n-type dopant with implantation. Arsenic has an inherent advantage over phosphorus for producing shallow junctions because its larger atomic size results in less penetration. However, more experimental effort has been carried out to date with phosphorus implantation, in part because successful annealing of the implantation damage has been achieved.
2. The peak dopant concentration should fall continuously from the surface. In practice, this is quite difficult to accomplish without using oxide or nitride layers as preabsorbers. However, these layers can result in knock-on oxygen or nitrogen implants. Furthermore, the use of an absorber increases the implant dose required and reduces implanter throughput.
3. Retrograde fields in depth must be avoided. It is necessary to minimize the channeling of ions along crystal axes which can produce a second peak in the implanted/annealed dopant profile. A severe case of channeling is shown in Figure 2-17. Reduction of channeling is achieved by intentionally misaligning the ion beam and the silicon wafer by 7 to 15°.

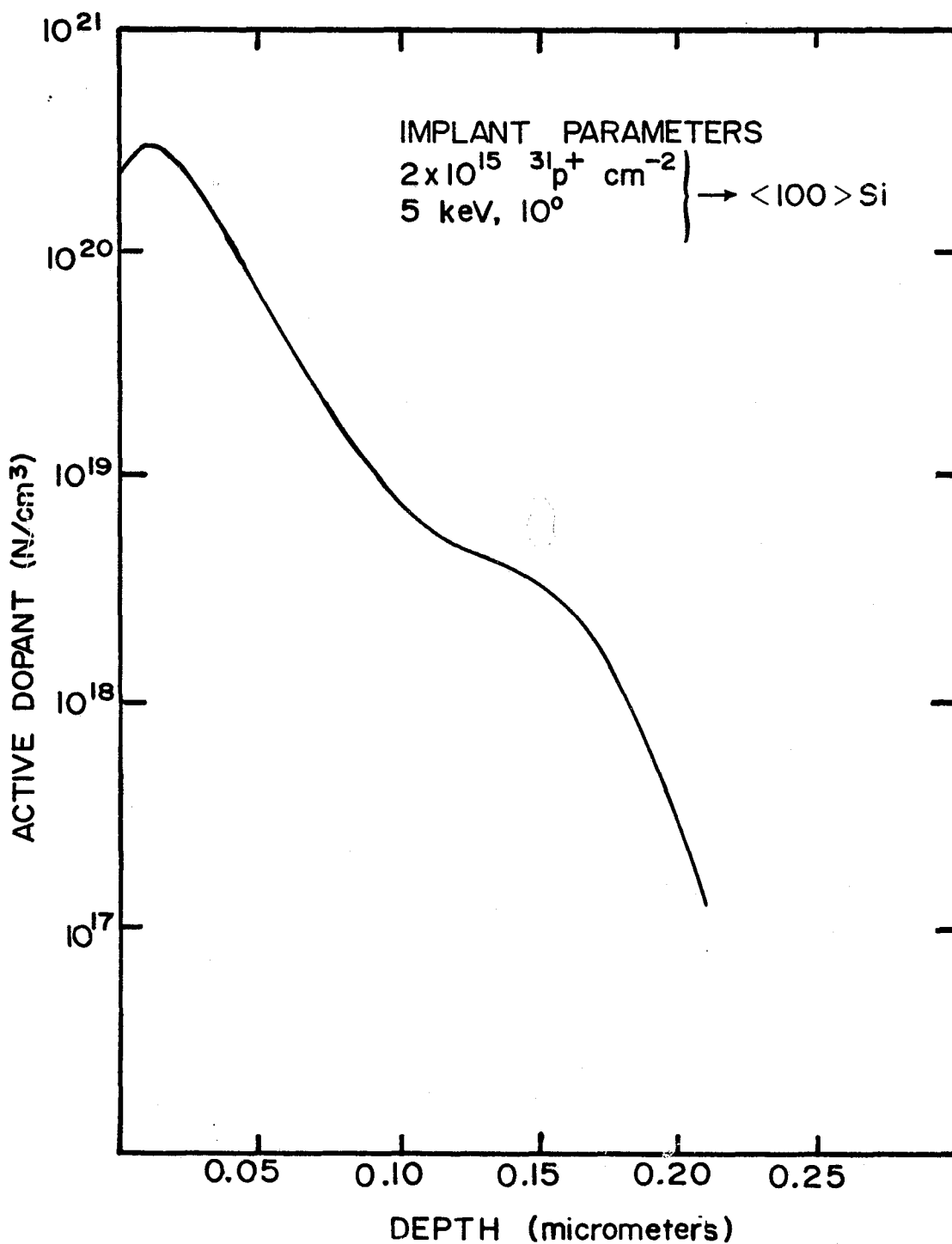


FIGURE 2-16. MEASURED JUNCTION IMPLANT PROFILE FOR n^+/pp^+ CELL STRUCTURE

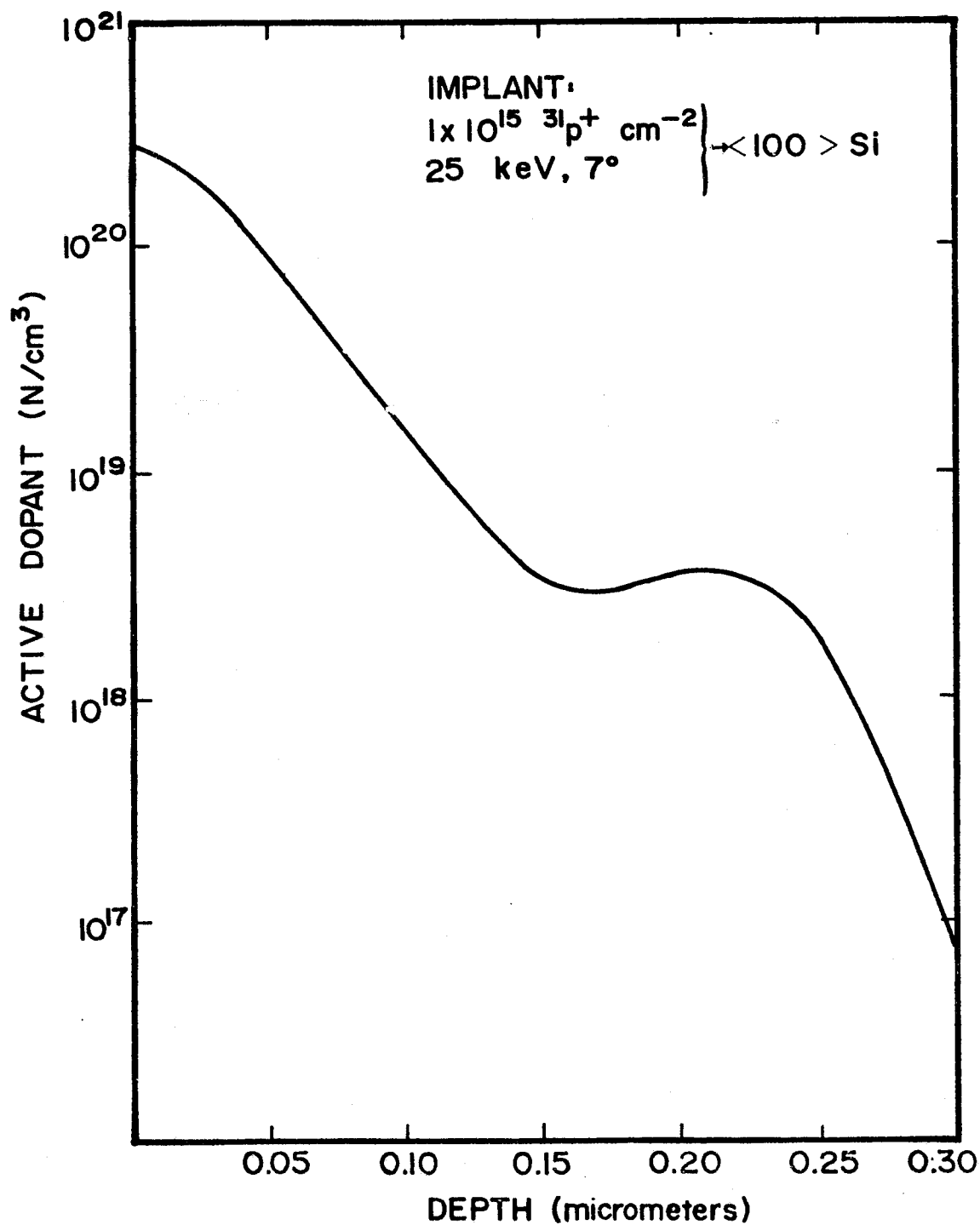


FIGURE 2-17. HIGHLY CHANNELED IMPLANT JUNCTION PROFILE

Back Surface Field Layer for n^+/pp^+ Structures

Selection of implant parameters for back surface layers depends upon the solar cell design requirements. For silicon with resistivities greater than 10 ohm-cm and with high minority carrier lifetime, the p^+ layer can act as a high-low junction or back surface field (BSF). For lower lifetime silicon of 1.0 ohm-cm resistivity, the p^+ layer only provides a heavily doped layer for ohmic contacts.

Choice of the implanted p^+ ion species depends on its intended function. For BSF's, either $^{11}\text{B}^+$ or $^{27}\text{Al}^+$ ions are effective with proper annealing procedures. For simple ohmic contact $^{11}\text{B}^+$, $^{27}\text{Al}^+$, or $^{49}\text{BF}_2^+$ can be used. The advantage of $^{49}\text{BF}_2^+$ molecular ions is that higher beam currents and therefore higher throughputs can be realized.

A measured boron, $^{11}\text{B}^+$ impurity profile after annealing is shown in Figure 2-18. Because the depth of implanted ions and the p - p^+ junction location does not necessarily have to be shallow in this case, higher ion energies have been used. However, as with junction implants, channeling must be avoided to prevent retrograde electric fields. A second requirement is the desirability to maintain the peak dopant level at or near the back surface. Both channeling and surface dead layers due to retrograde fields can be minimized by selecting a relatively high anneal temperature which redistributes the implanted boron ions by diffusion.

Boron implants for p^+ back surface fields have been successfully included in high efficiency cell structures. The back surface field effect was first demonstrated under this program by the use of boron ion implantation and furnace annealing. Back surface field effects, after optimized furnace annealing of boron implants, increase V_{oc} from 550 mV to 600 mV. Pulse-annealed, boron-implanted back surface fields have also been demonstrated to be effective in increasing the V_{oc} of 10-ohm-cm, crucible grown silicon substrates from 550 mV to 570 mV. $5 \times 10^{15} \text{ cm}^{-2}$ boron ions were implanted at 25 keV into the back surface of each wafer. The implants were then pulse-annealed using a fluence of approximately 0.3 cal/cm^2 for a 0.1-microsecond, pulsed electron beam.

2.2.3 Ion Implantation Damage Annealing

Successful device optimization requires adequate annealing of the crystal lattice damage induced by ion implantation. The characteristics of the lattice damage depend on the implant energy, dose, and temperature of the substrate during implantation.

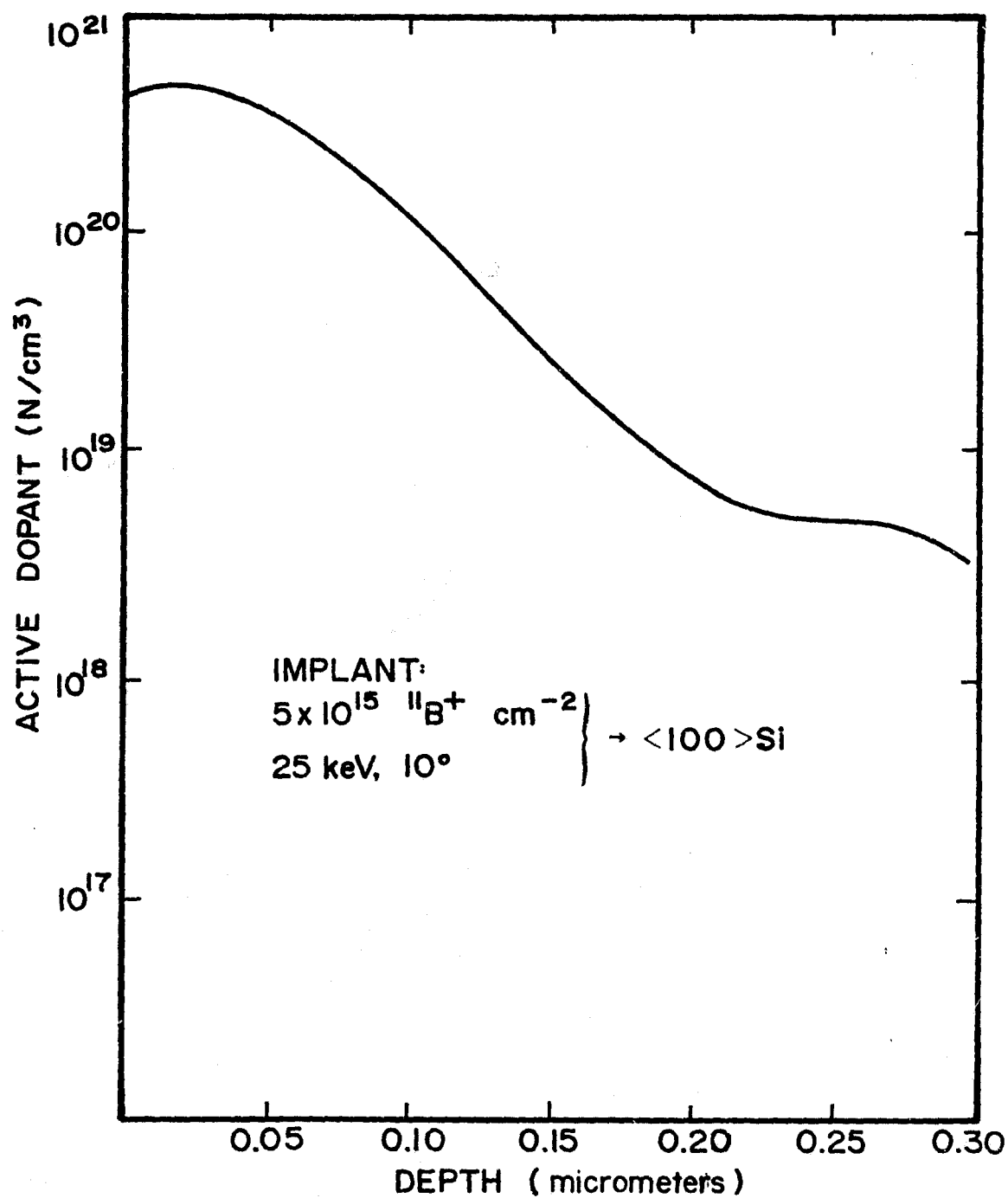


FIGURE 2-18. BACK SURFACE IMPLANT PROFILE FOR n^+/pp^+ CELL

Three generalized cases with different annealing requirements can be distinguished. These are shown in Figure 2-19 and summarized below:

Low Dose Implants:

For some semiconductor devices the implant dose is less than 10^{14} ions/cm². This level results in isolated defect clusters. Effective annealing can occur by epitaxial regrowth from the surrounding, undamaged silicon at very low temperatures. Under some conditions, the damage can be annealed during implant by using elevated substrate temperatures, usually about 500°C.

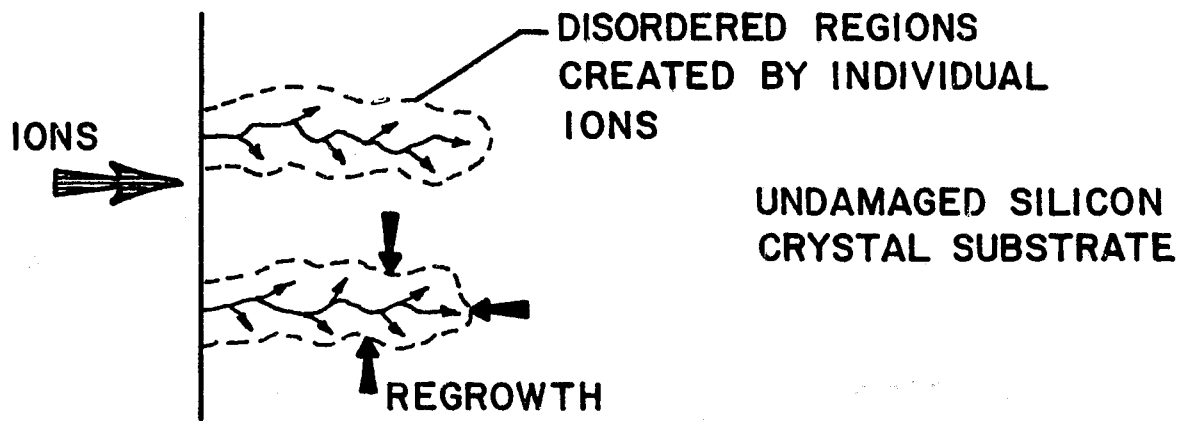
Intermediate Dose Implants:

Solar cell implants fall within this range of approximately 10^{15} ions/cm². At these levels, localized crystalline nucleation sites remain within the heavily damaged amorphous layer. As a result, competition exists between epitaxial regrowth from the unimplanted single-crystal substrate and regrowth from the localized nucleation sites within the implanted layer. This can cause polycrystallite formation, detrimental to cell performance, if only simple annealing procedures are followed.

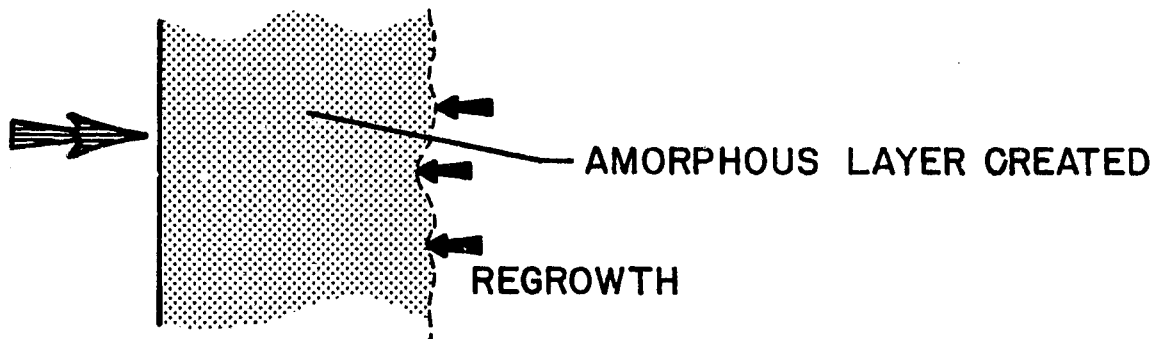
High Dose Implants:

Depending on the ion species, doses higher than 5×10^{15} to 1×10^{16} can produce a totally amorphous layer, providing the wafer temperature is not allowed to rise during implant causing polycrystalline regrowth. Temperature increases can result from the large amount of energy deposited during high-current, high-energy implants. Starting with completely amorphous material, well-controlled, single-crystal, epitaxial regrowth from the undamaged substrate through the implanted amorphous layer can be made to occur. The regrowth rate depends on the anneal temperature. Commonly, these temperatures are within 550 and 850°C.

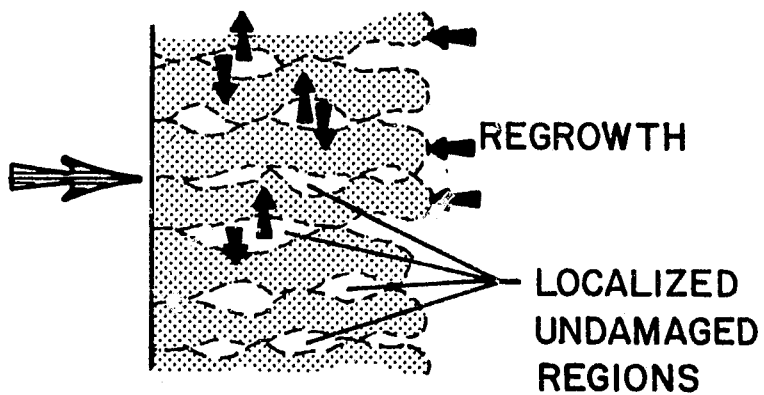
Optimum solar cell implant parameters fall within the intermediate dose range. As such, careful procedures are necessary to produce implanted layers with minimum defects. If the required solar cell ion dose is implanted with liquid



LOW DOSE



HIGH DOSE



INTERMEDIATE DOSE

FIGURE 2-19. TYPICAL IMPLANT DAMAGE FOR VARIOUS IMPLANT DOSES

nitrogen cooling of the wafer, completely amorphous layers can be produced, making good epitaxial regrowth easier; however, such low-temperature implants are not amenable to automation.

Requirements for annealing room-temperature implants can be summarized as:

1. To restore the silicon crystal lattice while minimizing defect sites which increase minority carrier recombination rates
2. To activate the implanted dopant ions for achieving the required sheet resistance, by causing them to take positions within the crystal lattice.

This must be achieved while:

3. Maintaining a shallow junction depth for adequate blue response
4. Preserving or enhancing the bulk silicon minority carrier lifetime.

Much effort has been expended in developing furnace annealing parameters that promote single-crystal epitaxial regrowth and minimize defect concentration. Figure 2-20 shows results from a helium ion backscattering and channeling analysis for multiple-step furnace annealing with resultant lattice structures⁽⁵⁾. The absence of backscattering signal is due to channeling, which depends upon the quality of the regrowth. The data shows that better lattice recovery results from multiple-step anneals. Multiple-step annealing schedules have been developed, such as the following:

1. First-step anneal: Temperature range between 450 and 600°C; time of 1 hour. This step causes slow, single-crystal epitaxial regrowth to occur. Figure 2-21 shows typical regrowth rates for (100) and (111) oriented silicon.⁽⁶⁾
2. Second-step anneal: Temperature range between 800 and 900°C; time of 15-30 minutes. This step causes the substitution of the dopant atoms into the lattice and allows minor redistribution of the as-implanted dopant concentration.
3. Third-step anneal: Temperature range between 450 and 550°C; time of 1 hour. This step causes bulk lifetime recovery by complexing any residual defects, such as point defects, to carbon or oxygen impurities inherent in any silicon.

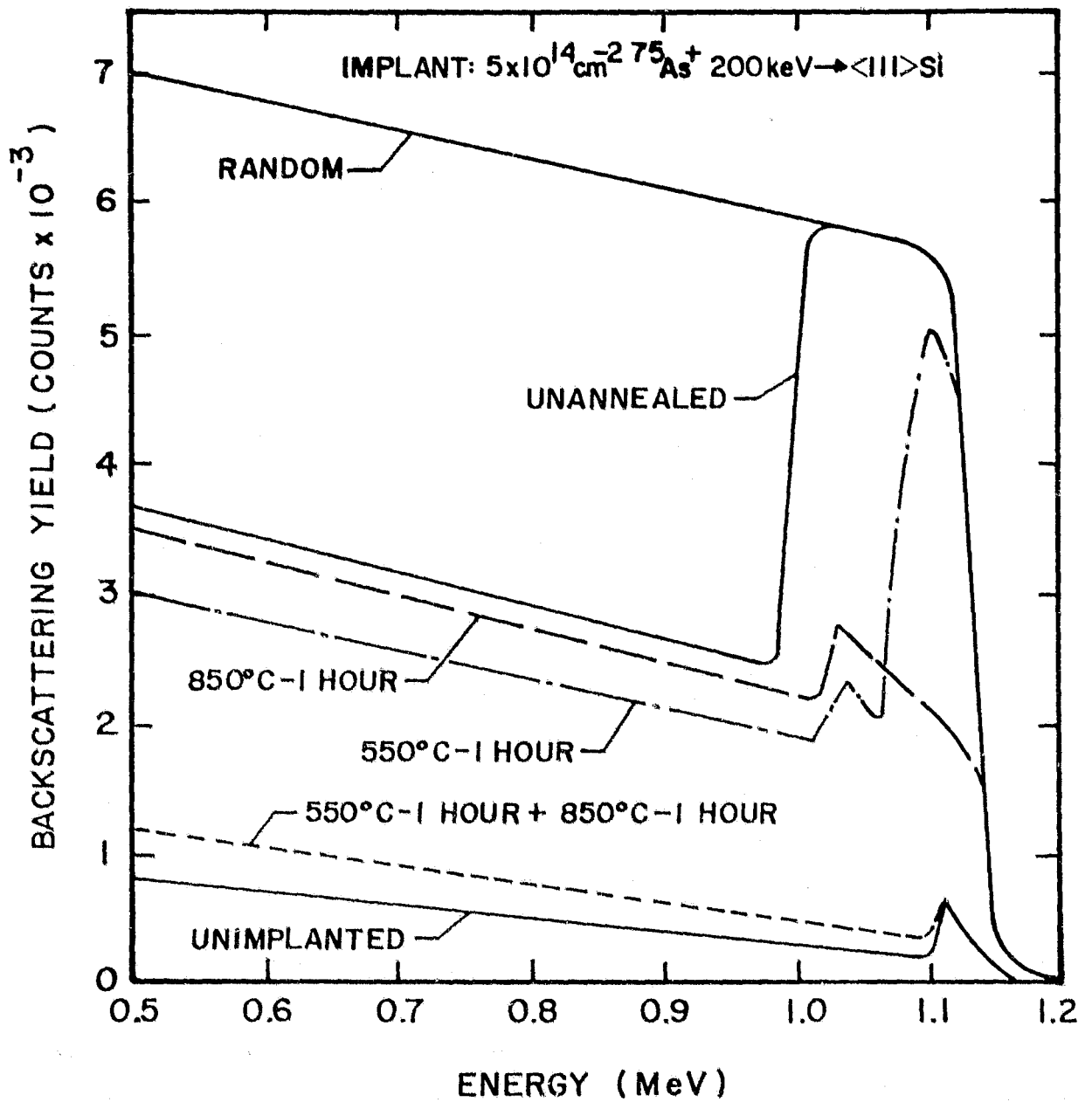


FIGURE 2-20. HELIUM ION BACKSCATTERING AND CHANNELING ANALYSIS OF IMPLANTED AND ANNEALED LAYER(S)

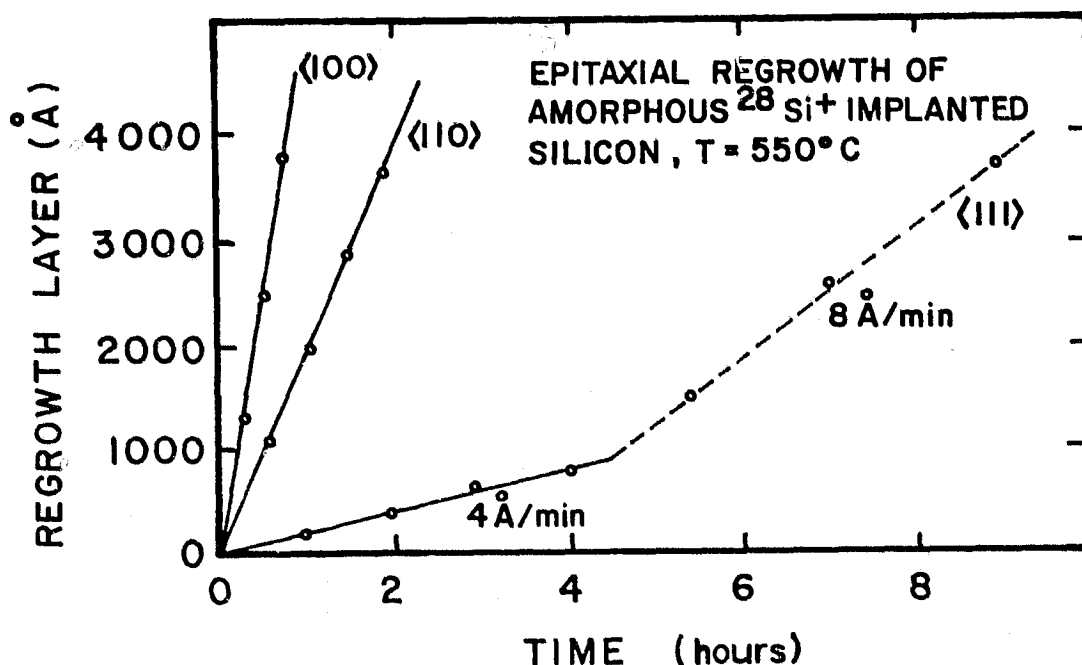


FIGURE 2-21. EPITAXIAL REGROWTH BEHAVIOR FOR IMPLANTED LAYERS AT 550°C

Development and optimization of any anneal schedule requires consideration of heating and cooling rates between anneal steps.

2.2.4 Annealing Optimization for Solar Cell Implant Parameters

Using the annealing approach summarized above, a test matrix for optimization was designed in which 1- and 10-ohm-cm (100) Czochralski and float zone materials were used. Test procedures consisted of 60-minute, isochronal, first-step anneals for all samples at either 450° or 550°C ; and 30-minute, high-temperature, second-step anneals over a range of 650° to 850°C , using a new specimen from the samples of the first step at each 50°C temperature increment. The second-step anneal approach differs from earlier attempts by others in which the same samples were used for progressively higher temperatures steps. In effect, these earlier schedules were equivalent to two- or more-step, anneals. Results from the optimization test matrices, as shown in Figures 2-22 through 2-25, indicate that a first-step 450° to 550°C anneal does not change the final sheet resistance following a second high-temperature anneal, for either the 1- or 10-ohm-cm Czochralski silicon. It was also determined, as shown in these figures, that the final junction depth is not significantly deeper if 450° or 550°C , 1-hour,

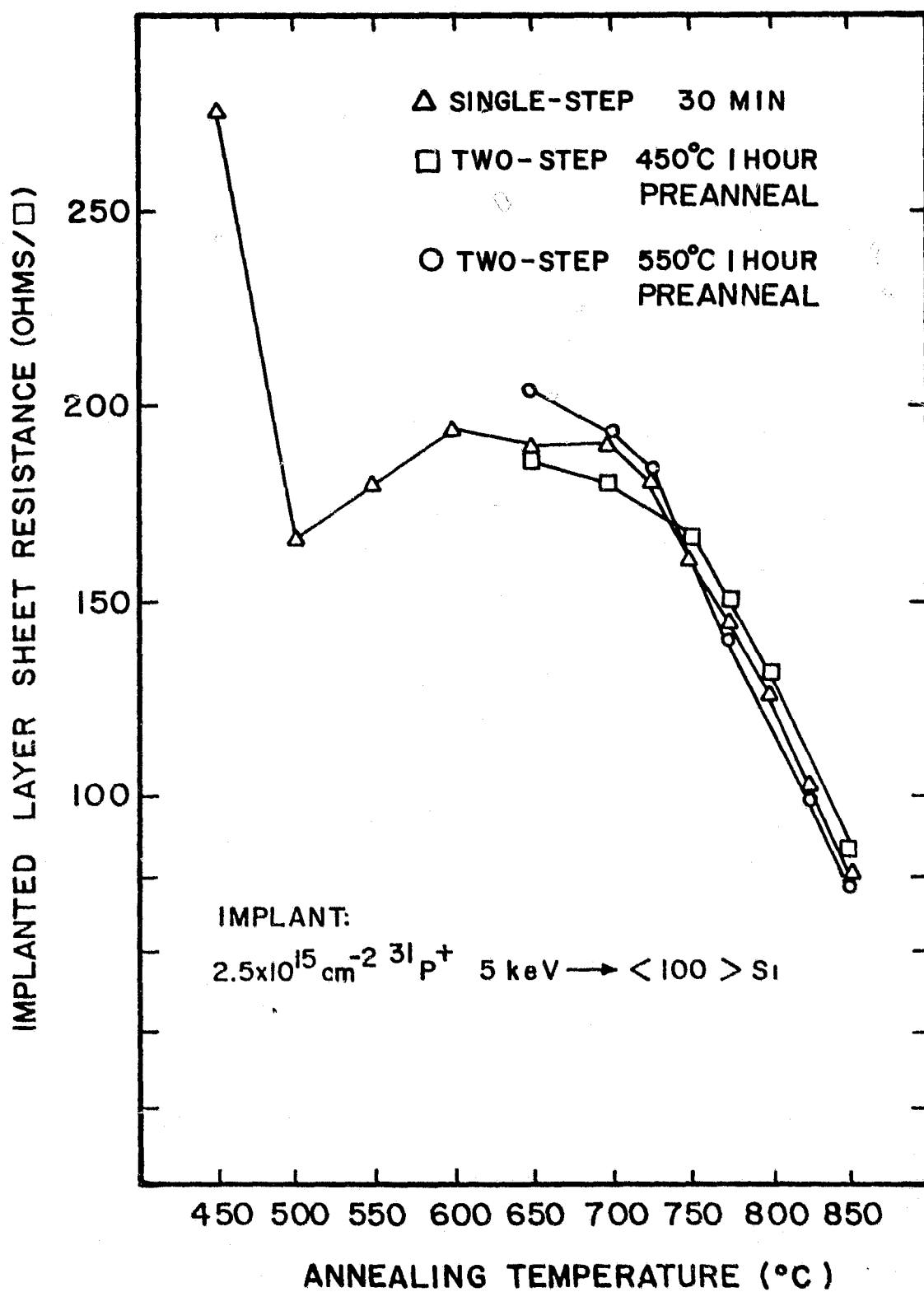


FIGURE 2-22. ISOCHRONAL ANNEALING OF 10-OHM-CM CZ SILICON

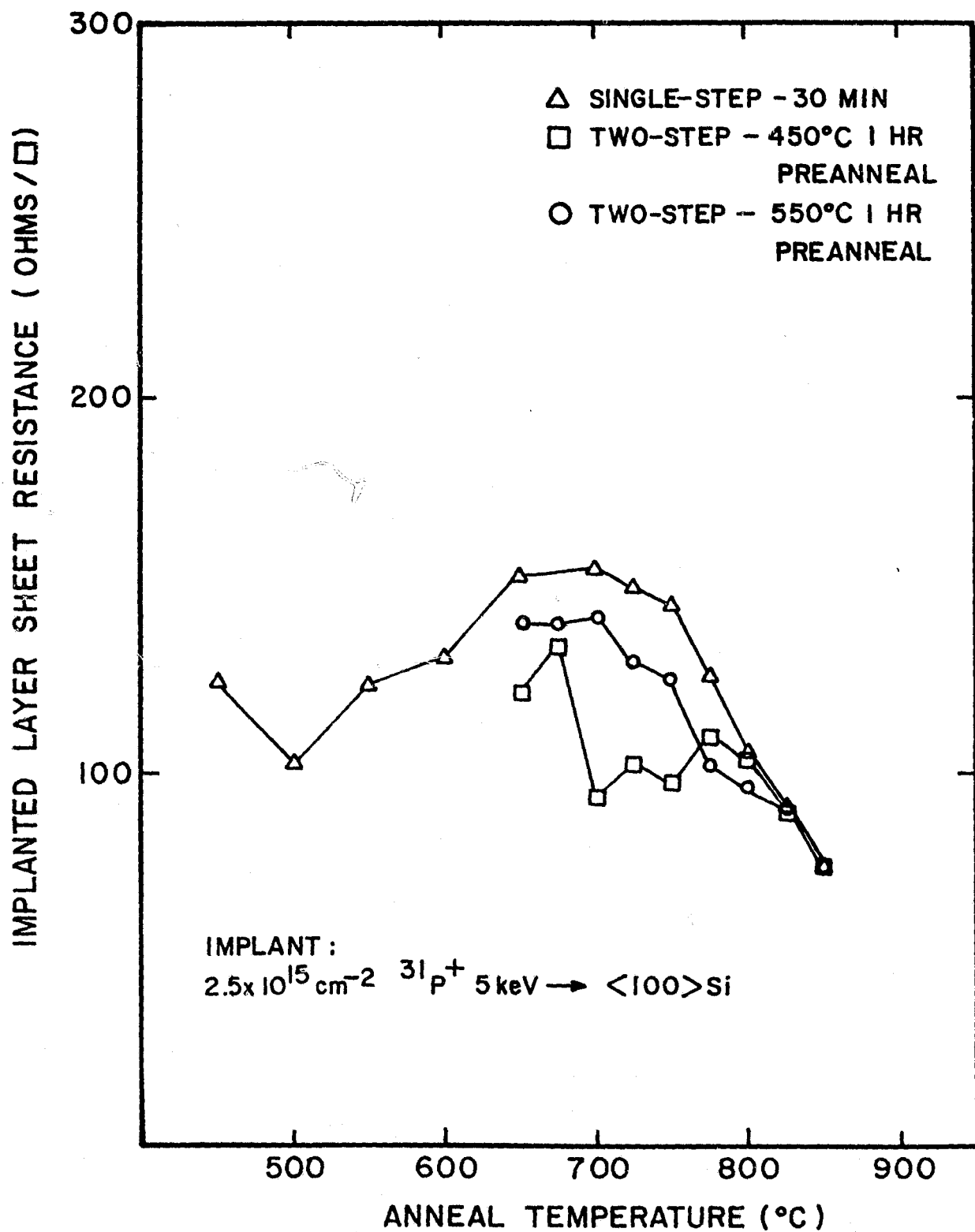


FIGURE 2-23. ISOCHRONAL ANNEALING OF 1-OHM-CM CZ SILICON

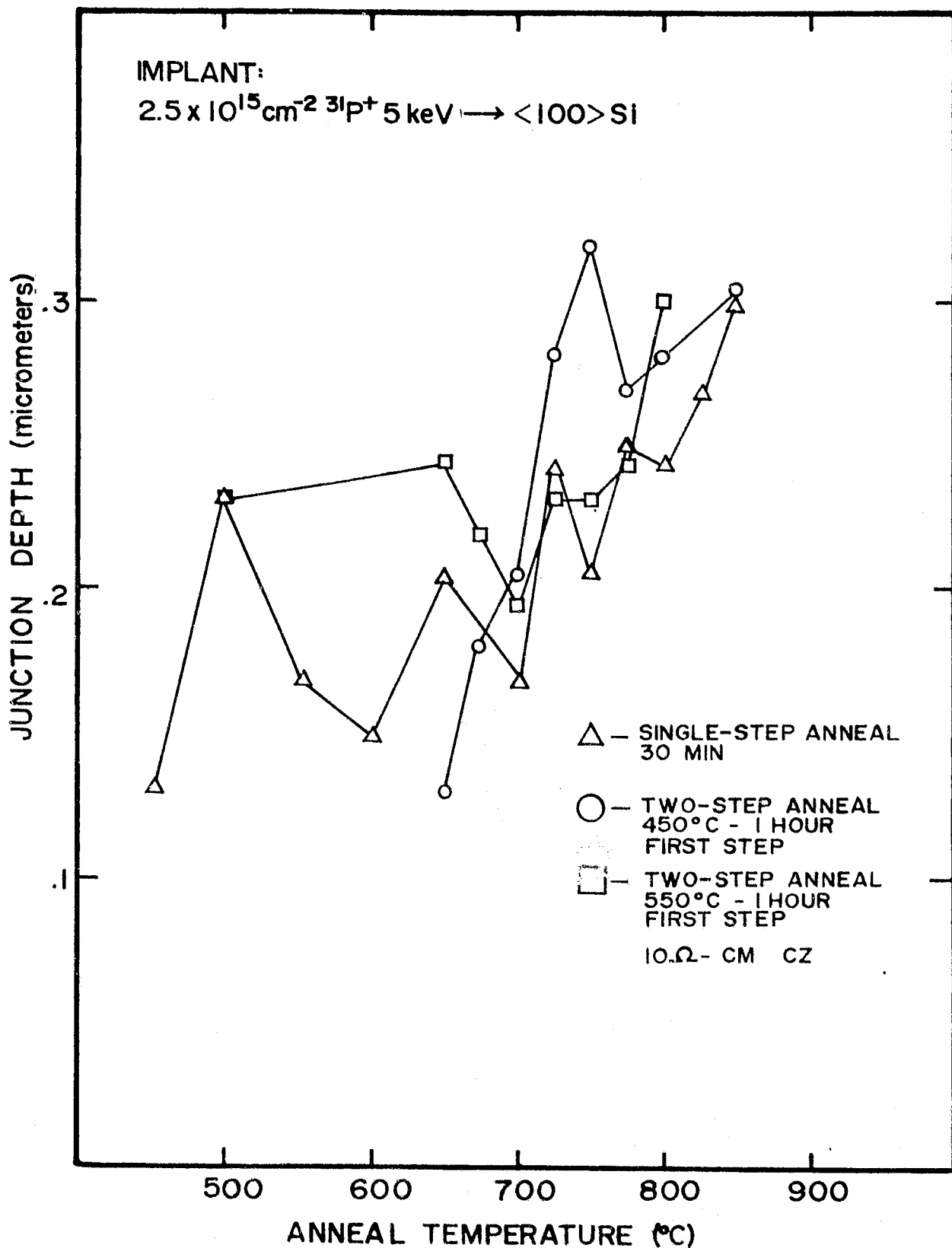


FIGURE 2-24. JUNCTION DEPTH AS A FUNCTION OF TEMPERATURE FOR SINGLE- AND TWO-STEP ANNEALS OF 10-OHM-CM CZ

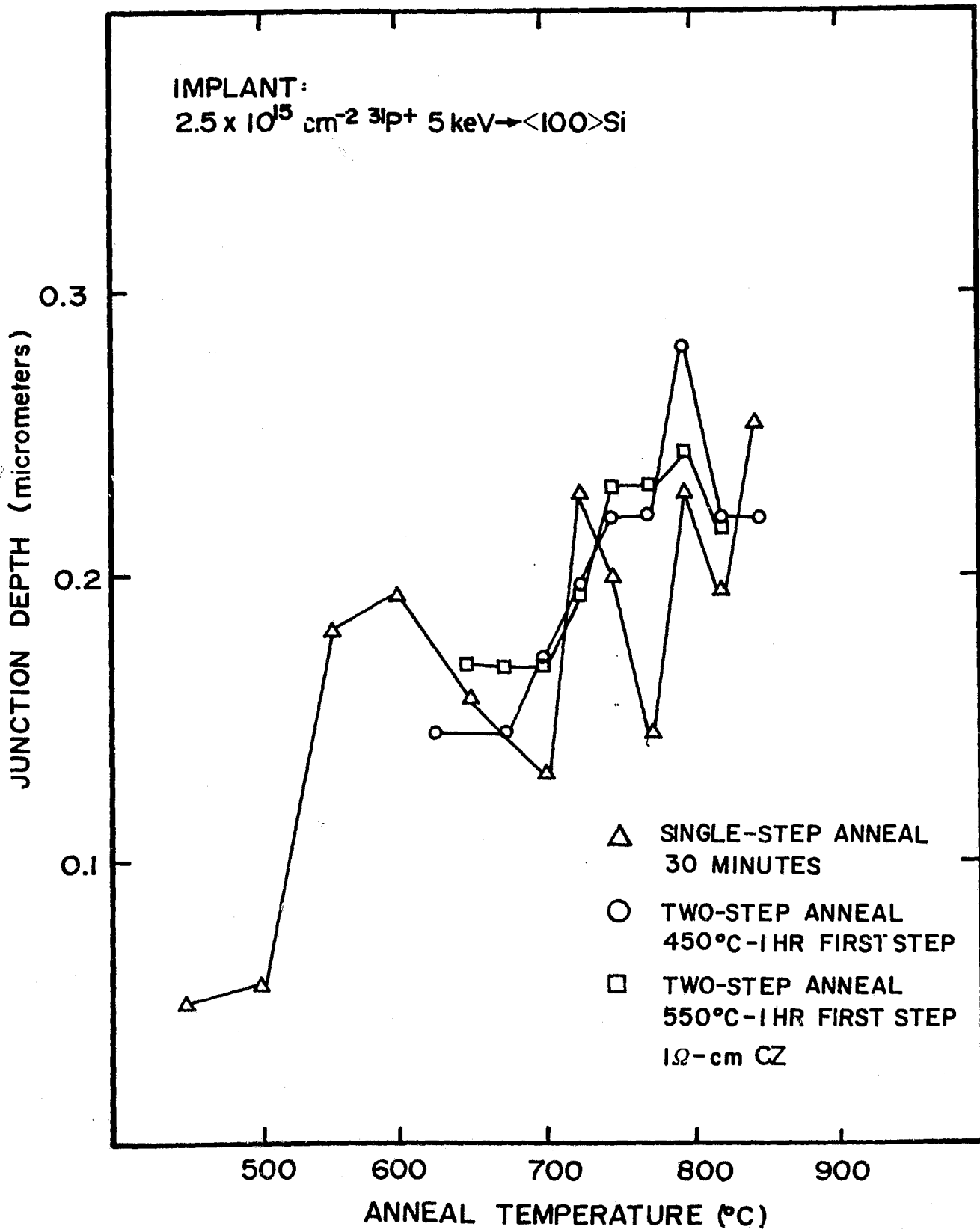


FIGURE 2-25. JUNCTION DEPTH AS A FUNCTION OF TEMPERATURE FOR SINGLE- AND TWO-STEP ANNEALS OF 1-OHM-CM CZ

first-step anneals are used. The procedure described is based on normal pulling rates from a tube furnace; further lifetime enhancement can be expected if controlled heating and cooling rates are incorporated.

2.2.5 Contact Design

Ion implantation provides exacting control over total dopant density in the junction layer. Optimization of cell performance is dependent on the selection of a dopant level which does not cause dead-layer effects. Unless a very effective front contact structure is employed, this selection could be compromised by the need to reduce junction-layer sheet resistance to limit series resistance losses. For this reason, analytical studies related to front contact configurations have been carried out as part of the implanted solar cell development effort. The purpose of these studies has been twofold: to optimize existing contact patterns for use with high-efficiency ion implanted cells, and to design new contact patterns with improved performance. The result of these studies has been the design of a contact pattern used on the 3-inch-diameter ion implanted cells of this program. The basic analytic approach and grid design selected are discussed below.

The losses of cell power output due to the front contacts can be assumed to result from four sources:

1. Shadowing of cell area by metal
2. Resistive losses in line and buss grids
3. Sheet resistance losses on the silicon front surface implanted layer
4. Contact resistance

For simplicity, the cross section of a contact grid line is assumed to be ohmic. Most contact patterns can be analyzed by conceptually breaking them down into many simple geometries, and summing the losses from each of these units to find the loss for the whole cell⁽⁷⁾. The simplest such geometry, the rectangular unit, is shown in Figure 2-26. Other simple units may be triangular or trapezoidal.

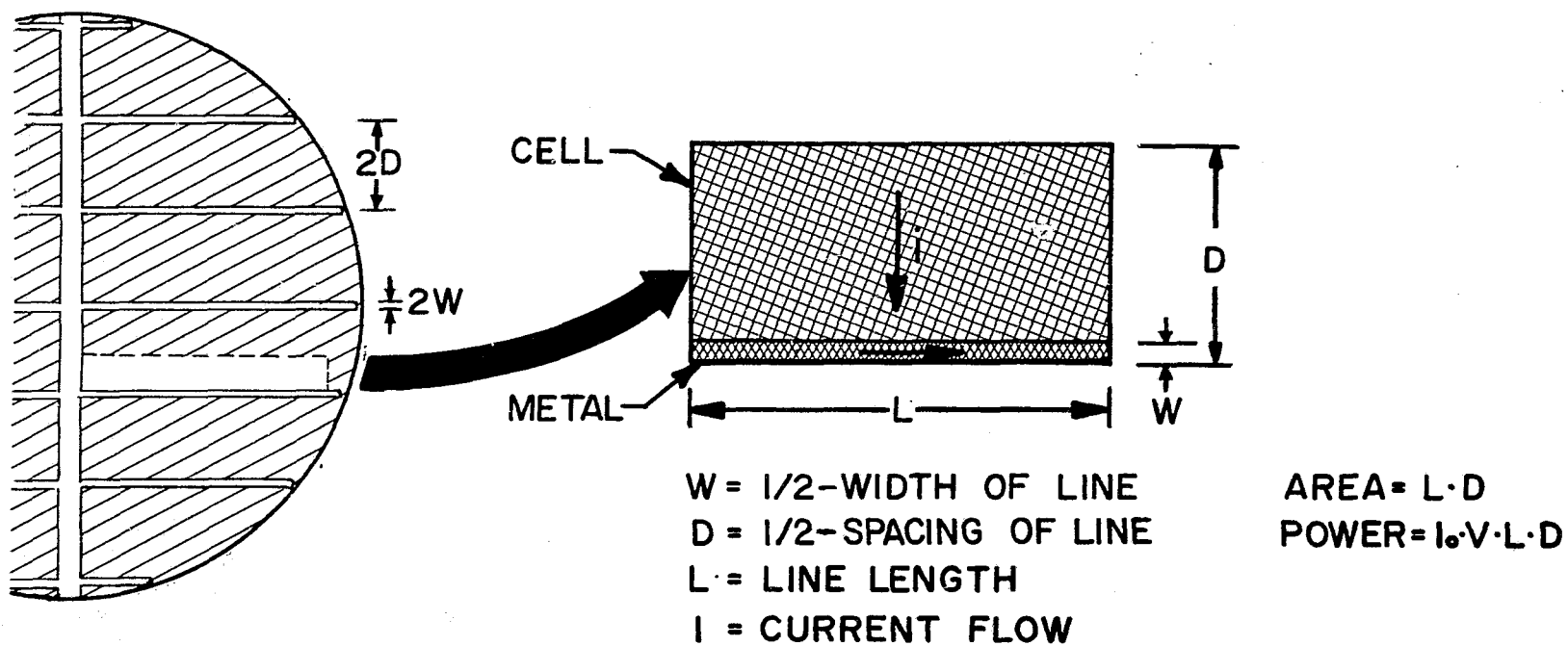


FIGURE 2-26. GENERALIZED RECTANGULAR GEOMETRY UNIT CELL

For analysis, power loss due to resistance is taken to be $I^2 R$, integrated over the appropriate area^(8,9). For example, in the case of the rectangular unit:

P_r = Power loss due to resistance in the line

$$= \int I^2 dR$$

$$dR = \rho_m \frac{dx}{WT}$$

so

$$P_r = \frac{I_o^2 \rho_m D^2 L^3}{3 WT}$$

P_o = Power loss due to sheet resistance

$$= \int_A I^2 dR$$

$$dR = R_{sh} \frac{dy}{dx}$$

$$dI = I_o y \, dx \quad (\text{current assumed to flow perpendicularly to contact})$$

$$P_i = 1/3 R_{sh} I_o^2 D^3 L$$

P_c = Power loss due to contact resistance

$$= \frac{I_o^2 R_c D^2 L}{W}$$

To find the losses as a fraction of total possible power from this area, divide by the total power, $I_o VLD$. To this must be added the fractional loss due to shadowing:

P_s = Fractional loss due to shadowing = W/D

To find the total fractional power loss:

$$\bar{P}_s = \frac{I_o D L^2 \rho_m}{3 WTV} + \frac{R_{SH} I_o D^2}{3V} + \frac{I_o R_c D}{WV} + \frac{W}{D}$$

where I = current flow

W = half-width of line

L = line length

D = half-spacing of line

ρ_m = metallization resistivity in ohm-cm

R_{SH} = implanted layer sheet resistivity in ohm/square

R_c = contact resistance in ohm-cm² (assumed ohmic)

V = operating voltage

I_o = operating current production density in A/cm²

T = metallization thickness.

Several linearizing assumptions are made regarding the independence of the operating point on grid pattern. As long as power loss in the contact is low, which is true for any case likely to be considered, these assumptions will not affect the results. It is possible to reduce metal-to-silicon contact resistance to low levels by the proper choice of contact metals and sintering cycle, so contact resistance has been assumed to be negligible for grid configuration analysis.

Note that if the line half-width and spacing could both be decreased while metal thickness is held constant, the total losses would uniformly decrease. This implies that the metallization lines should be designed as thin as the appropriate technology allows. In fact, since metal thickness cannot be much larger than line width, extremely thin lines are not practical. As indicated in Figure 2-27, this constraint added, lines of width less than about 15 micrometers prove to lose efficiency. The initial cell grid pattern selected is based on a total line width of 35 micrometers.

Since loss is also directly dependent on line length, loss can be minimized by lowering the length. This is done by increasing the number of output terminals. The advantage of adding output terminals levels out at around three to four terminals. For terminals have been selected for the designs used in this program.

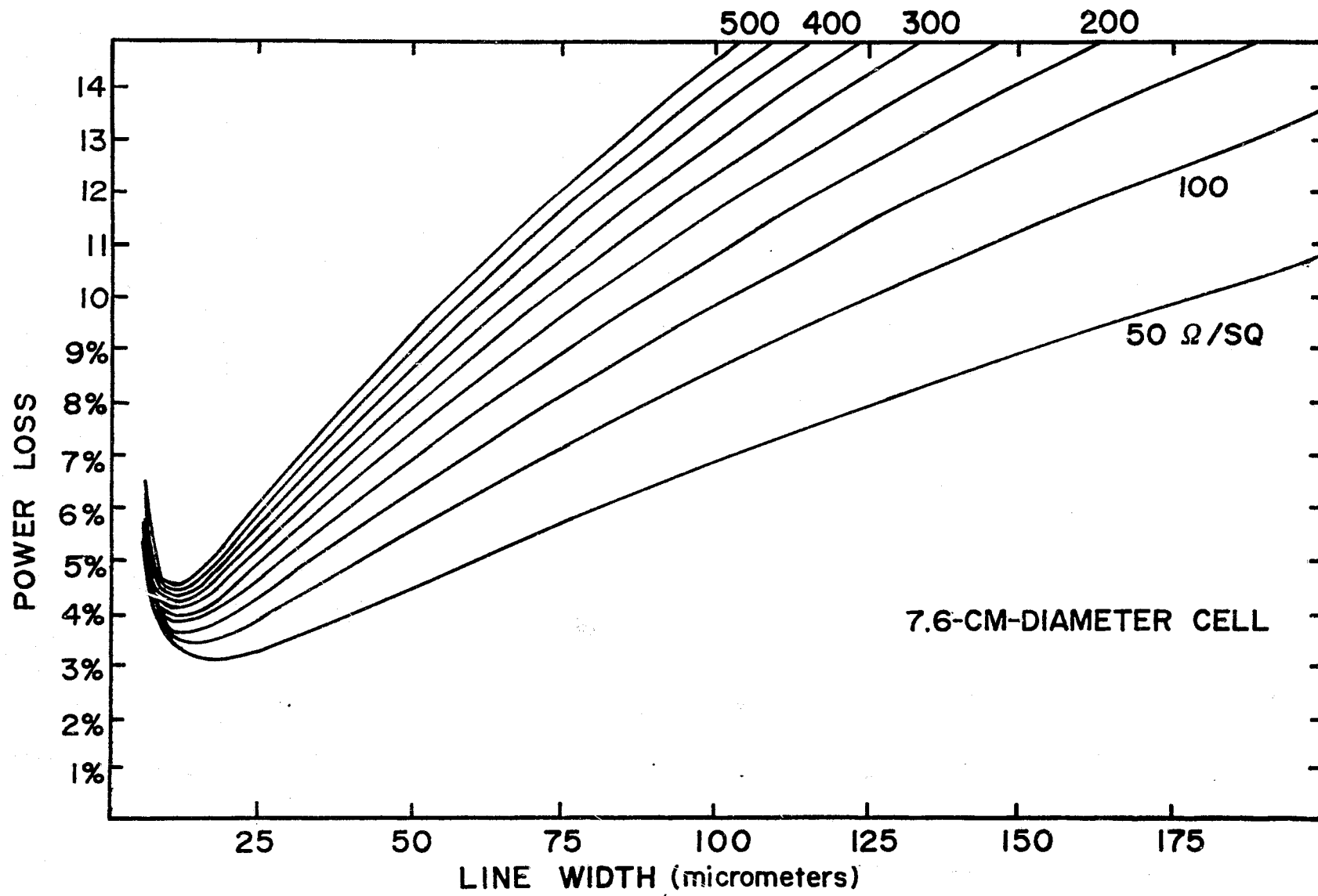


FIGURE 2-27. PERCENT OF TOTAL CELL POWER LOST BY RESISTANCE AND SHADOWING VERSUS LINE WIDTH FOR SEVERAL SHEET RESISTANCES

A computer program was written to calculate the power losses of various metallization patterns using the approach outlined above. Line spacings were optimized while other parameters were held constant. This program was used both to design optimum grid patterns, and to graph the effects of variations in cell process parameters (such as line width and sheet resistivity) as an aid in cell design.

Several different grid patterns were analyzed for this study. In order to take maximum advantage of very narrow line widths, patterns were designed specifically to reduce the distance traveled along the line to an output terminal. This permits extremely narrow lines to be used without excess loss due to resistance. Figure 2-28 shows the Spire "Starburst" contact pattern selected for use on 3-inch-diameter implanted cells. Total power losses by the contact grid (shadow and resistive) are predicted to be slightly less than 5 percent.

2.2.6 Process Development

A high-efficiency, n^+/pp^+ solar cell design and process specification has been developed under this program. The baseline process specification includes requirements on starting material, surface preparation, implant parameters, furnace annealing conditions, and the contact mask design.

The cell structure employs an implanted junction and implanted back surface field (BSF), starting with 10-ohm-cm, (100) oriented, Czochralski-grown silicon. The front contact, as was described in Section 2.2.4, has been designed specifically for implanted junction layer characteristics such as sheet resistance and junction depth. The metallization system employed during most of Phase I has been Cr Au Ag, but more recently Ti Pd Ag has been substituted because of improved adherence and the higher temperature capability of this contact system. The less reactive nature of the Ti Pd Ag contacts with respect to silicon allows sintering to be included in the manufacturing process. Experience with this contact metallurgy and mask design indicates that ultimate line widths of 25 micrometers can be fabricated. Metallization line widths of 25 micrometers and of this design result in shadowing of only 4 percent of the cell active area, so that nearly ideal performance of the structure can be achieved.

In this structure, the p^+ layer provides an effective BSF which increases both V_{oc} and the voltage at the maximum power point. For example, V_{oc} for a simple n^+/p solar cell under one-sun, AM0-25°C conditions is 550 mV; with the inclusion of an effective BSF, the V_{oc} is increased to 600 mv.

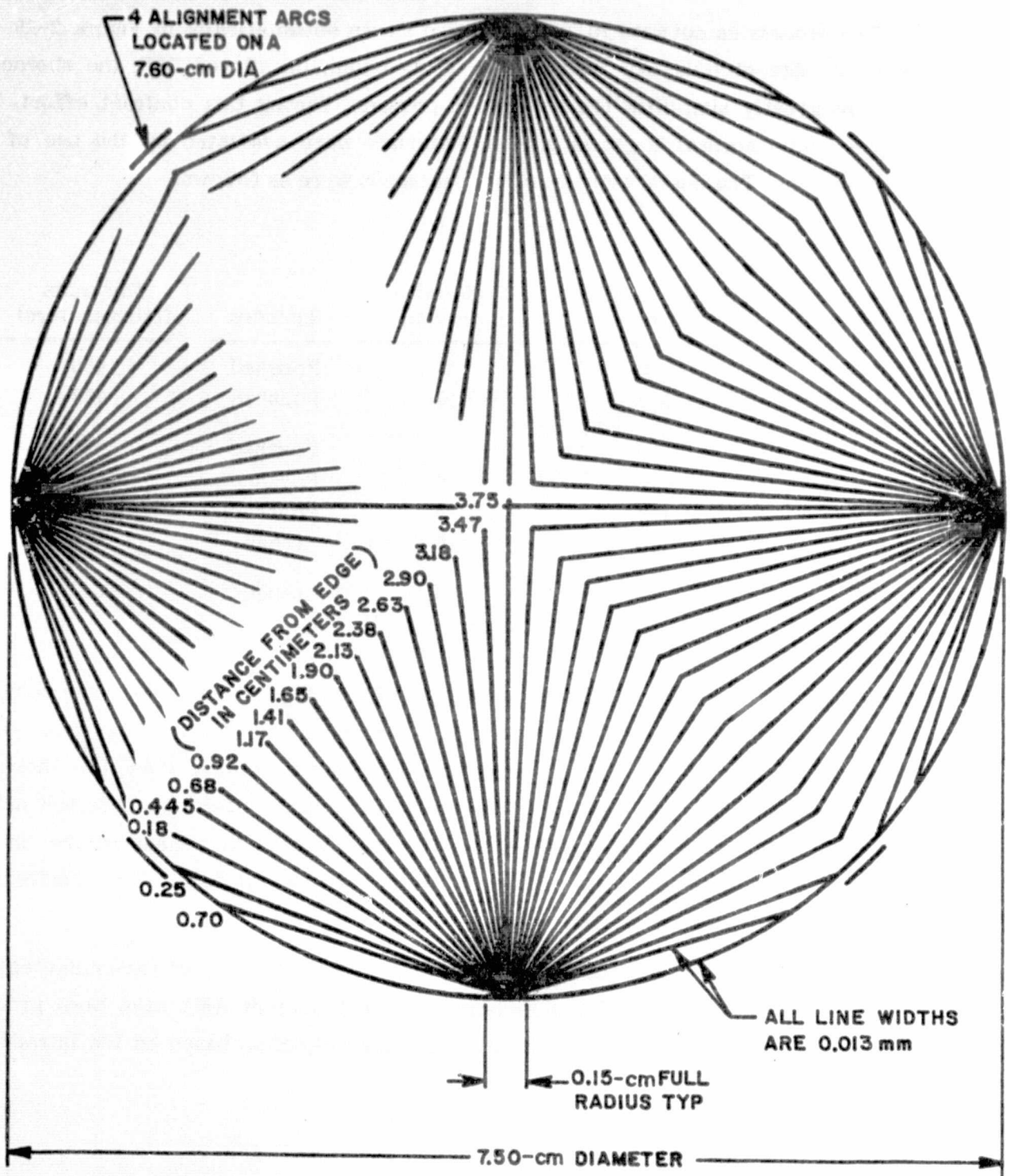


FIGURE 2-28. OPTIMIZED FRONT CONTACT METALLIZATION PATTERN FOR 7.6-CM (3-INCH) CELLS

The process as outlined in Table 2-8 and shown schematically in Figure 2-29 does not include edge etching, nor does it include an aluminum alloyed BSF; the absence of these steps greatly simplifies the production process. During this contract effort, both float-zone and Czochralski-grown silicon materials were evaluated by the use of this baseline process. The characteristics of the materials were as follows:

Growth Technique	Defect Density (no./cm ²)	Resistivity (ohm-cm)	Surfaces	Thickness (micrometers)
Float-zone	0	1	Polished	450
Float-zone	400	10	Polished	450
Czochralski	400	1	Polished	450
Czochralski	400	10	Polished	450
Czochralski	400	10	Polished	375
Czochralski	400	10	Etched	300
Cast	—	5	Etched	375

No advantages in improved efficiency were noted for float-zone material when compared to Czochralski-grown material when processed according to this specification. Higher efficiencies were measured for wafers 450 micrometers thick than for those 300 micrometers thick, but the cost-effectiveness of increased wafer thickness has not yet been determined. Extensive data was collected during the manufacture of 500 deliverable cells, starting with 300-micrometer, etched wafers. The performance distributions are presented in Section 2.3.

As a result of efforts under this contract, the performance of ion-implanted solar cells has been greatly advanced. Efficiencies of 16.5 percent AM1 have been produced and 17.5 percent efficiencies can be conservatively projected, based on the introduction of texturized surfaces.

TABLE 2-8. BASELINE PROCESS SPECIFICATION FOR ION-IMPLANTED,
n⁺/pp⁺, HIGH-EFFICIENCY SOLAR CELLS

Silicon Material	10-ohm-cm, (100), CZ, p-type Surfaces: Bright Etched
<u>Process Sequence</u>	
Implant:	Junction - 2×10^{15} 31P ⁺ cm ⁻² , 10 keV, 10° Back Surface Field - 5×10^{15} 11B ⁺ cm ⁻² , 25 keV, 10°
Implant Uniformity:	No worse than <u>±</u> 10 percent
Anneal:	Simultaneous phosphorus and boron implant anneal in nitrogen: 550°C - 2 hours 850°C - 15 minutes 550°C - 2 hours
Clean:	Buffered HF Deionized water rinse
Front Metallization:	Evaporate 400A Ti + 400A Pd + 1,000A Ag Define Spire Starburst pattern with standard Kodak KTFR process Electroplate 12 micrometers of Ag
Clean:	Buffered HF Deionized water rinse
Back Metallization:	Evaporate 400A Ti + 400A Pd + 1 micrometer of Ag
AR Coating:	Evaporate 700A TiO ₂
Sinter:	400°C - 10 minutes in nitrogen
Test:	AM0 I-V

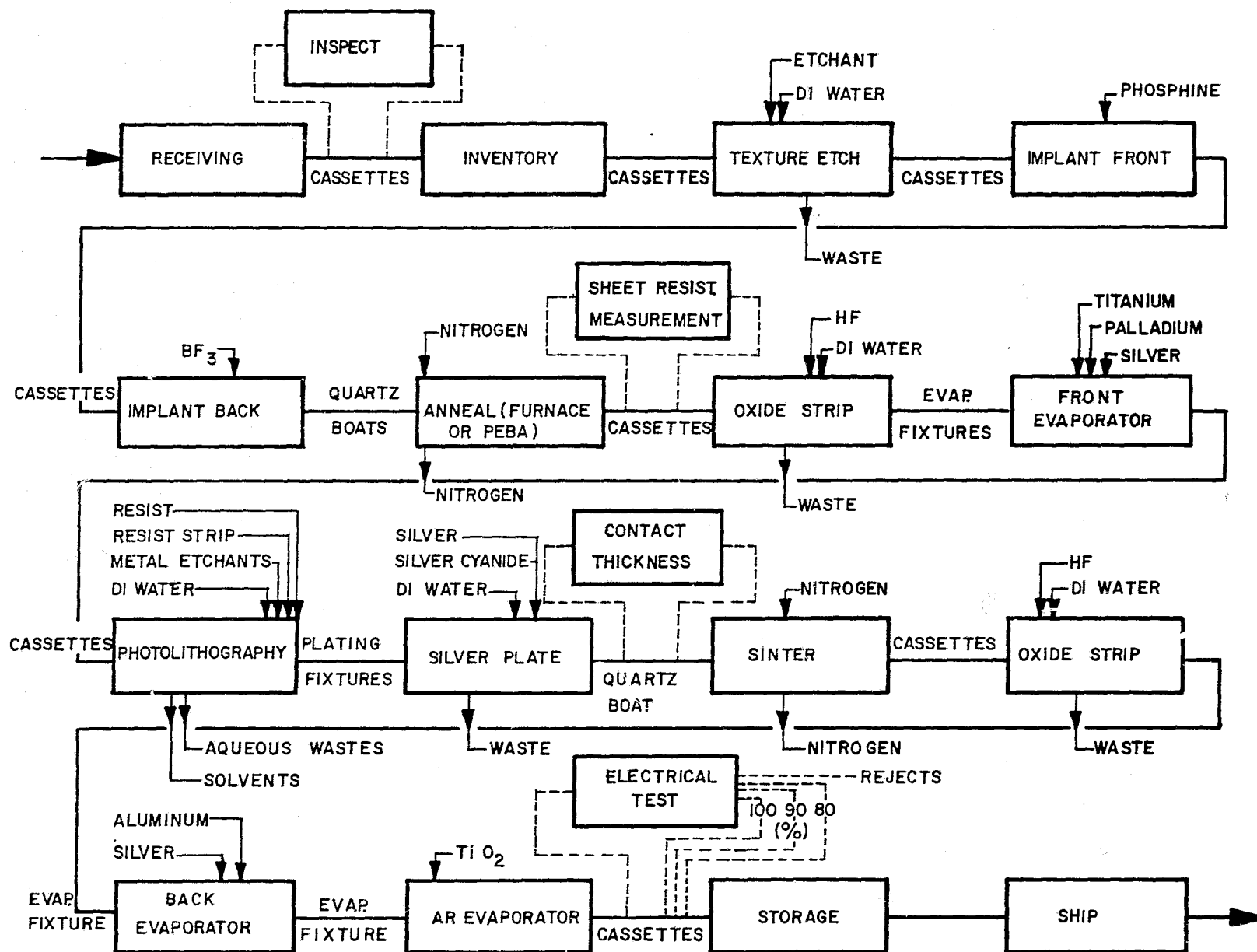


FIGURE 2-29. SCHEMATIC OF BASELINE, HIGH-EFFICIENCY, IMPLANTED CELL PROCESS

2.3 SOLAR CELL PERFORMANCE STATUS

As a result of the efforts under this contract, the performance of ion-implanted solar cells has been greatly advanced. Processing based on ion implantation and pulse annealing has been applied to both Czochralski and large-grain polycrystalline silicon materials to manufacture high-efficiency solar cells. In addition, performance distributions have been determined for large numbers of ion-implanted/pulse annealed, ion-implanted/furnace annealed, and diffused junction solar cells for comparison purposes. These comparisons of diffusion and implantation technologies for junction and back surface field applications are described in the following sections.

2.3.1 Single-Crystal Starting Material

Based upon experience with the high-current ion implanter, manufacturing and quality control procedures were determined for cell processing. To assess the effectiveness of these procedures, 660 wafers with diameters of 7.6 cm were implanted for complete processing into solar cells; the characteristics of the starting material are summarized below:

	Resistivity (ohm-cm)	Thickness (μ m)	Orien- tation	Surface	Growth Technique	No. of Wafers Started
Type A	10	300	(100)	Bright- Etched	Czochralski	600
Type B	10	450	(100)	Front- Polished Back- Etched	Czochralski	60

Both types were crucible-grown, semiconduction-grade silicon wafers; however, 60 out of the 600 wafers had polished front surfaces while the remaining 600 wafers had etched surfaces. All the wafers were implanted, using the JPL-LSA, high-current ion implanter, to provide both junction and back surface held regions. The ion dose uniformity across each wafer was between ± 7 percent and ± 10 percent. This level of uniformity did not produce a measureable performance loss when compared with cell characteristics produced with a dose uniformity controlled to better than ± 1 percent.

The remaining cell processing included furnace annealing, TiPdAg contacts, and AR coating; no edge etching or other treatments were used to isolate the edges of the cells. The process was as outlined in Table 2-8. Out of the 660 wafer starts, 80 wafers were broken during handling and were electrical rejects. The cause of these rejects was surface plating of silver along the cell edge, which caused a reduction of the internal cell shunt resistance and curve fill factor.

The average and peak characteristics for the 500 cells delivered to JPL are as shown in Table 2-9. Performance distributions of I_{sc} , V_{oc} , I_{490} mV, and efficiency are shown in Figures 2-30 through 2-33. The highest cell efficiency was measured to be 14.1 percent (AM0-25°C) at Spire, as shown in Figure 2-34.

TABLE 2-9. SUMMARY OF PERFORMANCE CHARACTERISTICS FOR 500 ION-IMPLANTED, FURNACE ANNEALED CELLS

Parameter		Measured (AM0-25°C) Characteristics		
		Average	Peak	Std. Deviation
	V_{oc} (mV)	594	600	2.8
	I_{sc} (mA)	1780	1955	74
	I_{490} (mA)	1611	1780	82
AM0	Efficiency (%)	12.8	14.1	0.65
AM1	Efficiency (%)	15.0	16.5	(Measured at JPL)

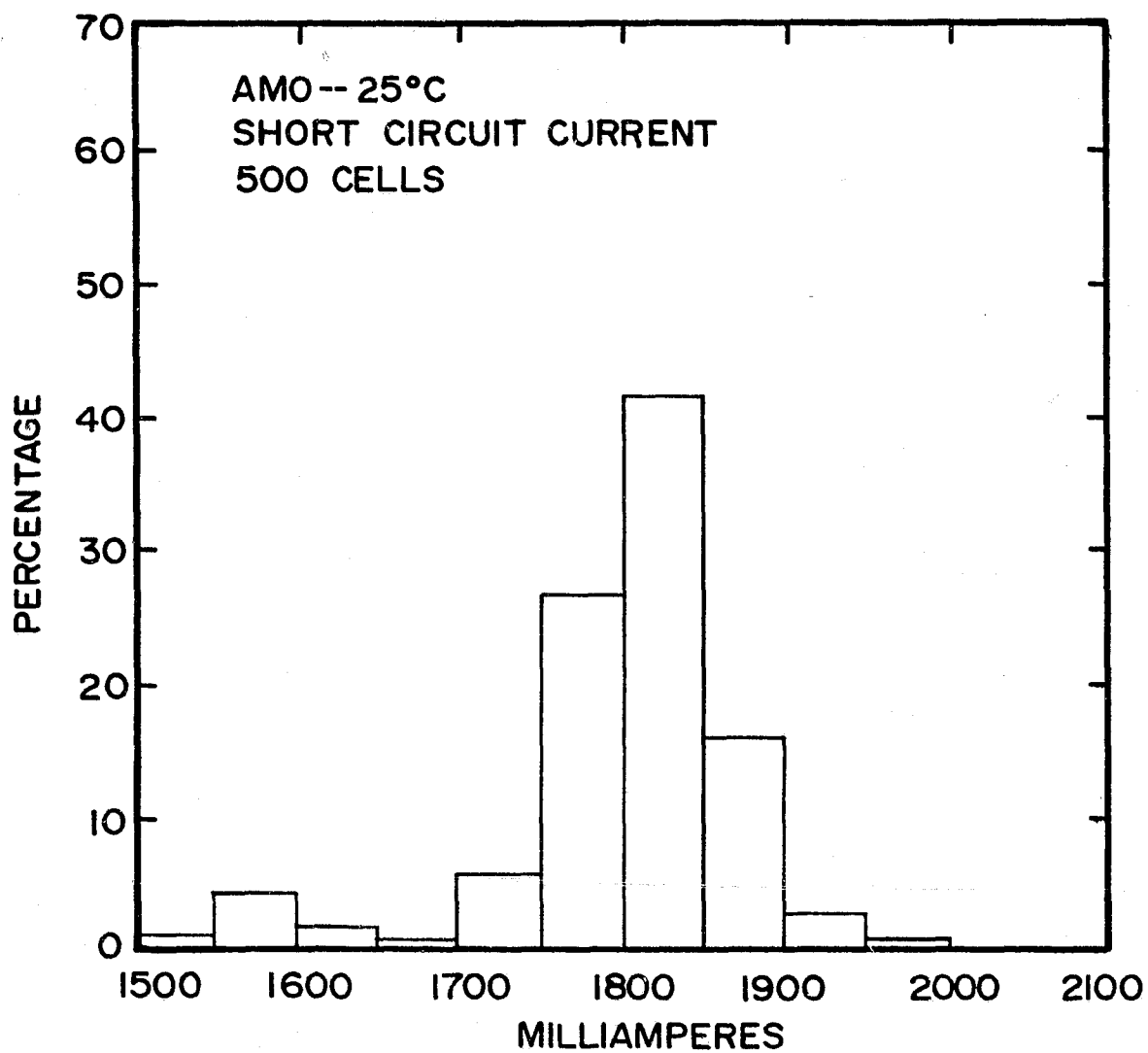


FIGURE 2-30. DISTRIBUTION OF SHORT-CIRCUIT CURRENT FOR n^+/pp^+ IMPLANTED, FURNACE ANNEALED SOLAR CELLS WITH 7.6-cm DIAMETERS

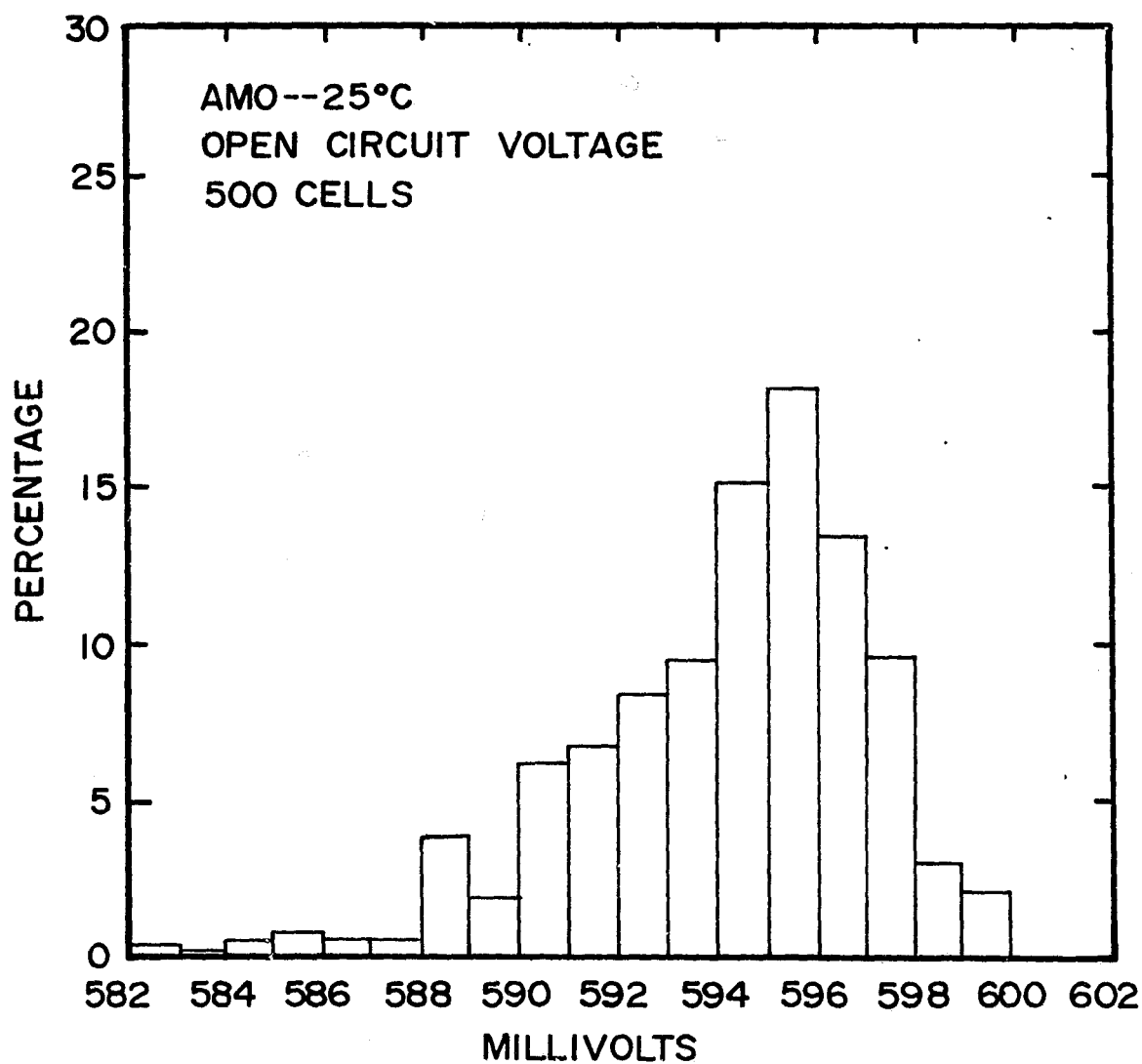


FIGURE 2-31. DISTRIBUTION OF OPEN-CIRCUIT VOLTAGE FOR n^+/pp^+ IMPLANTED, FURNACE ANNEALED SOLAR CELLS WITH 7.6-cm DIAMETERS

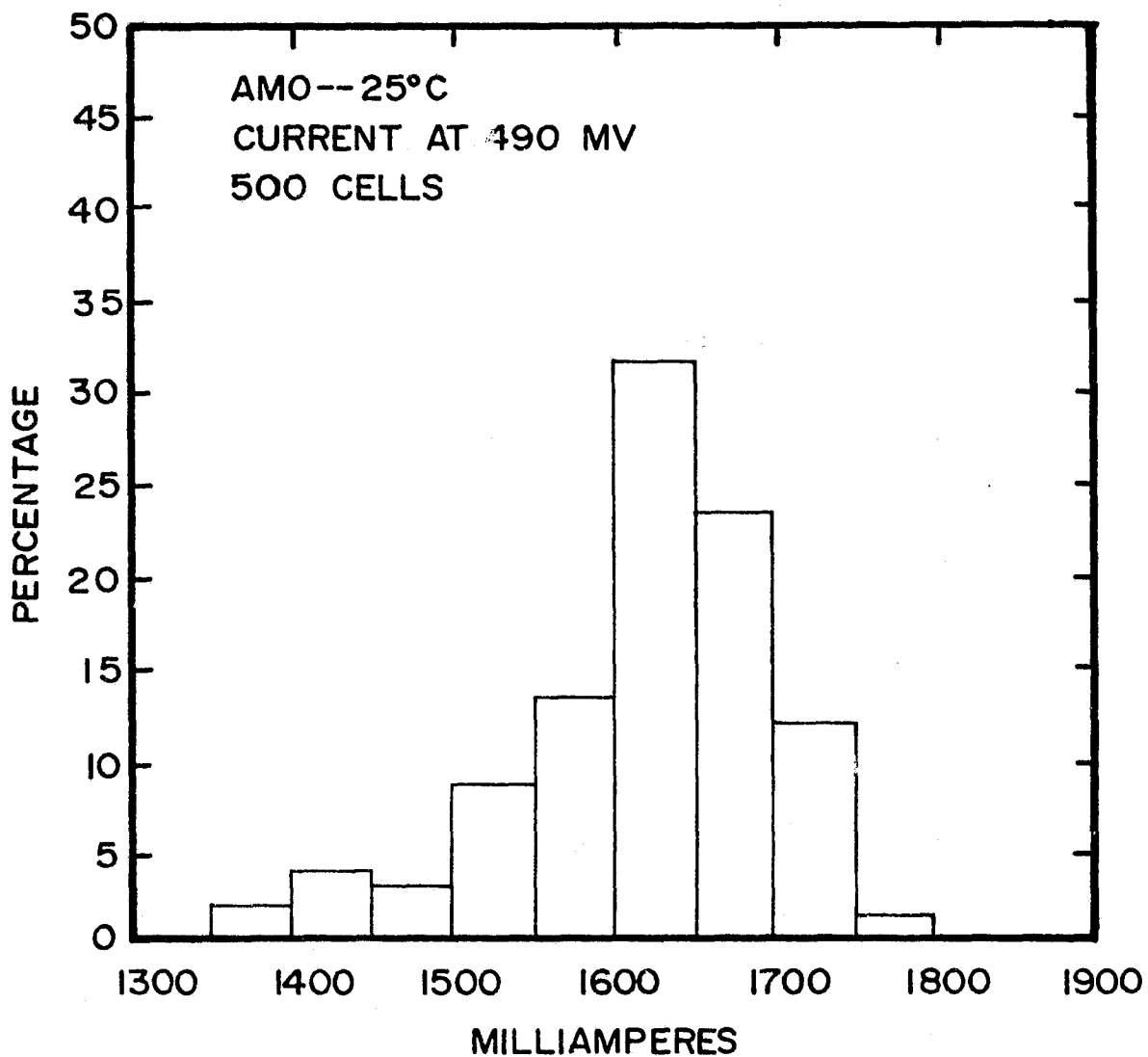


FIGURE 2-32. DISTRIBUTION OF CURRENT AT 490 mV FOR n^+/pp^+ IMPLANTED, FURNACE ANNEALED SOLAR CELLS WITH 7.6-cm DIAMETERS

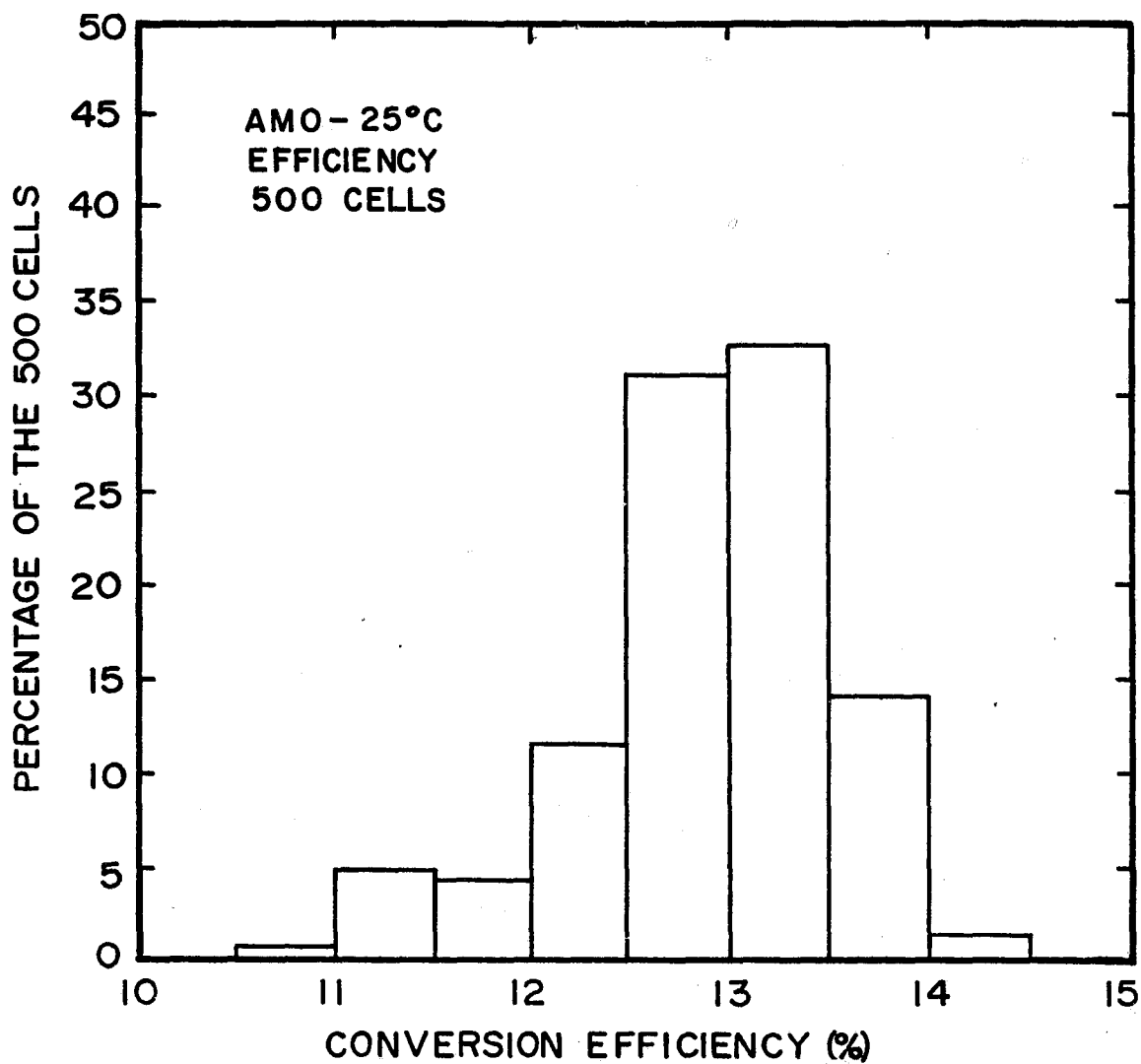


FIGURE 2-33. DISTRIBUTION OF AM0 CONVERSION EFFICIENCY FOR n^+/pp^+ ION IMPLANTED/FURNACE ANNEALED SOLAR CELLS WITH 7.6-cm DIAMETERS

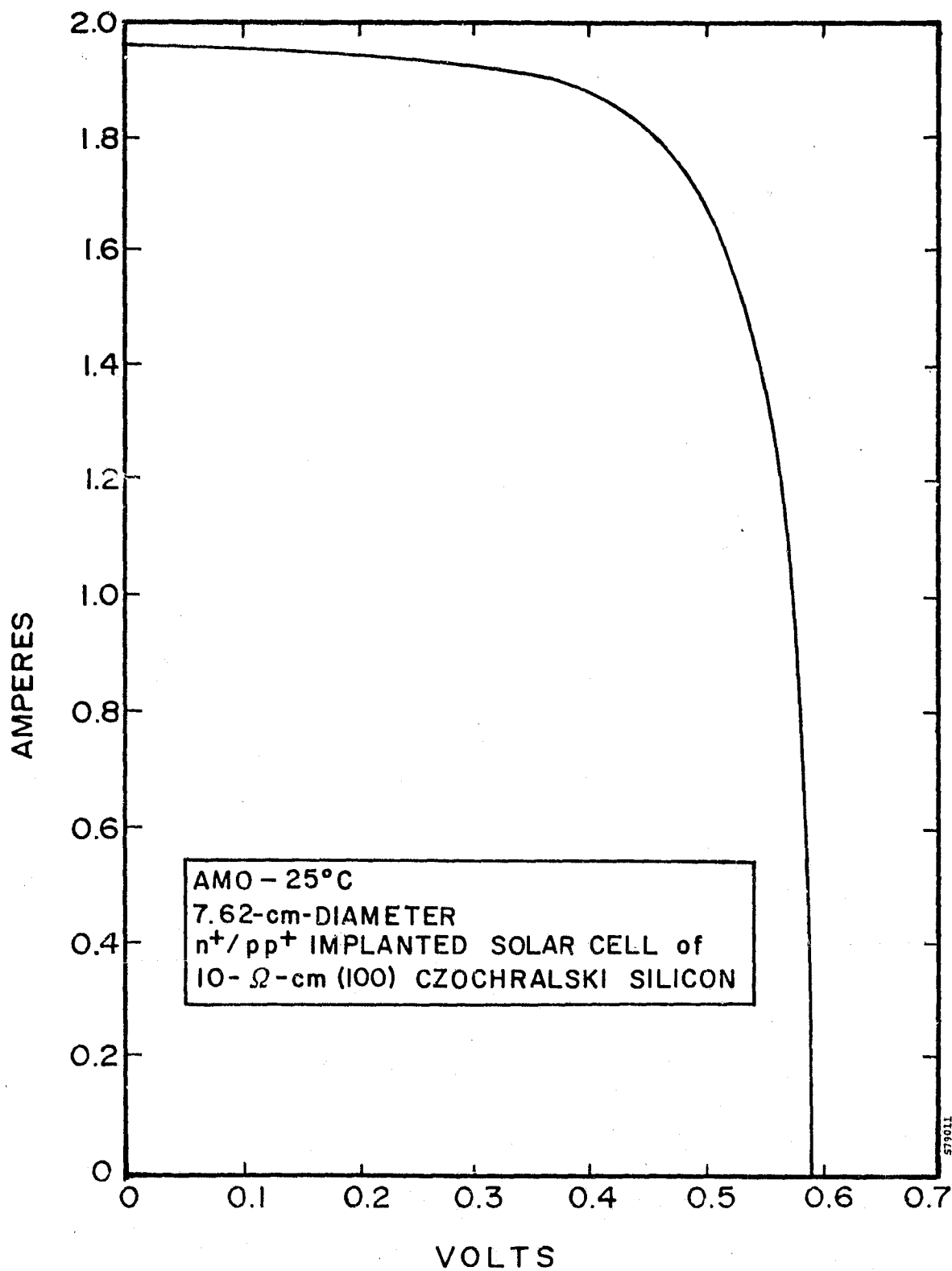


FIGURE 2-34. AMO I-V CHARACTERISTICS FOR AMO-25°C, 7.62-cm DIAMETER, n⁺/pp⁺ IMPLANTED SOLAR CELL OF 10-ohm-cm CZOCHRALSKI SILICON

2.3.2 Cast Polycrystalline Silicon Solar Cells

Non-single-crystal silicon materials such as sheet and ribbons present no particular problems for implantation processing. Considerations of grain boundary diffusion effects, preferential dopant collection in grain boundaries are minimized for properly conducted implantation, and implant damage annealing procedures. As a part of this program, processes have been shown feasible for manufacturing ion-implanted cells from cast polycrystalline sheet silicon.

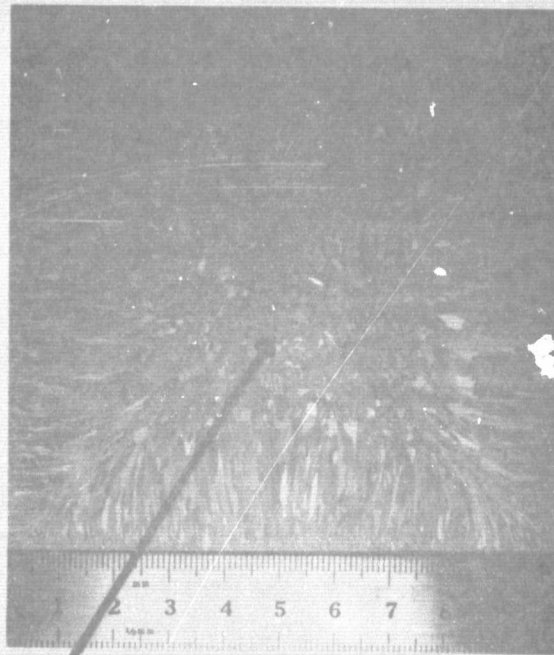
The starting material was manufactured by Wacker Chemical Corporation under the trade name of SILSO. This material is characterized by a large grain structure, as shown in Figure 2-35, and was produced by casting boron-doped, 5-ohm-cm silicon in a graphite mold.

The cell process incorporated ion implantation for the introduction of n^+/pp^+ structure. The process used for the manufacture of the 100 cells delivered to JPL is outlined below:

1. Saw to 5 x 5 cm.
2. Etch to remove saw damage.
3. Implant Front: $2 \times 10^{15} \text{ }^{31}\text{P}^+ \text{ cm}^{-2}$, 10 keV, 10° .
4. Implant Back: $5 \times 10^{15} \text{ }^{11}\text{B}^+ \text{ cm}^{-2}$, 25 keV, 10° .
5. Anneal: $550^\circ\text{C} - 2 \text{ hr}$, $850^\circ\text{C} - 15 \text{ min}$, $550^\circ\text{C} - 2 \text{ hr}$.
6. HF clean.
7. Front contact metallization: TiPdAg.
8. Back contact metallization: TiPdAg.
9. AR evaporation: TiO_2 .

Insufficient time was available to optimize this process for the sheet silicon used, but efficiencies up to 10.3 percent ($\text{AM1} - 28^\circ\text{C}$) were obtained with front contact line widths of 75 micrometers. Figure 2-36 shows one of the cells processed with SILSO material.

ORIGINAL PAGE IS
OF POOR QUALITY



8790019

FIGURE 2-35. TYPICAL GRAIN CONFIGURATION OF
POLYCRYSTALLINE SILSO WAFER

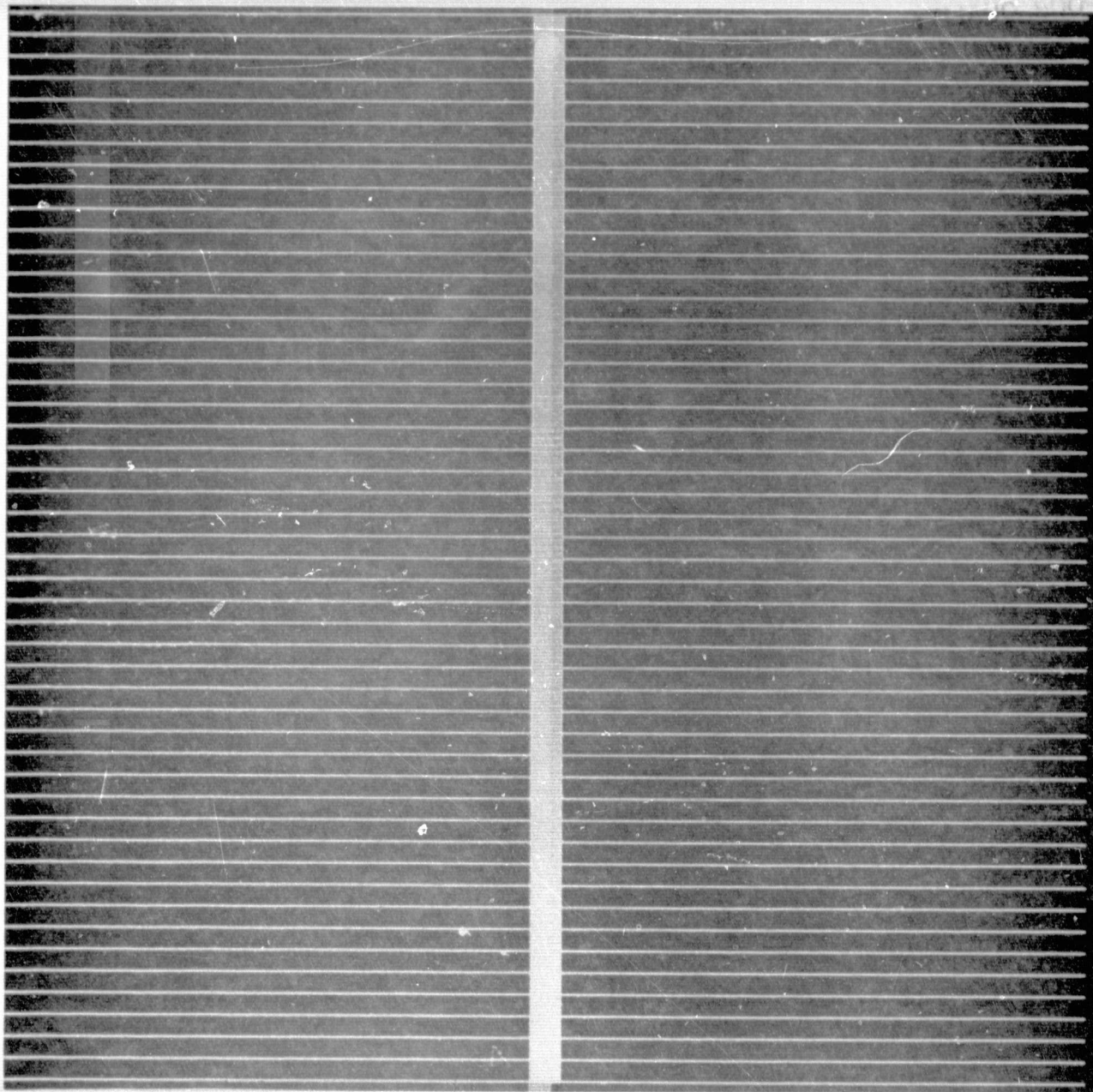


FIGURE 2-36. POLYCRYSTALLINE SHEET SILICON (SILSO) SOLAR CELL

To assess the effect of the p^+ layer on polycrystalline cell performance, three different types of p^+ layers were employed to manufacture the deliverable solar cells. All junctions were formed by ion implantation and a furnace annealing schedule which had been optimized for Czochralski silicon. The various p^+ layers evaluated in the n^+/pp^+ device structure were formed as follows:

Lot 1584:	evaporated aluminum alloy (5 micrometers thick), 850°C - 30 min
Lot 1473:	no p^+
Lots 1469:	$\left\{ \begin{array}{l} \text{Implant - } 5 \times 10^{15} \text{ }^{11}\text{B}^+ \text{ cm}^{-2}, 25 \text{ keV}, 10^\circ \\ \text{Anneal - } 500^\circ\text{C} - 2 \text{ hr} \\ \text{ } 850^\circ\text{C} - 15 \text{ min} \\ \text{ } 550^\circ\text{C} - 2 \text{ hr} \end{array} \right.$
1470:	
1471:	
1472:	
1474:	

The results from this comparison show that a p^+ layer is essential to form an ohmic contact, Lot 1473, processed without an implanted or alloyed p^+ layer, shows extremely poor curve factors. Figures 2-37 through 2-39 show the performance distributions of V_{oc} , I_{sc} , and I_{450} for all the material processed with a p^+ layer. The highest cell performance was obtained with implanted $^{11}\text{B}^+$ back surface layers, as shown in Figure 2-40.

Although the implanted or alloyed p^+ layers can provide back surface field (BSF) effects and improve cell performance in single-crystal solar cells, the minority carrier lifetime of SILSO material is insufficient to allow the BSF effects to be demonstrated. Higher cell efficiencies would therefore be attainable with polycrystalline silicon that has been doped to 1.0 ohm-cm because of the higher open circuit voltages which would be realized.

The most notable performance deficiency measured for the deliverable cells was the internal shunting of cell output power by individual grains which appear to have extremely high doping or contaminant concentration. Such heavily doped grains can occur during the casting process, and are a result of the segregation of impurities during solidification of the molten silicon. The presence of the highly doped grains is delineated during electroplating of the front contact grids. During the electroplating process, any highly doped silicon regions act as conductors and cause silver to be electrodeposited from the bath onto the silicon. Table 2-10 lists the performance measurements for each

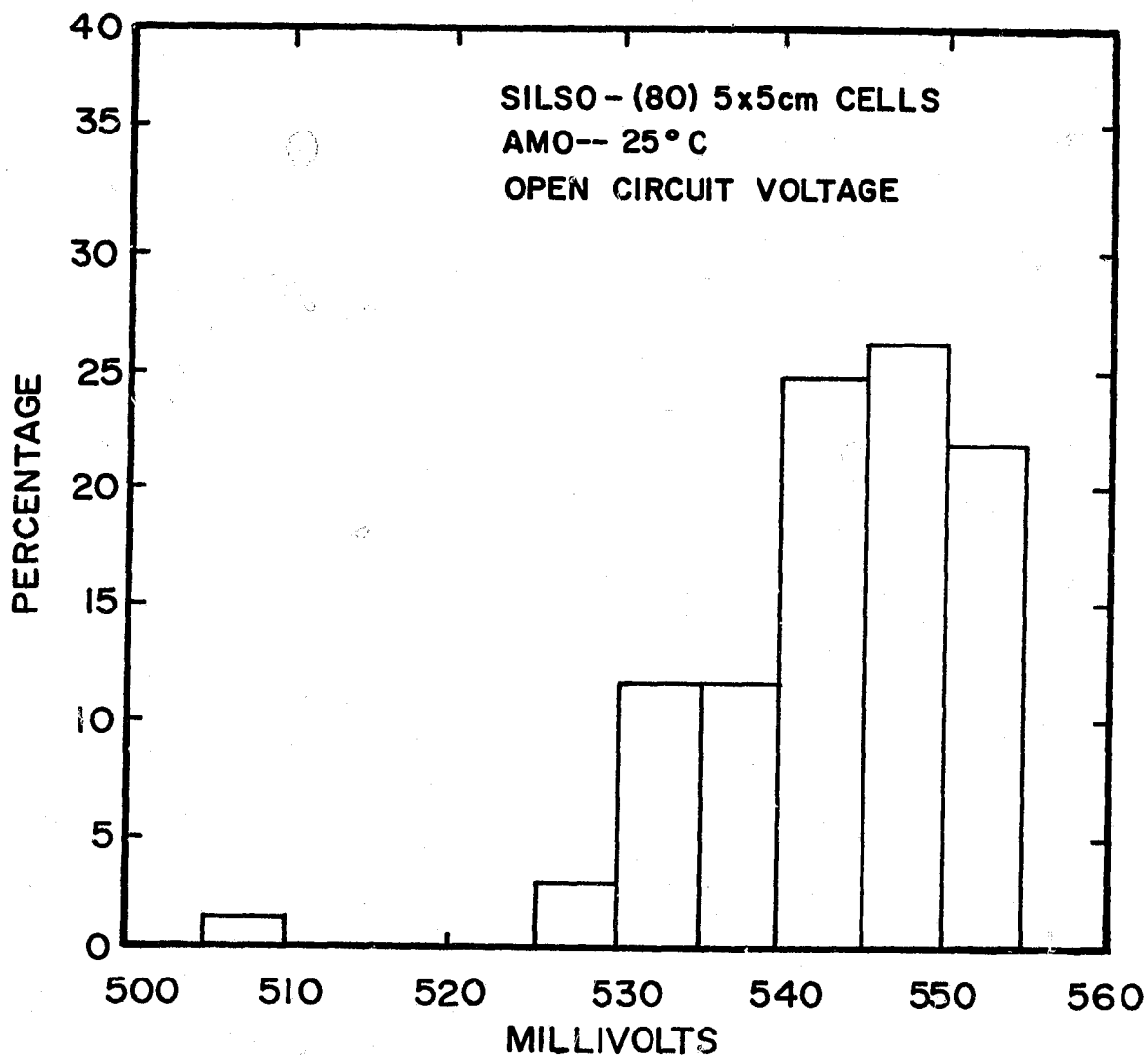


FIGURE 2-37. DISTRIBUTION OF OPEN-CIRCUIT VOLTAGE FOR n^+/pp^+ IMPLANTED POLYCRYSTALLINE SOLAR CELLS

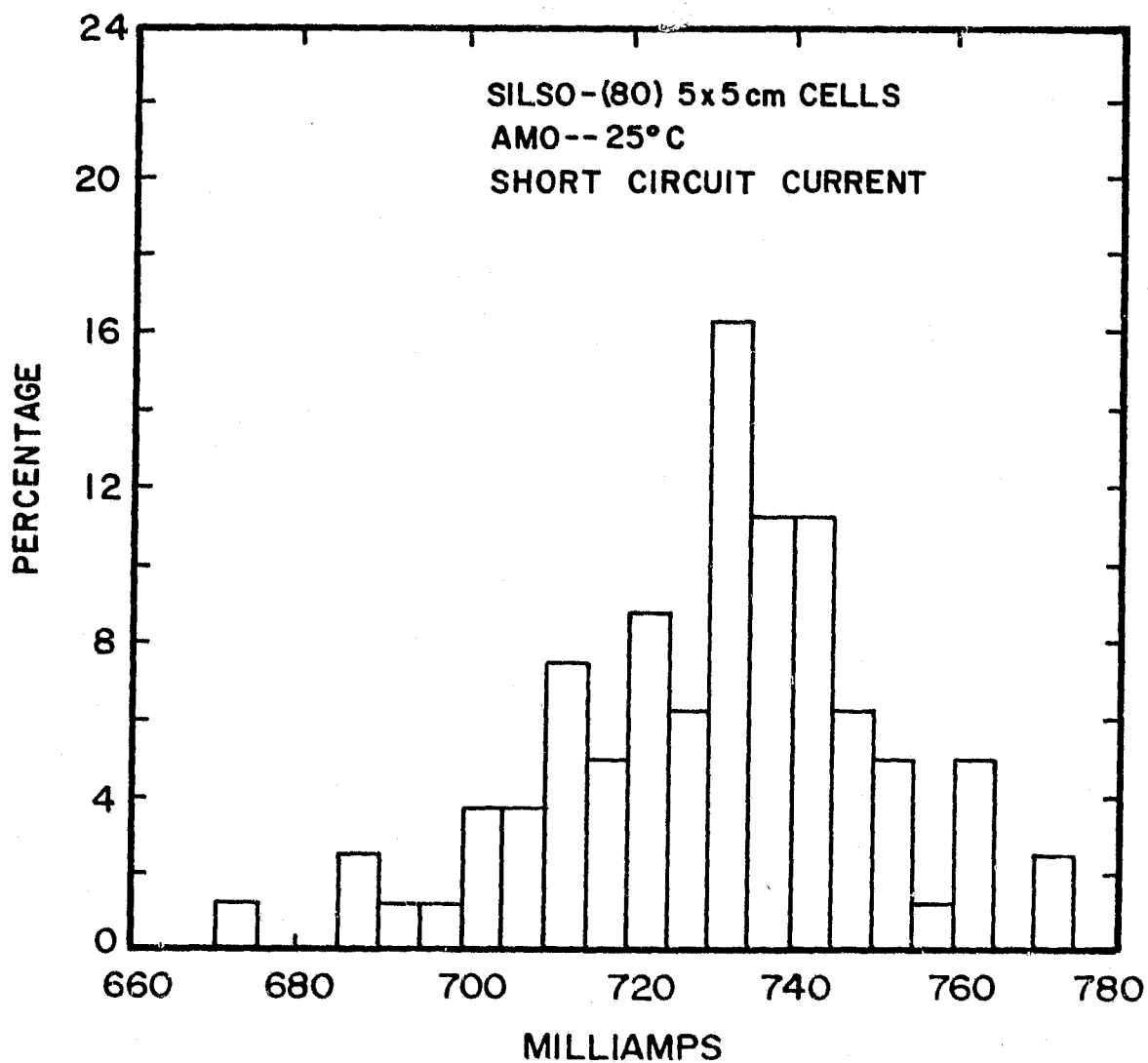


FIGURE 2-38. DISTRIBUTION OF SHORT-CIRCUIT CURRENT FOR n^+/pp^+ IMPLANTED POLYCRYSTALLINE SOLAR CELLS

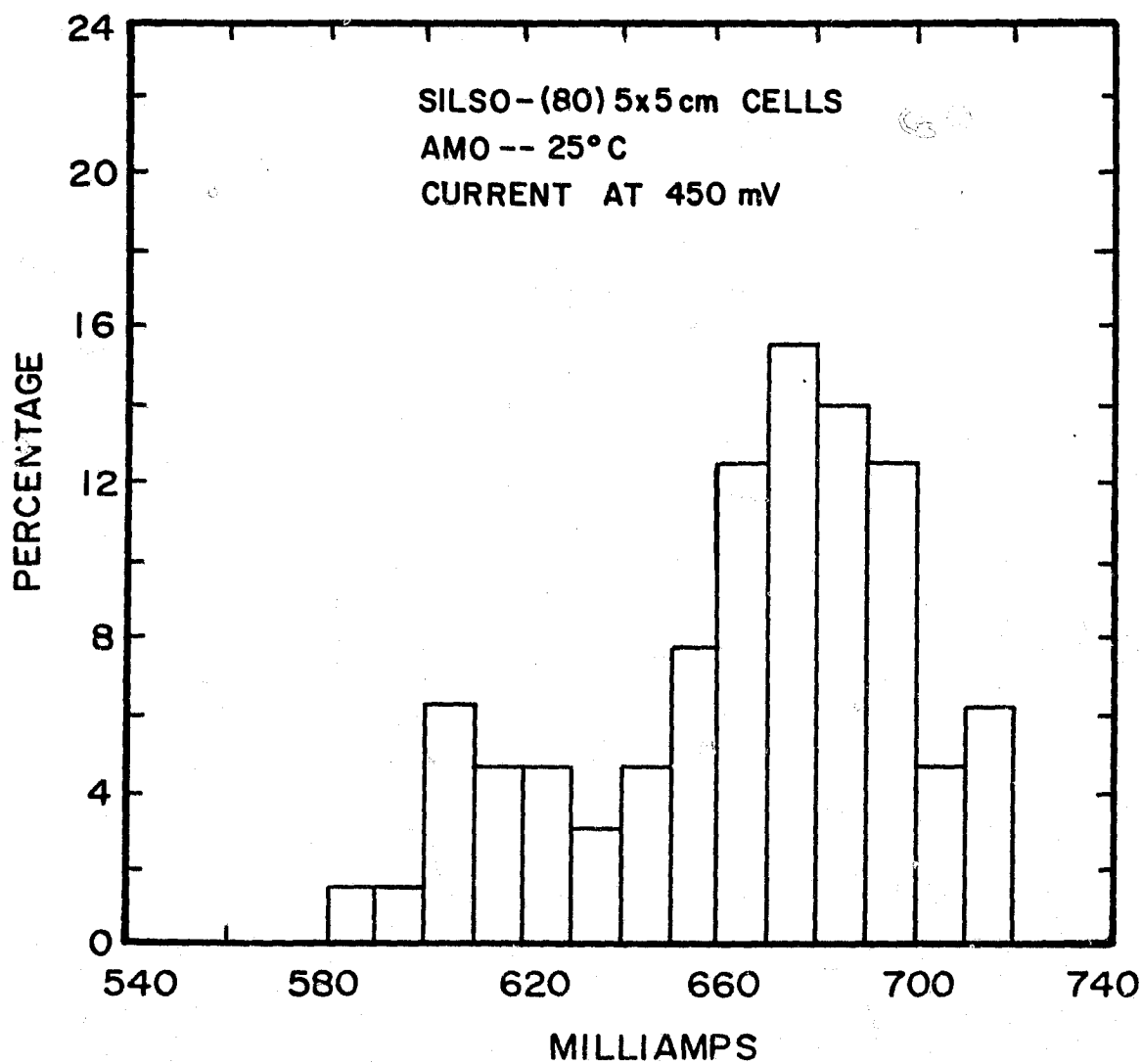


FIGURE 2-39. DISTRIBUTION OF CURRENT AT 450 mV FOR n^+/pp^+ IMPLANTED POLYCRYSTALLINE SOLAR CELLS

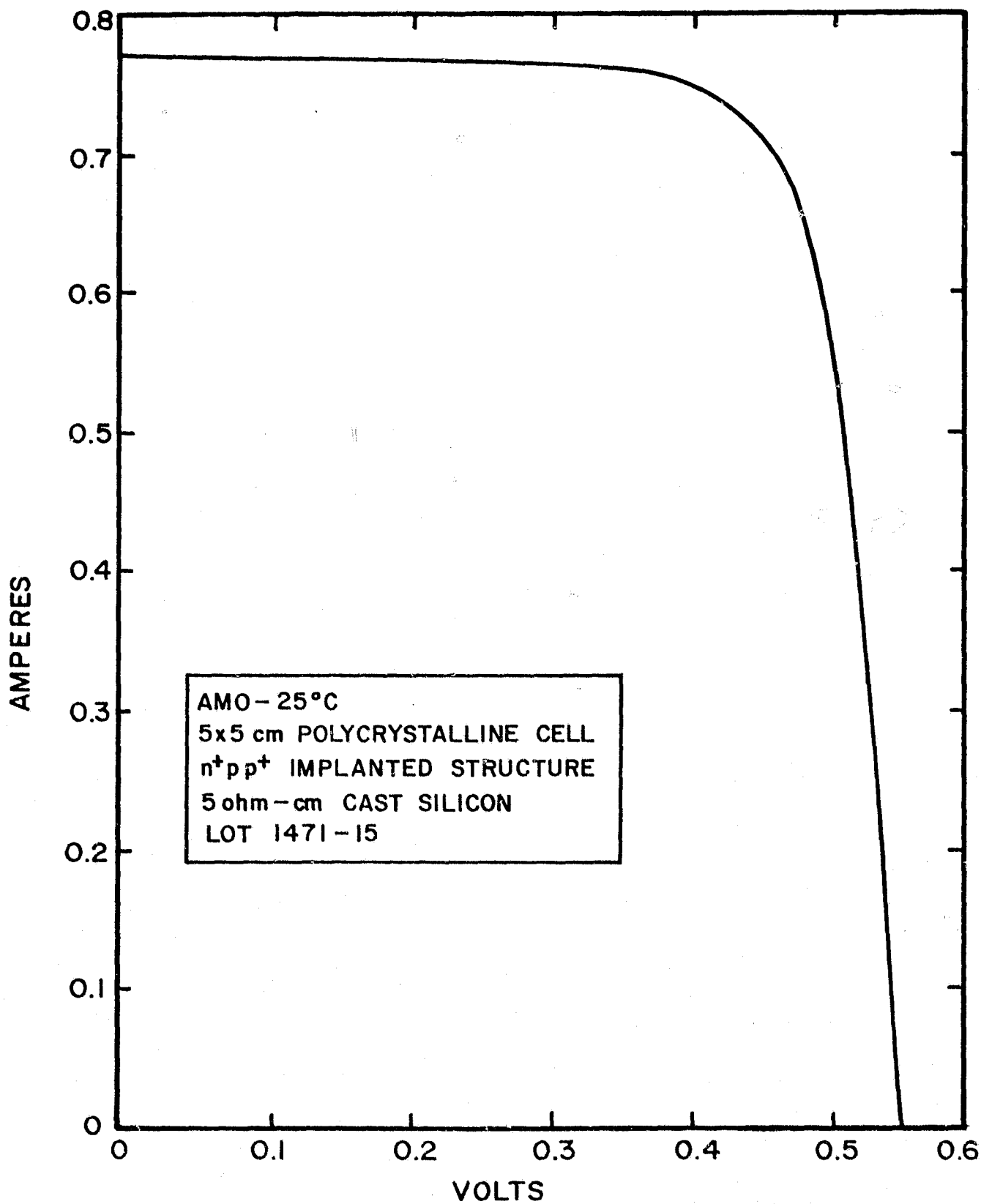


FIGURE 2-40. I-V CHARACTERISTICS FOR 5x5 cm ION IMPLANTED n⁺/pp⁺ POLYCRYSTALLINE SOLAR CELL

TABLE 2-10. POLYCRYSTALLINE SOLAR CELL PERFORMANCE DATA

Lot No.	Cell No.	AM0-25°C CHARACTERISTICS				p ⁺ layer
		I _{sc} (mA)	V _{oc} (mV)	I ₄₂₀ (mA)	I ₄₅₀ (mA)	
52-1469	1	709	535	670	640	Implanted Boron ↓
	2	763	541	720	690	
	3	744	550	705	680	
	5	734	549	695	665	
	6	750	537	695	650	
	7	720	476	250	135	
	8	754	549	715	690	
	9	741	548	705	680	
	10	749	542	710	670	
	11	762	550	725	700	
	12	670	402	*	*	
	14	764	548	730	710	
52-1470	1	735	553	700	680	Implanted Boron ↓
	2	740	542	705	680	
	3	726	548	695	675	
	4	734	547	695	670	
	5	728	540	645	605	
	6	724	546	695	675	
	7	695	393	*	*	
	10	734	550	690	670	
	11	714	534	640	610	
	12	720	529	590	520	
	13	730	538	690	660	
	16	726	554	685	660	
	17	720	540	640	600	

Note: * Indicates internal shunting of cell power by highly doped grains.

TABLE 2-10. POLYCRYSTALLINE SOLAR CELL PERFORMANCE DATA (Continued)

Lot No.	Cell No.	AM0-25°C CHARACTERISTICS				p ⁺ layer
		I _{sc} (mA)	V _{oc} (mV)	I ₄₂₀ (mA)	I ₄₅₀ (mA)	
52-1471	2	708	530	660	630	Implanted Boron ↓
	3	715	535	632	590	
	4	580	115	*	*	
	5	714	542	670	640	
	7	703	542	650	625	
	9	706	532	615	560	
	10	743	553	715	695	
	13	731	534	695	660	
	14	728	546	695	670	
	15	770	546	740	720	
52-1472	1	748	542	710	675	Implanted Boron ↓
	3	750	549	720	690	
	4	739	552	710	685	
	6	756	551	730	710	
	7	749	553	720	705	
	8	714	530	600	540	
	9	733	506	520	415	
	10	724	539	650	600	
	11	744	553	720	700	
	12	738	550	710	690	
	13	720	544	682	655	
	14	719	530	685	650	
	15	686	397	*	*	
	17	738	552	705	680	
	18	640	150	*	*	
	2	733	550	*	685	

Note: * Indicates internal shunting of cell power by highly doped grains.

TABLE 2-10. POLYCRYSTALLINE SOLAR CELL PERFORMANCE DATA (Continued)

Lot No.	Cell No.	AM0-25°C CHARACTERISTICS				p ⁺ layer
		I _{sc} (mA)	V _{oc} (mV)	I ₄₂₀ (mA)	I ₄₅₀ (mA)	
52-1474	2	740	542	700	665	Implanted Boron ↓
	3	736	546	690	660	
	4	739	547	700	675	
	6	733	536	675	635	
	7	703	424	20	*	
	8	717	542	685	660	
	10	710	453	205	*	
	11	734	544	700	670	
	12	711	530	670	625	
	13	733	546	700	675	
	14	734	537	680	645	
	15	737	548	710	680	
	16	715	480	—	200	
	17	742	530	650	600	
	18	733	545	690	660	
	19	726	537	650	610	
		737	527	570	500	
52-1584	1	743	543	625	580	Aluminum Alloy ↓
	2	735	544	695	615	
	4	746	544	710	680	
	5	691	416	*	*	
	6	724	545	680	650	
	7	748	552	715	690	
	8	700	360	*	*	
	9	734	531	560	500	
	10	764	546	715	690	
	11	754	547	720	695	
	12	774	555	740	715	
	13	712	342	*	*	
	14	740	541	690	655	
	15	686	395	*	*	

Note: * Indicates internal shunting of cell power by highly doped grains.

TABLE 2-10. POLYCRYSTALLINE SOLAR CELL PERFORMANCE DATA (Concluded)

Lot No.	Cell No.	AM0-25°C CHARACTERISTICS				p ⁺ layer
		I _{sc} (mA)	V _{oc} (mV)	I ₄₂₀ (mA)	I ₄₅₀ (mA)	
52-1473	1	570	87	550	362	None ↓
	3	622	334			
	4	400	270			
	5	580	332			
	6	653	432	Very		
	7	600	398	Poor		
	8	660	420	Curve		
	9	565	400	Factors		
	10	665	440			
	12	430	262			
	13	572	272			
	14	684	500			
	15	670	482			
	16	750	280			
	17	600	230			
	18	760	352			
	19	410	300			
	20	350	230			

completed cell and indicates the frequency of shunting due to material defects. It is important to note that this material was manufactured in September 1977; since then the growth technology may have been improved by Wacker.

2.3.3 Cell Process Comparisons: 1-ohm-cm Silicon

The first of three cell junction performance assessments was performed to compare ion implantation and diffusion technology for dopant introduction. The starting material was (100), 1.0-ohm-cm, Czochralski silicon with bright-etched surfaces. Three groups of cells having both implanted and diffused junctions were processed, as follows:

1. Diffused junction and alloyed aluminum p^+ back surface introduced at OCLI
2. Ion-implanted/furnace-annealed junction and alloyed aluminum p^+ back surface introduced at Spire
3. Ion-implanted/pulsed electron beam annealed junction and alloyed aluminum p^+ back surface introduced at Spire.

Contacts, multiple-layer AR coating, and AM0 performance measurements were completed at OCLI for all three types of processing. Table 2-11 summarizes the peaks, means, and standard deviations of AM0 efficiencies, for each type of cell junction. Appendix C shows the performance distributions of each type. Note that the highest short-circuit currents were attained with the ion-implanted junctions. However, the results also showed lower cell efficiencies for the implanted and pulse or furnace annealed junctions than for the diffused junctions. These lower efficiencies were due to curve factors limited by series resistance, and not to lower I_{sc} or V_{oc} . The higher series resistance for the implanted cells was a result of the mismatch between the OCLI contact design (4 lines/cm) and the implanted junction sheet resistance of 120-ohms per square. Subsequent process comparisons will use a violet cell grid design (10 lines/cm) to preclude this problem.

TABLE 2-11. SUMMARY OF FIRST PERFORMANCE COMPARISON
OF CELL JUNCTION FORMATION TECHNIQUES

Junction Formation	AM0 Efficiency (%)		
	Mean	Peak	Std. Deviation
Diffused	12.1	12.9	0.4
Ion-Implanted/ Furnace-Annealed	11.5	12.5	0.6
Ion-Implanted/ Pulse-Annealed	11.0	12.3	0.8

NOTES:

- (1) Silicon: 1-ohm-cm (100) CZ
Bright-etched surfaces
300 micrometer thick
- (2) Cell Structure: Alloyed aluminum p⁺ layer
TiPdAg contacts
Multi-layer AR coating

2.3.4 Cell Process Comparisons: 10-ohm-cm Silicon

The second of three cell junction and back surface field (BSF) performance assessments was performed to compare ion implantation and diffusion technology for dopant introduction. The starting material was (100), 10-ohm-cm, crucible grown silicon with etched surfaces. Three groups of cells having both implanted and diffused junctions were processed, as follows:

1. Diffused junctions and back surface fields introduced at OCLI.
2. Furnace-annealed, ion-implanted back surface fields and furnace-annealed, ion-implanted junctions.
3. Furnace-annealed, ion-implanted back surface fields and pulse-annealed, ion-implanted junctions.

The third type of cells employed furnace-annealed back surface fields because efforts at the time of this comparison were still underway to pulse anneal the necessary boron implant effectively. Contacts, multiple-layer AR coating, and AM0 performance measurements were completed at OCLI for all three types of processing. Table 2-12 summarizes the peak and mean cell characteristics under AM0 conditions for each type. Appendix D shows the open-circuit voltage, short-circuit current, and maximum power performance distribution of each. The highest short-circuit currents were obtained by processing both the junction and the BSF by ion implantation and furnace annealing. The highest cell efficiency attained was 13.8 percent AM0 for furnace-annealed and 12.7 percent AM0 for pulse-annealed junctions. The second process comparison utilized a violet cell grid design with 10 lines/cm to match the ion-implanted junction layer sheet resistance.

TABLE 2-12. SUMMARY OF SECOND PERFORMANCE COMPARISON OF CELL JUNCTION AND BACK SURFACE FIELD FORMATION

Junction and BSF Formation	AM0-25°C Performance						No. of Cells
	I _{sc} (mA)		V _{oc} (mV)		P ₄₅₀ (mW)		
	Mean	Peak	Mean	Peak	Mean	Peak	
Diffused and Alloy	157	162	589	599	62.4	66.3	67
Implant/ Furnace Anneal	157	165	564	582	64.2	71.9	80
Implant/Pulse Anneal	154	158	563	571	58.4	68.8	79

NOTES:

- (1) Silicon: 10-ohm-cm (100) Czochralski
Bright-etched surfaces
300 micrometers thick
- (2) Cell Structure: n⁺/pp⁺ with BSF
TiPdAg contacts
Multi-layer AR coating

2.3.5 Cell Process Comparisons: Pulsed Laser and Electron Beam Annealing

The third performance assessment is still active, and will evaluate and compare both pulsed electron beam annealing and laser annealing of the junction layers. The back surface field layers to be incorporated in the 10-ohm-cm material will have been implanted and furnace annealed prior to implant of junction layer. As in previous performance assessments, OCLI will complete processing by applying contacts and the AR coating, then measuring cell performance.

2.4 ADVANCED PRODUCTION TECHNOLOGY

2.4.1 Ion Implanted/Pulse Annealed Solar Cells

Ion implantation can be utilized in a number of variations of the solar cell production process. One approach with considerable potential for becoming extremely effective for automated production at high-volume levels involves the combination of ion implantation and pulsed energy processing techniques.⁽¹⁰⁾

Pulsed energy, deposited into the region being processed by an electron beam, a laser or some other directed energy source, has been demonstrated as a replacement for the thermal operations normally considered necessary in the fabrication of a junction solar cell. Directly or indirectly, elevated temperature steps are responsible for most of the energy consumption, waste generation, process complexity and time required to produce a silicon solar cell from adequate starting material. Each thermal step has the purpose of performing some treatment, annealing, sintering, etc., in the vicinity of the device surface. Very short duration pulses of directed energy can cause equivalent process effects to occur. Major process simplifications and cost reductions are expected as a result.

Pulsed processing has been under development as a replacement for the furnace operations normally used in solar cell fabrication. However, it has been found that the pulsed energy techniques produce somewhat different results, which in many instances are technically superior to those produced by a furnace process (see Section 2.5.2). This appears to be the case for the annealing of ion implantation damage, a key process in the fabrication of an implanted cell and the subject of the pulsed energy process studies under this program.

The basis for producing processing effects by momentary temperature transients is the ability to achieve and then quickly quench a high temperature in the localized region being treated. Spire has investigated the use of several types of lasers, high-intensity flash lamps, and pulsed electron beams. Because of the considerations of obtaining sufficient energy deposition, uniformity, and reproducibility over reasonably large areas, together with being able to build efficient production machines with high repetition rates, Spire is emphasizing the use of the pulsed electron beam.

2.4.2 Automated Production Process Concept

A concept for total cell production has been developed by Spire for use in automated production machines, which involves ion implantation in conjunction with directed energy pulse annealing that replaces all furnace operations. The result is high-speed, room-temperature processing conducted in a vacuum environment common to all steps. A schematic of the design concept is shown in Figure 2-41.

The most important and demanding pulsed energy process steps are those used to anneal to the silicon lattice following radiation damage caused by ion implantation. Investigations related to pulsed energy processes under the present program have emphasized the development of parameters for implant damage annealing and the identification of the mechanisms associated with these submicrosecond processing effects. Mechanism studies are discussed in Section 2.5.

Annealing of implantation damage is an essential step in the fabrication of an ion-implanted solar cell. Experimental work in the development of optimized pulsed electron beam parameters for the annealing of solar cell junction implants is in progress. The facility being employed generates an almost uniform beam spot approximately 5.7 cm in diameter. Parameters of the beam used for silicon solar cell junction annealing are as follows:

Pulse duration:	10^{-7} second
Mean electron energy:	12 keV
Beam fluence:	0.1 - 0.3 cal/cm ²

CONCEPT FOR TOTAL AUTOMATED PRODUCTION - 100 MW_e of Solar

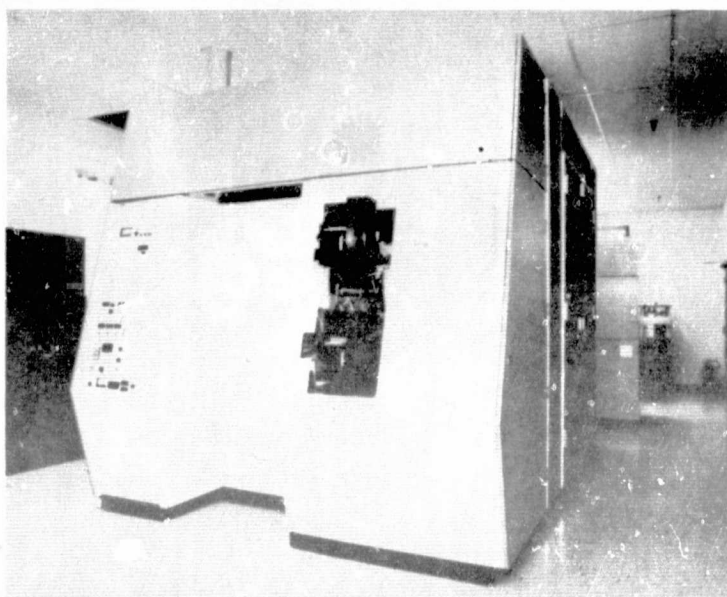
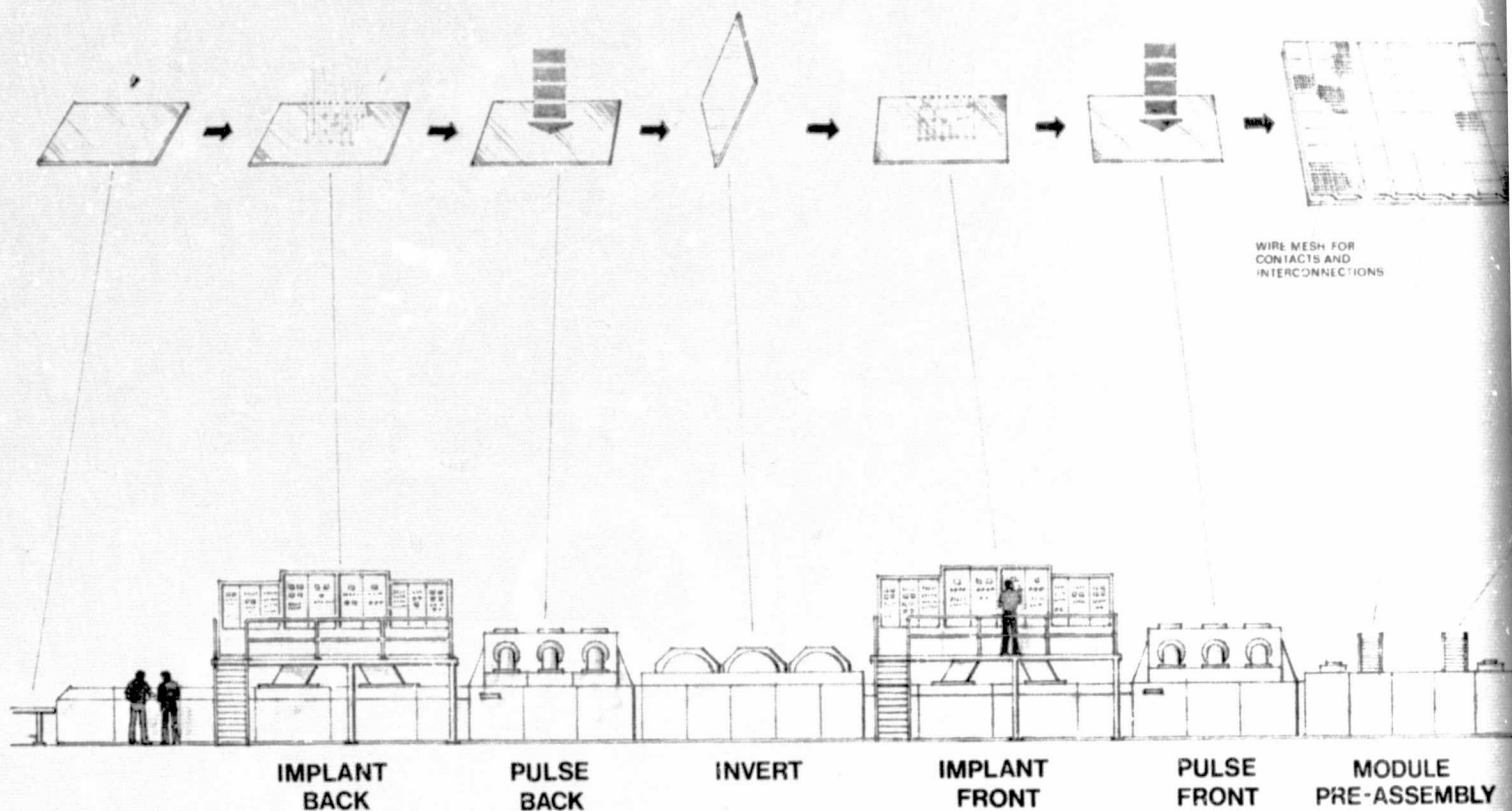
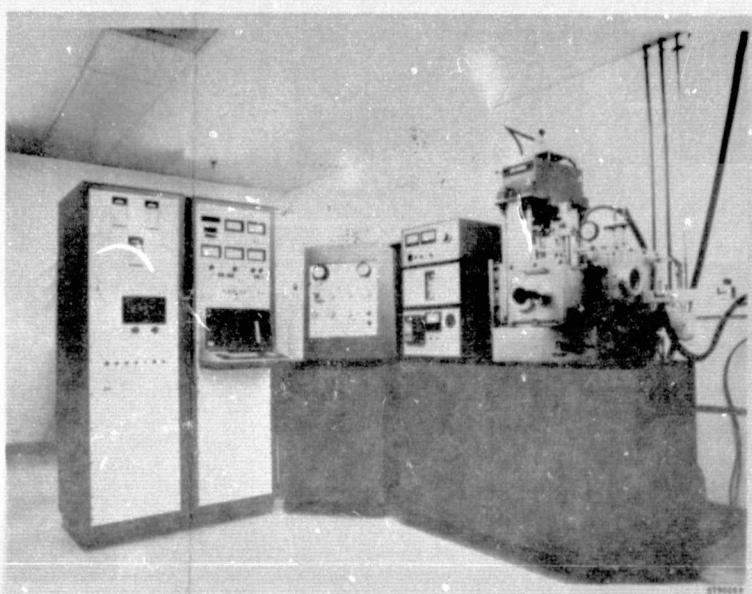
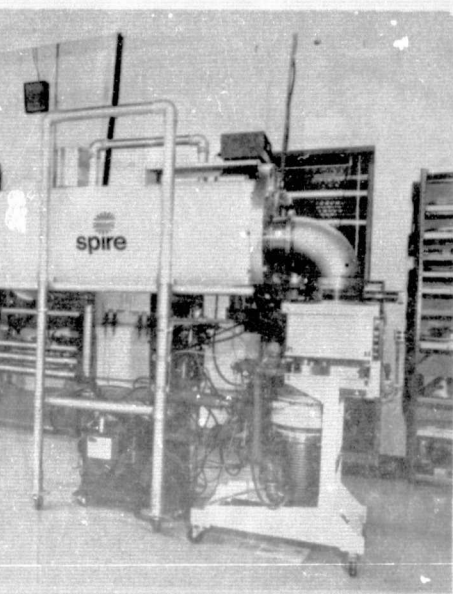
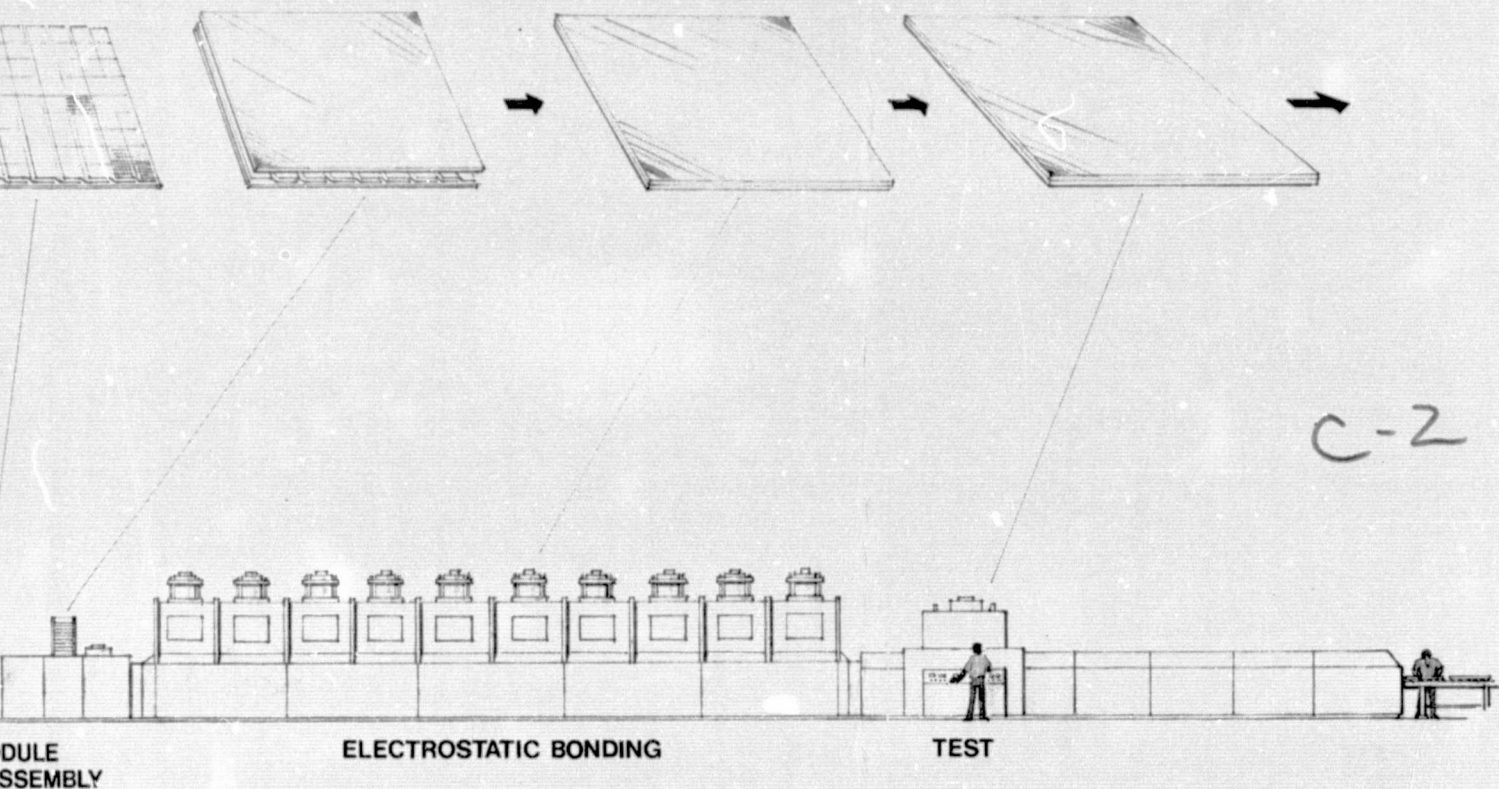


FIGURE 2-41. CONCEPT FOR TOTAL
AUTOMATED PRODUCTION -
100 mW_e OF SOLAR CELLS
PER YEAR

of Solar Cells Per Year

FOLDOUT FRAME 2



A process was developed which exclusively relies on pulsed electron beam annealing of the implantation damage for junction and back surface field layers and sintering of contact metals to form ohmic interfaces. A summary of the all-vacuum, in-line process is outlined in Table 2-13.

At the present time, facilities do not exist to allow the evaluation of the performance of cells processed entirely in vacuum and not exposed to ambient conditions between process elements. However, the feasibility has been demonstrated for each of the process elements shown in Table 2-13, and cells have been fabricated using only implantation, pulse annealing, and other room-temperature vacuum processes. Pulse-annealed, boron-implanted back surface fields (BSF) have been demonstrated to be effective in increasing the V_{oc} of 10-ohm-cm, Czochralski silicon substrates from 550 mV to 570 mV. Comparable BSF effects after optimized, furnace-annealed, boron implants increase V_{oc} from 500 mV to 580 mV.

TABLE 2-13. OUTLINE FOR ALL-VACUUM, IN-LINE PROCESSING

Implant Back Surface Field -	$5 \times 10^{15} \text{ }^{11}\text{B}^+ \text{ cm}^{-2}$, 10° incidence (± 10 percent dose tolerance)
Pulse Anneal Back Surface Field Implant -	0.3 cal/cm^2 , 10-30 keV, 100 ns pulsed electron beam
Implant Front Surface Junction -	$2 \times 10^{15} \text{ }^{31}\text{P}^+ \text{ cm}^{-2}$, 10 keV, 10° incidence (± 10 percent dose tolerance)
Pulse Anneal Front Surface Junction Implant -	0.2 cal/cm^2 , 10-30 keV, 100 ns pulsed electron beam
Deposit Back Contact -	1 micrometer AlAg (method to be defined)
Deposit Front Contact Grid -	400Å Ta, W, Mo, or Pd by charged- particle writing
Pulse Sinter Front Contact -	0.1 cal/cm^2 , pulsed electron beam (pulse width and energy to be defined)
Deposit AR Coating -	Si_3N_4 700Å layer by plasma- assisted CVD
Attach Bus Bars/Interconnects -	Electrostatic bonding
Encapsulate -	Electrostatic bonding

In the feasibility experiments, $5 \times 10^{15} \text{ }^{11}\text{B}^+ \text{ cm}^{-2}$ ions were implanted at 25 keV into the back surface of each wafer. The implants were then pulse-annealed using a fluence of approximately 0.3 cal/cm^2 for a 0.1-second pulsed electron beam. Following pulse annealing of the $^{11}\text{B}^+$ implant, the junction was implanted with $2.5 \times 10^{15} \text{ }^{31}\text{P}^+ \text{ cm}^{-2}$ at 10 keV, and also pulse annealed at an electron beam fluence of 0.2 cal/cm^2 . Typical I-V characteristics of cells processed using only pulse annealing are shown in Figure 2-42. Cell efficiencies have been measured at 11.8 percent under AM0 conditions.

The pulsed electron beam method of annealing the ion implantation radiation damage was also demonstrated on polycrystalline material. The effectiveness of pulse annealing was determined using the following process sequence:

1. Saw to 5x5 cm.
2. Bright-etch to remove saw damage.
3. Evaporate 400Å aluminum p^+ layer.
4. Alloy 650°C - 15 min.
5. Implant n^+ junction $2 \times 10^{15} \text{ }^{31}\text{P}^+ \text{ cm}^{-2}$, 10 keV, 10° .
6. Pulse anneal.
7. Front/back metallization: TiPdAg.
8. AR evaporation: TiO_2 .
9. Saw finished device 2x2 cm.

Typical performance characteristics for pulse-annealed, ion-implanted polycrystalline cells are shown in Figure 2.43.

Cell efficiencies for pulse-processed, ion-implanted cells equal those attained by furnace annealing; also, the measured short-circuit density is higher than furnace-annealed devices. For example, the highest measured current density under AM0 conditions was 33.25 mA/cm^2 for pulse-annealed devices and 30.52 mA/cm^2 for furnace-annealed devices.

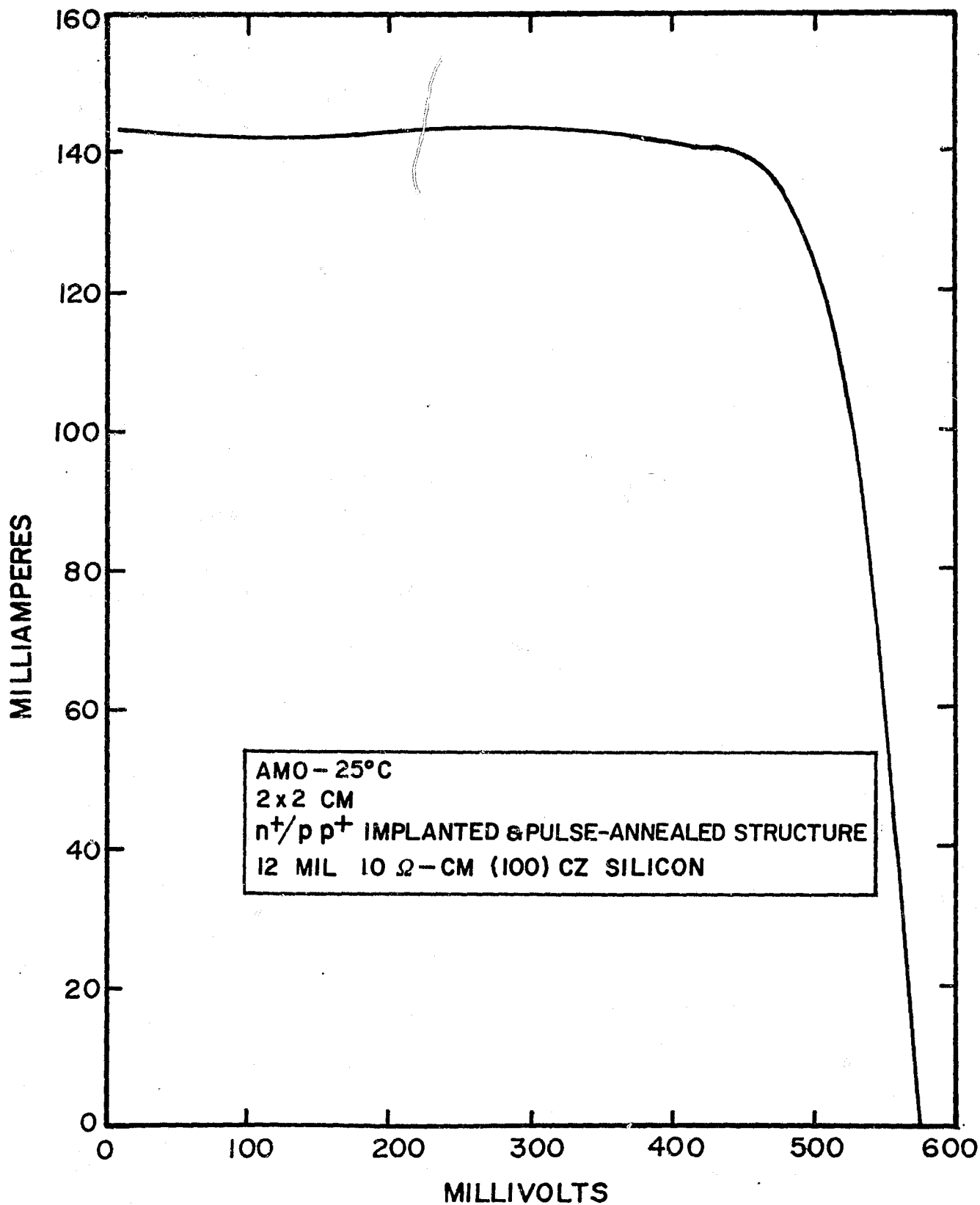


FIGURE 2-42. I-V CHARACTERISTICS FOR CELLS PROCESSED USING PULSED ELECTRON BEAM ANNEALING OF BOTH PHOSPHORUS JUNCTION AND BORON BSF IMPLANTED LAYERS

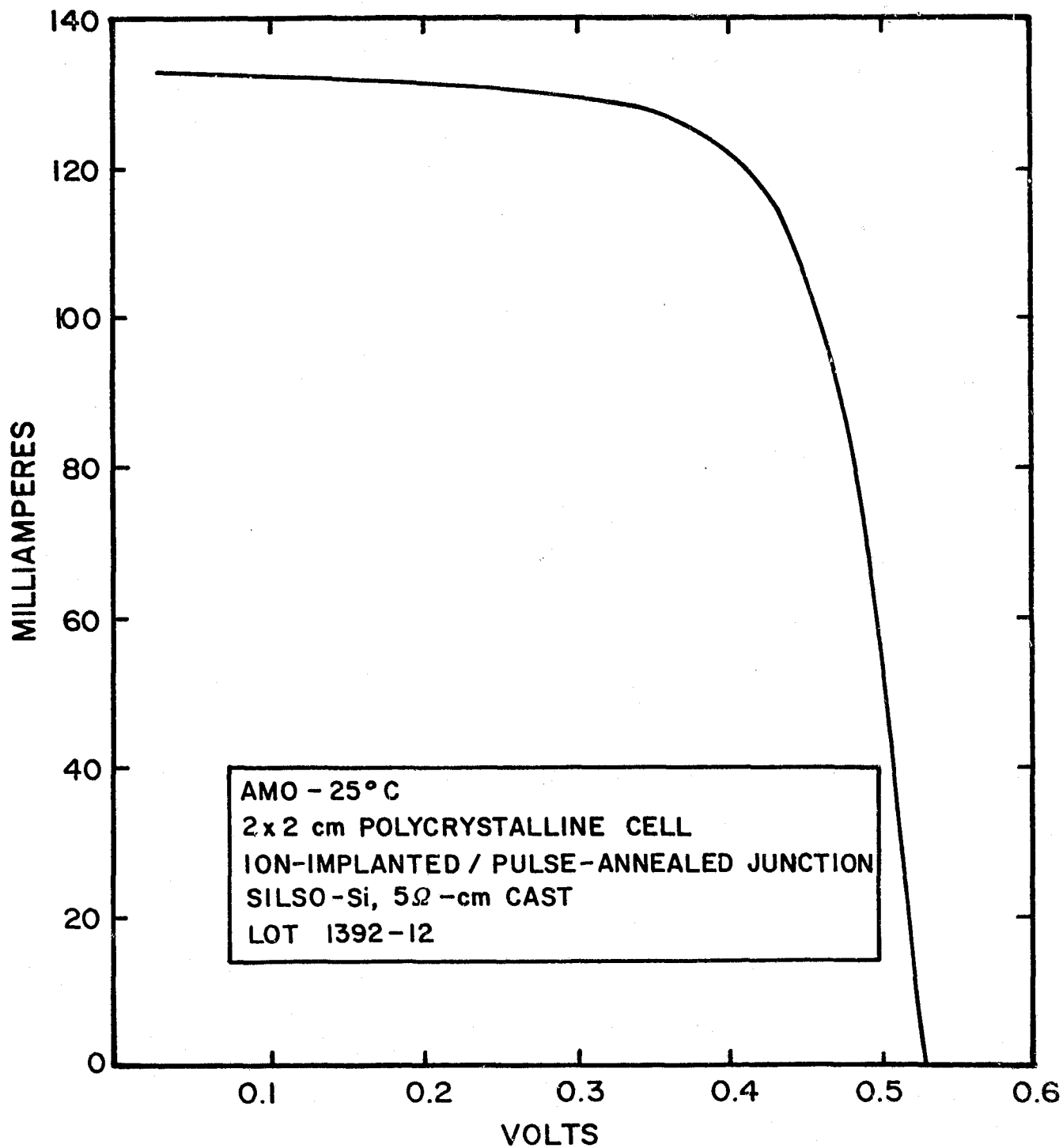


FIGURE 2-43. I-V CHARACTERISTICS FOR PULSE ANNEALED ION IMPLANTED POLYCRYSTALLINE SOLAR CELLS

The use of pulsed energy sources other than pulsed electron beams was also investigated for annealing ion implantation damage. Experimental data has been obtained for the pulsed laser annealing of phosphorus junction implants. The cell process sequence was as outlined below:

Silicon: 2-ohm-cm (100) Czochralski
p⁺: aluminum alloy 650°C
n⁺: implant - $2 \times 10^{15} \text{ }^{31}\text{P}^+ \text{ cm}^{-2}$, 10 keV
anneal - pulsed Nd:YAG laser
Contacts: CrAuAg
AR: TiO_2

No additional furnace annealing was incorporated in this process following laser pulse annealing. Laser parameters used were as follows:

Wavelength: Nd:YAG at 1.06 micrometers
Pulse Width: 120-150 ns
Average Power: 10 watts continuous
Repetition Rate: 6 KHz
Annealing Rate: approximately $0.5 \text{ cm}^2/\text{sec}$
Spot Size: approximately 100 micrometers
Mode: single

Typical electrical performance of cells with laser-annealed, ion-implanted junctions is shown in Figure 2-44. The open-circuit voltage is 570 mV under AM0 conditions. The cells show a similar V_{oc} performance loss as previously obtained with pulsed electron beam annealing of implants without post-pulse, low-temperature annealing. Cell efficiencies have been measured at 9.2 percent AM0. For comparison and reference the best cells with electron beam pulse-annealed junctions show efficiencies up to 12.3 percent AM0 with the same cell structure.

2.5 PULSED ENERGY PROCESSING STUDIES

The application of ion implantation to solar cell processing requires an annealing technique to remove the inherent radiation damage to the silicon lattice. As discussed in Section 2.2.3, the requirements for successful furnace annealing depend upon the implant parameters. Another approach to annealing ion implantation damage is to utilize pulsed energy deposition. In this technique, a pulsed energy source, such as an electron or laser beam, is directed onto the surface to be heated. Almost all the energy carried by source is deposited into the first few micrometers of the surface being processed, resulting in momentary, high-temperature transients. A mechanism which can explain the annealing effects obtained by pulsed energy transients has been identified, and is described below. Pulsed energy sources can replace the thermal operations ordinarily performed in a furnace.

2.5.1 Advantages of Pulsed Energy Processing

The potential advantages of pulsed energy processing can be separated into technical and cost categories and summarized as follows:

Technical Advantages:

1. Higher efficiency cells may be achievable. Better lattice regrowth occurs with pulse annealing, as will be discussed. Rapid dopant diffusion during annealing may result in a better junction profile. During pulse processing, the bulk silicon is never brought to a high temperature, thereby precluding lifetime degradation by thermally induced defects.

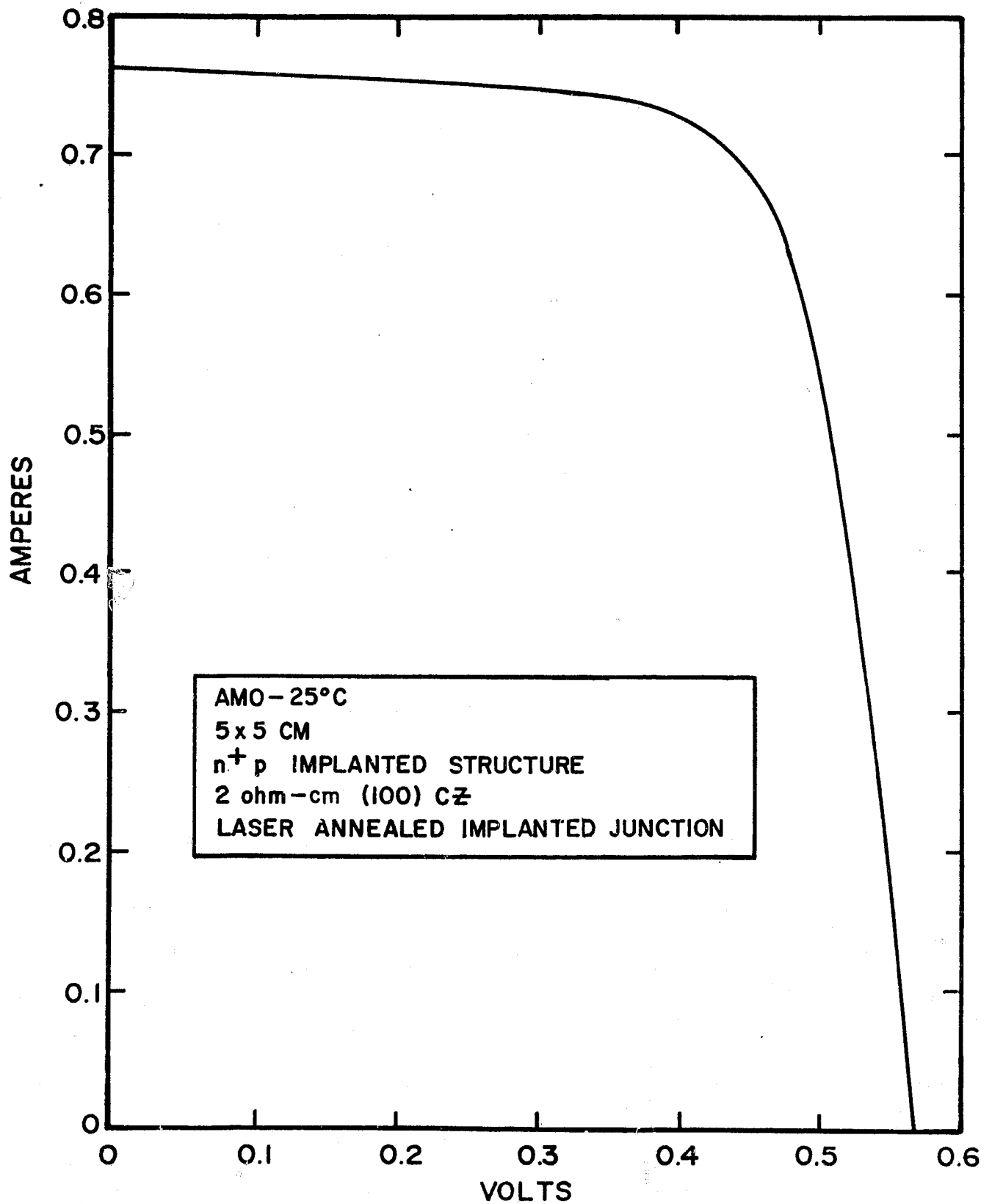


FIGURE 2-44. I-V CHARACTERISTICS FOR CELLS PROCESSED USING LASER-ANNEALED IMPLANTED JUNCTIONS AND ALLOYED p⁺ LAYERS

2. Pulse processing may prove advantageous for fabricating cells from advanced polycrystalline sheet materials. Transient, surface heating will minimize grain boundary effects such as the diffusing of dopants and contact metallization. Also, thermally unstable materials and substrates can be processed.
3. Pulse annealing facilities, analogous to ion implantation facilities, are amenable to in-line processing for automation. Also, pulse annealing is a vacuum process, and is compatible with ion implantation equipment.

Cost Advantages:

1. The cost of pulse processing should be considerably less than conventional processing, because no wet chemistry or forming gases are required. Furthermore, pulse processing is an efficient use of input utility supplied power significantly reducing solar cell pay-back time.
2. Capital equipment costs for pulse processing will be less than those associated with diffusion processing or ion implantation with annealing furnaces. Since the projected size of a pulse annealer is comparable to a 100-mA implanter, relatively small building space is required. In-line annealing should also reduce the number of silicon carrying cassettes thereby reducing cost.
3. Since the process is amenable to automation and compatible with ion implantation, common cassettes can be implemented.
4. Reduced capital equipment requirements allow production scale-up to be achieved relatively easily.

Other Advantages:

1. Reduced environmental impact can be expected due to the elimination of wet chemistry, forming-gas processes, and waste treatment facilities.

2.5.2 Advantages of the Pulsed Energy Product

Phosphorus, arsenic, and boron implanted junctions have demonstrated superior structural quality after pulse annealing compared to optimized furnace annealing. The best implanted structures achieved to date, as defined by the absence of dislocation networks or interstitial atoms, have been obtained by pulsed electron beam annealing and combined pulsed electron beam and low-temperature furnace annealing. Studies have been completed to evaluate and compare the dislocation densities of ion-implanted silicon wafers after furnace and pulse annealing. The material used included FZ and CZ grown (100) silicon. Following $2 \times 10^{15} \text{ }^{31}\text{P}^+ \text{ cm}^{-2}$, 5-keV implants, the wafers were annealed by optimized furnace schedules and pulsed electron beam.

Measurement techniques for assessing the quality of the epitaxially regrown implanted/annealed junctions included preferential etching to delineate dislocation networks, helium ion backscattering, and transmission electron microscopy. The dislocation density below the surface was also determined by repetitive anodic oxidation and layer stripping techniques. The results of these measurements on furnace annealed implanted junctions are shown in Figure 2-45. The important conclusions for furnace- and pulse-annealed implants are summarized below:

1. Furnace annealing results in a dislocation density of about 10^8 cm^{-2} at the wafer surface, with a gradual reduction toward the metallurgical junction. This is due to slow regrowth from the unimplanted base material. No evidence was found that implantation-induced defects propagate beyond the projected ion range after optimized furnace annealing.
2. Pulse annealing results in a decreased dislocation density, even when compared to the unimplanted CZ or FZ material. No evidence was found that implantation-induced defects remain in the implant region or propagate to the underlying substrate after pulse annealing.

The implanted layers were found to exhibit better structural quality after pulsed electron beam annealing than after furnace annealing. Structural evaluations of importance to this program were performed by S.S. Lau, W. Tseng and J. Mayer of California Institute of Technology⁽¹¹⁾. Figure 2-46 shows the helium ion backscattering measurement results obtained on identical implanted samples without annealing, with furnace annealing, and with pulsed electron beam annealing. The unannealed sample

LAYERS (THICKNESS)
REMOVED

SAMPLE NO.

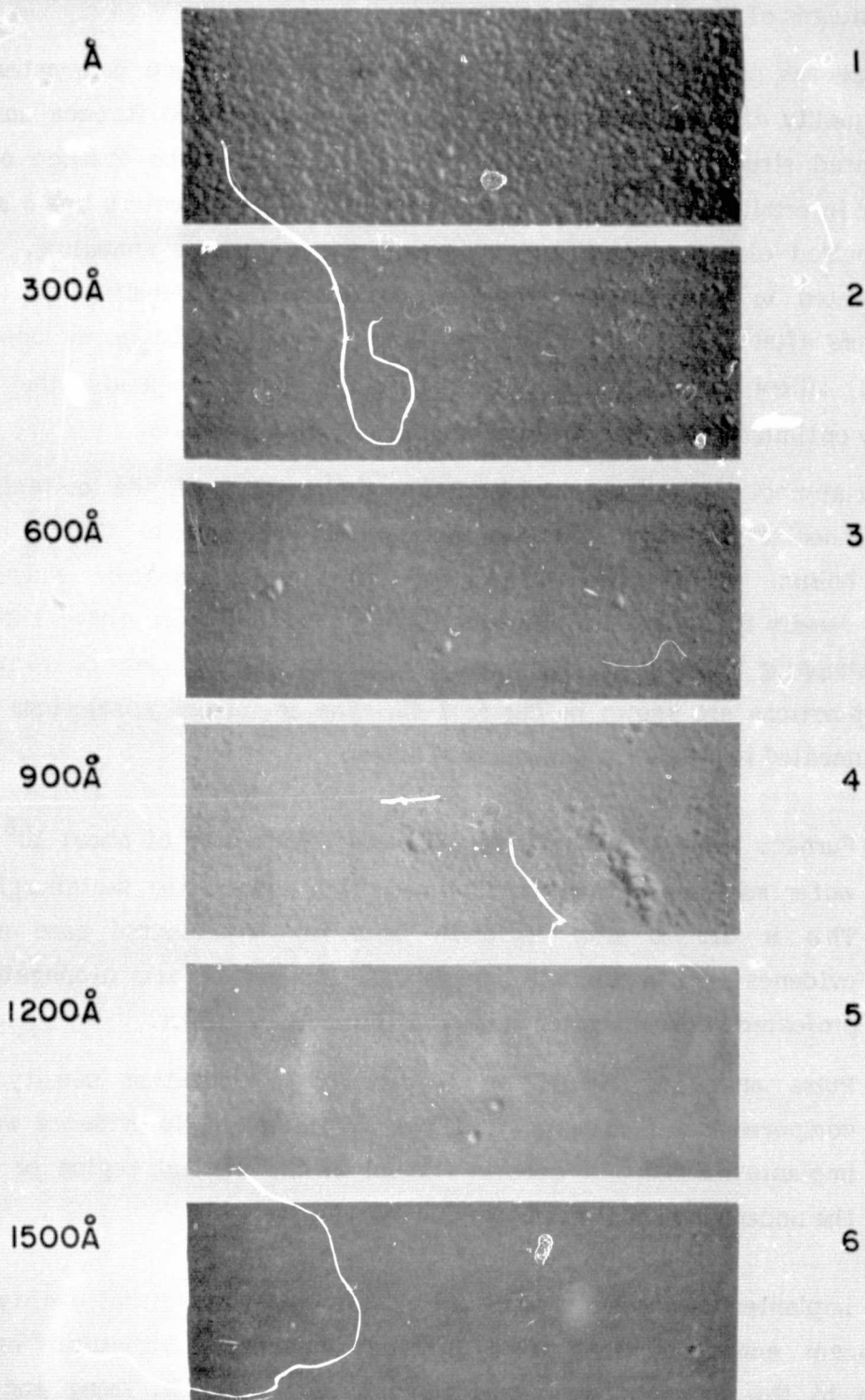


FIGURE 2-45. DISLOCATION DENSITY AS A FUNCTION OF DEPTH INTO CRYSTAL REVEALED BY LAYER STRIPPING

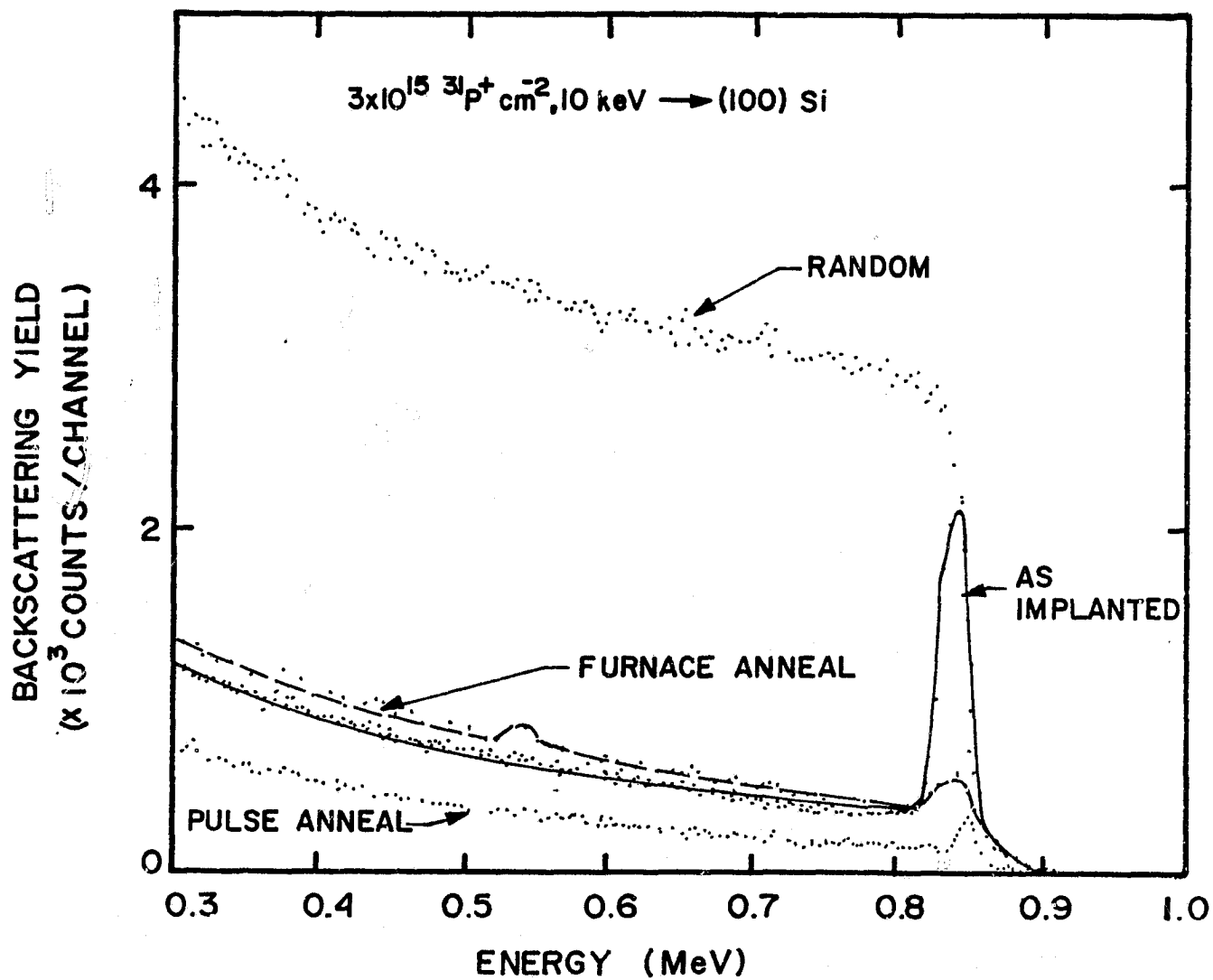


FIGURE 2-46. HELIUM ION BACKSCATTERING FROM FURNACE AND ELECTRON BEAM ANNEALED IMPLANTED WAFERS

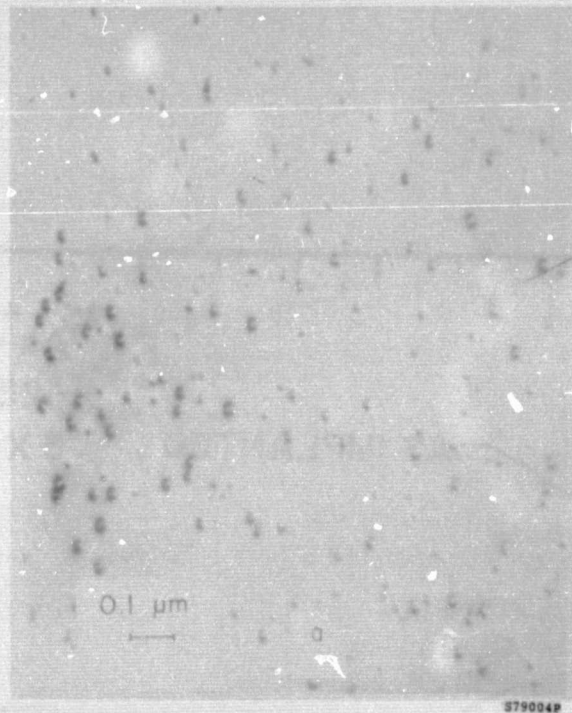
exhibited the surface region backscattering characteristic of amorphous material. The furnace-annealed sample showed backscattering typical of good conventional annealing procedure. The backscattering was much reduced by the crystalline regrowth of the implanted layer, but not eliminated because of the formation of polycrystallites within the layer. The sample annealed with the pulsed electron beam exhibited very low backscattering comparable to that produced by virgin, single-crystal silicon. The pulsed-annealed layer was recrystallized to single-crystal condition.

Transmission electron microscopy (TEM) studies were also conducted upon the furnace and pulsed electron beam annealed, implanted layers. Typical results are shown in Figure 2-47. Under TEM examination, the furnace-annealed layers show dislocation loops and residual disorder effects characteristic of conventional annealing practice. However, the layers annealed with the pulsed electron beam exhibit virtually the total absence of dislocations or any other mechanical defects.

Pulse annealing is found to produce more complete electrical activation of the implanted dopant. Redistribution of impurities as a result of pulsing is found to occur. Figure 2-48 shows a typical result measured using helium ion backscattering methods. The figure shows the as-implanted profile of a heavy, 25-keV arsenic implant and the profile of the same implant after pulsed electron beam anneal. The arsenic atoms have moved appreciably deeper into the silicon, and the profile peak below the surface has been eliminated. The correct utilization of these effects is to be an important factor in the development of high-efficiency, pulse processed cells.

Both laser and electron beam pulse annealed, ion-implanted cells have typically exhibited a 20-mV lower V_{oc} than furnace-annealed implanted cells or diffused cells of the same silicon resistivity. However, the 20-mV degradation has been restored by a low-temperature, postpulse anneal in the range of 400°C to 500°C. This is typical of the annealing requirements for lattice point defects.

Point defects remaining in the implanted/pulse-annealed layer can be due to incomplete annealing during the rapid recrystallization occurring within microseconds. It is possible that such rapid regrowth can result in dislocation-free material with excellent structural characteristics, but possessing residual point defects due to the remaining stresses. These point defects are not detectable by TEM or backscattering techniques; however, they do introduce electronic levels in the bandgap which increase carrier



A. Thermally Annealed, Implanted Layer

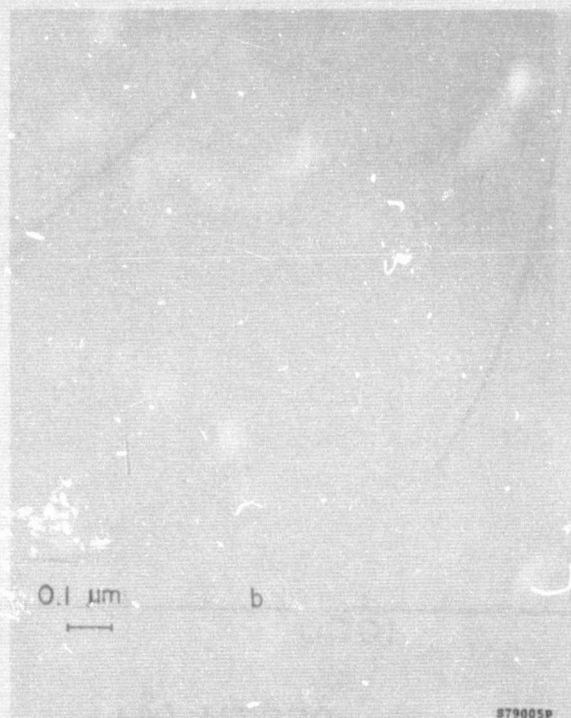


FIGURE 2-47. TRANSMISSION ELECTRON MICROSCOPE PHOTOS OF FURNACE-ANNEALED AND ELECTRON BEAM ANNEALED LAYERS ON (100) SILICON (Implants: $10 \text{ keV } P^{31+} 10^{15} \text{ cm}^{-2}$)

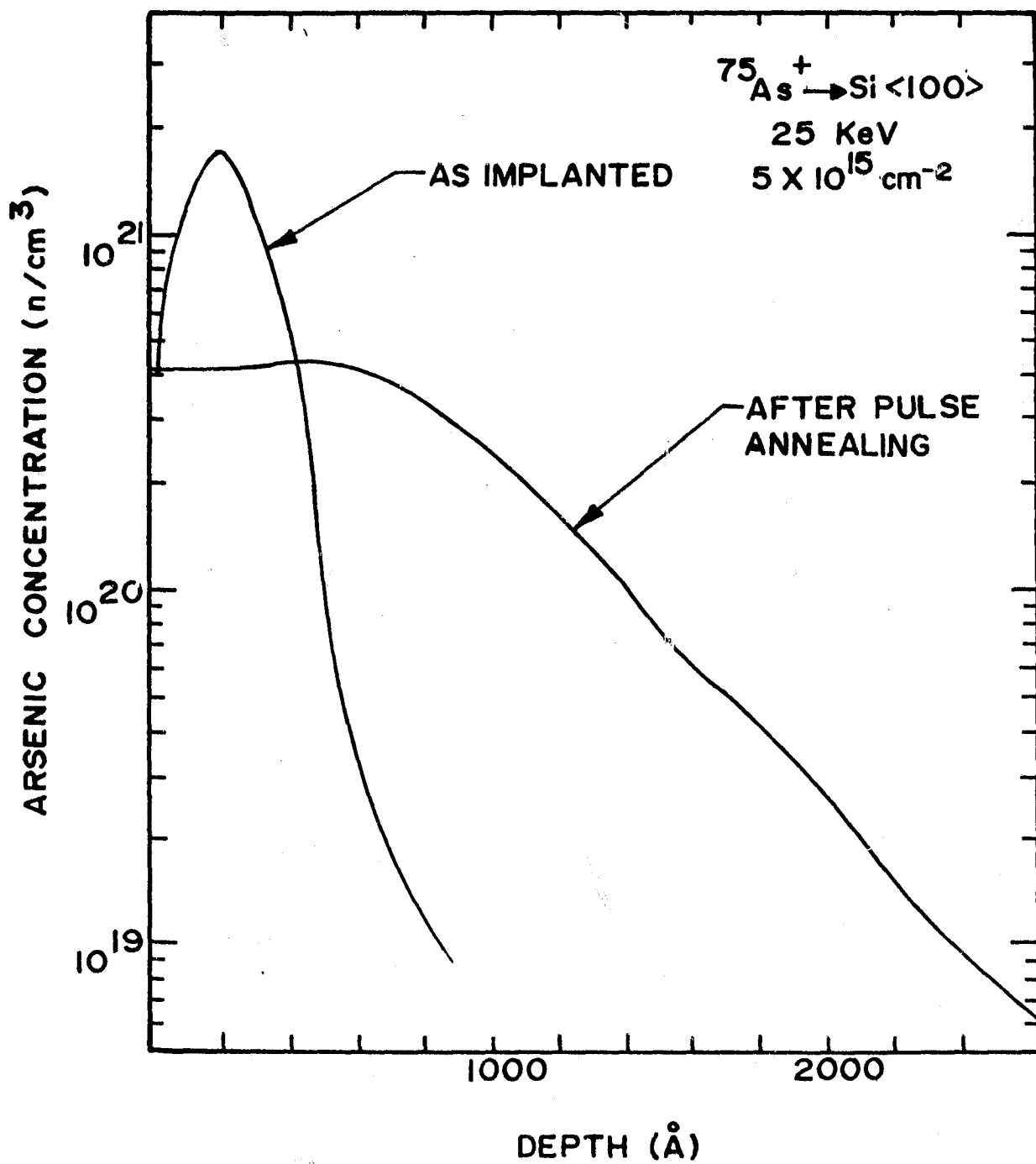


FIGURE 2-48. MEASURED ARSENIC IMPURITY PROFILES FOR (1) AS-IMPLANTED AND (2) AFTER PULSE ANNEALING

recombination. These higher recombination rates increase diode leakage currents and, as a result, decrease V_{oc} under illumination. Transient capacitance analysis has been used to determine the trap energy levels within the bandgap, but such measurements are difficult.

Additional electronic properties of implanted/pulse-annealed junction layers have been determined. Both laser and electron beam pulse annealed junction solar cells exhibit higher average short-circuit currents when compared to implanted/furnace-annealed cells. These higher average short-circuit currents may be related to more complete electrical activation of the implanted dopant. Fewer interstitials remaining after annealing result in a decreased recombination center density in the junction layer.

2.5.3 Theoretical Models for the Pulsed Energy Processes

Spire has been utilizing pulsed electron beams and lasers for the annealing of ion implantation damage since early 1974. Development as a potential production processing technique had been hampered because of the complexity of the interrelated phenomena and ignorance about the mechanism or mechanisms involved in the high-speed transient annealing. As part of this program, the following investigation was made to identify the primary factors associated with the pulse annealing mechanism.

From the damage thresholds measured for silicon and an understanding of the mechanism of pulse annealing, a theoretical model was developed for pulse energy processing. The model was constrained by the requirements for producing the annealing effects without reaching the damage thresholds in silicon.

To formulate the model, calculations were performed using a computer program (VXTEMP) and analytical methods to determine the stress levels produced in the silicon as a result of temperature gradients. Physical effects associated with a solid-liquid phase change were integrated into a heat transfer equation through numerical techniques. The heat transfer equation, along with the proper boundary conditions, allowed computer calculations of the temperatures of spatial grid points immediately adjacent to a melt interface. Other modifications to the computer program included (1) entering multiple-slab material properties as input data to model the effects of implanted layers on temperature profiles, and also (2) entering each of the slabs in the deposit as input data to model the effects of phase changes on temperature profiles.

The configuration chosen for testing of the numerical calculations consisted of a two-material composite with a square electron beam deposition profile penetrating through half the first material. This problem could be easily solved analytically for the equilibrium temperature distribution. The result could be compared with a numerical computer output for very long times, i.e., steady-state equilibrium conditions.

The VXTEMP computer program, described in flow chart form in Figure 2-49, was used to determine the temperature profile generated by the standard pulsed electron beam at a fluence of 0.2 cal/cm^2 and an energy distribution as shown in Figure 2-50. The deposition profile as used in this calculation is shown in Figure 2-51. The actual deposition profile varied as a function of both time and depth due to the changing electron beam energy and current levels as shown in Figure 2-52. For the purposes of this calculation, the depth/dose profile as a function of time was assumed not to change in shape, and was assumed to vary in amplitude in a Gaussian fashion, i.e., in terms of $\int D(x,t) dt$, as shown in Figure 2-51. This approximation was supported by experiments performed earlier in the program.

The thermal parameters used in this study were as follows. The specific heat as a function of temperature, $C(T)$, of both crystalline and amorphous silicon was assumed to vary as the crystalline value with

$$C(T) = 0.8628 + 8.3452 \times 10^{-5} T - (1.6243 \times 10^{-4})/T^2$$

where $C(T)$ is in joules/gram-°K and T is the temperature in degrees Kelvin. The variation of the thermal conductivity of the various silicon states is shown in Figure 2-53, with the amorphous values being estimated from fused quartz and crystal quartz analogs. Since we were assuming a glassy, amorphous layer with little or no heat of fusion⁽¹²⁾ during phase change, the melt and "pre-melt" thermal conductivity values for the amorphous layer were assumed equal.

The amorphous layer was assumed to be 0.1 micrometer thick, although ion channeling during implantation probably produces a semicrystalline transition region between amorphous and crystalline material.

The results of the VXTEMP calculations are shown in Figures 2-54 and 2-55. The front surface temperature as a function of time is shown in Figure 2-54. Note that the front surface does rise above melt, and the surface stays at the melt temperature of $1,410^\circ\text{C}$ for approximately 175 nsec. The flat-band portion of the temperature profile represents the time required for solidification at the melted surface layer.

FINITE - ELEMENTS,
NUMERICAL SOLUTION
TO DIFFUSION EQUATION

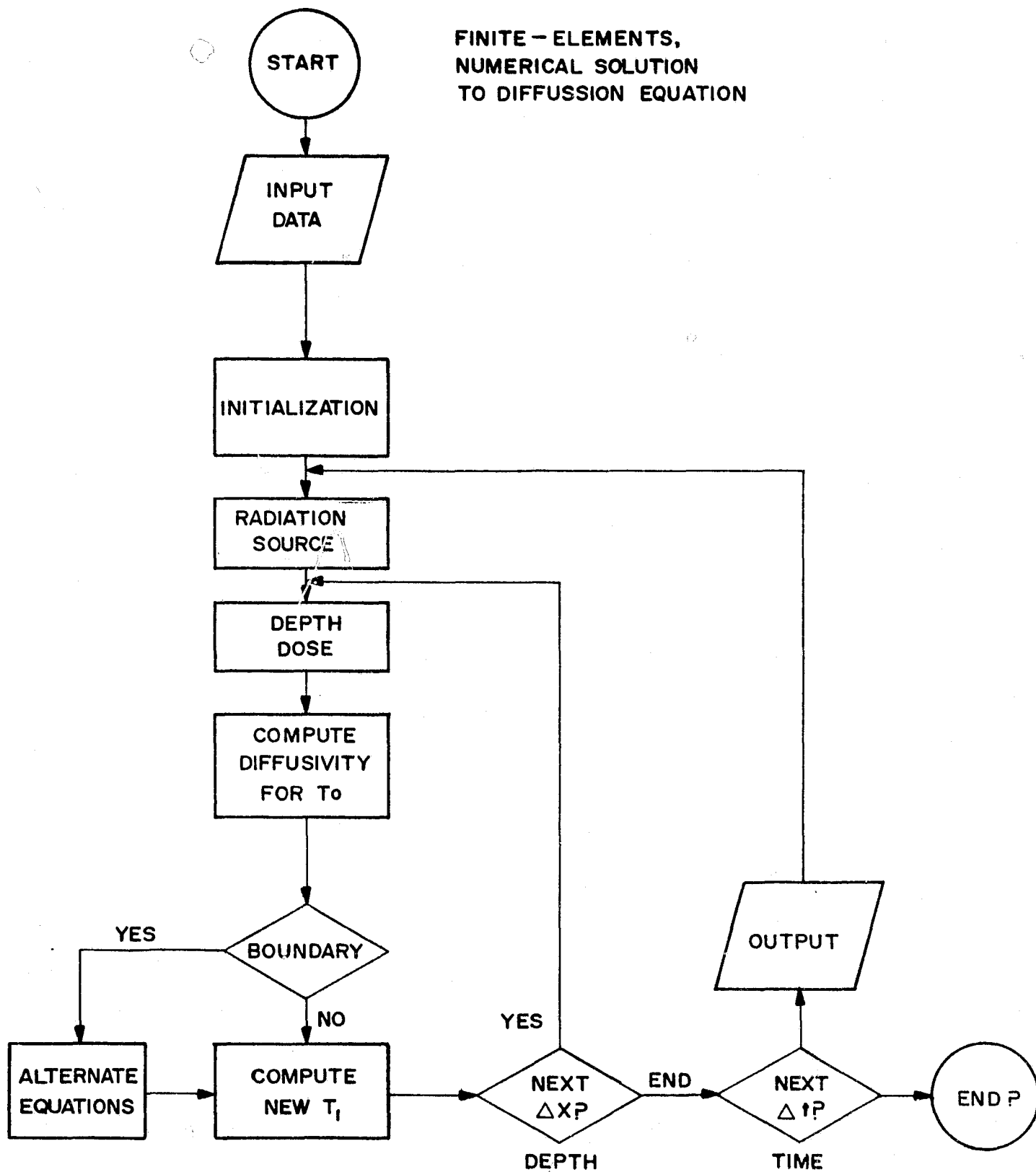


FIGURE 2-49. FLOW CHART FOR VXTEMP

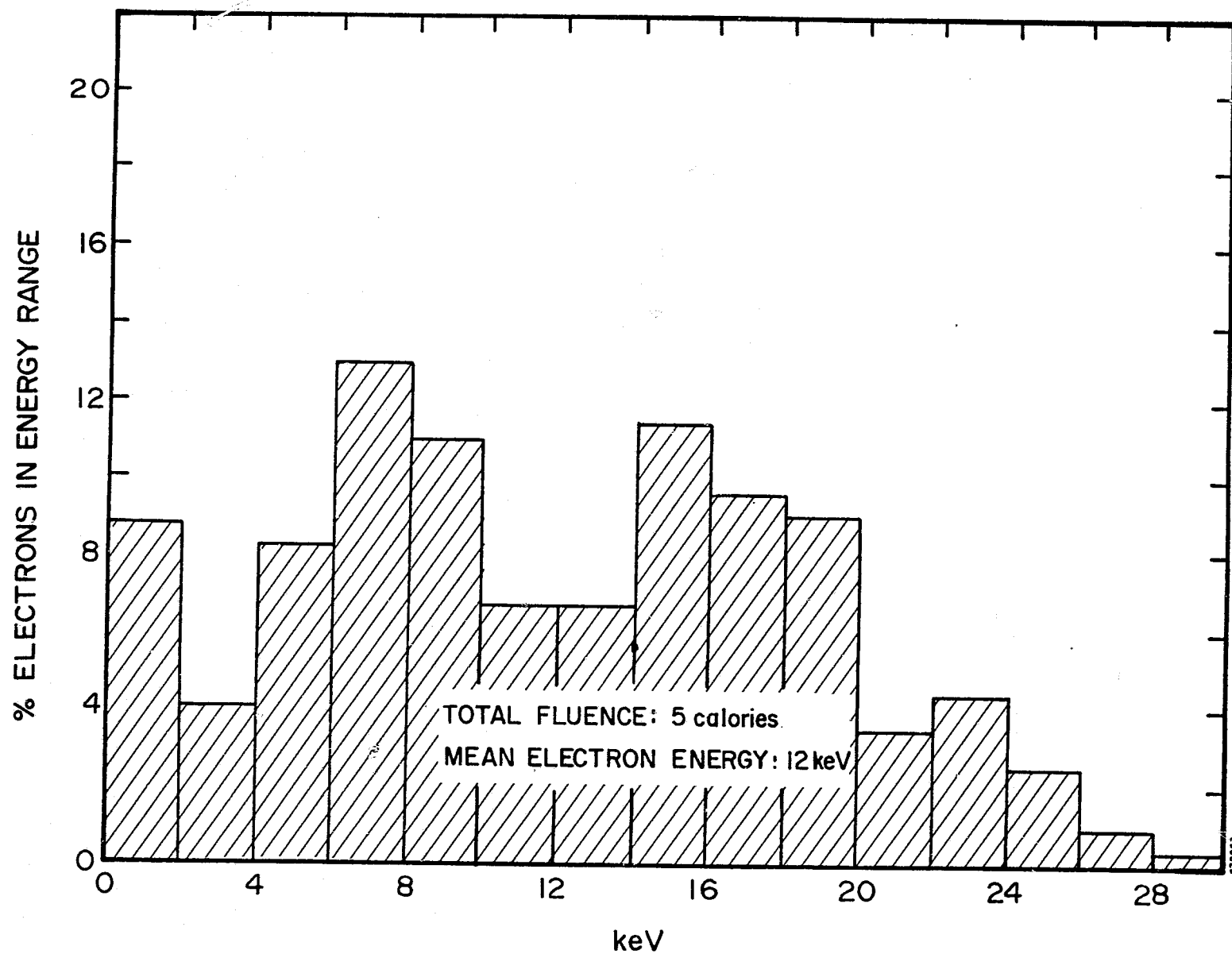


FIGURE 2-50. ELECTRON BEAM ENERGY SPECTRUM

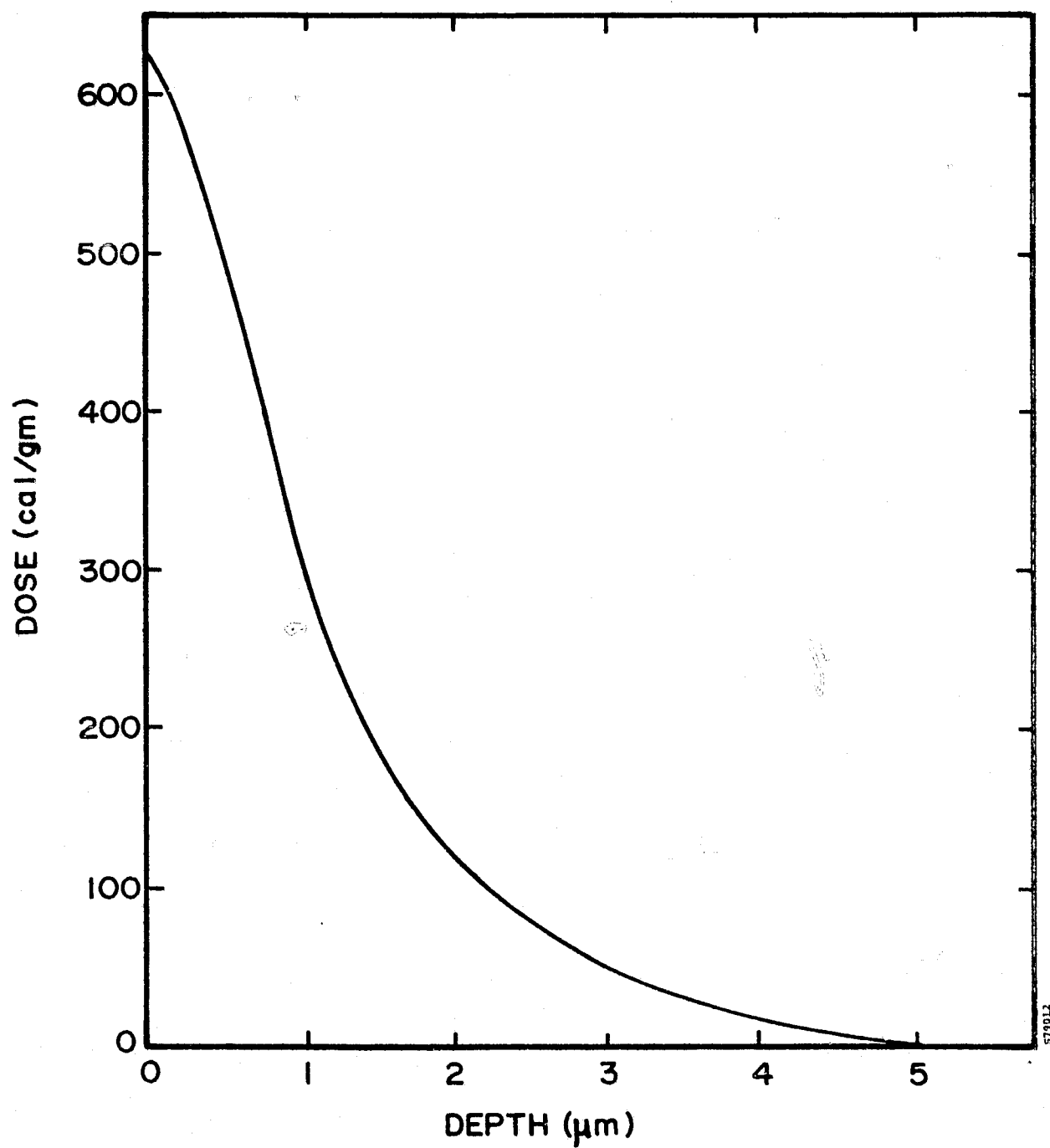


FIGURE 2-51. ENERGY DEPOSITION VERSUS DEPTH PROFILE IN SILICON FOR PULSED ELECTRON BEAM

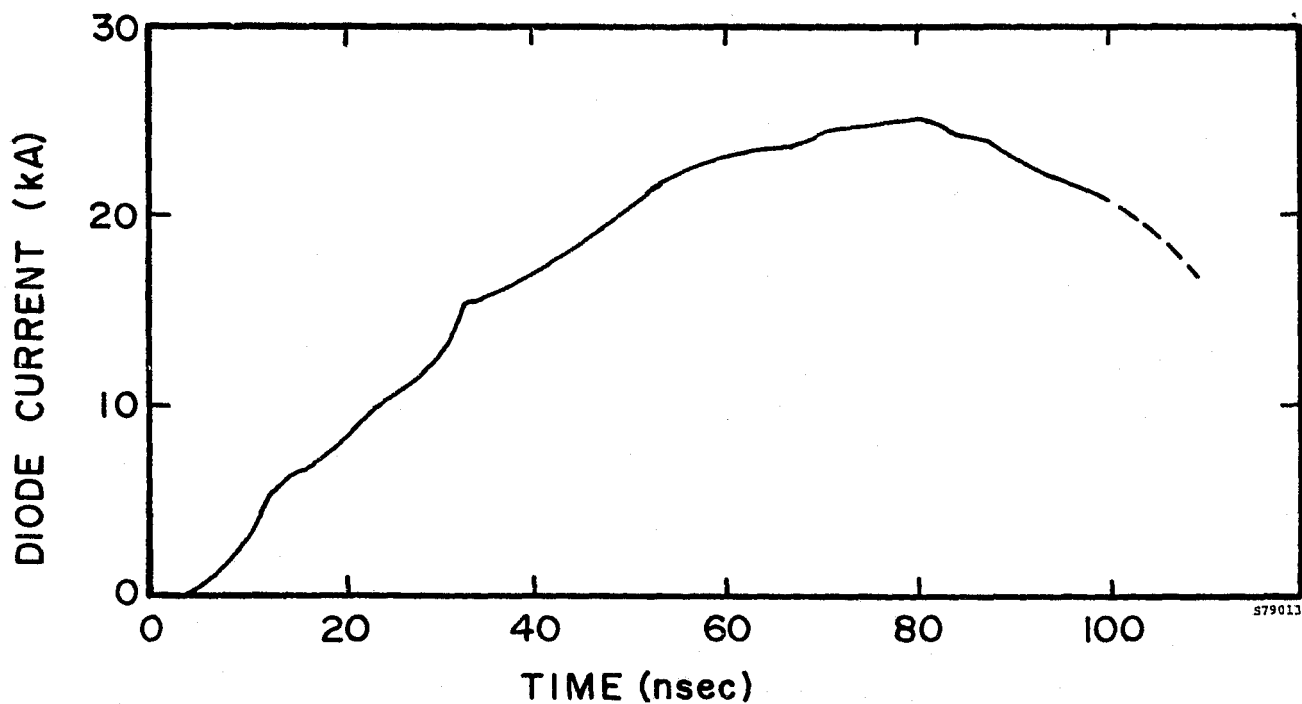
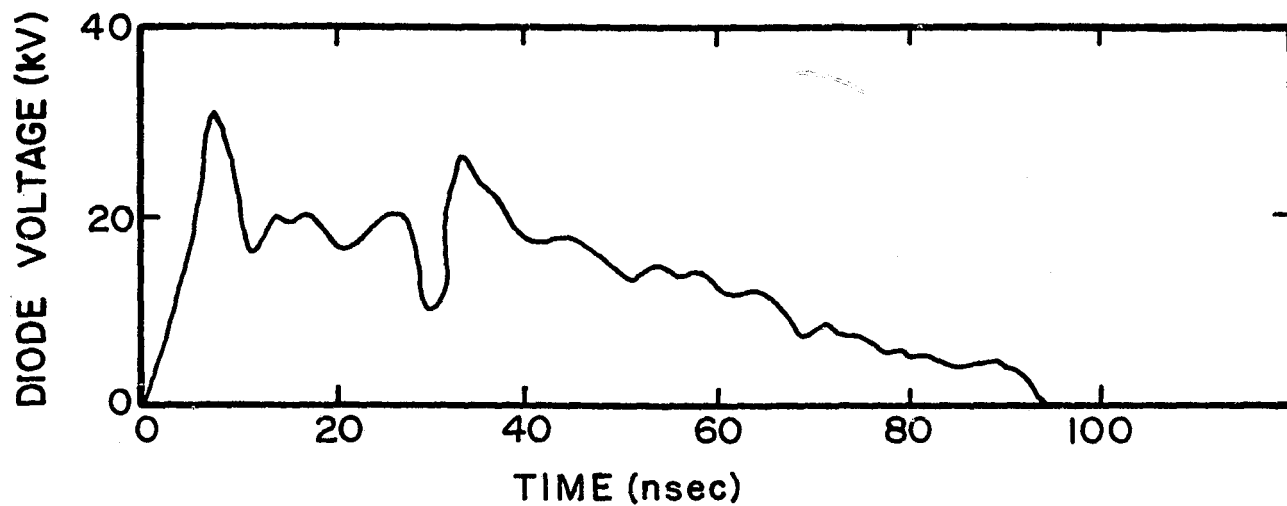


FIGURE 2-52. VOLTAGE (CORRECTED FOR di/dt) AND CURRENT ACROSS CATHODE-ANODE GAP

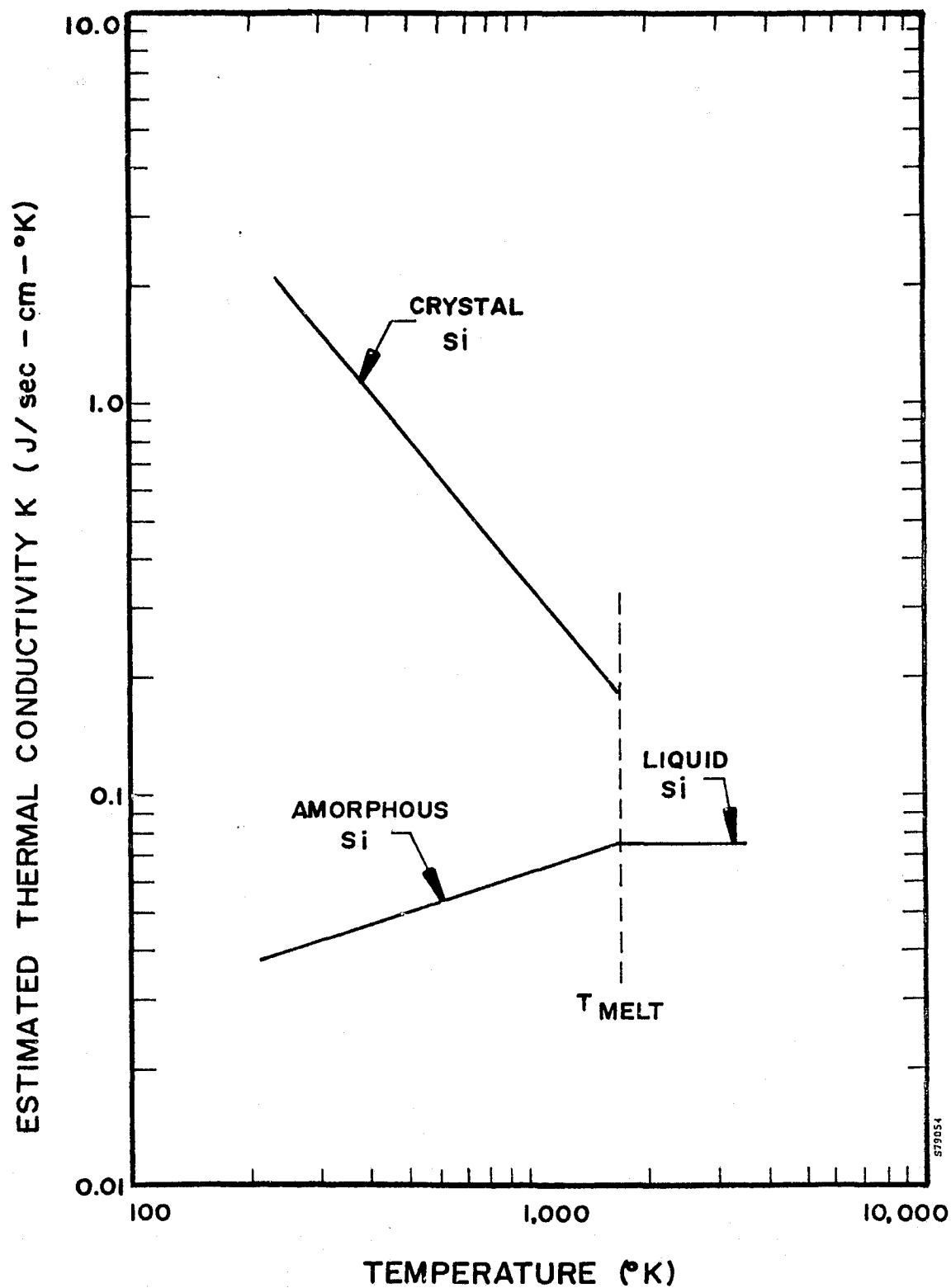


FIGURE 2-53. VARIATION OF THERMAL CONDUCTIVITY WITH TEMPERATURE FOR AMORPHOUS AND CRYSTALLINE SILICON

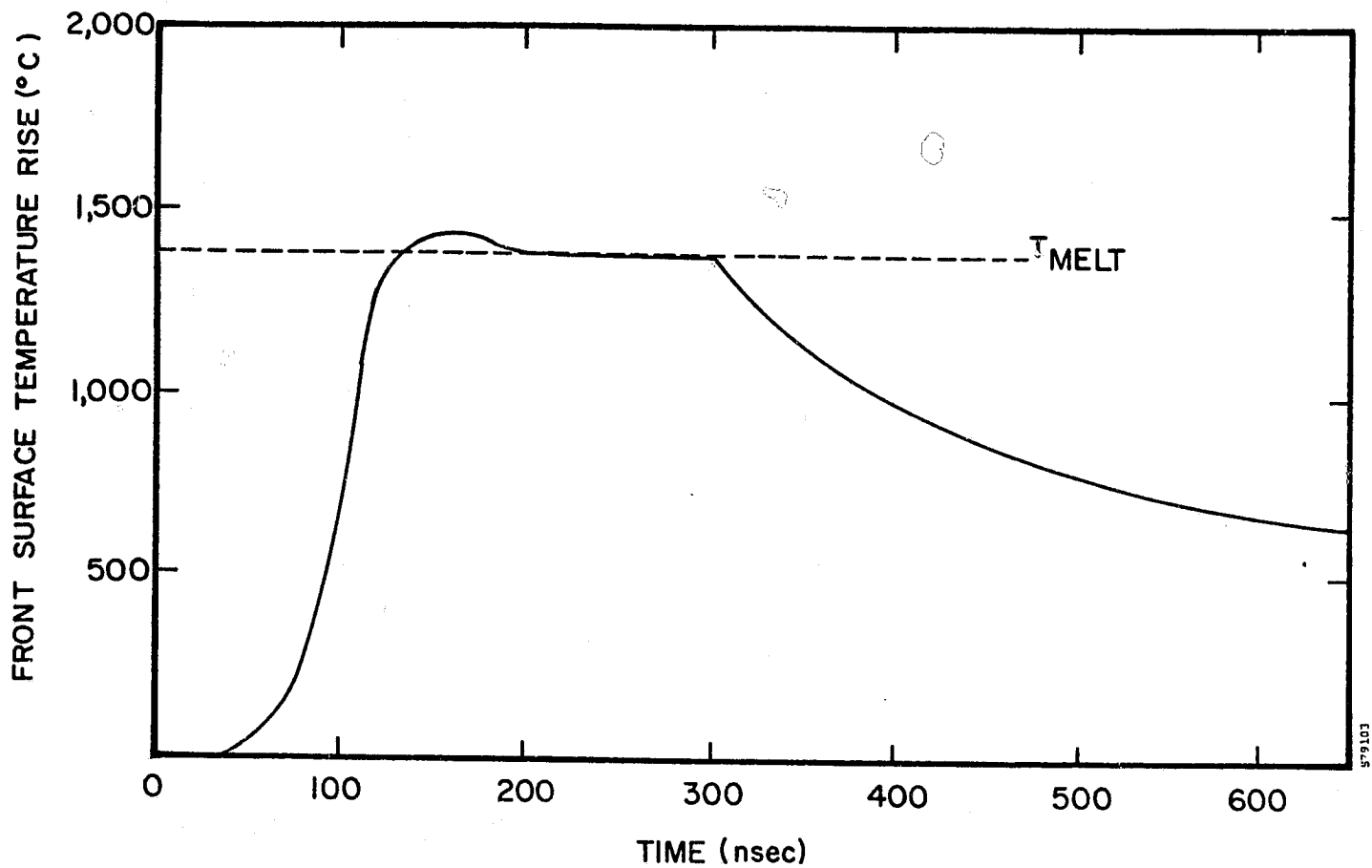


FIGURE 2-54. FRONT SURFACE TEMPERATURE AS A FUNCTION OF TIME FOLLOWING DEPOSITION OF PULSED ELECTRON BEAM

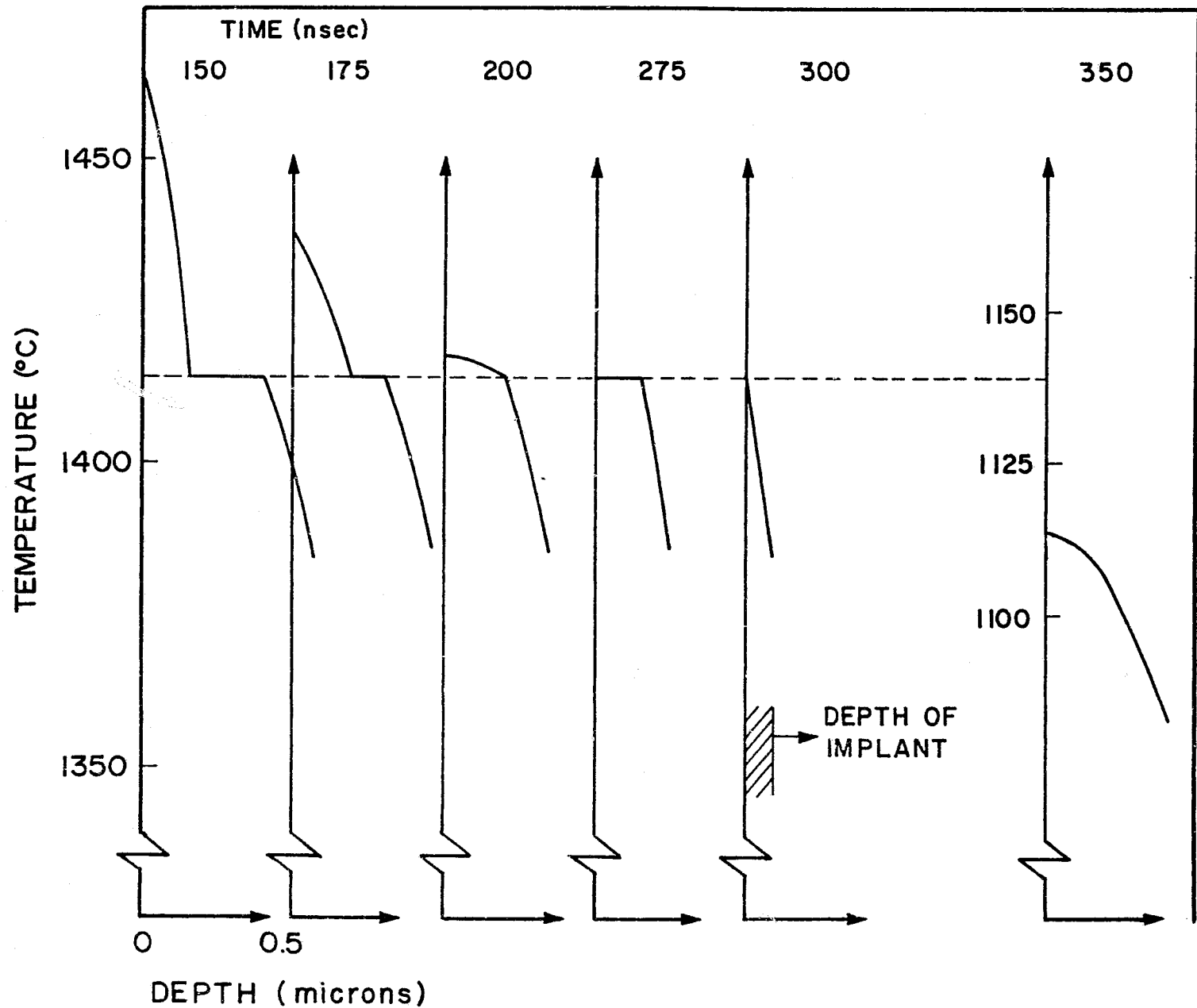


FIGURE 2-55. CALCULATED TEMPERATURE PROFILE DURING PULSED ELECTRON BEAM ANNEALING FROM VXTEMP OUTPUT

The in-depth temperature history profiles are shown in Figure. 2-55. Note that the region above melt temperature expands to about 0.2 micrometer before starting to contract as cooling takes place. After about 175 nsec, the energy being deposited is very small, since the injected electron beam pulse is almost complete except for the very low-energy spike of decaying current, and thus the temperature starts to decline. As the melted silicon crystallizes, the heat of fusion is released ($H_{\text{fusion}} = 1,803$ joules/gram). This effect keeps the first few tenths of a micrometer at the melt temperature for more than an additional 100 nsec. After the front surface solidifies, the temperature drops rapidly, reaching the neighborhood of 600°C after a total elapsed time of about 600 nsec.

The structural perfection exhibited by implanted layers after pulse annealing indicates that the damaged layer recrystallizes epitaxially on the undamaged substrate during the anneal. The underlying silicon crystal lattice serves as the nucleation surface for recrystallization, which takes place directionally from the undamaged region to the surface. An explanation is required of how this regrowth is able to take place so flawlessly as a result of a single energy pulse lasting less than a microsecond.

A number of factors are involved in the pulse anneal mechanism, including:

1. Spatial distribution of the deposited energy
2. Resulting maximum temperature distribution and temperature gradient at the profile edge
3. Manner in which heat can be lost from the surface layer

A complete, quantitative explanation may also have to consider certain other factors, including the effects of ionization and detailed properties of the nearly amorphous, implanted silicon.

Calculations of temperature profiles produced in single-crystal silicon material by the electron beam used for implant annealing show that the implanted layer reaches melting temperature. However, insufficient additional energy is introduced to allow the complete melting of the region and an additional temperature rise because of the heat of fusion. The surface layer can also be considered to be in a glassy, amorphous condition, in which case the temperature will rise above the melting point. At some point below the surface a steep temperature gradient exists between this material and the single-crystal silicon of the substrate.

During time frames on the order of microseconds, appreciable heat losses from the silicon layer at melting temperature can take place only by conduction into the crystalline material below. No temperature gradient exists across the layer at melting temperature; consequently, heat is effectively trapped within this layer. Only the material at the temperature gradient interface is able to undergo cooling. Thus epitaxial regrowth takes place at this interface, energy is given up at the interface, and the crystal front progresses monotonically toward the surface. Because of the absence of a temperature gradient within the noncrystallized region at melting temperature, cooling can occur only as the crystal structure grows. The cooling sequence is suggested in the last two frames of Figure 2-55.

If the time frames involved in the recrystallization process were to be appreciably greater than tens of microseconds, significant heat loss would also occur by radiation from the heated, front surface. Figure 2-56 shows Arrhenius plots of experimentally measured regrowth rates of silicon as a function of temperature^(13,14). When these plots are extrapolated seven orders of magnitude to the melting temperature of silicon, it can be seen that a growth rate exceeding 10^8 A/sec is predicted. Consequently, the implanted layer, on the order of 10^3 A thick, can be expected to recrystallize in a period of microseconds.

The dopant redistribution effect shown in Figure 2-48 must also be explained. If it is assumed that the redistribution indicated takes place in approximately 10^{-6} sec, then it can be calculated that the effective diffusion coefficient of the arsenic impurity atoms must be roughly 10^{-5} cm²/sec during the process. Existing information^(15,16) regarding the abrupt changes in diffusion coefficient which take place between the solid and liquid phases of silicon at melting temperature indicate a value on the order of 10^{-5} cm²/sec can be expected. Known diffusion coefficient values, D, for phosphorus and arsenic in solid and liquid silicon are shown in Figure 2-57.

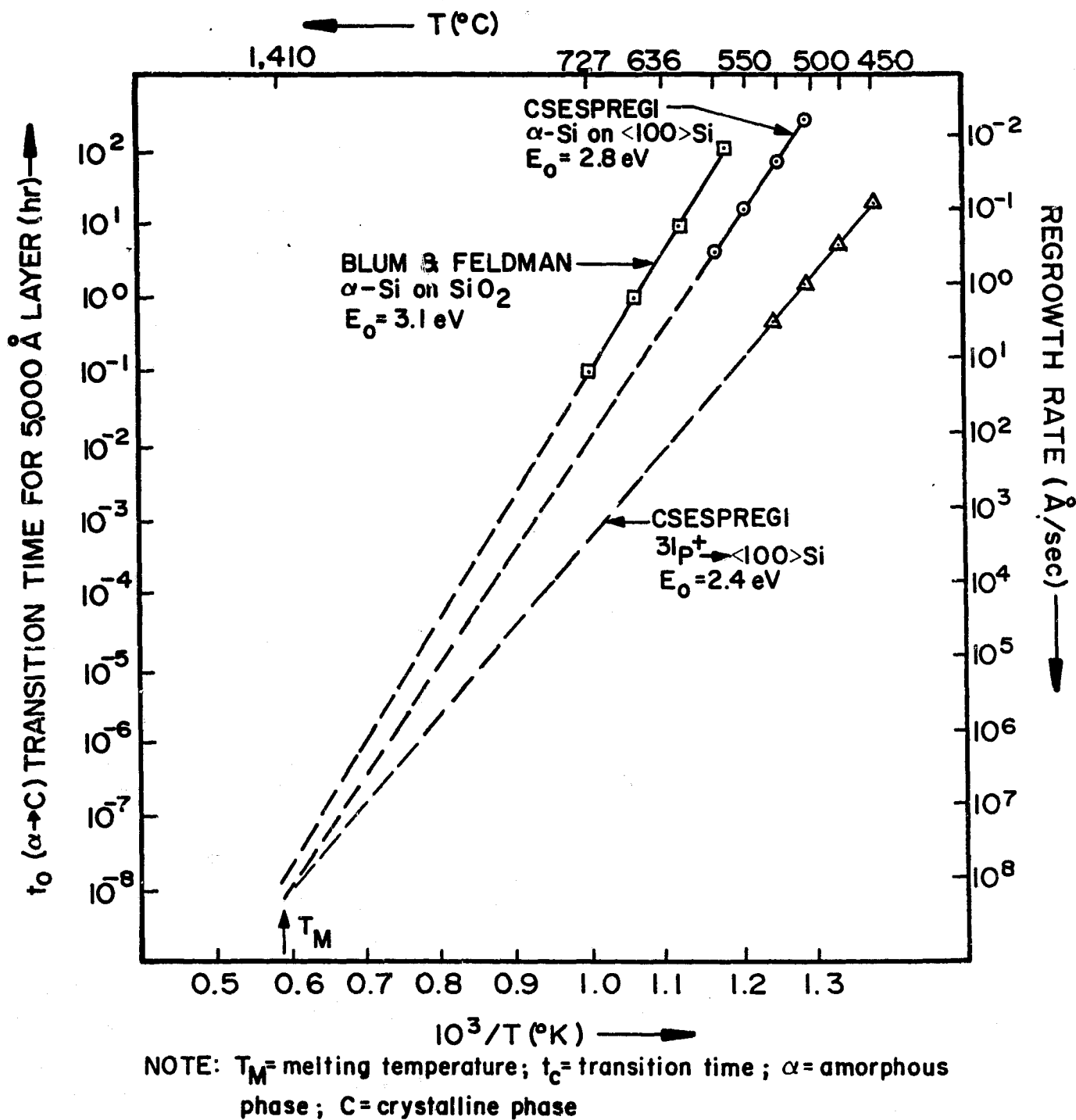
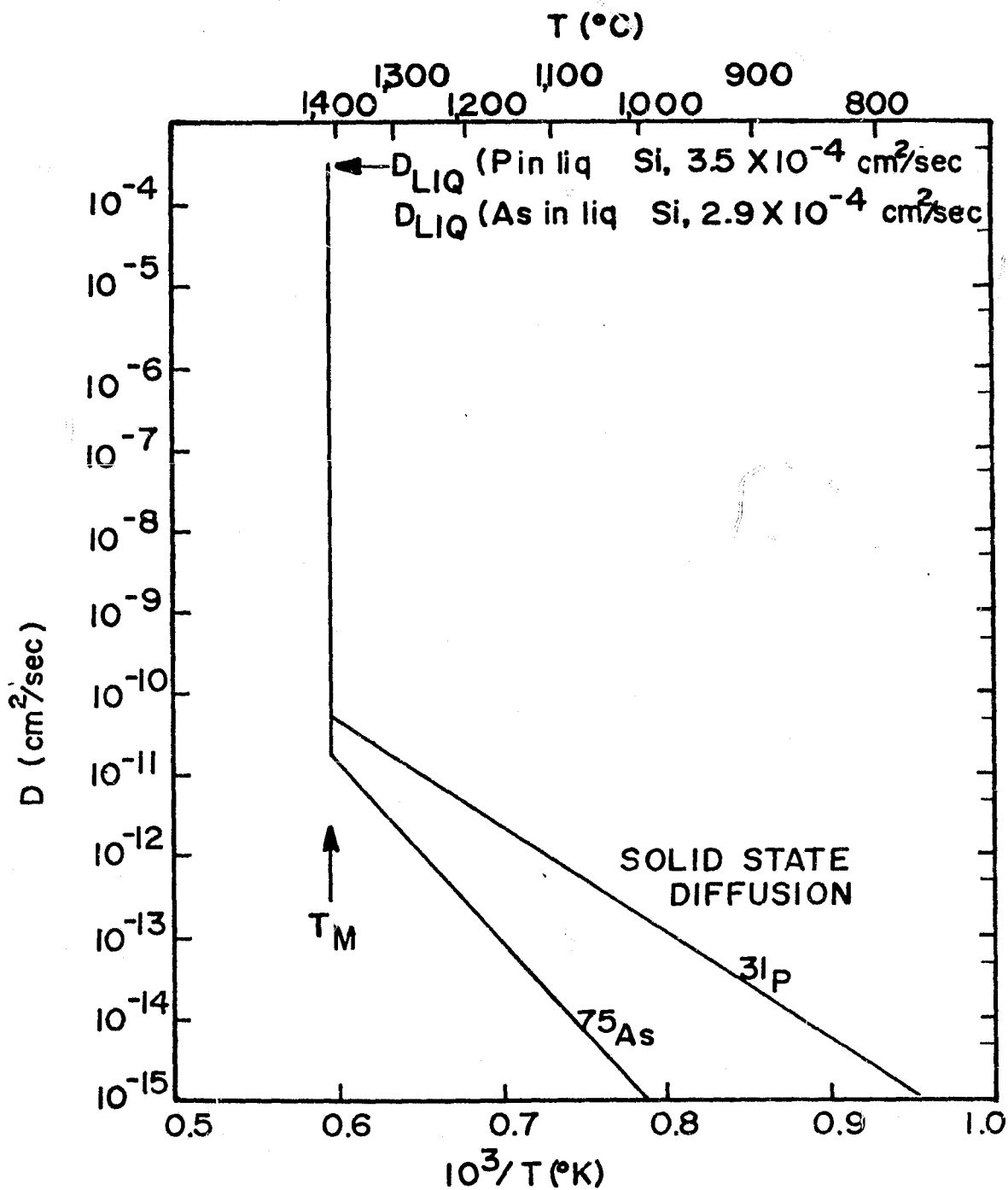


FIGURE 2-56. REGROWTH RATES FOR α -Si TO RECRYSTALLIZE WITH AND WITHOUT SINGLE CRYSTAL SUBSTRATE



NOTE: T_M = melting temperature

FIGURE 2-57. DIFFUSION COEFFICIENTS FOR ARSENIC AND PHOSPHORUS IN SOLID AND LIQUID SILICON

All the redistribution results with pulse annealing are consistent with the diffusion coefficients between the solid and liquid values at melting temperature. This is in agreement with the annealing mechanism now believed to be involved.

2.5.4 Stress Analysis

A description of the stress analysis and results related to damage mechanisms in pulsed electron beam processing is contained in the following sections.

Thermoelastic Stress Generation

The stresses generated by variations in temperature within a medium can be determined by the equation of motion and the relation between stress and strain (displacement) in the material. Hooke's Law for the relationship between stress and strain in a homogeneous, isotropic medium can be written as⁽¹⁷⁾:

$$S_{ij} = \lambda \theta \delta_{ij} + 2 \mu \epsilon_{ij} - \frac{E \alpha_v T}{3(1-2\nu)} \delta_{ij}$$

where

$$\theta = \epsilon_{11} + \epsilon_{22} + \epsilon_{33},$$

$$\begin{aligned} \delta_{i,j} &= 0 \text{ if } i \neq j \\ &= 1 \text{ if } i = j \end{aligned}$$

$$\epsilon_{ij} = \frac{1}{2} \left(\frac{\partial u_i}{\partial x_j} + \frac{\partial u_j}{\partial x_i} \right)$$

$$i, j = 1, 2, \text{ or } 3$$

and λ and μ are the Lamé constants, E is Young's modulus, α_v is the volume coefficient of expansion, and ν is Poisson's ratio. The quantity T represents the temperature change in a given region of the medium, the ϵ_{ij} are strains, and the quantity \vec{u} is a displacement vector which we ultimately wish to determine. The equation of motion for a volume element in the material can be written as:

$$\rho \frac{\partial^2 x_j}{\partial t^2} = \rho x_j + \frac{\partial S_{ij}}{\partial x_i}$$

where x_j are due to body forces (i.e., gravity) and S_{ij} are stresses acting on the volume surfaces. If we consider the case of no body forces with the volume element remaining in equilibrium, then the above equation reduces to

$$\frac{\partial S_{ij}}{\partial x_j} = 0$$

If Hooke's Law for the stresses S_{ij} is inserted in the above equation, it is possible to arrive at the differential equation for the displacement vector components⁽¹⁸⁾

$$\frac{3(1-\nu)}{1+\nu} \nabla (\nabla \cdot \vec{u}) - \frac{3(1-2\nu)}{2(1+\nu)} \nabla \times \nabla \times \vec{u} = \alpha_v \nabla T$$

Once \vec{u} is determined, subject to appropriate boundary conditions, then the stresses and strains can in principle be determined.

Calculation of Normal Stresses

The normal stresses induced in the silicon wafer in the directions parallel to the surface (x,y) have been calculated using a model which does not allow bending. The effects of bending on the magnitude of the stresses will be addressed after the results of the simple planar model are presented. The deviation of the normal stress produced by the pulsed electron beam anneal (PEBA) temperature profile is as follows.

The planar constraint requires that $u_z = f(z)$ only since no curvature or bending of the wafer is allowed. If there are no external forces on the wafer and the above conditions hold, then it is reasonable to assume that there will be no shear forces, or $u_x = f(x)$ only and $u_y = f(y)$ only. Under these conditions, the equations for the components of the displacement vector reduce to

$$\frac{d^2 u_x}{dx^2} = 0$$

$$\frac{d^2 u_y}{dy^2} = 0$$

$$\frac{d^2 u_z}{dz^2} = K \frac{dT(z)}{dz}$$

Solving these for the strains results in the following

$$\epsilon_{xx} = \epsilon_{yy} = A$$

$$\epsilon_{zz} = B + KT(z)$$

where A and B are constants to be determined and $K = 1 + \nu/3(1-\nu)$. Since the silicon is free to expand in the z direction, and the wafer is unconstrained, $S_{zz} = 0$ and using Hooke's law one obtains the relation

$$A = - \frac{(\lambda + 2\mu)}{\lambda} \frac{B}{2}$$

Using the above relation and Hooke's Law for S_{xx} , we find:

$$S_{xx} = - \frac{E\alpha_v T(z)}{3(1-\nu)}$$

This stress distribution does not produce zero stress at the ends of the wafer for an arbitrary temperature distribution $T(z)$, nor does it allow a zero net force and moment at the surface. Saint-Venant's principle⁽¹⁸⁾ allows the addition of stress terms $X + Wz$ which yields

$$S_{xx} = F + Wz - \frac{E\alpha_v T(z)}{3(1-\nu)}$$

The values of F and W are chosen so that $\int S_{xx} dz = \int S_{xx} z dz = 0$; i.e., there is no net force or torque present at the ends of the wafer, while the effects of these additional stresses will be negligible at distances from the wafer ends comparable to the wafer thickness. For very shallow temperature profiles the maximum normal stress approaches

$$S_{xx}^{\max} \approx \frac{E\alpha_v T_{\max}}{3(1-\nu)}$$

For silicon just below melt temperature with values of $\alpha_v = 15 \times 10^{-6}/^{\circ}\text{C}$, $\nu = 0.25$, $E = 1.9 \times 10^{12}$ dynes/cm, and $T_{\max} = 1,385^{\circ}\text{C}$, the calculated normal stress approaches a maximum of 17.5×10^9 dynes/cm² for the (111) orientation. Data on fracture stress in silicon⁽¹⁹⁾ as shown in Table 2-14, indicates that the stress necessary for fracture rises rapidly above $1,000^{\circ}\text{C}$ and approaches 8×10^9 dynes/cm² at $1,200^{\circ}\text{C}$. Small silicon whiskers are reported as having breking strengths in excess of 20×10^9 dynes/cm².⁽¹⁹⁾ Since plastic deformation starts at about 600°C for silicon⁽²⁰⁾, the calculated stresses are probably two or three times higher than the actual stresses generated by the electron beam pulse. In addition, if bending of the silicon wafer is allowed, the stress levels are reduced by factors of three to four⁽¹⁹⁾. Therefore, it seems likely that the normal stresses generated by the temperatures near melt are not the primary cause for the observed fractures.

Calculation of Shear Stresses

A straightforward solution of the differential equations for the displacement vector previously presented is difficult when arbitrary shear forces are included in the problem. Therefore, a solution by inspection was chosen in an attempt to

TABLE 2-14. SUMMARY OF MEASURED FRACTURE THRESHOLDS FOR PULSED ELECTRON BEAM HEATING AS A FUNCTION OF SILICON CRYSTALLOGRAPHIC ORIENTATION

Threshold (cal/cm ²)	Crystallographic Orientation	
	(111)	(100)
Microfracture of Unimplanted Wafer	0.22 ± 0.02	0.30 ± 0.02
Microfracture of Junction Implanted Wafer	0.27 ± 0.03	0.30 ± 0.02
Implant Anneal	0.2	0.2
Young's Modulus	1-9x10 ¹² dynes/cm ²	1-3x10 ¹² dynes/cm ²

Notes: Si: 7.6-cm-diameter, p-type, 3 ± 1 ohm-cm

Implant: 10¹⁵ 31P⁺ cm⁻² at 10 keV

estimate the magnitude of shear forces that would be produced by the temperature gradients predicted by VXTEMP. For a region with a linear temperature gradient $g = dT/dz$, a simple solution which satisfies the differential equations for u and allows for shear forces is

$$u_x = Axz, u_y = Ayz, u_z = Bz^2$$

Substitution of this solution into the differential equation yields the relation

$$2B + 2A(1-K) = K^1 g$$

where

$$K = \frac{1}{2} \frac{(1-2\nu)}{(1-\nu)} \quad \text{and} \quad K^1 = \frac{\alpha_v(1+\nu)}{3(1-\nu)}$$

Using the conditions of zero force and moment at the wafer ends plus Hooke's Law, the additional relation

$$2A(\lambda + \mu) + \lambda 2B - \frac{E\alpha_v g}{3(1-2\nu)} = 0$$

is obtained. The solution for A is

$$A = \frac{\alpha_v g(1+\nu)}{3(1-2\nu)}$$

and therefore the shear stress is

$$S_{xz} = 2\mu \epsilon_{xz} \approx \mu \frac{\alpha_v g}{3} \frac{(1+\nu)}{(1-2\nu)} x$$

where μ is the modulus of rigidity and x is the position from the center of the wafer. Note that the shear stress depends on the temperature gradient and modulus of rigidity for a given position. For the short deposition times used in PEBA, the temperature gradient is roughly proportional to the incident energy density, since the induced temperature profile is almost identical to the deposition profile because very little heat flow is possible during the electron beam pulse. In addition, the modulus of rigidity is related to Young's modulus by the relation

$$\mu = \frac{E}{2(1+\nu)}$$

Thus shear stresses produced by the pulsed electron beam should be proportional to the incident energy density and the value of Young's modulus for the appropriate orientation.

Pressure Wave Generation

The technical aspects of pressure generation by the rapid deposition of energy in a material was examined (Spire Rep. No. TR-78-02). The peak pressure developed for a Gaussian energy deposition profile was shown to be

$$\Delta P_{\max} = \frac{GF_o}{2V_o t_p}$$

where G is the Grueneisen parameter, F_0 is the fluence, V_0 the velocity of sound in the medium, and t_p is the pulse width. Using the values $G = 1.9$ dyne-cm/erg, $F_0 = 1.25$ j/cm², $V_0 = 1.3 \times 10^6$ cm/sec, and $t_p = 60 \times 10^{-9}$ sec, a maximum pressure of about 1.5×10^8 dynes/cm² was predicted. This level is 10 times lower than the fracture stress for silicon⁽⁴⁾ at room temperatures, so pressure waves are not a primary fracture mechanism. The calculation was checked by computer, with similar results as described below.

Computer Calculation of Thermomechanical Stress

A numerical computer calculation was completed to determine the magnitude of thermomechanical stress as a result of pulsed energy deposition. Such stress waves are generated when the front surface layer of silicon is heated and a pressure wave propagates through the silicon. The calculations showed that the stress wave is reflected from the back surface of a 250-micrometer thick wafer and reaches the front surface in 35 nanoseconds.

The computer program, PUFF, that was utilized is a hydrodynamic model. It computed the pressure and volume of a material as a function of the energy deposited. This equation of state does not explicitly compute the temperature profiles and thermal conductivity, nor does it predict whether melting occurs. However, the numerical approximation can be used to determine if spalling will occur for a given set of beam parameters.

Two assumptions made in the code were that the material is homogeneous and that the change in temperature near the surface will not significantly affect the propagation of the shock wave. The code used a temperature independent model of the pressure and volume internal energy relationship to compute the shock velocity and magnitude. The pressure due to thermal gradients was calculated, as a function of internal energy, for a homogeneous material. Changes in material properties with a phase change were considered; however, the phase change was assumed to occur at time $t=0$, not at the appropriate point. This, plus the fact that thermal conduction of internal energy was not considered, reduced the accuracy of this calculation for PEBA.

The predicted shock wave as a function of time is plotted in Figure 2-58. The total fluence was 0.2 cal/cm² in a 50-nsec square pulse. The propagating shock wave peak shown in the figure is launched very early as a compression wave, is reflected from

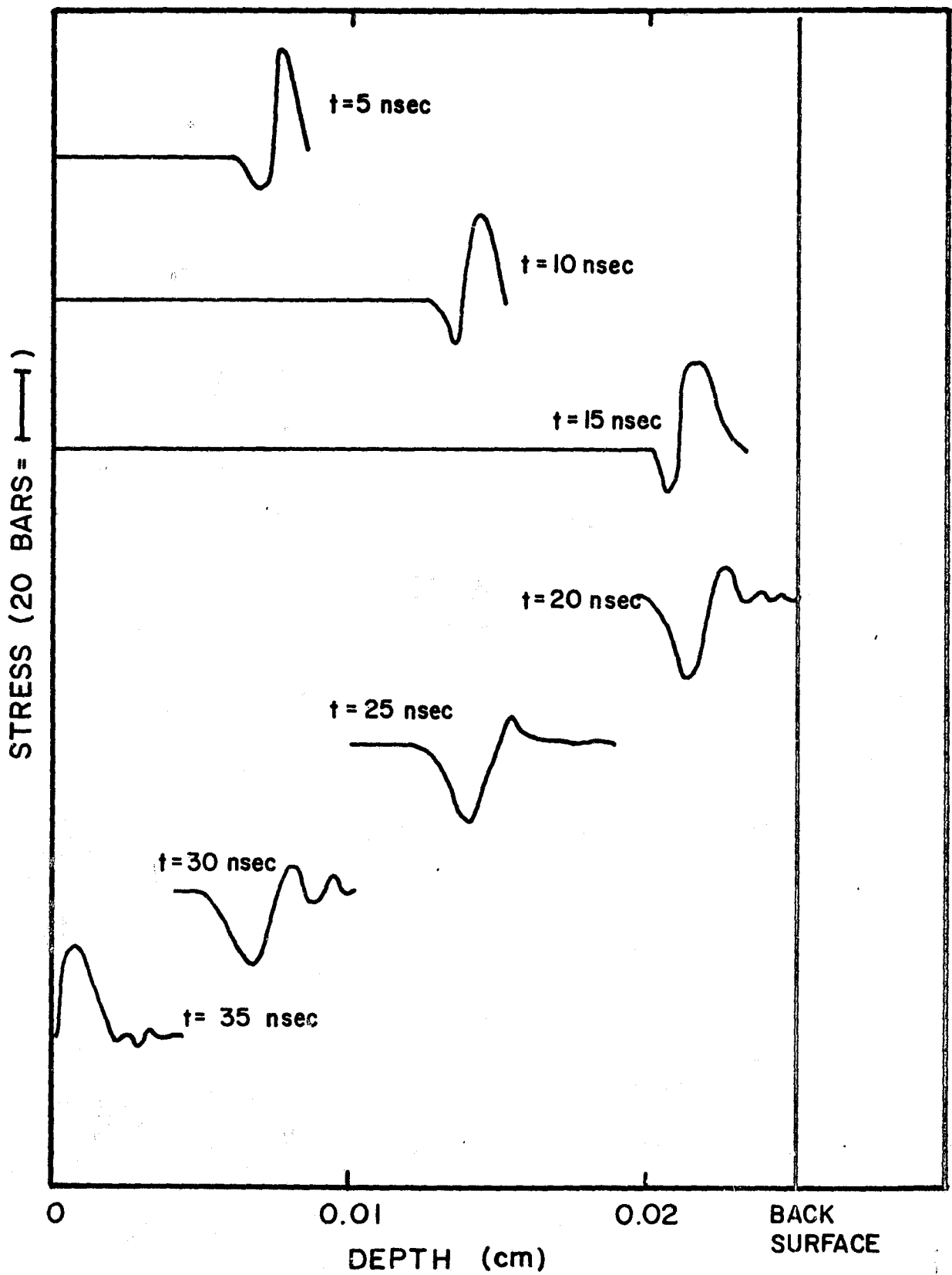


FIGURE 2-58. SHOCK WAVE PROPAGATION INDUCED BY ELECTRON BEAM PULSE

the back surface of the wafer, and reaches the front surface again before the end of the pulse. The computer calculation was halted at this point, about 35 nsec after the beginning of the pulse.

The stress perpendicular to the surface can be computed from the homogeneous model:⁽¹⁷⁾

$$P = -1/3 (S_{xx} + S_{yy} + S_{zz})$$

where S_{xx} is the stress in the x direction, perpendicular to the surface, and is negligible since the material can expand in that direction. The stress perpendicular to x, parallel to the surface, is uniform, so that $S_{yy} = S_{zz} \approx -3/2 P$. The pressure, P, output from PUFF is plotted as a function of time and depth in Figure 2-59. Note that P is increasing with time, and at the end of the calculation only 0.14 cal/cm^2 were deposited in the front layer extrapolation to the full-fluence (0.2 cal/cm^2) yields 24K bars for the peak stress which is parallel to the surface.

This value greatly exceeds the dynamic fracture thresholds of silicon. The program, however, overestimated the stress by neglecting thermal conductivity, deformation in the y or z direction, and anisotropy of the crystal silicon. It also neglected the melting of a thin surface layer which would relieve the stress and any pre-existing stress in the implanted region.

Implant Strain

Lattice strain may be produced by impurities placed in the silicon during the doping procedure, depending on the nature of the implant ion. The strain can be calculated from⁽⁴⁾

$$\epsilon = 1 = f(\gamma^3 - 1)^{1/3} - 1$$

where f is the atom fraction of the dopant and γ is the ratio of the Pauling covalent radii of the two different atoms. Using $\gamma = 0.932$ and a dopant concentration of $10^{19} \text{ atoms/cm}^3$, strains of the order of $\epsilon = 10^{-6}$ are produced. Stresses of the order of 10^6 dynes/cm^2 are produced, which for silicon is on the order of $2 \times 10^6 \text{ dynes/cm}^2$, three orders of magnitude below fracture levels. These stress levels may, however, be responsible for lattice slips⁽¹⁹⁾ which could alter the ultimate fracture strength of the amorphous material.

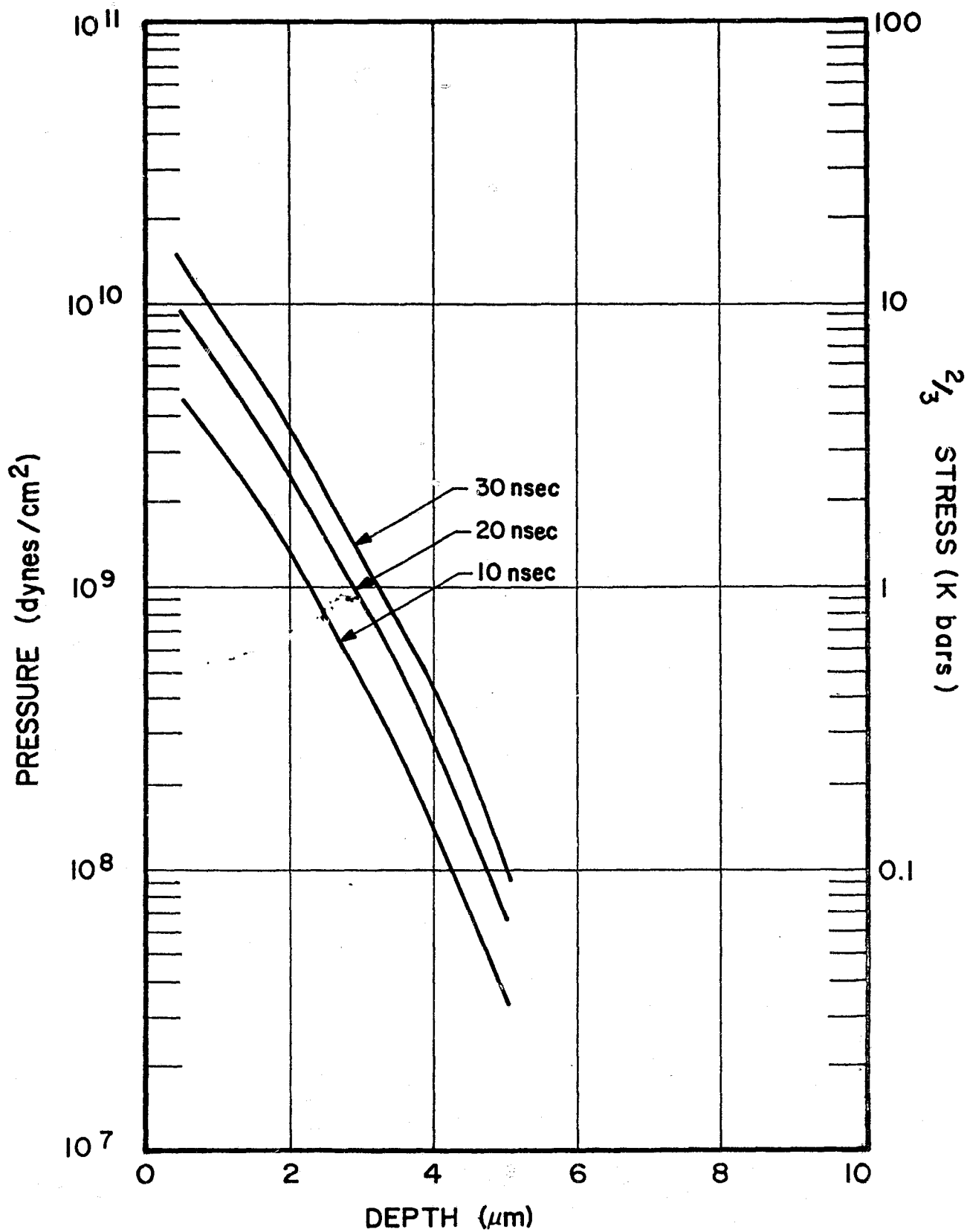


FIGURE 2-59. PRESSURE AS A FUNCTION OF DEPTH AT VARIOUS TIMES AFTER BEGINNING OF PULSE

2.5.5 Pulse Sintering of Contact Metals

Prior experience at Spire with silicide formation by pulse heating thin metal films deposited on silicon was limited to the formation of aluminum BSF layers only. Efforts during this contract have considered metals which form silicides at much higher temperatures than the aluminum-silicon system. The use of pulsed electron beams to sinter Mo, Ti, V, and Pd contacts has been shown feasible under this task element.

If a thin layer of metal is evaporated over a silicon substrate, then pulse heating will momentarily raise the metal silicon interface up to the eutectic temperature, where a stable alloy (liquid-phase) forms. Further heating can result in melting either the metal, or the silicon, or both components near the surface and allow diffusion of the alloy components into the melted region. Rapid quenching cools the interface below the melt temperature of the alloy, which is less than the melt temperature of either the metal or silicon, before diffusion of the metal into the solid substrate can occur. There are two cases to consider. The metal may have a melting point below that of silicon, such as aluminum, or it may have a melting point greater than that of silicon, such as molybdenum.

The aluminum-silicon system has been studied at high temperatures by H. E. Cline and T. R. Anthony⁽²¹⁻²⁴⁾. The migration velocity V of an aluminum film in silicon is given by:

$$V = D(\partial X/\partial T)\nabla T/(1-X)$$

where D is the diffusion coefficient of silicon in the molten alloy at the eutectic temperature, $\partial X/\partial T$ is the liquidus slope in the phase diagram, ∇T is the thermal gradient, and X is the silicon concentration in the alloy. Near the melting point of silicon the value of V approaches 2×10^{-4} cm/sec, by theory and experimental evidence⁽²¹⁾. In fast pulse heating, when the temperature drops below the eutectic point in about 1 microsecond, the depth of alloying would be only approximately 21 or one monolayer if the silicon was not melted. This calculation shows that diffusion of silicon in the alloy, which was the limiting process in experiments by Anthony and Cline, is not the limiting process in pulsed alloy formation where the silicon has to be melted to form a sufficiently thick eutectic. Pulsed alloy formation experiments at Spire using 400A of aluminum results in an alloy with a minimum depth of 1,000A.

For a metal with a melting point greater than that of silicon but with a smaller heat capacity, such as Mo or W, the electron beam would deposit sufficient energy to melt the metal unless cooling by radiation from the surface and conduction to the silicon substrate would prevent this. The dose to melt molybdenum (230 cal/g) is about one third the dose to melt silicon (over 620 cal/g), and the peak dose delivered to each material in terms of energy per unit mass is nearly the same, despite the difference in atomic mass for identical fluence. However, for a thin film the silicon below the metal would melt and act as a heat sink, keeping the heavy metal solid (1,400°C) at the metal-silicon interface. Thus, a silicide could be formed for a thin metal layer (with melt point over 1,400°C) by a pulsed electron beam at a fluence below that necessary to melt pure silicon. This makes it easy to sinter front contacts on solar cells by pulsed heating the whole surface without damage to the area not covered by the metal contact fingers.

Normally, prior to metal evaporation, there is a thin, 20A-to-50A layer of SiO₂ on the wafer which remains between the pure silicon and the metallic film. With a low melting point metal such as aluminum, this layer would prevent the formation of a silicide at the eutectic temperature. The oxide necessitates melting the silicon. With a high melting point material, such as molybdenum, this layer will be melted and will not interfere with silicide formation.

Experimental evaluation of the effectiveness of pulsed electron beam sintering was performed using Auger analysis. Silicon wafers were used as substrates for the vacuum deposition of 400A-to-500A layers of Mo, Pd, Ti, and V. Samples of each metal layer on silicon wafers were then sintered, using one of the following techniques: 500°C-10-minute furnace sinter, 600°C-10-minute furnace sinter, and irradiation with a 100-nanosecond pulsed electron beam. The total electron beam fluence was 0.2 cal/cm² and the electron energy was 12 keV.

Auger electron spectroscopy was used to determine the relative volumetric concentration of silicon, oxygen, and the deposited metal as a function of sputtering time using 3-keV argon ions. The Auger signals for the sintered sample (600°C) and the pulsed electron beam sample with a molybdenum layer are shown in Figure 2-60 and 2-61. The depth scale is only approximate, since the sputtering-etch rate (about 50A per minute) depends upon the material composition, which varies with depth. The drop in the molybdenum signal level at the surface of both samples is due to the presence of impurities which reduce the relative abundance of the metal in the sensitive volume. The reduction of the molybdenum signal as a function of depth, accompanied by an

PULSED SINTERED Mo ON Si

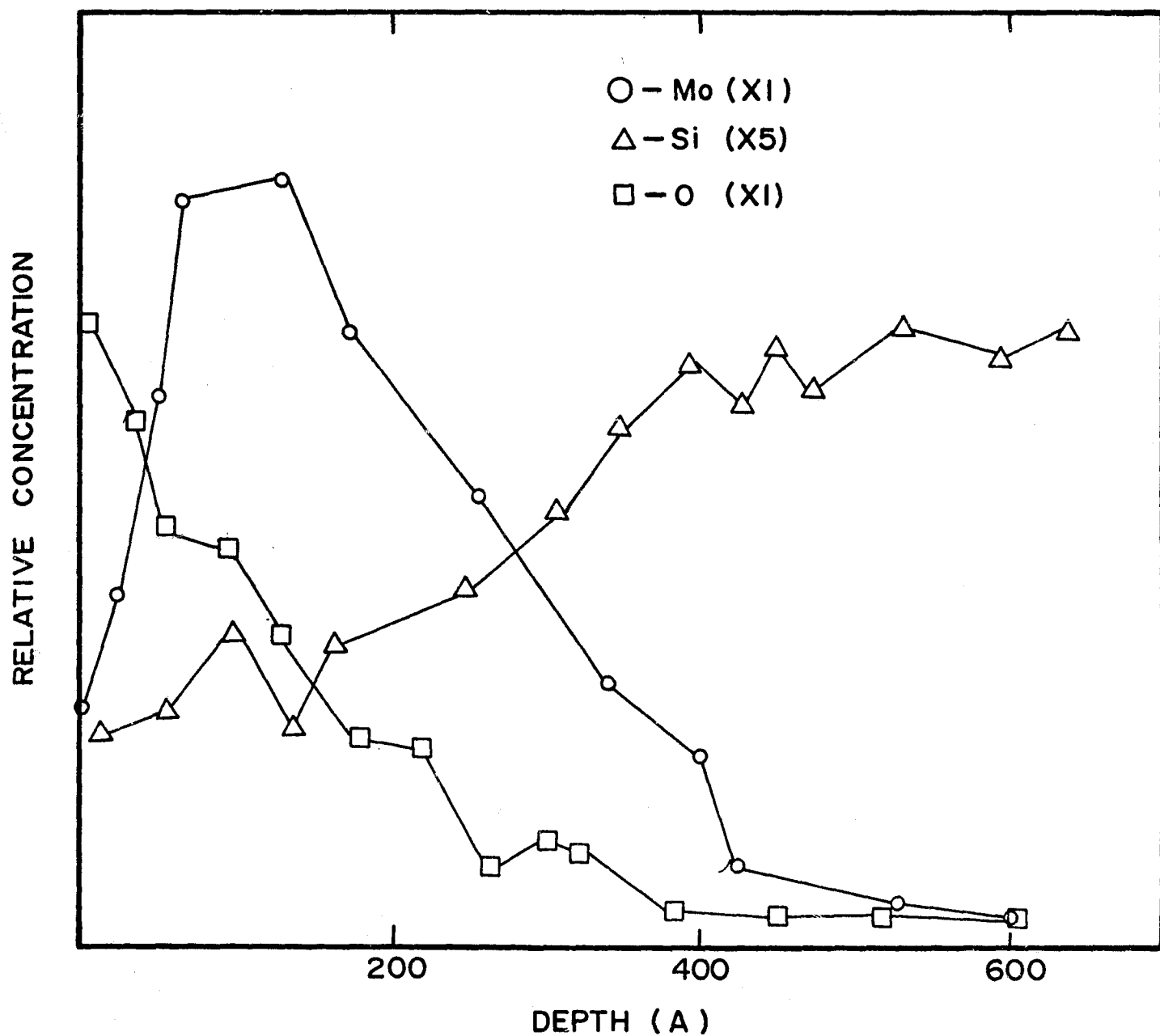


FIGURE 2-60. AUGER ANALYSIS OF PULSE-SINTERED, THIN-FILM MOLYBDENUM ON SILICON

600°C-10min SINTER Mo/Si

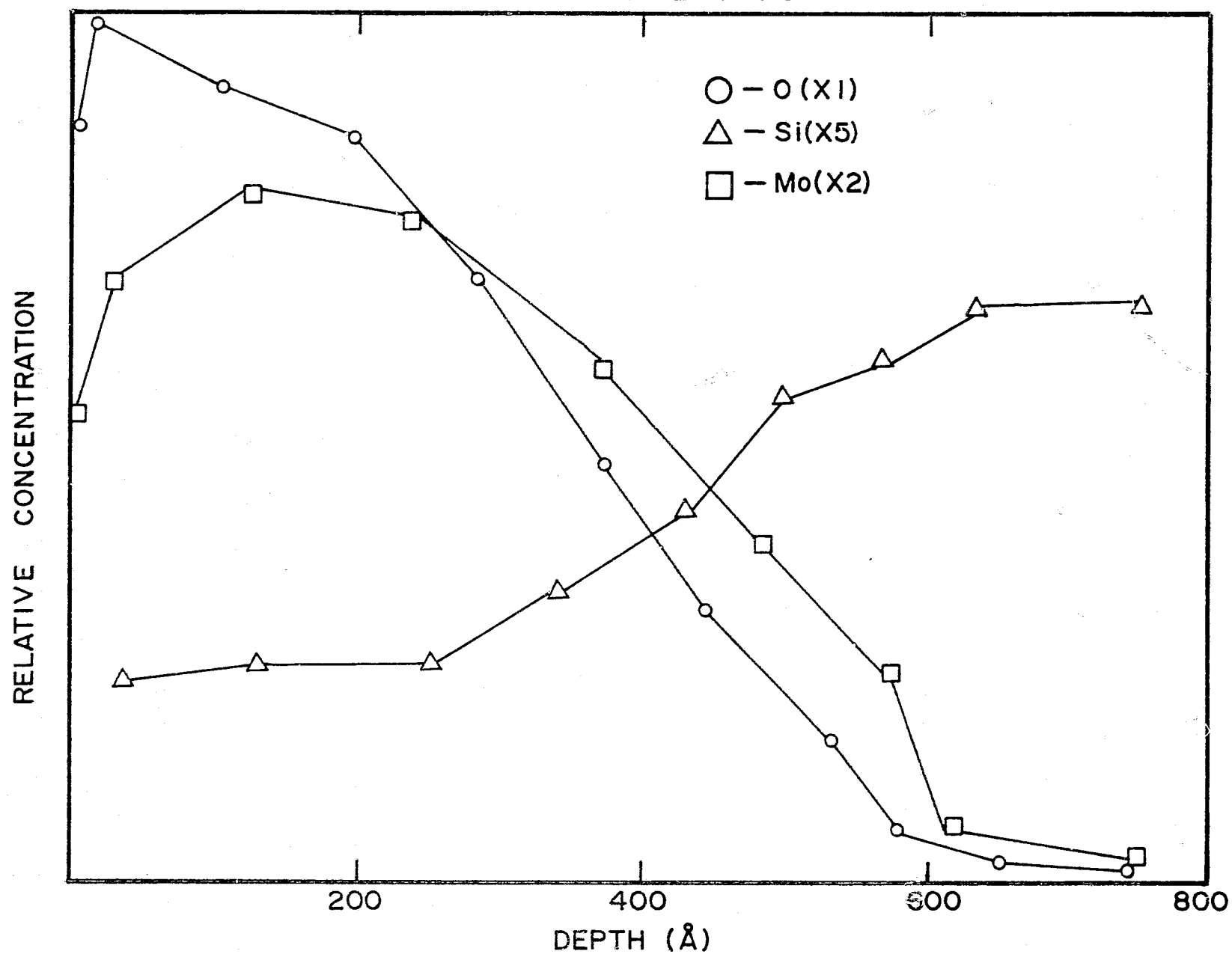
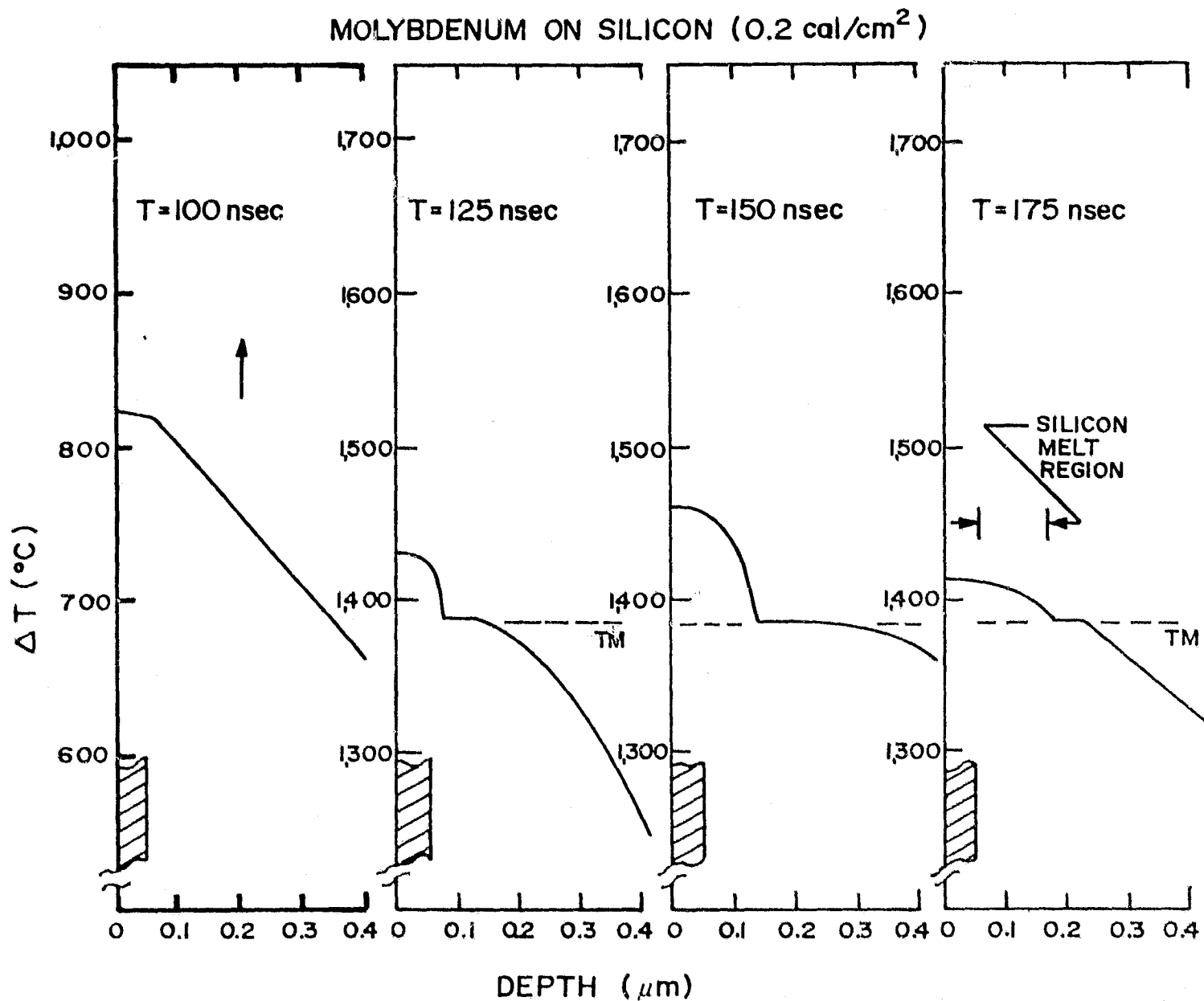


FIGURE 2-61. AUGER ANALYSIS OF FURNACE-SINTERED, THIN-FILM MOLYBDENUM ON SILICON

increasing silicon concentration up to the level in the pure single crystal region of the substrate, is caused by diffusion at the metal-silicon interface during sintering. This behavior was evident in both samples implying that furnace sintering and pulse processing can produce comparable results. For diffusion limited processes the Dt product, where D is the diffusion coefficient and t is the time, must be comparable for the two techniques if the metal/silicon distributions are similar. The ratio of the time intervals for the two types of processes falls between 0.6×10^7 and 1.2×10^7 . The ratio of the diffusion constants at the temperatures achieved in the pulse heated sample and furnace sintered samples must also be the same. This ratio for the diffusion constants is reasonable if the metal or silicon was melted during the pulsed electron beam sintering. For reference, values of this ratio for slow diffusers in solid silicon, such as arsenic, are on the order of 10^{11} .

Measurements of titanium and vanadium pulse sintered contacts were similar to the results for molybdenum. Titanium and the samples processed by pulse techniques have a deeper (600Å) metal-silicon interface and less oxygen than identical samples processed in a furnace at 500°C or 600°C for 10 minutes in a nitrogen atmosphere.

A computer calculation of the expected temperature profile produced by the pulsed electron beam was generated for the molybdenum sample to help interpret the Auger data. The front surface temperature rise and spatial variation of the temperature at various times during and after the electron beam pulse are shown in Figures 2-62 and 2-63. In the calculation, the electron beam pulse had a Gaussian shape with a 60-nanosecond FWHM and a peak intensity at 113 nanoseconds. In the calculation a 500Å molybdenum layer was assumed to be deposited upon a single-crystal silicon substrate 250 micrometers thick. Temperature dependent values of thermal properties (heat capacity and thermal conductivity) were used for materials in the solid phase, while liquid phases were assumed to have temperature independent properties. The effect of impurities was not considered. The change in these thermal properties with the formation of a silicide was also not considered in the calculation. This introduced a small error for metals such as molybdenum where the lowest eutectic formed with silicon occurs at a temperature of 1,400°C. The most important feature of the results was the prediction of a silicon melt region 1,000 - 2,000Å thick below the deposited molybdenum which remains melted for a period of 100 nanoseconds. This melt region allows metal, from the formation of a eutectic alloy, to diffuse rapidly into the silicon to the depth melted.



Note: Initial temperature is 27°C , and ΔT represents the increased temperature above ambient.

FIGURE 2-62. CALCULATED SPATIAL TEMPERATURE PROFILES FOR THIN-FILM MOLYBDENUM ON SILICON FOLLOWING PULSED ELECTRON BEAM DEPOSITION

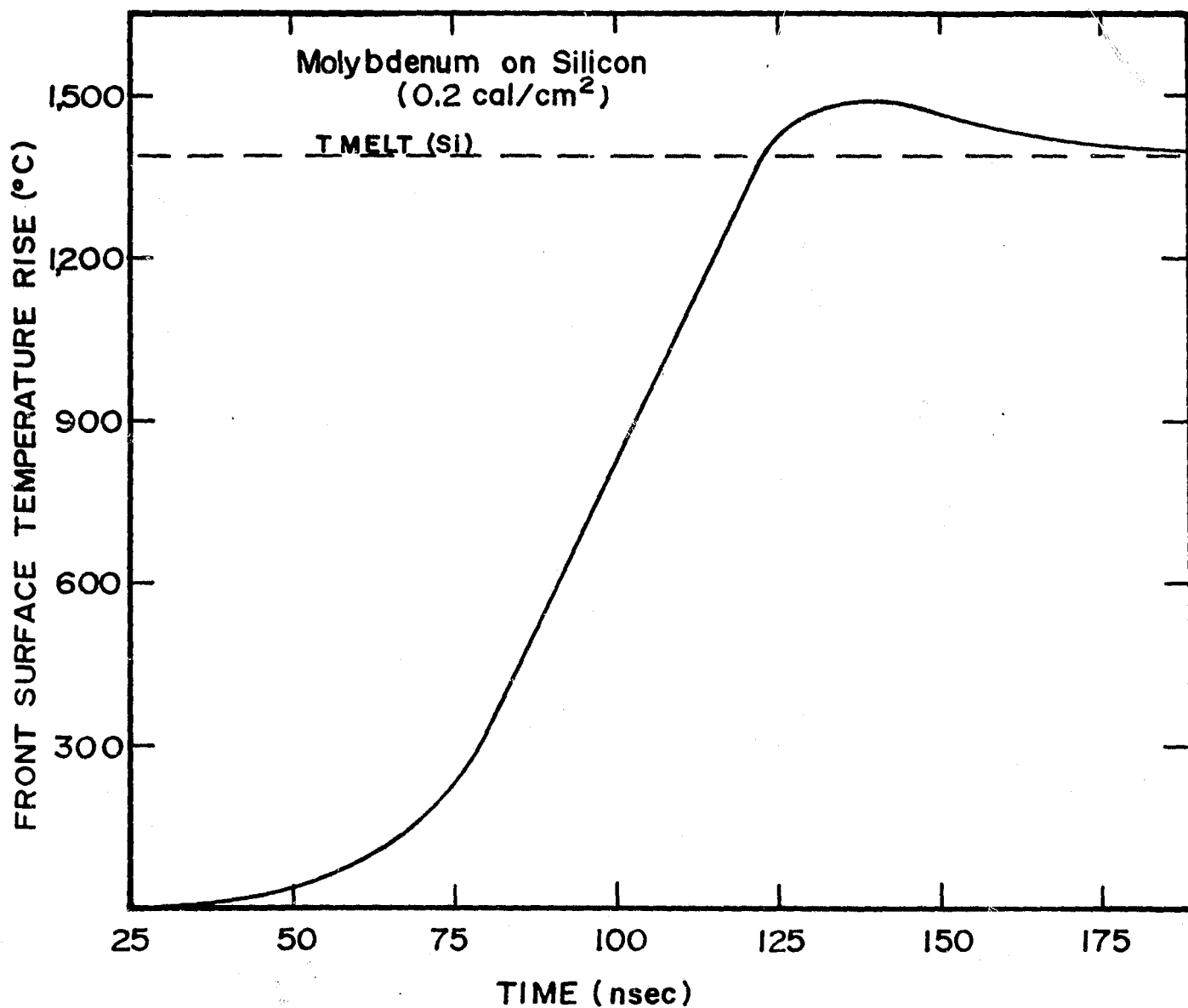


FIGURE 2-63. CALCULATED FRONT SURFACE TEMPERATURE RISE FOR 500Å MOLYBDENUM THIN FILM ON SILICON FOLLOWING 0.2 cal/cm² PULSED ELECTRON BEAM DEPOSITION

For palladium, with a melt temperature ($1,552^{\circ}\text{C}$) close to that of silicon and a low-temperature eutectic of 720°C , a greater amount of material may become liquid by the end of the electron beam pulse. Also, this material will remain in the liquid state for a longer time after the pulse, which enhances diffusion at the metal-silicon interface. This is implied by a relatively flat Auger profile for silicon recorded for the pulse-sintered palladium sample. However, the maximum depth of alloy formation is still defined by the limit of melt.

In conclusion, pulsed electron beam sintering of high melting point metal contacts on silicon has been shown to be feasible. The depth of silicide formation is defined by the region of silicon heated to the melt point, which can be controlled by varying the electron beam fluence. Reduction of contaminants has been achieved, and further reduction is possible if evaporation and sintering operations are performed in a common vacuum environment.

2.5.6 Functional Requirements for Pulsed Electron Beam Processor

The functional requirements for the electron beam processor have been defined, as listed in Table 2-15, to represent the minimum performance objectives to be met. These functional requirements will provide continuous, uniform, reproducible annealing throughput at a rate compatible with that of a 100-mA ion implanter. In addition to being compatible with the ion implanter throughput, the design philosophies of the prototype electron beam processor are similar to those of the ion implanter. A particularly important aspect is that the prototype pulser has multiple electron beam sources analogous to the ion sources of the 100-mA implanter. Multiple sources allow for system redundancy for reliability, continuous processing, and ease of maintenance. The components of the processor are identified in Figure 2-64.

The available fluence, or energy deposited per square centimeter, is adjustable over a large enough range such that either the solid- or liquid-phase epitaxial regrowth mechanism can be utilized for pulse annealing with this processor.

Each of the major subsystems for the electron beam processor is shown diagrammatically in Figure 2-65. Approximately 20 electron sources are required.

**TABLE 2-15. FUNCTIONAL REQUIREMENTS FOR PROTOTYPE
PULSED ELECTRON BEAM PROCESSOR**

(Compatible With 100-mA Implanter Throughput)

Item	Requirement
Energy Source:	Electrons
Electron Energy:	Multispectral components: Maximum 50 keV Average 10-15 keV
Fluence:	Less than 0.5 cal/cm ²
Electron Beam Current Density:	Less than 1,000 A/cm ²
Electron Beam Pulse Width:	Between 1.0 and 0.1 microsecond
Beam Uniformity/ Reproducibility	No worse than <u>+10</u> percent over all material processed; no material fractured, and all material annealed.
Substrate Throughput:	Variable, minimum of 1,000 cm ² /sec per unit
Materials To Be Handled:	Silicon wafers, ribbon sheet, etc., to maximum individual item dimension of 20 cm x 20 cm
Surfaces To Be Processed:	Planar and texturized
Processing Mode:	Continuous flow
Operational Mode:	Continuous throughput, routine operations, predictable component failure, and easy maintenance.

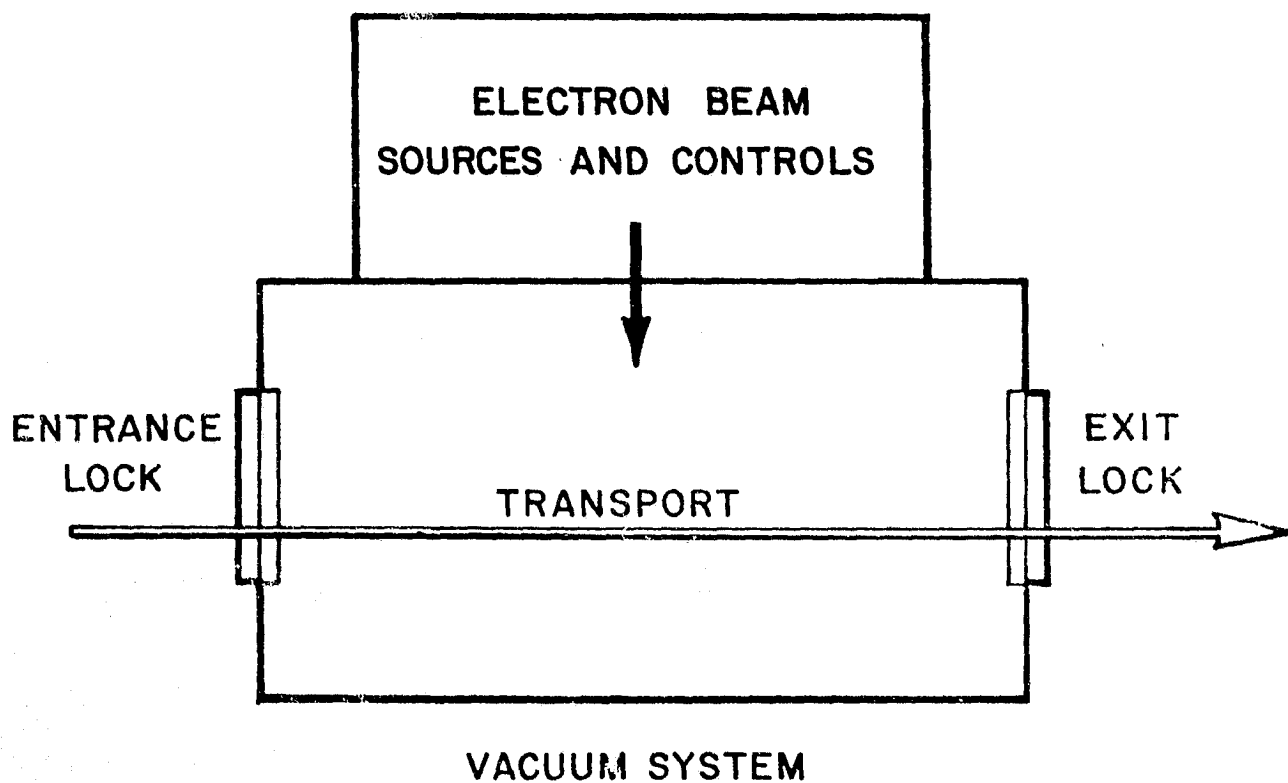


FIGURE 2-64. COMPONENTS OF AUTOMATED PRODUCTION PROCESSOR

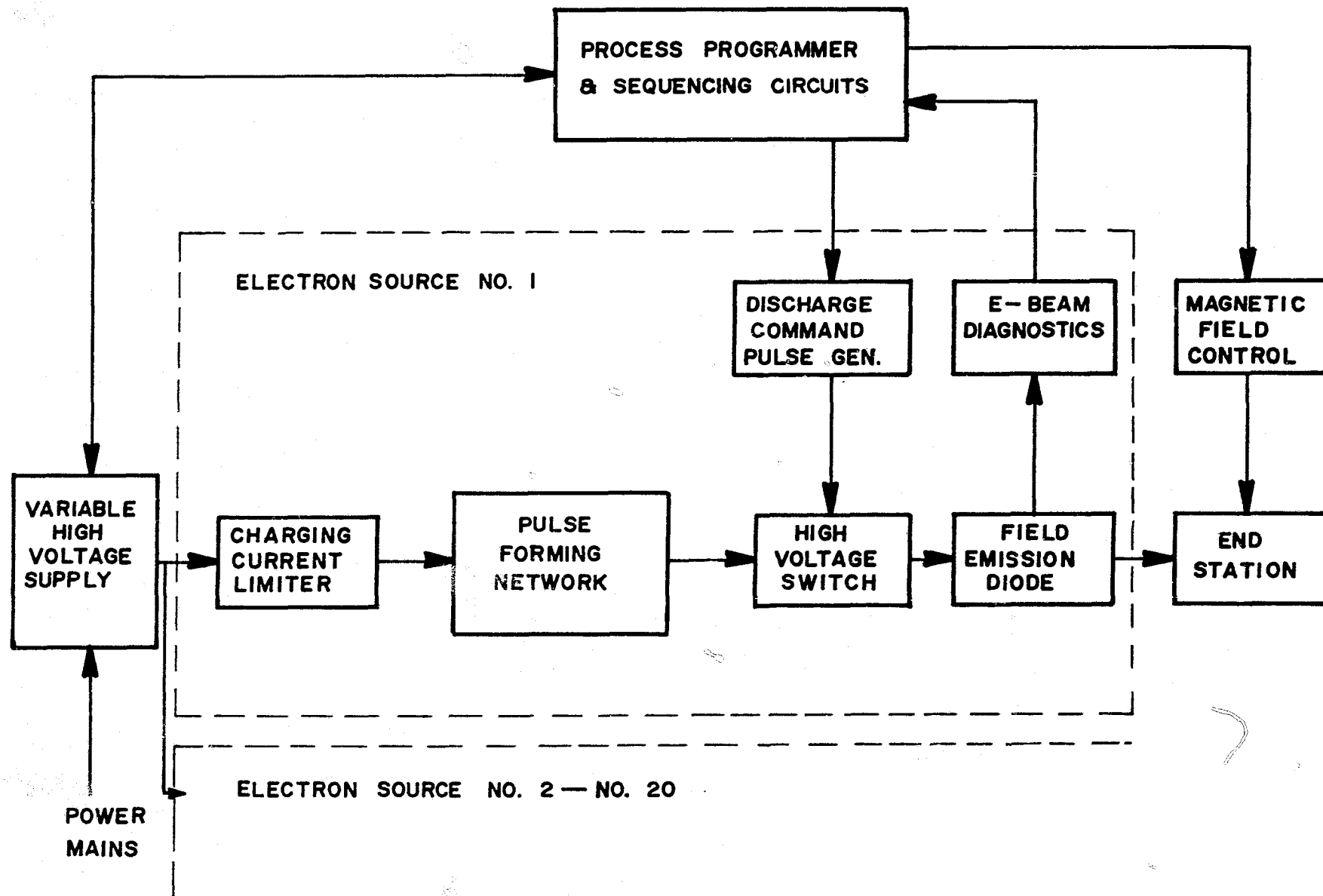


FIGURE 2-65. ELECTRON BEAM PROCESSOR SYSTEM ELEMENTS

The functional requirements of the major subsystems are as follows:

Variable High-Voltage Power Supply

A variable high-voltage power supply will provide basic electrical energy for the pulse electron beam processor. The power supply will be powered by conventional 110 volts, 60 Hz AC. The high-voltage generation range of the supply will be between 50 and 300 kilovolts. The current which it can supply will be up to 10 milliamperes. Power supply regulation in both current and voltage will be ± 2 percent.

Charging Current Limiter

Charging of the pulse forming network (PFN) of the pulsed electron beam sources will be from the high-voltage power supply through a charging current limiter. This limiter is necessary to prevent power supply burnout should shorting occur within the high-voltage PFN. This charging current limiter will be a high-power resistor of 10,000-ohm, 100-watt continuous power.

Pulse Forming Network

A PFN capable of being charged to a high voltage will be the basic energy store from which the electron beam pulse energy is extracted. This PFN will be a transmission line geometry with an impedance of between 1 and 50 ohms. The voltage to which this transmission line will be charged is between 50 and 300 kilovolts, compatible with the high-voltage power supply.

High-Voltage Switch

A command switch is required for discharge of the PFN once it has been charged by the high-voltage power supply. This switch will consist of a trigatron geometry with high-voltage spark initiation occurring on the ground side of the system, i.e., the diode. The trigatron switch will be initiated with a high-voltage pulse not less than 10 percent of the transmission line charging voltage. Switch jitter will be controlled to within ± 1 microsecond.

Field Emission Diode

Energy from the PFN will be switched via a trigatron to the field emission diode. The field emission diode will consist of a vacuum coax region, a dielectric high-voltage insulating structure, a field/plasma emission cathode, and a transmission anode. Associated with the diode will be fast, high-voltage diagnostics consisting of a return current shunt and a capacitive voltage monitor, both built into the vacuum coax wall. These diagnostics will be calibrated for performance at the levels of processing.

End Station

The end station subsystem will be compatible with that of the 100-mA automated production ion implanter, that is, the vacuum interlocks and silicon transport will be identical to those used by the ion implanter. An additional requirement, however, is the presence of a 1-10 kilogauss magnetic field normal to the surface of the silicon to be processed. This will be provided for all electron sources by one large electromagnet. Vacuum requirements for the electron beam processor will also be compatible with that of the ion implanter. When final integration processor and implanter are accomplished, a common vacuum and silicon transport system will be used.

Process Programmer and Sequencer Controls

A microprocessor control console will be used to monitor and control the electron beam processor parameters and timing sequences. Eventually, this will be linked with the console of the 100-mA, automated production ion implanter. The processor will initiate a discharge upon command, via an intermediate voltage pulse generator which breaks down the trigatron switch in the high voltage system. The control console will also record the response of the diagnostics for the field emission diode such that beam parameters are precisely monitored on a pulse-to-pulse basis. The magnetic field parameters in the transport system will also be programmable.

The electron beam source will become a basic building block in the automated processing line to be developed to achieve 1986 and greater production goals. The processor described will satisfy the requirements of an ion implanter

with 100 milliamperes of current and a throughput of $500 \text{ cm}^2/\text{sec}$ for junction implants. Individual electron beams, similar to the case of ion sources, will be provided by transmission line pulse forming networks. This approach offers advantages similar to those of the multisource ion implanter. Electron beam source redundancy and off-line startup are achieved. The reliability of moderate level individual sources is improved, and the entire system reliability, reproducibility, and duty cycle are thereby enhanced.

2.6 ECONOMIC ANALYSIS

Economic analyses have been performed to assess the relative potential costs of the ion implantation and pulsed electron beam annealing methods for junction introduction. Solar Array Manufacturing Industry Costing Standard (SAMICS) analyses were conducted for ion implantation and pulse annealing of the implantation damage. To determine the cost sensitivity of these processes with throughput, a Tektronix 4051 calculator was programmed to accept JPL's Format A Statements (see Figures 2-66 through 2-68), then compute the product quantities, price calculations, and labor costs, based on Format B and C Statements (see Figures 2-69 and 2-70).

2.6.1 Ion Implantation

The ion implantation economic analyses were conducted according the JPL SAMICS-A for solar cell junction parameters. Input data for three types of implantation machines were determined based on experience at Spire, including ion implantation facility labor requirements, material utilization, energy consumption, process yield and product throughput. Input data for the 100-mA automated production implanter were obtained from design development efforts under this contract. SAMICS input data for the Format A Statements are shown for each of the three ion implanters considered in Figure 2-71.

The results of these analyses (see Figures 2-72 through 2-77) show that the manufacturing cost is decreased as the ion beam current is increased from microampere to milliampere levels, as shown in Table 2-16. These analyses show that a 100-mA automated production facility can introduce junctions in silicon material at a cost of only \$1.28 per square meter. Based on conversion efficiencies greater than 10 percent AM1, this results in a cost of less than \$0.01/watt.

SOLAR ARRAY MANUFACTURING INDUSTRY COSTING STANDARDS

FORMAT A



JET PROPULSION LABORATORY
California Institute of Technology
4800 Oak Grove Dr. / Pasadena, Calif. 91103

PROCESS DESCRIPTION

A1 Process Referent NIMP-I

A2 Description (Optional) Phosphorous Front Layer Implant

PART 1 – PRODUCT DESCRIPTION

A3 Product Referent IMPSL

A4 Name or Description Phosphorous Implanted Slices

A5 Units Of Measure M²

PART 2 – PROCESS CHARACTERISTICS

A6 Output Rate 1.883 x 10⁻³ Units (given on line A5) Per Operating Minute

A7 Average Time at Station 60 Calendar Minutes

A8 Process Usage Time Fraction .85 Average Number of Operating Minutes Per Minute

PART 3 – EQUIPMENT COST FACTORS

A9 Component Referent	<u>200-20A</u>	<u></u>	<u></u>
A10 Base Price Year For Purchase Price	<u>1978</u>	<u></u>	<u></u>
A11 Purchase Price (\$ Per Component)	<u>160,000</u>	<u></u>	<u></u>
A12 Anticipated Useful Life (Years)	<u>15</u>	<u></u>	<u></u>
A13 Salvage Value (\$ Per Component)	<u>11,000</u>	<u></u>	<u></u>
A14 Cost of Removal & Installation (\$/Component)	<u>1,500</u>	<u></u>	<u></u>

FIGURE 2-66. FORMAT A STATEMENT: PROCESS DESCRIPTION FOR 0.3 mA, MEDIUM-CURRENT ION IMPLANTATION

PART 4 – DIRECT REQUIREMENTS PER MACHINE

A16 Catalog Number	A17 Requirement Description	A18 Amount Required Per Machine	A19 Units
A2064D	Manufacturing Space Type A	156.0	SQFT
B3096D	Semiconductor Assembler	1.0	PRSN*YRS
B3704D	Electronics Technician	0.1	"
B3736D	Mechanical Technician II	0.1	"

PART 5 – DIRECT REQUIREMENTS PER BATCH (A continuous process has a "batch" of one unit)

A20 Catalog Number	A21 Requirement Description	A22 Amount Required Per Batch	A23 Units
C1032B	Electricity	.3	KWHR
C1080D	Liquid N ₂	1.6×10^{-3}	CUFT
C1128D	Cooling water	7.0×10^{-3}	KWHR
D1016B	Fumes	600	CUFT
E1472D	PH ₃ (5% in H ₂)	1.5×10^{-4}	CUFT
E1608D	Spare parts	.03	\$Dollars

PART 6 – INTRA-INDUSTRY PRODUCT(S) REQUIRED

A24 Product Reference	A25 Product Name	A26 Yield Factor (Usable Output/Input)	A27 Units

Prepared by _____ Date _____

FIGURE 2-66. FORMAT A STATEMENT: PROCESS DESCRIPTION FOR
 0.3 mA, MEDIUM-CURRENT ION IMPLANTATION (Concluded)

SOLAR ARRAY MANUFACTURING INDUSTRY COSTING STANDARDS

FORMAT A



JET PROPULSION LABORATORY
California Institute of Technology
4800 Oak Grove Dr. / Pasadena, Calif. 91103

PROCESS DESCRIPTION

A1 Process Referent NIMP-II

A2 Description (Optional) Phosphorous Front Layer Implant

PART 1 – PRODUCT DESCRIPTION

A3 Product Referent IMPSL

A4 Name or Description Phosphorous Implanted Slices

A5 Units Of Measure _____

PART 2 – PROCESS CHARACTERISTICS

A6 Output Rate .0228 Units (given on line A5) Per Operating Minute

A7 Average Time at Station 5 min Calendar Minutes

A8 Process Usage Time Fraction 0.8 Average Number of Operating Minutes Per Minute

PART 3 – EQUIPMENT COST FACTORS

A9 Component Referent	<u>200-1000WF</u>	_____	_____
A10 Base Price Year For Purchase Price	<u>1977</u>	_____	_____
A11 Purchase Price (\$ Per Component)	<u>315,000</u>	_____	_____
A12 Anticipated Useful Life (Years)	<u>15 yrs</u>	_____	_____
A13 Salvage Value (\$ Per Component)	<u>25000</u>	_____	_____
A14 Cost of Removal & Installation (\$/Component)	<u>5000</u>	_____	_____

FIGURE 2-67. FORMAT A STATEMENT: PROCESS DESCRIPTION FOR
3-mA HIGH-CURRENT ION IMPLANTATION

PART 4 – DIRECT REQUIREMENTS PER MACHINE

A16 Catalog Number	A17 Requirement Description	A18 Amount Required Per Machine	A19 Units
<u>A2064D</u>	<u>Mfg. Space Type A</u>	<u>210</u>	<u>sq ft.</u>
<u>B3096D</u>	<u>Semiconductor Assembler</u>	<u>1</u>	<u>PRSN*YRS</u>
<u>B3704D</u>	<u>Electronics Technician</u>	<u>.1</u>	<u>PRSN*YRS</u>
<u>B3736D</u>	<u>Mechanical Technician</u>	<u>.1</u>	<u>PRSN*YRS</u>

PART 5 – DIRECT REQUIREMENTS PER BATCH (A continuous process has a "batch" of one unit)

A20 Catalog Number	A21 Requirement Description	A22 Amount Required Per Batch	A23 Units
<u>C1032B</u>	<u>Electricity</u>	<u>.417</u>	<u>KWHR/min</u>
<u>C1080D</u>	<u>Liquid N₂</u>	<u>1.6 x 10⁻³</u>	<u>CUFT</u>
<u>C1128D</u>	<u>Cooling water</u>	<u>8 x 10⁻³</u>	<u>KWHR/min</u>
<u>D1016B</u>	<u>Fumes</u>	<u>1.4 x 10³</u>	<u>CUFT</u>
<u>E1472D</u>	<u>PH₃ (5% in H₂)</u>	<u>3.5 x 10⁻⁴</u>	<u>CUFT</u>
<u>E1608D</u>	<u>Spare parts</u>	<u>.06</u>	<u>Dollars \$</u>

PART 6 – INTRA-INDUSTRY PRODUCT(S) REQUIRED

A24 Product Reference	A25 Product Name	A26 Yield Factor (Usable Output/Input)	A27 Units
<u> </u>	<u> </u>	<u> </u>	<u> </u>
<u> </u>	<u> </u>	<u> </u>	<u> </u>

Prepared by _____ Date _____

FIGURE 2-67. FORMAT A STATEMENT: PROCESS DESCRIPTION FOR 3-mA, HIGH-CURRENT ION IMPLANTATION (Concluded)

SOLAR ARRAY MANUFACTURING INDUSTRY COSTING STANDARDS

FORMAT A



JET PROPULSION LABORATORY
California Institute of Technology
4800 Oak Grove Dr. / Pasadena, Calif. 91103

PROCESS DESCRIPTION

A1 Process Referent NIMP-III

A2 Description (Optional) Phosphorous Front Layer Implant

PART 1 - PRODUCT DESCRIPTION

A3 Product Referent IMPSL

A4 Name or Description Phosphorous Implanted Slices

A5 Units Of Measure M²

PART 2 - PROCESS CHARACTERISTICS

A6 Output Rate 3 Units (given on line A5) Per Operating Minute

A7 Average Time at Station 1.4 Calendar Minutes

A8 Process Usage Time Fraction .90 Average Number of Operating Minutes Per Minute

PART 3 - EQUIPMENT COST FACTORS

	solar cell prod. mach.		
A9 Component Referent	<u>1978</u>		
A10 Base Price Year For Purchase Price	<u>1,050,000</u>		
A11 Purchase Price (\$ Per Component)	<u>15</u>		
A12 Anticipated Useful Life (Years)	<u>50,000</u>		
A13 Salvage Value (\$ Per Component)	<u>15,000</u>		
A14 Cost of Removal & Installation (\$/Component)			

FIGURE 2-68. FORMAT A STATEMENT: PROCESS DESCRIPTION FOR 100-mA, AUTOMATED ION IMPLANTATION

PART 4 – DIRECT REQUIREMENTS PER MACHINE

A16 Catalog Number	A17 Requirement Description	A18 Amount Required Per Machine	A19 Units
A2064D	Manufacturing Space	500	sq. ft.
B3096D	Semiconductor Assembler	1	PRSN*YRS
B3704D	Electronics Technician	.1	"
B3736D	Maintenance Mech II	.1	"

PART 5 – DIRECT REQUIREMENTS PER BATCH (A continuous process has a "batch" of one unit)

A20 Catalog Number	A21 Requirement Description	A22 Amount Required Per Batch	A23 Units
C1032B	Electricity	3	KWHR
C1128D	Cooling water	2.05×10^{-2}	KWHR
D1016B	Fumes	4.2×10^3	CUFT
E1472D	PH3 (in H ₂)	2.1×10^{-1}	CUFT
E1608D	Spare parts	1.4×10^{-1}	\$
E1780D	N ₂ gas-high pressure	1.5×10^{-1}	CUFT

PART 6 – INTRA-INDUSTRY PRODUCT(S) REQUIRED

A24 Product Reference	A25 Product Name	A26 Yield Factor (Usable Output/Input)	A27 Units

Prepared by _____ Date _____

FIGURE 2-68. FORMAT A STATEMENT: PROCESS DESCRIPTION FOR 100-mA, AUTOMATED ION IMPLANTATION (Concluded)

SOLAR ARRAY MANUFACTURING INDUSTRY COSTING STANDARDS

FORMAT B



COMPANY DESCRIPTION

B1 Company Referent SPIRESL

B2 Description (Optional) Manufacturer of ion implanted silicon wafers

B3 Product Produced IMPSL

B4 Process NIMP-I, II, III

B5 Intermediate Product _____ Process _____

Intermediate Product _____ Process _____

Intermediate Product _____ Process _____

Intermediate Product _____ Process _____

Intermediate Product _____ Process _____

Intermediate Product _____ Process _____

Intermediate Product _____ Process _____

Intermediate Product _____ Process _____

Intermediate Product _____ Process _____

Intermediate Product _____ Process _____

Intermediate Product _____ Process _____

Intermediate Product _____ Process _____

Intermediate Product _____ Process _____

Intermediate Product _____ Process _____

B6 Purchased Product Clean wafers (CLSL)

B7 Supplier Company Reference SAMICS Waferco Percent Supplied 40%

Supplier Company Reference _____ Percent Supplied _____

Prepared by _____ Date 4-6-78

FIGURE 2-69. FORMAT B STATEMENT: COMPANY DESCRIPTION FOR MANUFACTURER OF ION-IMPLANTED SILICON WAFERS

SOLAR ARRAY MANUFACTURING INDUSTRY COSTING STANDARDS

FORMAT C



JET PROPULSION LABORATORY
California Institute of Technology
4800 Oak Grove Dr. / Pasadena, Calif. 91103

INDUSTRY DESCRIPTION

C1 Industry Referent SAMICS-78

C2 Description (Optional) 1978 Standard Industry

INDUSTRY OBJECTIVE

C3 Industry Result New Photovoltaic Power Capability

C4 Quantity Produced 1.83×10^6 Peak-watts/year

DESCRIPTION OF THE FINAL PRODUCT OF THE INDUSTRY

C5 Reference PSM Name Packaged Solar Modules

C6 Production is Measured in Modules/year

C7 Hardware Performance _____ (C4 per C6)

C8 Product Design Description (Optional) _____

MAKERS OF THE FINAL PRODUCT OF THE INDUSTRY

C9 Company Reference SAMICS MODULCO A Market Share 40%

Company Reference * Market Share _____

Company Reference _____ Market Share _____

* Remaining companies are smaller than MODULCO and are not listed.

Prepared by _____ Date 4-6-78

FIGURE 2-70. FORMAT C STATEMENT: 1978 STANDARD
INDUSTRY DESCRIPTION

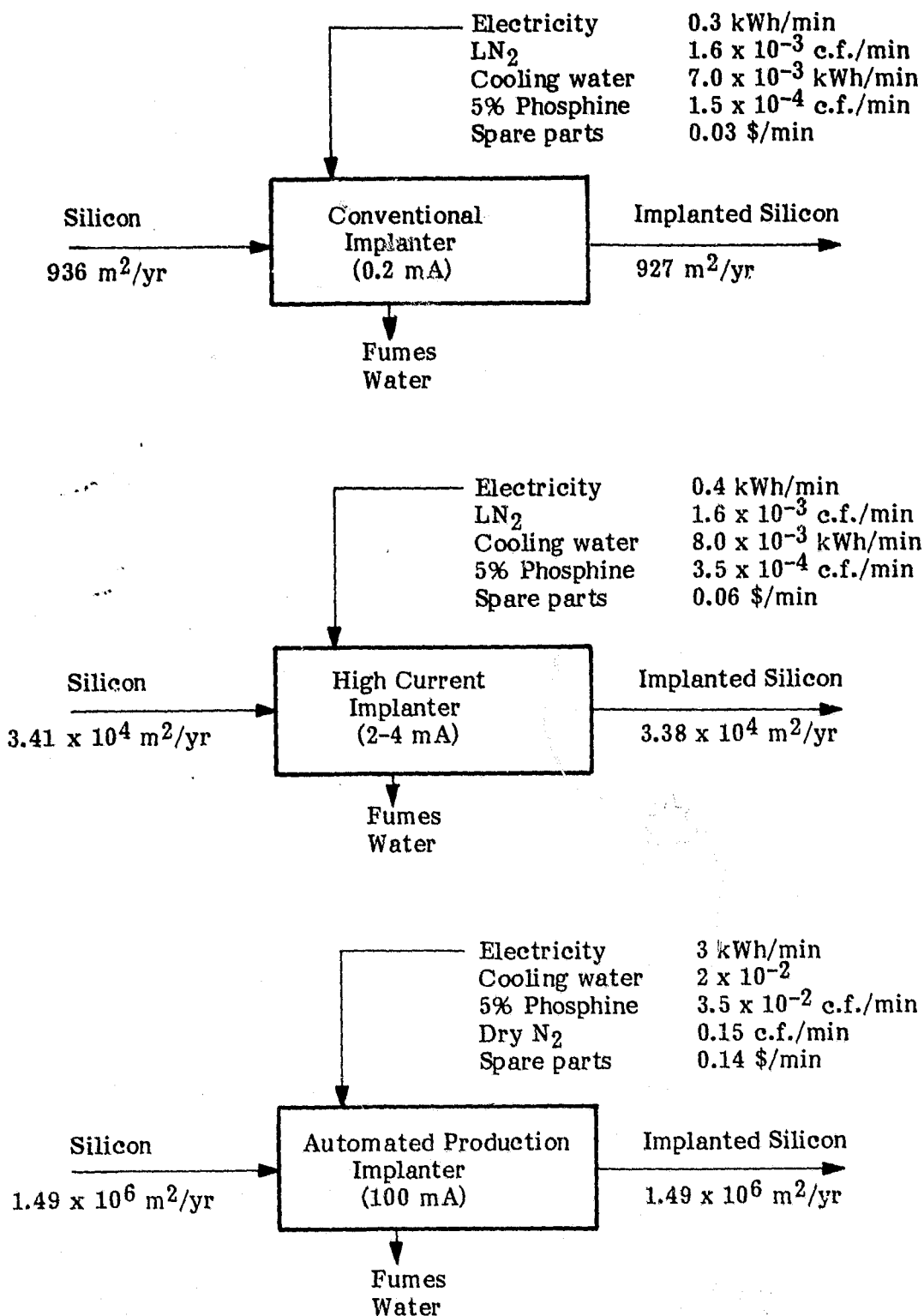


FIGURE 2-71. SAMICS INPUT DATA

PY = 78

NIMP-II

PRODUCTION YEAR 1978

20-1000 WF
No End Station
Alterations

\$.26/3" cell

\$.216/3" cell

57.11/m²

47.47/m²

W1 COMPANY REFERENCE SPIRESL
W2 PRODUCT PRODUCED IMPSL

ANNUAL AMOUNT 5600 m²/yr
QJAH (units)

W30 INFLATED PRICE

W31 DEFLATED PRICE



COMPANY WORK SHEET

W3	W4	W5	W6	W7	W8	W9	W10	W11	W12	W13	W14	W15	W16	W17	W18	W19
Process	Product	Yield	Annual Amount	Req'd Machine Cycles Per Year	Cycles Per Machine	Number of Machines	Cost Per Machine	Equipment Cost	Floor Space Per Machine	Total Floor Space	Labor Cost Per Machine	Total Direct Labor	Total Byproduct Expenses	Total Direct Materials & Supplies	Total Direct Utilities	Byproduct Revenue
NIMP-II	CLSL	.99	5656.57	2.48E5	3.97E5	.624 1	3.16E4	3.16E4	210	210	1.12E4	5.99E4	0	1.61E4	7.99E3	0
								3.16E4		210		5.99E4	0	1.61E4	7.99E3	0
								W20 EQPT		W21 SOFT		W22 DLAB		W24		W25 UTIL
													W23	0		W26 BVP
																Yield-Loss Expense
														2.59E6	2.59E4	
														2.60E6	4.20E4	
														W28 MATS	W29A	JPL 3041-B 11/77

W27 Price of Purchased Product 458/m²

W28 Purchased Product Expense

Prepared by _____ Date _____

FIGURE 2-73. SAMICS PROCESS COST FORECAST FOR ION IMPLANTATION WITH 3-mA ION IMPLANTERS IN 1978

PY = 82
NIMP-II PRODUCTION YEAR 1982

W2 PRODUCT PRODUCED IMPSL

ANNUAL AMOUNT $\frac{80,000 \text{ m}^2/\text{yr}}{\frac{\text{CUAN}}{(\text{seal})}}$

	\$.25/3" cell	\$.167/3" cell
W30 INFLATED PRICE	$55.67/m^2$	1975\$ $36.65/m^2$
		W31 DEFLATED PRICE

**COMPANY WORK SHEET**

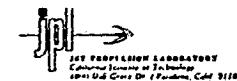
W2	W4	W5	W8	W7	W9	W10	W11	W12	W13	W14	W15	W16	W17	W18	W19	
Process	Product	Yield	Annual Amount	Req'd Machine Cycles Per Year	Cycles Per Machine	Number of Machines	Cost Per Machine	Equipment Cost	Floor Space Per Machine	Total Floor Space	Labor Cost Per Machine	Total Direct Labor	Total Byproduct Expenses	Total Direct Materials & Supplies	Total Direct Utilizers	Byproduct Revenue
NIMP-II				3.54E5	3.97E5	8.91 (9)	4.14E5	3.72E6	210	1890	1.85E4	7.81E5	0	3.69E5	9.70E4	0
	CLSL	0.99	8.08E4													

FIGURE 2-74. SAMICS PROCESS COST FORECAST FOR ION IMPLANTATION WITH 3-mA ION IMPLANTERS IN 1982

PRODUCTION YEAR 1982

\$.076/3" cell
16.58/m²

11 \$.05/3" cell
10.09/m²



COMPANY WORK SHEET

W2	W4	W5	W6	W7	W8	W9	W10	W11	W12	W13	W14	W15	W16	W17	W18	W19
Process	Product	Yield	Annual Amount	Req'd Machine Cycle Per Year	Cycle Per Machine	Number of Machines	Cost Per Machine	Equipment Cost	Floor Space Per Machine	Total Floor Space	Labor Cost Per Machine	Total Direct Labor	Total Byproduct Expenses	Total Direct Materials & Supplies	Total Direct Utilities	Byproduct Revenue
NIMP-III				2.67E4	447120	.06 1	1.92E6	1.92E6	500	500	1.41E4	6.62E4	0	1.31E5	6.05E3	0
	CLSL	.999	8.0E4													
								1.92E6		500		6.62E4	0	1.31E5	6.05E3	0
								W20 EQPT		W21 SOFT		W22 DLAB	W24 L _y			
													W23	0	W25 UTIL	W26 BYP
														Yield-Loss Expen		
														W28 Purchased Product Expense		
														1.47E5	1.55E4	

W27 Price of Purchased Product 194/m²

W29A JPL 3001-B 11/81

FIGURE 2-76. SAMICS PROCESS COST FORECAST FOR ION IMPLANTATION WITH 100-mA ION IMPLANTERS IN 1982

PRODUCTION YEAR 1986

W1 COMPANY REFERENCE	<u>SPIRESL</u>
W2 PRODUCT PRODUCED	<u>IMPSL</u>

\$.0058/3" cell

 $1.28/\text{m}^2$ 

JPL
California Inst.
of Tech.

COMPANY WORK SHEET

JET PROPULSION LABORATORY
California Institute of Technology
3801 Oak Grove Dr. Pasadena, Calif 91109

FIGURE 2-77. SAMICS PROCESS COST FORECAST FOR ION IMPLANTATION WITH 100-mA ION IMPLANTERS IN 1986

TABLE 2-16. SUMMARY OF SAMICS ANALYSIS FOR
ION IMPLANTED JUNCTIONS

Implanter	Ion Beam Current (mA)	Production Year	Annual Amount (m ²)	Price (\$/m ²)	
				Production Year Dollars	1975 Dollars
Varian Extrion 200-20A	0.1 - 0.2	1978	5.6 x 10 ³	1.01 x 10 ³	8.36 x 10 ²
Varian/Extrion Model 200-1000WF	2 - 4	1982	8.0 x 10 ⁴	55.67	36.65
		1986	1.7 x 10 ⁶	68.35	35.63
Automated Production System	100	1982	8.0 x 10 ⁴	16.58	10.09
		1986	1.7 x 10 ⁶	2.46	1.28

2.6.2 Pulse Annealing

Economic analyses were performed according to JPL - SAMICS-A for pulsed electron beam annealing. As was the case for implantation, the production throughput of the pulse processor was increased to 180 m²/hr, so that one processor can be used to anneal the product from a 100-mA ion implanter. This throughput corresponds to a manufacturing capacity of 100-mW peak power per year. Results of the analyses are shown in Table 2-17. Again, if a conversion efficiency of at least 10 percent AM1 is assumed, the cost for pulse annealing is less than \$0.01 per watt. It is important to note that this cost estimate is based on an independent, stand-alone facility. Cost savings would be realized by using a common vacuum process chamber and enhance/exit vacuum locks for both implantation and pulse annealing.

2.6.3 Cost Analysis and Production Schedule for Machine Fabrication

The manufacturing costs of the prototype implantation unit are summarized in Table 2-18. The costing is based on the experience gained with present-generation implanters which are much smaller, but more versatile and complex. The engineering of the prototype unit provided the documentation suitable to build the first unit. It is expected that experience with the first unit will generate a considerable number of engineering changes and these are reflected by a continuing engineering expense in later machines. The cost estimates are based on 1978 labor rates and on the production schedule shown in Figure 2-78.

TABLE 2-17. SUMMARY OF SAMICS ANALYSIS FOR
PULSED ELECTRON BEAM ANNEALING

Processor	Production Year	Annual Amount (m ²)	Price (\$/m ²)	
			Production-Year Dollars	1975 Dollars
Existing Laboratory Facility	1978	6.6 x 10 ³	530.79	441.23
Automated Production System	1986	1.7 x 10 ⁶	2.11	1.10

TABLE 2-18. ESTIMATED MANUFACTURING COST OF HIGH VOLUME
SOLAR CELL IMPLANTER

Item	Cost	
	Prototype Unit	Production Units
Project Management	\$100,000	\$10,000
Engineering	400,000	38,000
Documentation & ECO's (over 10 units)		14,000
Materials and Subassembly Labor		
Control Console	18,000	
Mass Analyzer Magnet	78,000	
Magnet Power Supplies	129,000	
Ion Sources	20,000	
Implanter Vacuum Chamber	107,000	
Entrance/Exit Vacuum Assembly	196,000	
Diffusion Pumps	15,000	
Mechanical Pumps	8,000	
Miscellaneous	19,000	
Subtotal	590,000	400,000
Other Manufacturing Costs	59,000	40,000
Assembly on Site	32,000	20,000
Test and Qualification	40,000	20,000
Software Development	60,000	10,000
Total	\$1,281,000	\$552,000

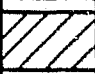
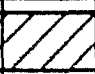
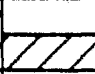
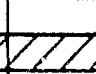
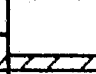


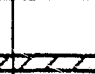
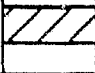
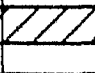



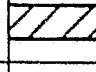
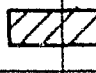
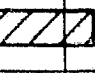

TASK	YEAR 1				YEAR 2			
ENGINEERING								
MANUFACTURING								
SUBASSEMBLY TEST								
SITE ASSEMBLY								
TEST								
QUALIFICATION								

FIGURE 2-78. PRODUCTION SCHEDULE OF PROTOTYPE SOLAR CELL IMPLANTER

SECTION 3

CONCLUSIONS

This report has described the phase I results of a 1-year program whose purpose is to develop ion implantation and associated processing for long-range automated production of solar cells. Significant accomplishments during this reporting period include:

1. A dedicated, state-of-the-art solar cell implanter has been operational for 9 months. Manufacturing and quality control procedures have been defined for implant uniformities better than ± 10 percent. Throughputs of 300 wafers per hour have been achieved at doses of $2 \times 10^{15} \text{ }^{31}\text{P}^+$. Cells processed using these implant specifications have average efficiencies of 15 percent AM1 and peak efficiencies as high as 16.5 percent AM1.
2. The design specifications for a 100-MW_e/yr automated production ion implantation have been completed. This implanter will deliver 100 mA of mass-separated ion beam onto silicon wafer, sheet, or ribbon material transported through the machine in carriers. Analysis, using JPL's Solar Array Manufacturing Industry Costing Standards (SAMICS) methods, shows that the cost for solar cell junction implants will be only \$0.01 per peak watt if 100-mA facilities are available. (This does not include annealing.)
3. High-efficiency back surface fields, prepared by the ion implantation of boron in an n^+/pp^+ structure, have been demonstrated with cell efficiencies of 14.1 percent AM0 (16.5 percent AM1). The feasibility of effectively annealing back surface field implants by pulsed electron beams has also been shown.
4. The functional requirements for a pulse processor compatible with the throughput and operational modes of a 100-mA ion implanter have been defined.
5. A model of the pulsed energy, transient process for the annealing mechanism has been identified and described.
6. The application of the pulsed energy annealing process has been investigated. The advantages of the process include the potential for higher cell efficiencies and its ability to be integrated into an automated ion implantation production process.

SECTION 4
NEW TECHNOLOGY

No new technology has been developed to completion during Phase 1 of this contract.

REFERENCES

1. A.R. Kirkpatrick, et al., "Development of Methods and Procedures for High-Rate, Low-Energy Expenditure Fabrication of Solar Cells", JPL Document No. 954289-76/4, Spire Corporation, Bedford, Massachusetts (1976).
2. M.G. Coleman and R. Pryor, "Quarterly Report No. 5, Automated Array Assembly Task", JPL Document No. 954363-77/6, Motorola Inc., Phoenix, Arizona (1977).
3. B.G. Carbajal, "Final Report, Automated Array Assembly Task", JPL Document No. 954405-77/7, Texas Instruments, Inc., Dallas, Texas (1977).
4. B.F. Williams, "Annual Report, Automated Array Assembly", JPL Document No. 954352-77/1, Radio Corporation of America, Princeton, New Jersey (1977).
5. L. Csepregi, W.K. Chu, et al., Radiat. Eff. 28, 227 (1976).
6. L. Csepregi, J.W. Mager, and J.W. Sigmon, Appl. Phys. Lett. 29, No. 2, 92 (1976).
7. R. Handy, Solid-State Electron. 10, 765 (1967).
8. M. Wolf, Proc. IRE 48, 1246 (1960).
9. W. Matzen, et al., 12th IEEE Photovoltaic Specialists Conf. Proc., 340 (1976).
10. A.R. Kirkpatrick, et al., IEEE Trans. Electron Devices ED-24, No. 4, 429 (1977).
11. J.W. Mayer, et al., private communications (1977-1978).
12. S.S. Lau, et al., "Comparison of Laser and Electron Beam Annealing", presented at Symposium H, "Laser-Solid Interactions and Laser Processing", Materials Research Society Annual Meeting, Boston, Nov.-Dec. 1978 (Symposium to be published as part of American Institute of Physics Conference Proceedings Series).
13. N.A. Blum and E.J. Feldman, J. Non-Cryst. Solids 11, 242 (1972).
14. L. Csepregi, et al., J. Appl. Phys. 48, 4234 (1977).
15. J.C. Brice, Solid-State Electron. 6, 673 (1963).
16. T.E. Seidel and A.U. MacRae, Trans. AIME 245, 491 (1969).
17. R.R. Long, Mechanics of Solids and Fluids, Prentice-Hall, Inc., Englewood Cliffs, NJ (1963).
18. L.D. Landau and E.M. Lifshitz, Theory of Elasticity, Pergamon Press, Long Island City, NY (1959), p. 19.
19. J.R. Dennis and E.B. Hale, J. Appl. Phys. 49 (3), 1119 (1978).
20. W.R. Runyan, Silicon Semiconductor Technology, McGraw-Hill Book Co., Inc., New York (1965), Chap. 10.

21. H.E. Cline and T.R. Anthony, J. Appl. Phys. 49, 2412 (1978).
22. H.E. Cline and T.R. Anthony, J. Appl. Phys. 47, 2332 (1976).
23. Ibid., 2325 (1976).
24. Ibid., 2316 (1976).

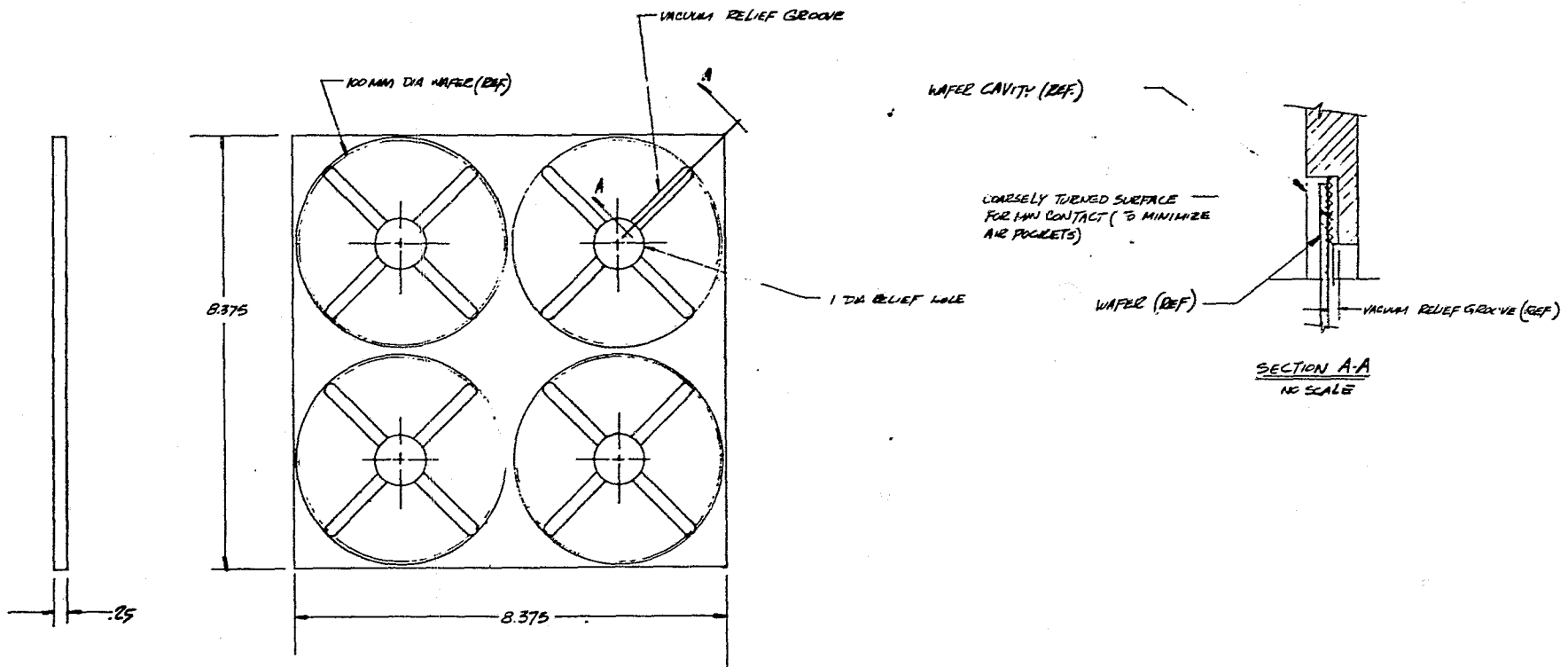
APPENDIX A

SYSTEM DETAIL DRAWINGS FOR AUTOMATED ION IMPLANTER WITH 500-cm²/sec THROUGHPUT

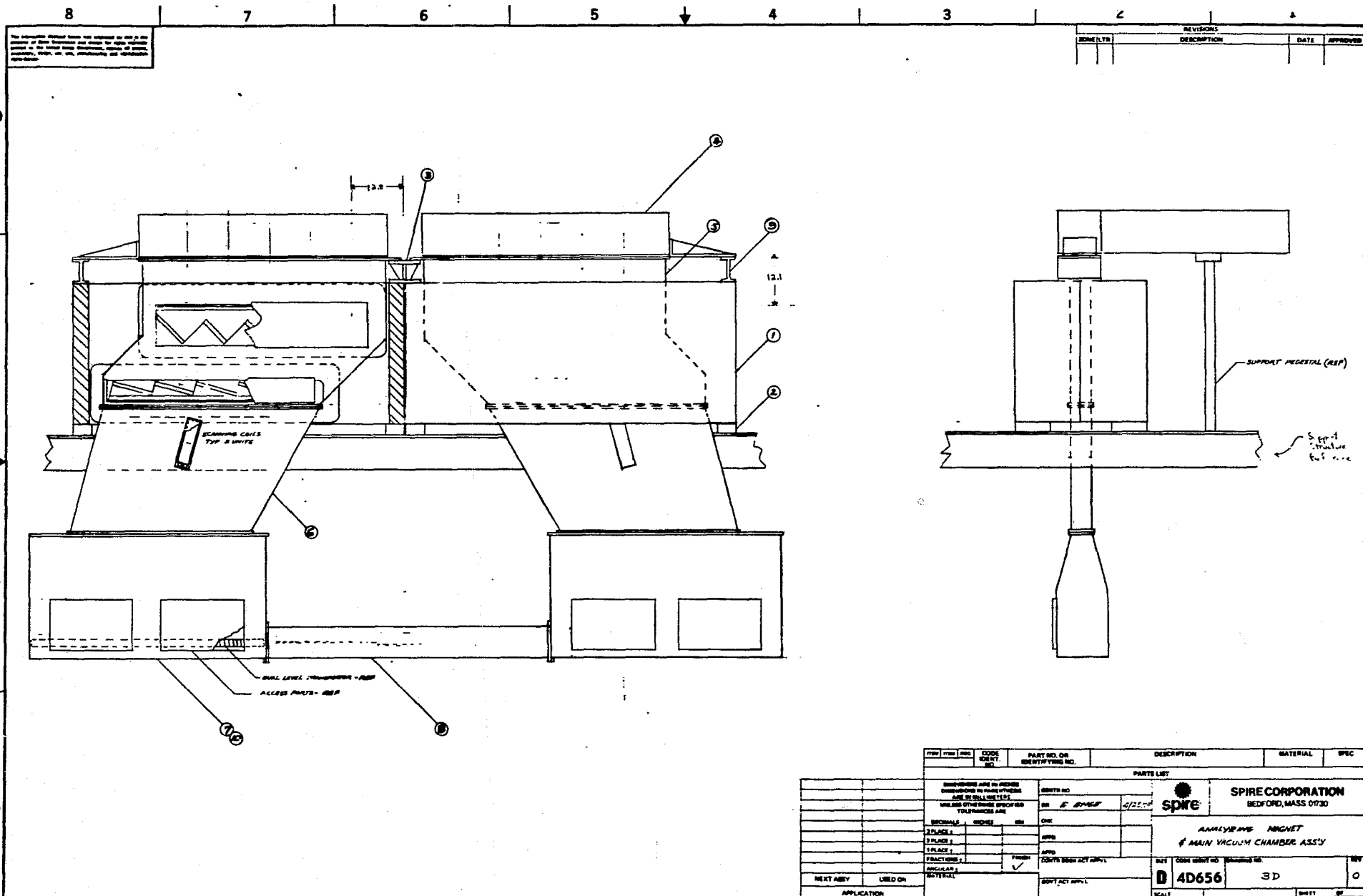
8 7 6 5 4 3 2 1

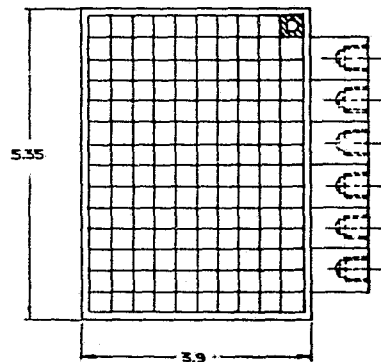
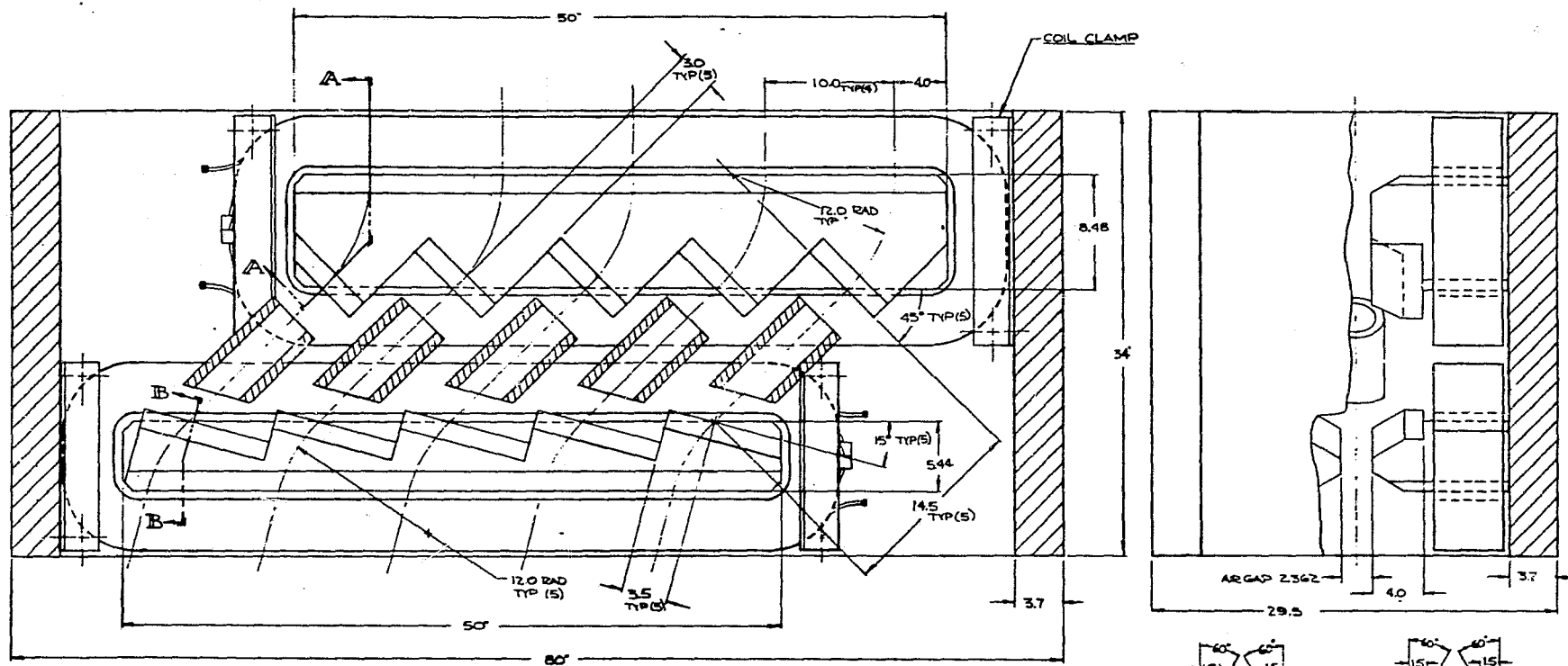
1. This drawing is the property of Spire Corporation and is not to be reproduced, stored in a retrieval system, or transmitted in any form or by any means, electronic, mechanical, photocopying, recording, or by any information storage and retrieval system, without the prior written permission of Spire Corporation.

REVISIONS			
REV	DESCRIPTION	DATE	APPROVED

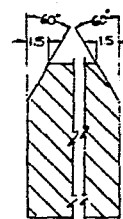


FORM 1000	REV	CODE	PARTY NO. OR IDENTIFYING NO.	DESCRIPTION	MATERIAL	SPEC
DIMENSIONS ARE IN INCHES DIMENSIONS IN PARENTHESES ARE IN MILLIMETERS UNLESS OTHERWISE SPECIFIED TOLERANCES ARE			PARTS LIST CENTR AC DNE APPD APPD CHECKED BY DATE			
DECIMALS FRACTIONS FINISH MATERIAL			SPIRE CORPORATION BEDFORD, MASS 01730 CARRIER FOR 100MM DIA WAFER D 4D656 16 D			
NEXT ASBY USED ON APPLICATION			GOVT ACT APPL SCALE SHEET 1 OF 1			

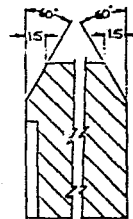




COIL BATING
 SIZE - 325 SQ WITH .181 I.D.
 POWER - 30 KW
 CURRENT - 700 A
 COOLING - 5 GPM (.35 LPS)
WEIGHT
 COILS - 1000 LB
 IRON - 11,400 LB
 TOTAL - 12,400 LB

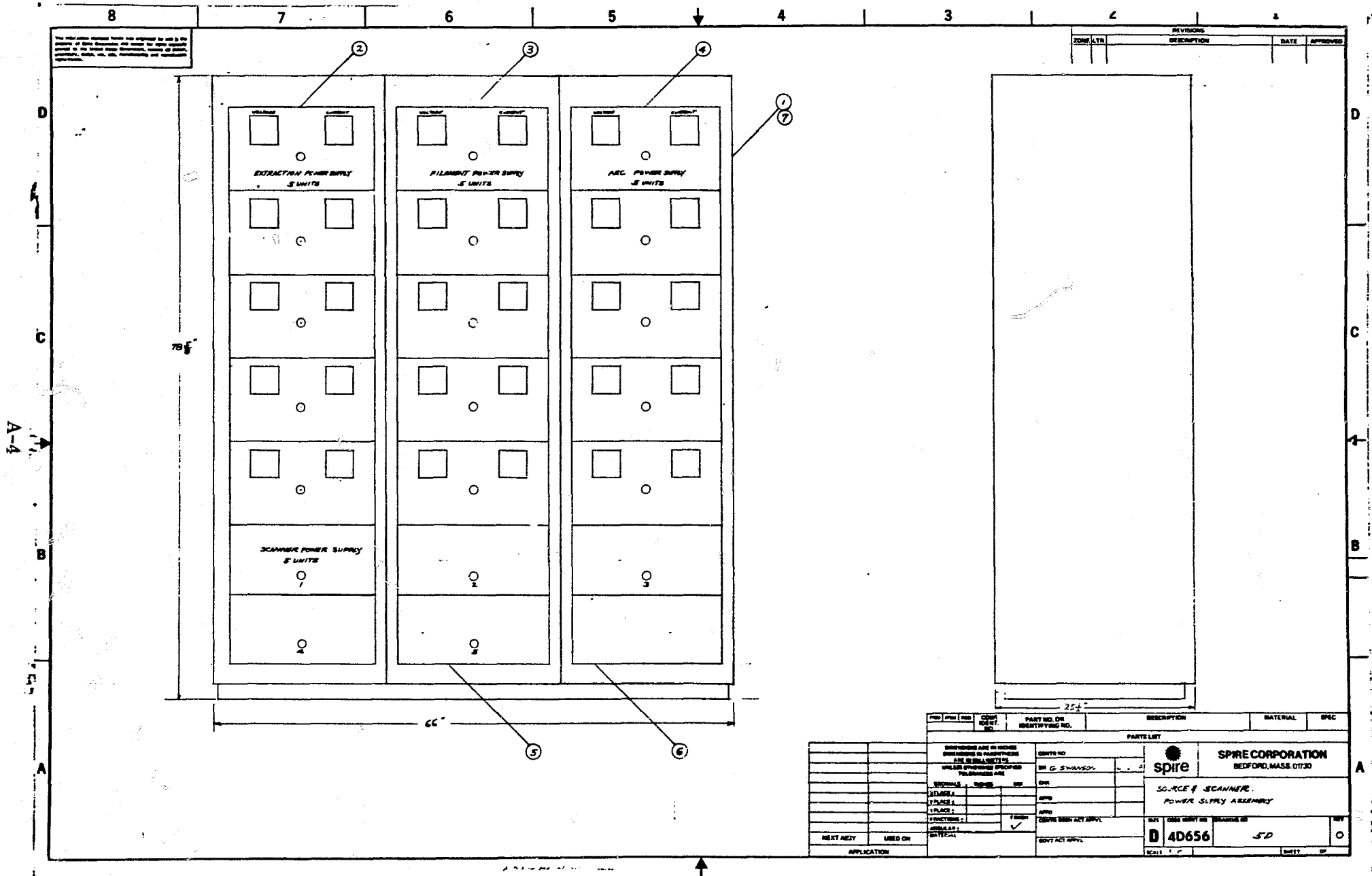


SECTION B-B



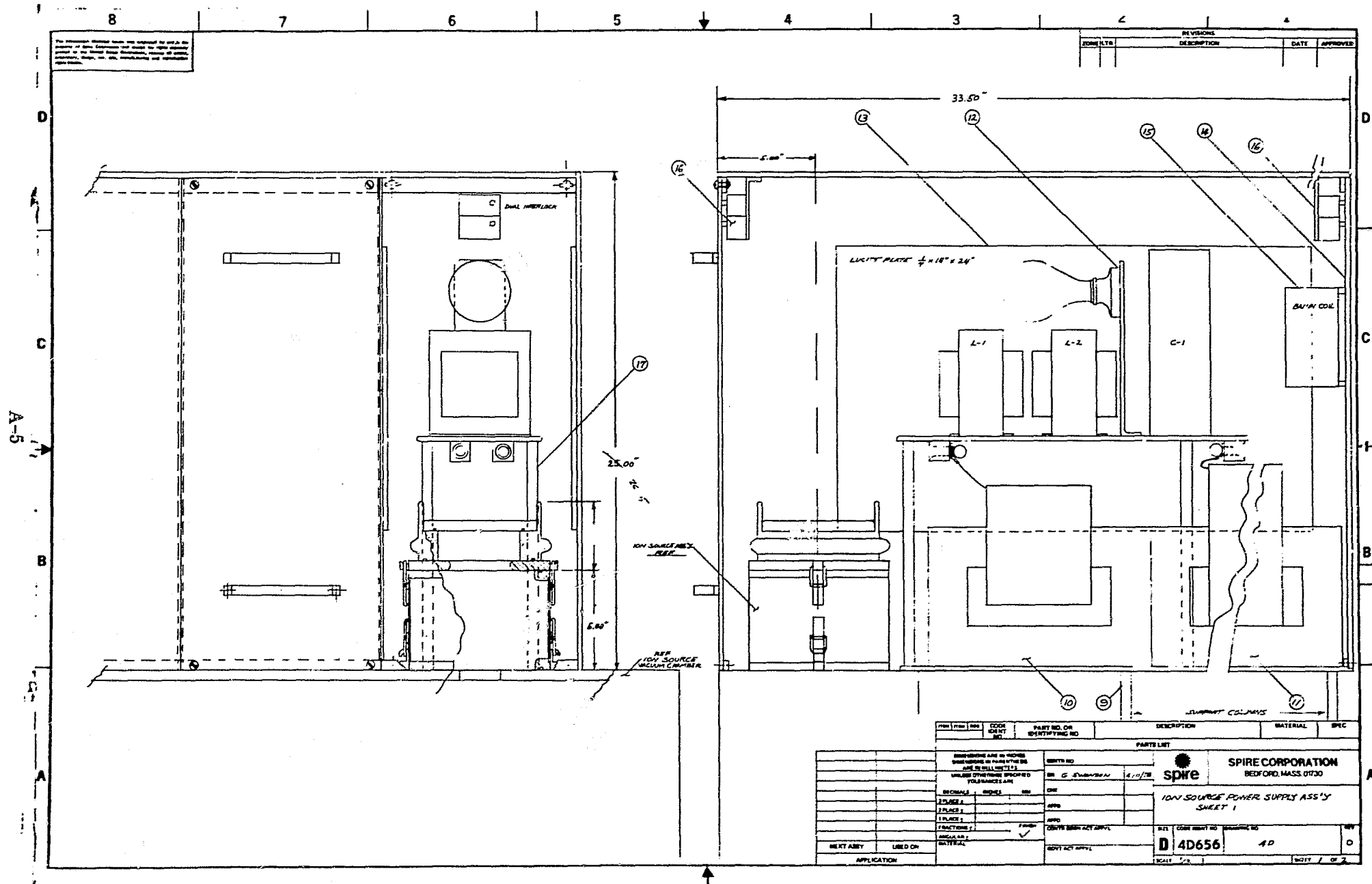
SECTION A-A

ITEM	PART NO.	DESCRIPTION	MATERIAL	QTY.
LIST OF MATERIAL				
FOR NO.				
1	1	DESIGN		
2	2	ENGINEER		
3	3	CHECKED		
4	4	APPROVED		
5	5	TEST ADP		
6	6	REVIEW		
V. [Signature]				
INDUSTRIAL COILS INC.				
POST OFFICE BOX 8 BIRCH STREET MIDDLETON, MASS. 01469 TEL. (617) 550-1000				
TITLE: SLAP CELL IMPLANTER				
F. H. J. S. HARTLEY				
SHEET NO. 13 D				
SHEET 13 D				

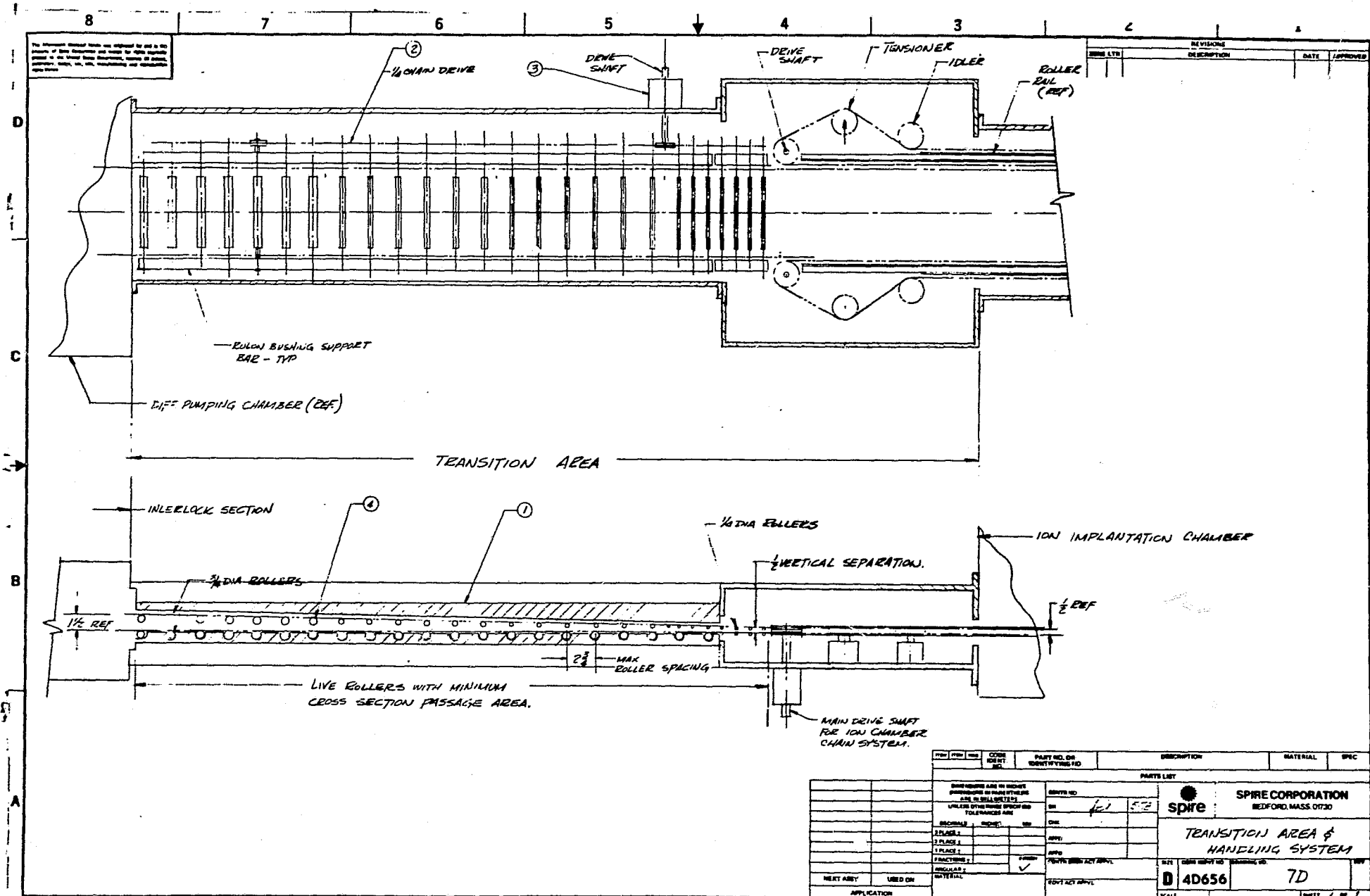


REV	APP	REV	DATE	DESCRIPTION	MATERIAL	SPEC
1						

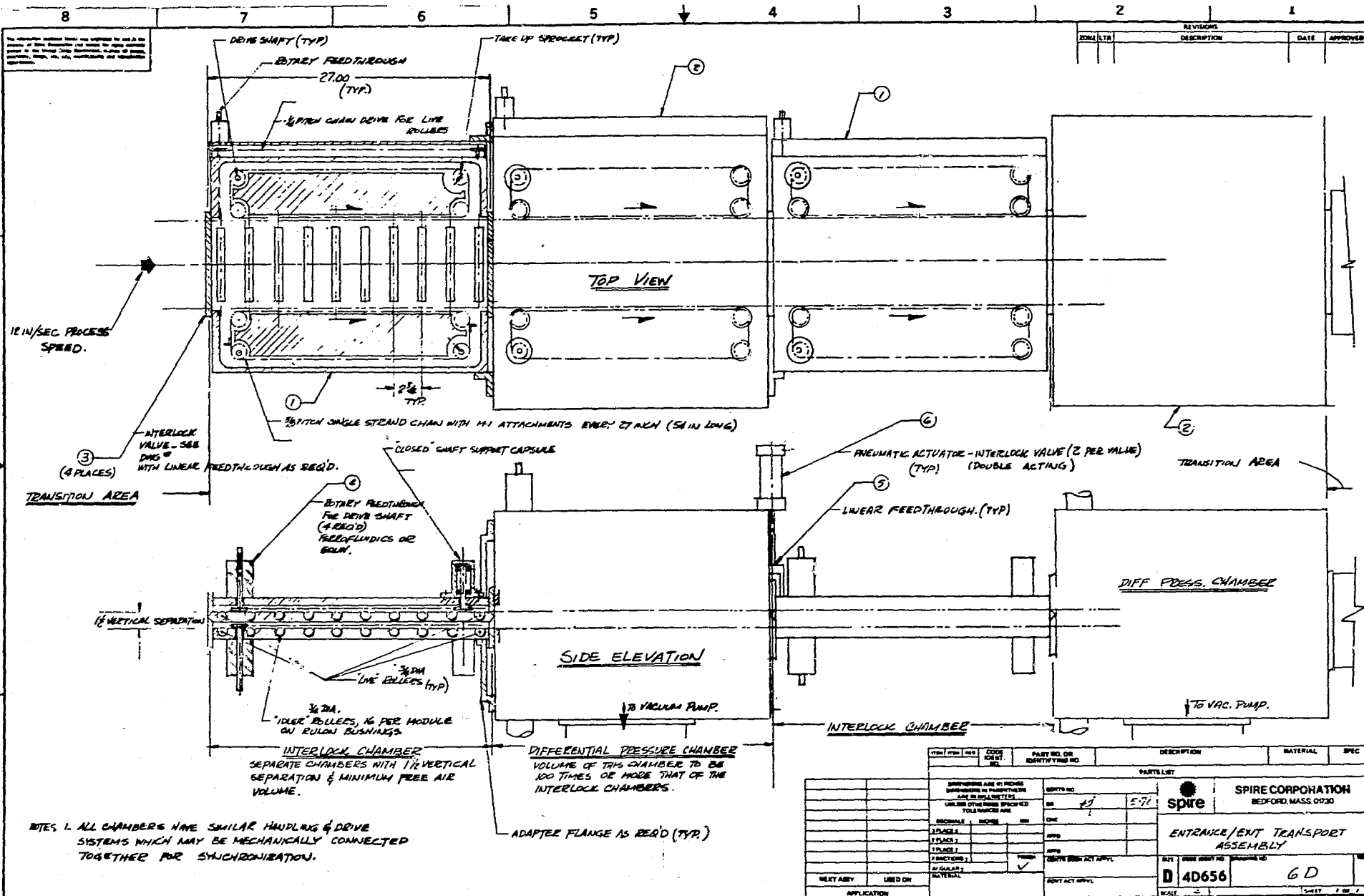
PART NO. OR IDENTIFYING NO.		PARTS LIST		DESCRIPTION		MATERIAL		SPEC	
BY G. SWANSON		DATE		SP-ICE		SP-ICE CORPORATION		BEDFORD, MASS. 01730	
REVISIONS		DATE		SC-ICE & SCANNER		POWER SUPPLY ASSEMBLY			
NEXT REV		USED ON		DATE		QTY		REV	
APPLICATION				D 40656		50			



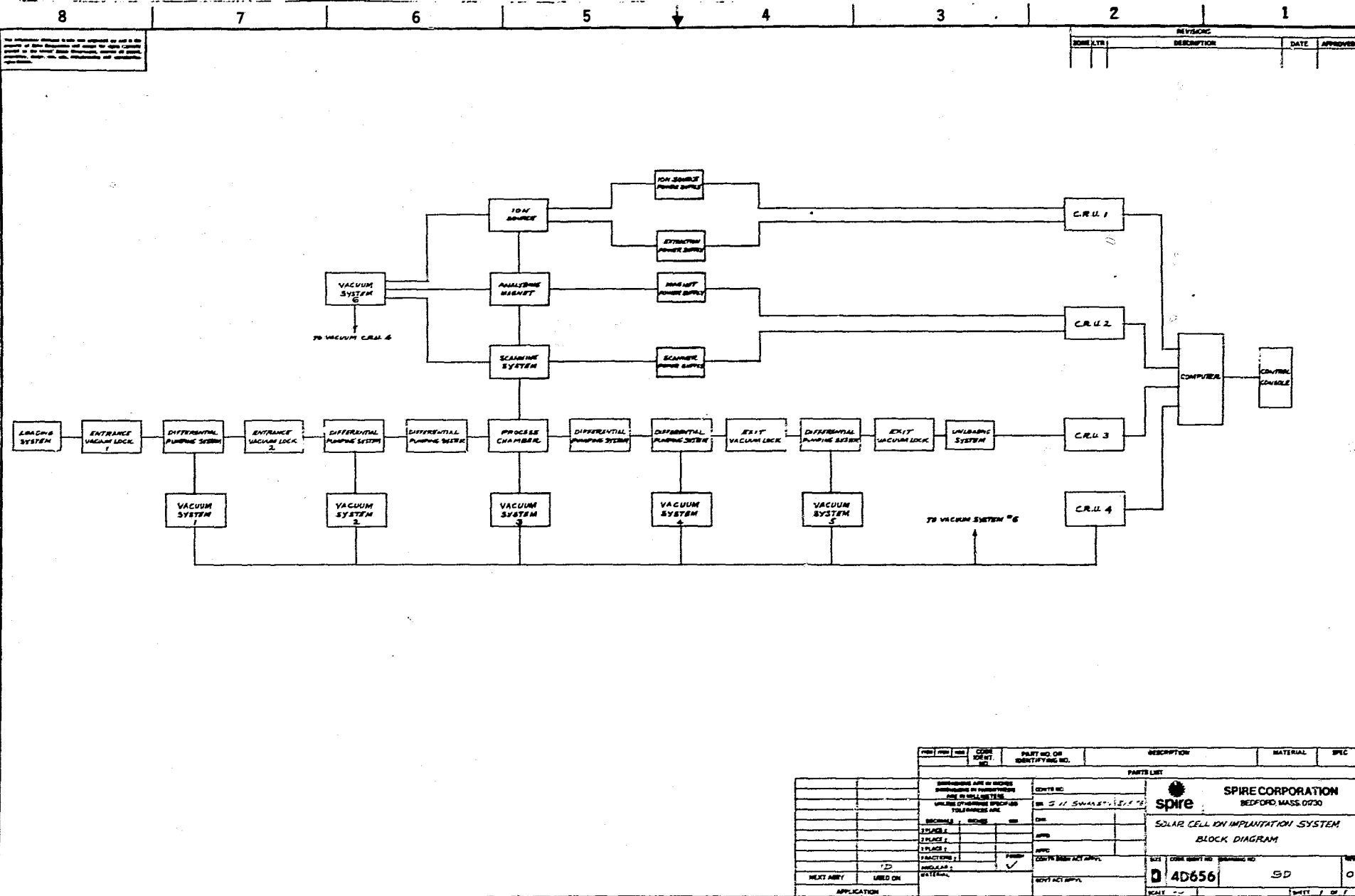
A-6

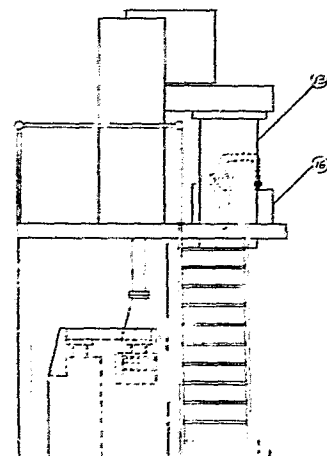
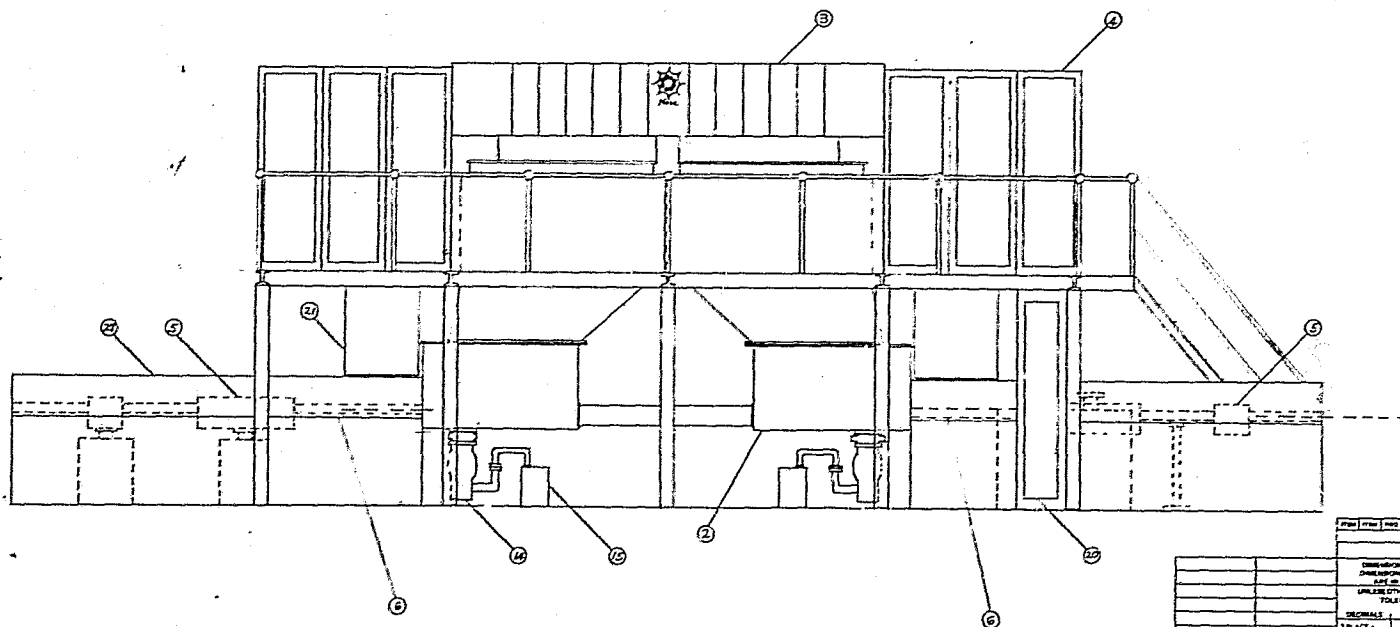


A-8



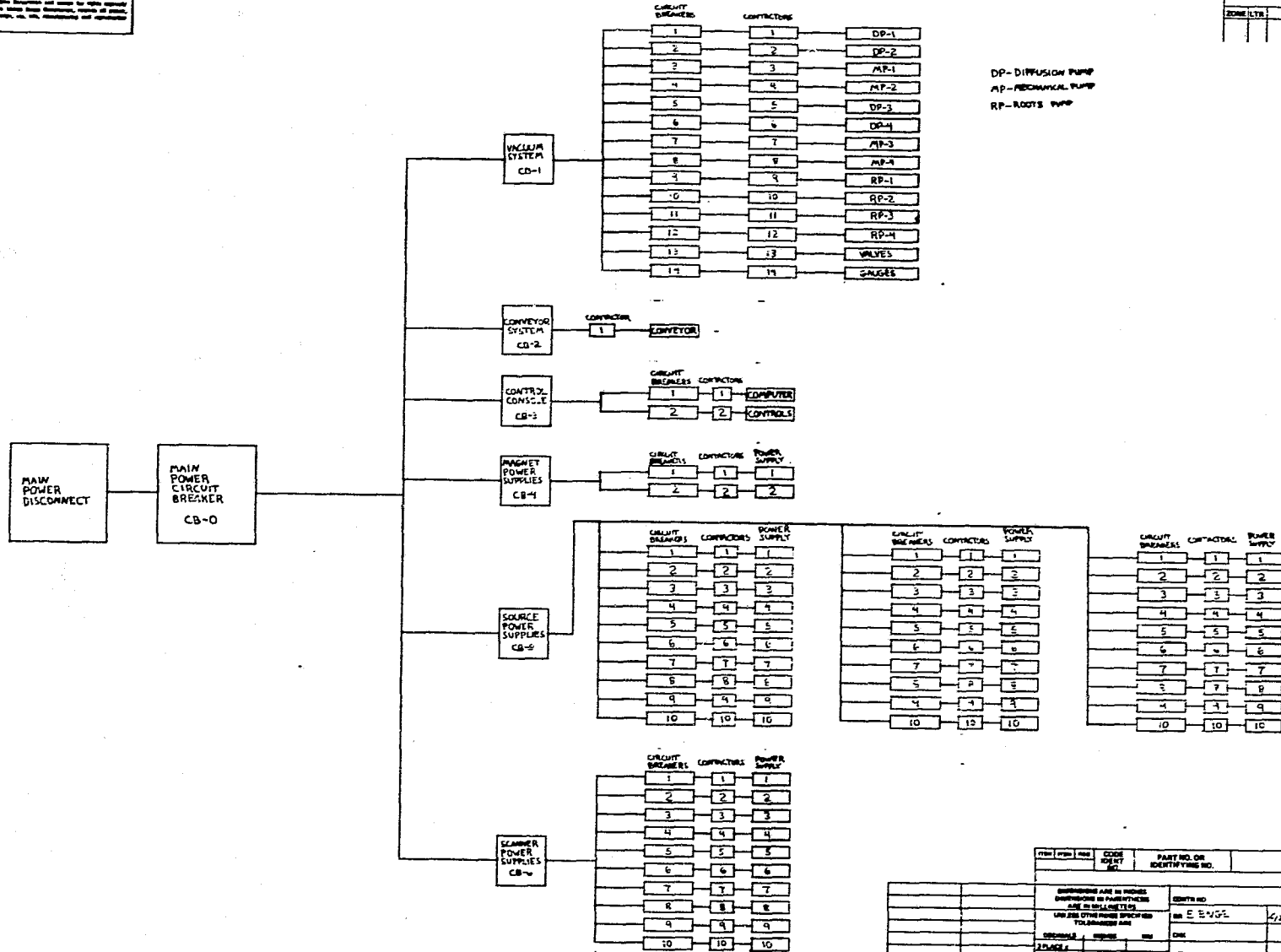
A-9




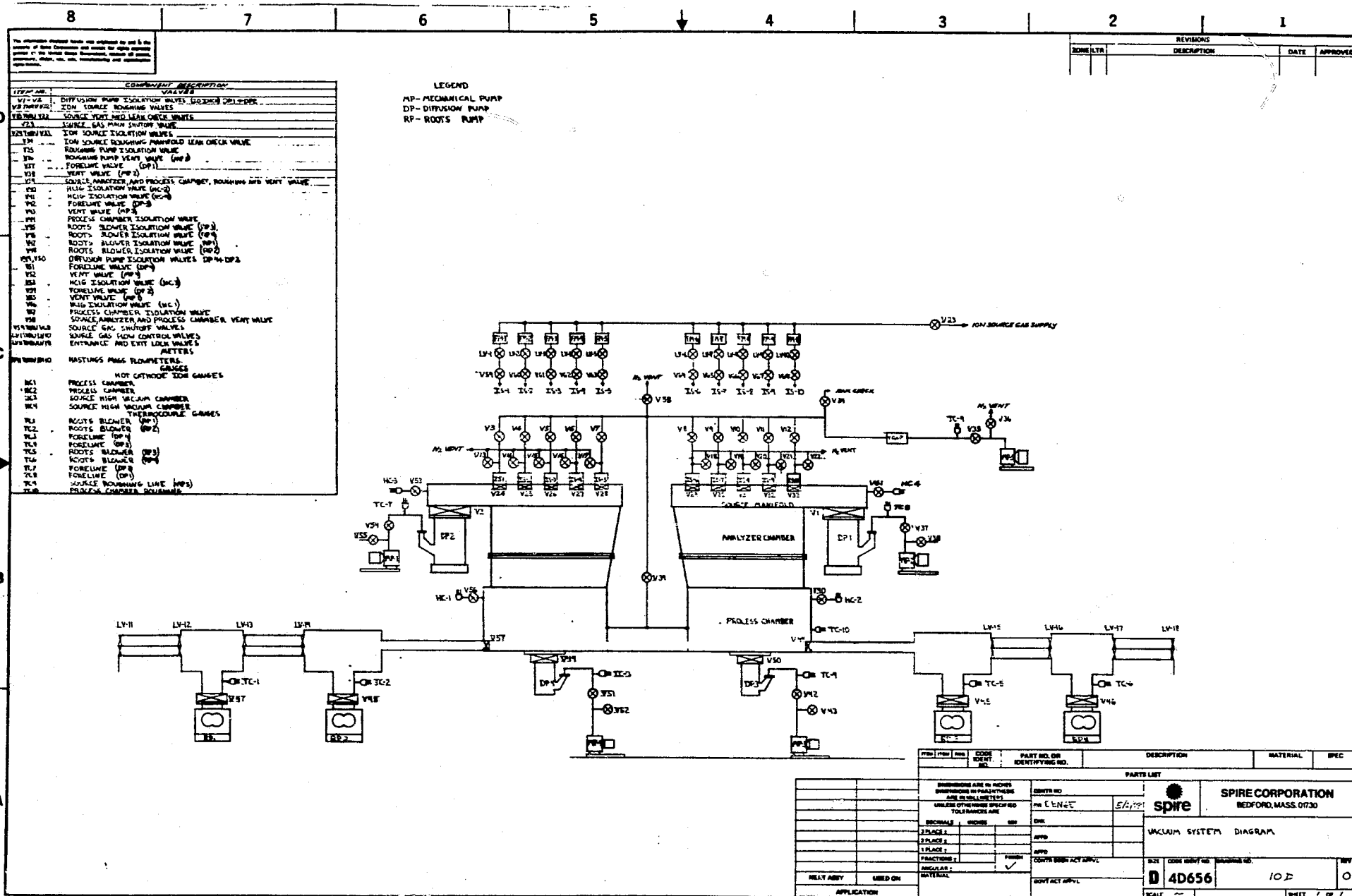
[illegible]

The Information Research Board was organized by and is the property of Spine International and except for rights expressly granted to the Library of Congress, reserves all patent, copyright, design, etc. etc. manufacturing and reproduction rights therein.

REVISIONS				
ZONE	LTR	DESCRIPTION	DATE	APPROVE



ITEM NO.	QTY	UNIT	CODE	PART NO. OR	DESCRIPTION	MATERIAL	SPEC
REQUEST				IDENTIFYING NO.			
PARTS LIST							
DIMENSIONS ARE IN INCHES DIMENSIONS IN PARENTHESES ARE IN MILLIMETERS USE ONE OR OTHER POWER SPECIFIC TOLERANCES ARE				COUNTRY NO.	SPIRE CORPORATION BEDFORD, MASS. 01730		
2 PLACES				ONE	 BLOCK DIAGRAM, OF POWER DISTRIBUTION		
2 PLACES				APPRO			
1 PLACE				APPRO			
2 PLACES				APPRO			
APPRO				APPRO			
NEXT ASBY				USED ON	SIZE: D 4D656 CASH IDENT NO.: 11D REV: 0		
APPLICATION							
SCALE: SHEET 1 OF 1							



APPENDIX B

**TABULAR DATA FOR (500) CELLS
DELIVERED TO JPL
WITH ION IMPLANTED n^+/pp^+ STRUCTURES**

AM0-25°C Characteristics

Cell #	Isc (mA)	Voc (mV)	I (at 490 mv) (mA)	P ₄₉₀ (mW)	Efficiency (%)	Comments
1	1858	591	1670	818.3	13.3	
2	1790	593	1640	803.6	13.1	
3	1839	595	1660	813.4	13.3	
4	1878	598	1720	842.8	13.7	
5	1849	596	1670	818.3	13.3	
6	1895	597	1750	857.5	14.0	
7	1829	596	1660	813.4	13.3	
8	1894	596	1750	857.5	14.0	
9	1768	591	1460	715.4	11.7	
10	1834	592	1660	813.4	13.3	
11	1867	596	1650	823.2	13.4	
12	1869	597	1720	842.8	13.7	
13	1864	594	1690	828.1	13.5	
14	1832	594	1670	818.3	13.3	
15	1769	594	1560	764.4	12.5	
16	1884	598	1740	852.6	13.9	
17	1873	598	1710	837.9	13.7	
18	1778	590	1510	739.9	12.1	
19	1840	591	1660	813.4	13.3	
20	1807	591	1590	779.1	12.7	
21	1850	595	1700	833.0	13.6	
22	1800	594	1640	803.6	13.1	
23	1817	597	1670	818.3	13.3	
24	1865	594	1680	823.2	13.4	
25	1847	597	1650	808.5	13.2	
26	1844	595	1680	823.2	13.4	
27	1858	596	1660	813.4	13.3	
28	1803	595	1650	808.5	13.2	
29	1847	591	1620	793.8	12.9	
30	1835	596	1720	842.8	13.7	
31	1882	596	1720	842.8	13.7	
32	1873	597	1720	842.8	13.7	
33	1898	595	1740	852.6	13.9	
34	1886	597	1700	833.0	13.6	
35	1765	593	1540	754.6	12.3	
36	1889	598	1740	852.6	13.9	
37	1845	595	1650	808.5	13.2	
38	1817	594	1580	774.2	12.6	
39	1812	595	1600	784.0	12.8	
40	1867	590	1690	828.1	13.5	
41	1839	596	1680	823.2	13.4	
42	1875	598	1650	808.5	13.2	
43	1778	594	1580	774.2	12.6	
44	1888	598	1730	847.7	13.8	
45	1896	595	1710	837.9	13.7	
46	1783	594	1575	771.7	12.6	
47	1834	595	1640	803.6	13.1	

AM0-25°C Characteristics

Cell #	Isc (mA)	Voc (mV)	I (at 490 mv) (mA)	P ₄₉₀ (mW)	Efficiency (%)	Comments
48	1844	592	1620	793.8	12.9	
49	1821	592	1640	803.6	13.1	
50	1866	595	1720	842.8	13.7	
51	1823	596	1660	813.4	13.3	
52	1800	593	1620	793.8	12.9	
53	1823	594	1660	813.4	13.3	
54	1802	594	1620	793.8	12.9	
55	1842	597	1510	739.9	12.1	
56	1850	596	1600	784.0	12.8	
57	1750	588	1590	779.1	12.7	
58	1800	595	1620	793.8	12.9	
59	1742	594	1520	774.2	12.6	
60	1785	593	1620	793.8	12.9	
61	1792	593	1640	803.6	13.1	
62	1759	593	1620	793.8	12.9	
63	1734	593	1590	681.1	11.1	
64	1817	593	1640	803.6	13.1	
65	1775	590	1620	793.8	12.9	
66	1742	591	1570	769.3	12.5	
67	1762	597	1550	759.5	12.4	
68	1750	588	1550	759.5	12.4	
69	1762	596	1600	784.0	12.8	
70	1750	588	1560	764.4	12.5	
71	1753	592	1500	735.0	12.0	
72	1778	591	1620	793.8	12.9	
73	1749	594	1530	749.7	12.2	
74	1740	592	1530	749.7	12.2	
75	1732	591	1520	744.8	12.1	
76	1790	588	1620	793.8	12.9	
77	1750	591	1590	779.1	12.7	
78	1820	596	1640	803.6	13.1	
79	1822	593	1660	813.4	13.3	
80	1730	591	1540	754.6	12.3	
81	1768	590	1580	774.2	12.6	
82	1781	590	1600	784.0	12.8	
83	1806	589	1620	793.8	12.9	
84	1860	595	1680	823.2	13.4	
85	1758	588	1480	725.2	11.8	
86	1783	590	1600	784.0	12.8	
87	1815	593	1620	793.8	12.9	
88	1850	597	1680	823.2	13.4	
89	1738	594	1400	686.0	11.2	
90	1800	590	1640	803.6	13.1	
91	1865	597	1680	823.2	13.4	
92	1868	597	1680	823.2	13.4	
93	1789	592	1580	774.2	12.6	
94	1767	592	1580	774.2	12.6	
95	1837	595	1660	813.4	13.3	
96	1832	595	1640	803.6	13.1	

AM0-25°C Characteristics

Cell #	Isc (mA)	Voc (mV)	I (at 490 mv) (mA)	P ₄₉₀ (mW)	Efficiency (%)	Comments
97	1700	588	1420	695.8	11.3	
98	1840	595	1680	823.2	13.4	
99	1838	596	1640	803.6	13.1	
100	1847	596	1640	803.6	13.1	
101	1809	588	1600	784.0	12.8	
102	1814	588	1640	803.6	13.1	
103	1849	597	1650	808.5	13.2	
104	1780	591	1640	803.6	13.1	
105	1800	595	1600	784.0	12.8	
106	1826	596	1650	808.5	13.2	
107	1809	595	1620	793.8	12.9	
108	1755	591	1520	744.8	12.1	
109	1735	590	1450	710.5	11.6	
110	1821	595	1620	793.8	12.9	
111	1746	588	1400	686.0	11.2	
112	1798	594	1600	784.0	12.8	
113	1811	595	1630	798.7	13.0	
114	1656	585	1320	646.8	10.5	
115	1790	595	1600	784.0	12.8	
116	1803	595	1620	793.8	12.9	
117	1825	595	1650	808.5	13.2	
118	1815	595	1640	803.6	13.1	
119	1807	594	1600	784.0	12.8	
120	1817	593	1630	798.7	13.0	
121	1759	593	1560	764.4	12.5	
122	1820	597	1660	813.4	13.3	
123	1820	594	1620	793.8	12.9	
124	1770	590	1570	769.3	12.5	
125	1827	595	1600	784.0	12.8	
126	1760	591	1630	798.7	13.0	
127	1800	594	1600	784.0	12.8	
128	1836	590	1670	818.3	13.3	
129	1820	595	1630	798.7	13.0	
130	1846	597	1630	798.7	13.0	
131	1830	588	1630	798.7	13.0	
132	1850	595	1630	798.7	13.0	
133	1840	590	1600	784.0	12.8	
134	1798	596	1620	793.8	12.9	
135	1893	597	1720	842.8	13.7	
136	1830	593	1520	744.8	12.1	
137	1822	588	1590	779.1	12.7	
138	1760	584	1480	725.2	11.8	
139	1784	588	1600	784.0	12.8	
140	1893	596	1690	828.1	13.5	
141	1835	595	1650	808.5	13.2	
142	1907	596	1680	823.2	13.3	
143	1895	600	1760	862.4	14.0	
144	1955	600	1600	784.0	12.7	

AM0-25°C Characteristics

Cell #	Isc (mA)	Voc (mV)	I (at 490 mv) (mA)	P ₄₉₀ (mW)	Efficiency (%)	Comments
145	1954	595	1780	872.2	14.1	No flat
146	1924	595	1740	852.6	13.8	No flat
147	1943	600	1780	872.2	14.1	No flat
148	1916	595	1740	852.6	13.8	No flat
149	1930	599	1760	862.4	14.0	No flat
150	1930	595	1740	852.6	13.8	No flat
151	1864	593	1650	808.5	13.1	No flat
152	1927	594	1740	852.6	13.8	No flat
153	1921	598	1760	862.4	14.0	No flat
154	1890	595	1660	813.4	13.2	No flat
155	1890	594	1700	833.0	13.5	No flat
156	1935	597	1580	774.2	12.5	No flat
157	1912	594	1720	842.8	13.7	No flat
158	1914	595	1560	764.4	12.4	No flat
159	1775	594	1580	774.2	12.6	
160	1777	595	1600	784.0	12.8	
161	1794	596	1580	774.2	12.6	
162	1745	592	1500	735.0	12.0	
163	1750	594	1500	735.0	12.0	
164	1772	592	1430	700.7	11.4	
165	1848	595	1700	833.0	13.6	
166	1788	595	1600	784.0	12.8	
167	1850	596	1700	833.0	13.6	
168	1853	595	1700	833.0	13.6	
169	1770	593	1600	784.0	12.8	
170	1870	595	1680	823.2	13.4	
171	1855	596	1680	823.2	13.4	
172	1774	593	1580	774.2	12.6	
173	1805	596	1620	793.8	12.9	
174	1769	588	1500	735.0	12.0	
175	1766	592	1530	749.7	12.2	
176	1844	596	1680	833.0	13.6	
177	1818	593	1680	823.2	13.4	
178	1860	597	1700	833.0	13.6	
179	1800	595	1620	793.8	12.9	
180	1733	591	1500	735.0	12.0	
181	1825	596	1660	813.4	13.3	
182	1780	590	1580	774.2	12.6	
183	1824	596	1640	803.6	13.1	
184	1820	596	1680	823.2	13.4	
185	1852	597	1720	842.8	13.7	
186	1835	595	1660	813.4	13.3	
187	1850	597	1700	833.0	13.6	
188	1780	592	1540	754.6	12.3	
189	1837	595	1690	828.1	13.5	
190	1811	594	1640	803.6	13.1	
191	1836	595	1690	828.1	13.5	
192	1816	595	1640	803.6	13.1	

AM0-25°C Characteristics

Cell #	Isc (mA)	Voc (mV)	I (at 490 mv) (mA)	P ₄₉₀ (mW)	Efficiency (%)	Comments
193	1844	594	1630	798.7	13.0	
194	1816	597	1680	823.2	13.4	
195	1849	596	1700	833.0	13.6	
196	1830	591	1600	784.0	12.8	
197	1837	594	1620	793.8	12.9	
198	1852	596	1720	842.8	13.7	
199	1799	594	1600	784.0	12.8	
200	1750	593	1540	754.6	12.3	
201	1790	592	1580	774.2	12.6	
202	1818	594	1640	803.6	13.1	
203	1840	597	1640	803.6	13.1	
204	1813	594	1640	803.6	13.1	
205	1800	595	1620	793.8	12.9	
206	1848	596	1680	823.2	13.4	
207	1859	596	1700	833.0	13.6	
208	1749	589	1480	725.2	11.8	
209	1748	591	1540	754.6	12.3	
210	1840	595	1660	813.4	13.3	
211	1809	595	1620	793.8	12.9	
212	1790	592	1600	784.0	12.8	
213	1863	599	1720	842.8	13.7	
214	1850	596	1700	833.0	13.6	
215	1772	593	1600	784.0	12.8	
216	1780	599	1600	784.0	12.8	
217	1772	591	1560	764.4	12.5	
218	1762	588	1520	744.8	12.1	
219	1853	595	1680	823.2	13.4	
220	1863	597	1670	818.3	13.3	
221	1850	595	1640	803.6	13.1	
222	1748	593	1580	774.2	12.6	
223	1825	596	1660	813.4	13.3	
224	1860	596	1660	813.4	13.3	
225	1800	596	1620	793.8	12.9	
226	1860	597	1720	842.8	13.7	
227	1808	594	1560	764.4	12.5	
228	1800	596	1640	803.6	13.1	
229	1785	592	1600	784.0	12.8	
230	1788	592	1600	784.0	12.8	
231	1815	596	1660	813.4	13.3	
232	1784	595	1640	803.6	13.1	
233	1792	595	1630	798.7	13.0	
234	1800	595	1650	808.5	13.2	
235	1748	594	1575	771.7	12.6	
236	1840	594	1660	813.4	13.3	
237	1845	597	1650	808.5	13.2	
238	1807	594	1620	793.8	12.9	
239	1823	597	1680	823.2	13.4	
240	1840	597	1700	833.0	13.6	

AM0-25°C Characteristics

Cell #	Isc (mA)	Voc (mV)	I (at 490 mv) (mA)	P ₄₉₀ (mW)	Efficiency (%)	Comments
241	1827	595	1670	818.3	13.3	
242	1785	595	1620	793.8	12.9	
243	1850	595	1700	833.0	13.6	
244	1772	594	1560	764.4	12.5	
245	1849	597	1700	833.0	13.6	
246	1840	594	1679	818.3	13.3	
247	1822	596	1700	833.0	13.6	
248	1827	597	1700	833.0	13.6	
249	1800	596	1620	793.8	12.9	
250	1789	594	1610	788.9	12.9	
251	1762	593	1590	779.1	12.7	
252	1799	596	1600	784.0	12.8	
253	1788	595	1620	793.8	12.9	
254	1800	596	1640	803.6	13.1	
255	1750	594	1570	769.3	12.5	
256	1795	594	1640	803.6	13.1	
257	1788	597	1540	754.6	12.3	
258	1780	595	1610	788.9	12.9	
259	1811	593	1640	803.6	13.1	
260	1829	595	1640	803.6	13.1	
261	1842	596	1700	833.0	13.6	
262	1840	594	1650	808.5	13.2	
263	1835	591	1600	784.0	12.8	
264	1819	590	1580	774.2	12.6	
265	1840	596	1690	828.1	13.5	
266	1820	597	1680	823.2	13.4	
267	1830	597	1690	828.1	13.5	
268	1856	596	1730	847.7	13.8	
269	1810	595	1630	798.7	13.0	
270	1834	594	1680	823.2	13.4	
271	1823	595	1660	813.4	13.3	
272	1830	596	1640	803.6	13.1	
273	1823	597	1640	803.6	13.1	
274	1770	593	1630	798.7	13.0	
275	1832	594	1660	813.4	13.3	
276	1863	595	1720	842.8	13.7	
277	1818	596	1650	808.5	13.2	
278	1839	595	1700	833.0	13.6	
279	1825	594	1640	803.6	13.1	
280	1820	596	1650	808.5	13.2	
281	1800	595	1600	784.0	12.8	
282	1839	597	1680	823.2	13.4	
283	1778	592	1600	784.0	12.8	
284	1800	592	1570	769.3	12.5	
285	1771	591	1530	749.7	12.2	
286	1852	594	1670	803.6	13.1	
287	1800	595	1560	764.4	12.5	
288	1854	597	1700	833.0	13.6	

AM0-25°C Characteristics

Cell #	Isc (mA)	Voc (mV)	I (at 490 mv) (mA)	P ₄₉₀ (mW)	Efficiency (%)	Comments
289	1824	595	1660	813.4	13.3	
290	1812	596	1670	818.3	13.3	
291	1834	595	1650	808.5	13.2	
292	1775	590	1530	749.7	12.2	
293	1800	594	1630	798.7	13.0	
294	1814	596	1670	818.3	13.3	
295	1800	595	1470	720.3	11.7	
296	1782	596	1630	798.7	13.0	
297	1831	594	1660	813.4	13.3	
298	1790	595	1620	793.8	12.9	
299	1775	593	1600	784.0	12.8	
300	1830	596	1670	818.3	13.3	
301	1845	595	1590	779.1	12.7	
302	1815	595	1630	798.7	13.0	
303	1818	596	1640	803.6	13.1	
304	1821	596	1650	808.5	13.2	
305	1766	592	1530	749.7	12.2	
306	1825	593	1640	803.6	13.1	
307	1816	596	1670	818.3	13.3	
308	1755	592	1600	784.0	12.8	
309	1850	596	1700	833.0	13.6	
310	1850	595	1690	828.1	13.5	
311	1789	589	1540	754.6	12.3	
312	1832	594	1590	779.1	12.7	
313	1810	596	1650	808.5	13.2	
314	1816	593	1620	793.8	12.9	
315	1825	593	1620	793.8	12.9	
316	1862	598	1710	837.9	13.7	
317	1828	593	1660	813.4	13.2	No flat
318	1880	598	1730	847.7	13.7	No flat
319	1800	593	1640	803.6	13.1	
320	1849	597	1690	828.1	13.4	No flat
321	1895	600	1730	847.7	13.7	No flat
322	1888	595	1690	828.1	13.4	No flat
323	1872	598	1700	833.0	13.5	No flat
324	1852	600	1630	798.7	12.9	No flat
325	1744	592	1540	754.6	12.3	
326	1800	597	1620	793.8	12.9	
327	1767	586	1580	774.2	12.6	
328	1811	593	1660	813.4	13.3	
329	1800	597	1660	813.4	13.3	
330	1875	595	1670	818.3	13.3	No flat
331	1800	594	1600	784.0	12.7	No flat
332	1910	600	1730	847.7	13.7	No flat
333	1912	599	1740	852.6	13.8	No flat
334	1870	598	1720	842.8	13.7	No flat
335	1812	596	1620	793.8	12.9	
336	1869	598	1680	823.2	13.4	

AM0-25°C Characteristics

Cell #	Isc (mA)	Voc (mV)	I (at 490 mv) (mA)	P490 (mW)	Efficiency (%)	Comments
337	1880	595	1700	833.0	13.5	No flat
338	1839	593	1670	818.3	13.3	No flat
339	1828	594	1550	759.5	12.4	
340	1800	595	1520	744.8	12.1	
341	1800	594	1580	774.2	12.5	No flat
342	1865	592	1610	788.9	12.8	No flat
343	1840	594	1600	784.0	12.7	No flat
344	1844	595	1600	784.0	12.7	No flat
345	1800	594	1620	793.8	12.9	
346	1860	598	1700	833.0	13.5	No flat
347	1754	591	1550	759.5	12.4	
348	1768	594	1620	793.8	13.0	
349	1768	591	1490	730.1	11.9	
350	1799	594	1580	774.2	12.6	
351	1718	585	1550	759.5	12.4	
352	1750	591	1500	735.0	12.0	
353	1830	596	1690	828.1	13.5	
354	1798	595	1600	784.0	12.8	
355	1800	595	1630	798.7	13.0	
356	1777	588	1570	769.3	12.5	
357	1812	590	1640	803.6	13.1	
358	1818	594	1610	788.9	12.9	
359	1770	588	1420	695.8	11.3	
360	1823	594	1670	818.3	13.3	
361	1832	596	1540	774.2	12.6	
362	1790	597	1600	784.0	12.8	
363	1785	595	1590	779.1	12.7	
364	1800	589	1530	749.7	12.2	
365	1824	595	1650	808.5	13.2	
366	1820	594	1680	823.2	13.4	
367	1786	590	1530	749.7	12.2	
368	1860	596	1700	833.0	13.6	
369	1722	590	1470	720.3	11.7	
370	1795	591	1530	749.7	12.2	
371	1815	594	1590	779.1	12.7	
372	1815	589	1640	803.6	13.1	
373	1846	595	1680	823.2	13.4	
374	1877	598	1710	837.9	13.7	
375	1823	594	1610	788.9	12.9	
376	1735	582	1550	759.5	12.4	
377	1794	592	1550	759.5	12.4	
378	1778	593	1560	764.4	12.5	
379	1840	595	1660	813.4	13.3	
380	1797	589	1610	788.9	12.9	
381	1768	591	1500	735.0	12.0	
382	1822	596	1660	813.4	13.3	
383	1789	595	1600	784.0	12.8	
384	1780	594	1580	774.2	12.6	

AM0-25°C Characteristics

Cell #	Isc (mA)	Voc (mV)	I (at 490 mv) (mA)	P ₄₉₀ (mW)	Efficiency (%)	Comments
385	1722	591	1500	735.0	12.0	
386	1790	595	1600	784.0	12.8	
387	1840	595	1600	813.4	13.3	
388	1795	596	1620	793.8	12.9	
389	1800	593	1640	803.6	13.1	
390	1790	587	1600	784.0	12.8	
391	1785	597	1600	784.0	12.8	
392	1829	594	1660	813.4	13.3	
393	1777	586	1560	764.4	12.5	
394	1803	593	1640	803.6	13.1	
395	1789	597	1620	793.8	12.9	
396	1833	596	1690	828.1	13.5	
397	1786	592	1640	803.6	13.1	
398	1779	594	1590	779.1	12.7	
399	1800	593	1610	788.9	12.9	
400	1819	595	1680	823.2	13.4	
401	1740	584	1540	754.6	12.3	
402	1800	592	1590	779.1	12.7	
403	1789	590	1560	764.4	12.5	
404	1765	592	1530	749.7	12.2	
405	1798	597	1630	798.7	13.0	
406	1789	596	1640	803.6	13.1	
407	1715	585	1540	754.6	12.3	
408	1860	597	1680	823.2	13.4	
409	1788	596	1620	793.8	12.9	
410	1750	587	1480	725.2	11.8	
411	1815	593	1580	774.2	12.6	
412	1850	594	1700	833.0	13.6	
413	1850	597	1700	833.0	13.6	
414	1830	597	1660	813.4	13.3	
415	1820	595	1650	808.5	13.2	
416	1846	595	1670	818.3	13.3	
417	1750	593	1550	759.5	12.4	
418	1752	594	1580	774.2	12.6	
419	1840	595	1620	793.8	12.9	
420	1850	596	1670	818.3	13.3	
421	1780	591	1520	744.8	12.1	
422	1790	594	1620	793.8	12.9	
423	1780	595	1610	788.9	12.9	
424	1780	594	1600	784.0	12.8	
425	1782	596	1650	808.5	13.2	
426	1830	597	1670	818.3	13.3	
427	1782	596	1620	793.8	12.9	
428	1790	594	1560	764.4	12.5	
429	1780	594	1600	784.0	12.8	
430	1790	592	1600	784.0	12.8	
431	1818	594	1650	808.5	13.2	
432	1772	592	1580	774.2	12.6	

AM0-25°C Characteristics

Cell #	Isc (mA)	Voc (mV)	I (at 490 mv) (mA)	P ₄₉₀ (mW)	Efficiency (%)	Comments
433	1850	593	1630	798.7	13.0	
434	1820	594	1670	818.3	13.3	
435	1785	592	1520	744.8	12.1	
436	1814	593	1620	793.8	12.9	
437	1844	597	1640	803.6	13.1	
438	1865	598	1730	847.7	13.8	
439	1789	595	1620	793.8	12.9	
440	1800	595	1620	793.8	12.9	
441	1838	594	1670	818.3	13.3	
442	1760	590	1550	759.5	12.4	
443	1800	596	1660	813.4	13.3	
444	1688	591	1520	744.8	12.1	
445	1770	593	1590	779.1	12.7	
446	1700	594	1520	744.8	12.1	
447	1735	592	1560	764.4	12.5	
448	1746	590	1550	759.5	12.4	
449	1750	594	1600	784.0	12.8	
450	1690	594	1540	754.6	12.3	
451	1713	592	1550	759.5	12.4	
452	1721	592	1450	744.8	12.1	
453	1597	592	1450	710.5	11.6	
454	1544	588	1380	676.2	11.0	
455	1590	592	1430	700.7	11.4	
456	1626	594	1500	735.0	12.0	
457	1578	590	1430	700.7	11.4	
458	1555	592	1410	690.9	11.3	
459	1560	592	1420	695.8	11.3	
460	1589	590	1440	705.6	11.5	
461	1567	592	1410	690.9	11.3	
462	1519	589	1380	676.2	11.0	
463	1565	593	1410	690.9	11.3	
464	1546	592	1430	700.7	11.4	
465	1584	592	1440	705.6	11.5	
466	1750	591	1520	744.8	12.1	
467	1820	590	1640	803.6	13.1	
468	1600	594	1450	710.5	11.6	
469	1594	593	1470	720.3	11.7	
470	1574	590	1370	671.3	10.9	
471	1550	590	1390	681.1	11.1	
472	1536	593	1380	676.2	11.0	
473	1833	593	1680	823.2	13.4	
474	1560	591	1420	695.8	11.3	
475	1620	593	1500	735.0	12.0	
476	1800	588	1670	818.3	13.3	
477	1602	590	1440	705.6	11.5	
478	1619	590	1460	715.4	11.7	
479	1882	597	1720	842.8	13.7	
480	1770	589	1590	779.1	12.7	

AM0-25°C Characteristics

Cell #	Isc (mA)	Voc (mV)	I (at 490 mv) (mA)	P ₄₉₀ (mW)	Efficiency (%)	Comments
481	1531	590	1380	676.2	11.0	
482	1576	592	1420	695.8	11.3	
483	1570	592	1420	695.8	11.3	
484	1596	593	1460	715.4	11.7	
485	1566	588	1380	676.2	11.0	
486	1600	592	1470	720.3	11.7	
487	1566	590	1370	671.3	10.9	
488	1800	591	1650	808.5	13.2	
489	1550	591	1380	676.2	11.0	
490	1600	594	1460	715.4	11.7	
491	1754	589	1560	764.4	12.5	
492	1584	590	1440	705.6	11.5	
493	1570	592	1440	705.6	11.5	
494	1820	593	1670	818.3	13.3	
495	1829	591	1560	764.4	12.5	
496	1810	594	1590	779.1	12.7	
497	1808	590	1620	793.8	12.9	
498	1842	593	1620	793.8	12.9	
499	1850	592	1600	784.0	12.8	
500	1800	591	1540	754.6	12.3	

APPENDIX C

TABULAR DATA FOR CELL MANUFACTURING PROCESS COMPARISON WITH 1-ohm-cm SILICON

TEST I
DIFFUSED JUNCTIONS AM0-25°C CHARACTERISTICS

Cell No.	V _{oc} (mV)	I _{sc} (mA)	I ₄₈₀ (mA)	P ₄₈₀ (mW)	η (%)
1	598	144.1	135.5	65.0	12.0
2	595	146.3	135.9	65.2	12.0
3	599	148.5	140.3	67.3	12.4
4	598	147.5	137.8	66.1	12.2
5	598	151.0	136.8	65.6	12.1
6	599	149.0	140.7	67.5	12.4
7	594	148.4	133.6	64.1	11.8
8	562	145.5	66.5	31.9	5.8
9	593	147.3	130.4	62.5	11.5
10	594	147.5	134.0	64.3	11.8
11	599	146.9	137.9	66.1	12.2
12	600	148.9	142.2	68.2	12.6
13	595	147.7	134.5	64.5	11.9
14	598	147.5	139.5	66.9	12.3
15	597	142.7	135.2	64.8	11.9
16	599	147.5	138.5	66.4	12.2
17	594	147.5	131.0	62.8	11.6
18	592	149.4	129.5	62.1	11.4
19	593	149.0	135.5	65.0	12.0
20	595	147.9	130.4	62.5	11.5
21	588	147.9	127.7	61.2	11.3
22	601	148.6	141.8	68.0	12.5
23	599	148.2	142.2	68.2	12.6
24	598	148.5	141.2	67.7	12.5
25	596	147.5	132.2	63.4	11.7
26	601	149.5	141.5	67.9	12.5
27	596	146.5	136.3	65.4	12.0
28	597	145.6	138.4	66.4	12.2
29	595	147.6	134.7	64.6	11.9
30	596	146.4	136.8	65.6	12.1
31	600	149.9	142.4	68.3	12.6
32	600	150.8	143.0	68.6	12.6
33	599	148.9	132.3	63.5	11.7
34	601	151.8	145.4	69.79	12.9
35	598	147.7	140.0	67.2	12.4
36	596	146.9	134.8	64.7	11.9
37	599	148.1	140.2	67.2	12.4
38	595	147.5	134.0	64.3	11.8
39	600	150.2	143.5	68.8	12.7
40	599	148.2	136.5	65.5	12.1
41	597	144.8	135.7	65.1	12.0
42	595	148.1	134.7	64.6	11.9
43	600	146.2	138.0	66.2	12.2
44	595	147.0	135.0	64.8	11.9

TEST I (Continued)

Cell No.	V _{oc} (mV)	I _{sc} (mA)	I ₄₈₀ (mA)	P ₄₈₀ (mW)	η (%)
45	600	151.5	143.2	68.7	12.7
46	591	143.1	112.3	53.9	9.9
47	590	142.4	130.6	62.6	11.5
48	596	145.2	135.6	65.0	12.0
49	595	146.7	132.6	63.6	11.7
50	597	148.7	142.4	68.3	12.6
51	600	146.9	140.2	67.2	12.4
52	597	149.0	140.0	67.2	12.4
53	598	148.2	138.9	66.6	12.3
54	598	148.8	139.6	67.0	12.3
55	598	146.7	138.7	66.5	12.3
56	599	147.4	137.1	65.8	12.1
57	597	148.7	139.4	66.9	12.3
58	598	147.7	140.6	67.4	12.4
59	595	146.0	136.0	65.2	12.0
60	601	148.4	141.0	67.6	12.5
61	595	144.4	136.7	65.6	12.1
62	597	147.5	137.6	66.0	12.2
63	598	145.6	138.5	66.5	12.2
64	599	148.3	142.4	68.3	12.6
65	600	151.3	142.7	68.4	12.6
66	600	149.6	141.2	67.7	12.5
67	597	148.2	136.7	65.6	12.1
68	600	148.0	140.0	67.2	12.4
69	597	148.3	139.4	66.9	12.3
70	598	146.3	138.0	66.2	12.2
71	595	146.0	133.9	64.2	11.8
72	597	148.4	141.0	67.6	12.5
73	591	147.6	127.5	61.2	11.2
74	599	150.4	141.9	68.1	12.5
75	594	147.0	126.9	60.9	11.2
76	597	148.2	138.5	66.4	12.2
77	599	150.5	140.7	67.5	12.4
78	592	142.5	132.0	63.3	11.7
79	599	148.5	138.8	66.6	12.3
80	596	147.7	131.9	63.3	11.6
81	600	147.6	140.9	67.6	12.4
82	599	148.6	139.3	66.8	12.3
83	593	142.6	133.0	63.8	11.7
84	599	146.6	139.5	66.9	12.3
85	595	149.2	134.4	64.5	11.9
86	592	147.4	133.1	63.8	11.8
87	598	148.7	140.5	67.4	12.4
88	599	149.7	141.3	67.8	12.5
89	592	145.7	120.9	58.0	10.7

TEST IIA
IMPLANTED/FURNACE ANNEALED JUNCTIONS
AM0-25°C CHARACTERISTICS

Cell No.	V _{oc} (mV)	I _{sc} (mA)	I ₄₈₀ (mA)	P ₄₈₀ (mW)	η (%)
1	576	139.4	123.3	59.1	10.9
2	576	142.7	110.9	53.2	9.9
3	591	149.9	133.9	64.2	11.8
4	592	151.2	134.5	64.5	11.9
5	586	150.2	128.5	61.6	11.4
6	568	140.6	96.8	46.4	8.2
7	582	147.0	120.4	57.7	10.7
8	590	151.0	129.6	62.2	11.5
9	587	148.2	129.9	62.2	11.5
10	582	146.2	125.6	60.2	11.1
11	588	147.7	130.6	62.6	11.6
12	584	144.5	123.9	59.4	11.0
13	582	145.9	123.7	59.3	11.0
14	579	146.8	120.7	57.9	10.7
15	582	143.3	124.3	62.0	11.5
16	590	148.0	131.8	63.2	11.7
17	592	150.7	129.9	62.3	11.6
18	584	129.7	124.7	59.8	11.0
19	592	150.2	133.4	64.0	11.9
20	581	143.9	123.9	59.4	11.0
21	586	145.6	118.9	57.0	10.7
22	581	148.0	121.8	58.4	10.9
23	571	144.5	102.7	49.2	9.1
24	585	147.7	127.7	61.2	11.3
25	580	148.0	120.2	57.6	10.7
26	591	149.5	134.1	64.3	11.9
27	581	148.5	107.8	51.7	9.6
28	592	151.4	132.4	63.5	11.8
29	594	150.9	137.2	65.86	12.2
30	590	147.8	133.6	64.1	11.9
31	583	145.9	122.2	58.6	10.9
32	587	148.0	129.6	62.2	11.5
33	579	144.0	119.0	57.1	10.6
34	579	142.4	122.9	58.9	11.0
35	574	150.5	109.8	52.7	9.7
36	591	150.5	131.5	63.1	11.7
37	579	147.9	103.7	49.7	9.2
38	577	146.9	118.7	56.9	10.6
39	581	147.6	119.7	57.4	10.7
40	586	150.8	118.1	56.6	10.4
41	589	147.2	132.3	63.5	11.8
42	582	147.7	127.4	61.1	11.2

TEST IIA (Continued)

Cell No.	V _{oc} (mV)	I _{sc} (mA)	I ₄₈₀ (mA)	P ₄₈₀ (mW)	η (%)
43	581	146.7	118.0	56.6	10.4
44	589	148.5	131.8	63.2	11.7
45	578	147.4	117.4	56.3	10.4
46	584	146.7	128.0	61.4	11.3
47	584	150.3	125.3	60.1	11.1
48	582	147.8	120.4	57.7	10.7
49	588	148.4	131.3	63.0	11.7
50	586	144.7	128.2	61.5	11.4
51	576	144.0	107.2	51.5	9.6
52	585	149.8	127.3	61.1	11.2
53	588	150.5	129.4	62.1	11.4
54	583	147.2	126.0	60.4	11.1
55	585	147.1	120.9	58.0	10.8
56	586	146.0	122.9	58.9	10.9

TEST II
IMPLANTED/FURNACE ANNEALED JUNCTIONS
AM0-25°C CHARACTERISTICS

Cell No.	V _{oc} (mV)	I _{sc} (mA)	I ₄₈₀ (mA)	P ₄₈₀ (mW)	η (%)
1	573	149.6	99.5	47.7	8.8
2	588	143.3	130.6	62.6	11.5
3	588	147.2	133.9	64.2	11.8
4	592	143.7	134.8	64.7	11.9
5	592	150.0	135.9	65.2	12.0
6	595	152.4	139.8	67.10	12.4
7	589	147.4	127.9	51.1	9.4
8	587	147.0	132.4	63.5	11.7
9	595	149.4	133.9	64.2	11.8
10	592	151.9	132.6	63.6	11.7
11	585	145.3	126.6	60.7	11.2
12	588	145.0	130.7	62.7	11.6
13	587	148.6	123.7	59.3	11.0
14	560	149.0	81.2	38.9	7.2
15	595	152.3	136.0	65.2	12.0
16	589	147.5	130.8	62.7	11.7
17	585	146.8	126.2	60.5	11.1
18	590	150.1	134.6	64.6	11.9
19	588	150.2	129.5	62.1	11.5
20	589	147.3	132.0	63.3	11.8
21	590	149.2	132.9	63.7	11.8
22	590	149.5	127.6	61.2	11.3
23	585	146.7	127.7	61.2	11.3
24	584	146.3	127.0	60.9	11.2
25	591	151.2	131.0	62.8	11.7
26	585	147.2	100.7	48.3	8.9
27	593	150.0	134.6	64.6	11.9
28	587	147.3	130.9	62.8	11.7
29	595	151.7	136.4	65.4	12.0
30	590	147.6	130.1	62.4	11.6
31	589	148.2	125.5	60.2	11.1
32	592	152.7	133.6	64.1	11.9
33	587	146.8	133.2	63.9	11.8
34	590	148.8	125.9	60.4	11.1
35	587	151.3	114.5	54.9	10.1
36	590	147.8	133.4	64.0	11.9
37	589	148.2	132.6	63.6	11.8
38	587	146.6	132.5	63.6	11.8
39	592	151.2	132.0	63.3	11.8
40	590	149.0	133.5	64.0	11.8
41	583	147.6	118.1	56.6	10.4
42	597	153.0	141.0	67.6	12.5
43	595	152.1	135.4	64.9	12.1

TEST IIB (Continued)

Cell No.	V _{oc} (mV)	I _{sc} (mA)	I ₄₈₀ (mA)	P ₄₈₀ (mW)	η (%)
44	597	152.9	141.7	68.0	12.5
45	592	151.3	135.0	64.8	11.9
46	588	149.8	129.5	62.1	11.4
47	593	148.6	134.2	64.4	11.9
48	524	142.5	30.2	14.4	2.6
49	592	150.0	134.3	64.4	11.9
50	589	149.5	130.7	62.7	11.5
51	589	149.9	121.6	58.3	10.7
52	586	147.2	127.7	61.2	11.3
53	591	148.9	134.5	64.5	11.9
54	590	148.6	133.4	64.0	11.8
55	593	149.6	131.0	62.8	11.6
56	585	147.7	125.4	60.1	11.1
57	592	147.7	130.2	62.4	11.5
58	588	149.2	130.5	62.6	11.5

TEST III
IMPLANTED/PULSE ANNEALED JUNCTIONS
AM0-25°C CHARACTERISTICS

Cell No.	V _{oc} (mW)	I _{sc} (mA)	I ₄₈₀ (mA)	P ₄₃₀ (mW)	η (%)
1	586	132.7	121.1	58.1	10.8
2	595	147.5	135.4	64.9	12.0
3	591	144.2	128.2	61.5	11.4
4	589	139.2	123.9	59.4	11.0
5	547	141.2	100.5	48.2	8.9
6	571	135.3	109.4	52.5	9.7
7	594	146.8	138.5	66.4	12.3
8	582	144.2	123.2	59.1	11.0
9	577	146.1	109.2	52.4	9.7
10	593	147.6	137.4	65.95	12.2
11	549	139.5	72.9	34.9	6.5
12	580	138.6	116.7	56.0	10.4
13	590	143.8	128.8	61.8	11.4
14	596	147.7	136.6	65.5	12.1
15	583	147.0	116.5	55.9	10.3
16	594	144.5	130.2	62.5	11.6
17	581	151.4	121.5	58.3	10.8
18	578	138.0	114.8	55.1	10.2
19	584	146.6	126.3	58.2	10.8
20	579	144.7	114.6	55.0	10.2
21	588	144.0	128.0	61.4	11.4
22	591	148.2	127.9	51.1	9.5
23	583	147.1	129.2	62.0	11.5
24	586	143.2	126.4	60.6	11.2
25	593	147.1	129.3	62.0	11.5
26	578	142.4	110.7	55.0	10.1
27	589	148.5	128.7	61.7	11.4
28	436	115.4	6.4	3.0	0.6
29	587	142.7	125.9	60.4	11.1
30	593	146.5	135.7	65.1	12.0
31	592	148.8	129.3	62.0	11.5
32	584	145.7	118.0	56.6	10.5
33	585	135.2	117.7	47.0	8.7
34	594	146.7	135.0	64.8	12.0
35	586	143.6	128.5	61.6	11.4
36	591	149.2	132.2	63.4	11.7
37	577	143.5	113.3	54.3	10.0
38	577	144.2	123.2	59.1	11.0
39	585	143.2	111.5	53.5	9.9
40	585	144.3	125.6	60.2	11.1
41	595	145.5	135.2	64.8	12.0
42	585	135.7	119.4	57.3	10.6
43	582	144.1	124.5	61.6	11.4
44	591	144.5	131.9	63.3	11.7

TEST III (Continued)

Cell No.	V _{oc} (mV)	I _{sc} (mA)	I ₄₈₀ (mA)	P ₄₈₀ (mW)	η (%)
45	592	146.9	131.9	63.3	11.7
46	592	148.8	130.2	62.4	11.5
47	592	147.7	128.8	51.8	11.4
48	580	146.3	124.3	59.6	11.0
49	570	129.3	105.6	50.6	9.4
50	589	142.7	125.9	60.4	11.1
51	593	145.7	131.2	62.9	11.6
52	588	139.9	124.7	59.8	11.0
53	592	147.7	132.5	63.6	11.8
54	593	147.2	132.8	63.7	11.8
55	590	144.1	125.6	60.2	11.1
56	591	145.2	131.7	63.2	11.7
57	589	146.0	130.5	62.6	11.6
58	444	124.0	6.4	3.0	0.5
59	587	142.7	123.5	59.2	11.0
60	578	129.9	107.5	51.5	9.5
61	593	146.1	132.5	63.6	11.8
62	588	144.4	125.7	60.3	11.1
63	593	147.9	132.3	63.5	11.7
64	561	145.5	83.7	40.1	7.4
65	582	148.0	126.5	60.7	11.2
66	593	146.7	130.9	62.8	11.7
67	587	138.5	121.1	58.1	10.8
68	584	148.0	110.6	53.0	9.8
69	592	147.5	135.5	65.0	12.0
70	586	149.2	129.5	62.1	11.5
71	581	147.0	120.3	57.7	10.7
72	582	145.0	116.3	55.8	10.3
73	585	143.1	115.0	55.2	10.1
74	593	147.1	132.8	63.7	11.8
75	579	142.7	120.8	57.9	10.8
76	587	146.5	125.9	60.4	11.2
77	590	144.0	130.4	62.5	11.6
78	591	150.9	128.2	61.5	11.4
79	589	145.6	120.6	57.8	10.7
80	594	145.9	135.7	65.1	12.0
81	590	146.7	128.2	61.5	11.4
82	587	139.1	124.3	59.6	11.0
83	567	138.5	97.4	46.7	8.6
84	588	143.2	126.8	6.08	11.2
85	588	140.2	126.0	6.04	11.2
86	351	133.3	6.5	3.1	0.05
87	579	132.9	105.5	5.06	9.4
88	573	137.2	110.7	53.1	9.8
89	587	144.2	127.4	61.1	11.3
90	473	126.7	6.4	3.0	0.05

APPENDIX D

TABULAR DATA FOR CELL MANUFACTURING

PROCESS COMPARISON WITH

10-ohm-cm SILICON

AM0-25°C CHARACTERISTICS FOR
TYPE I, DIFFUSED JUNCTIONS,
10 ohm-cm SILICON WITH BSF

Cell No.	V _{oc} (mV)	I _{sc} (mA)	I ₄₅₀ (mA)	P ₄₅₀ (mW)	η (%)
1	593	161.0	145.6	65.5	12.1
2	589	158.4	138.5	62.3	11.5
3	584	155.4	140.7	63.3	11.7
4	594	150.7	136.5	61.4	11.3
5	593	155.3	145.2	65.3	12.1
*6					
7	585	156.4	134.8	60.7	11.2
8	588	159.5	144.4	65.0	12.0
9	589	159.0	145.9	65.6	12.1
10	585	154.2	137.3	61.8	11.4
11	590	161.7	144.0	64.8	12.0
12	586	160.2	137.5	61.9	11.4
13	592	159.5	138.8	62.5	11.5
14	589	155.0	133.4	60.0	11.1
15	589	159.0	140.5	63.2	11.7
16	588	158.7	141.5	63.7	11.8
17	584	157.0	139.7	62.9	11.6
18	592	156.7	141.2	63.5	11.7
19	592	160.0	140.2	63.1	11.6
*20					
21	592	155.9	143.5	64.6	11.9
22	588	157.7	139.9	62.9	11.6
*23					
*24					
25	589	157.4	136.1	61.2	11.3
26	588	155.8	134.1	60.3	11.1
27	587	157.3	139.0	62.5	11.5
28	594	156.0	141.5	63.7	11.8
29	585	155.6	134.7	60.6	11.2
30	590	157.6	139.3	62.7	11.6
31	590	158.4	139.2	62.6	11.6
*32					
33	590	158.1	142.2	64.0	11.8
34	586	157.1	134.3	60.4	11.2
35	592	155.1	135.0	61.4	11.3
36	592	157.8	138.0	62.1	11.5
37	589	159.2	138.8	62.5	11.5
38	587	156.1	127.4	57.3	10.6
39	583	156.1	146.2	65.8	12.1
40	595	152.5	142.4	64.1	11.8
41	599	160.5	145.2	65.3	12.1
42	596	157.6	145.2	65.3	12.1

*Cell broke.

TYPE I (Continued)

Cell No.	V _{oc} (mV)	I _{sc} (mA)	I ₄₅₀ (mA)	P ₄₅₀ (mW)	η (%)
43	599	155.0	147.0	66.1	12.2
44	595	158.2	146.5	65.9	12.2
45	588	159.6	139.6	62.8	11.6
46	590	157.2	144.0	64.8	12.0
47	594	157.7	136.8	61.6	11.4
48	590	157.1	142.0	63.9	11.8
49	592	158.9	137.8	62.0	11.4
50	593	159.9	137.2	61.7	11.4
51	589	156.9	135.0	60.7	11.2
52	593	162.0	137.0	61.6	11.4
53	593	157.6	138.3	62.2	11.5
*54					
55	592	157.2	140.3	63.1	11.7
56	593	157.0	140.5	63.2	11.7
57	589	152.2	134.3	60.4	11.2
58	593	159.0	147.2	66.2	12.2
*59					
60	591	156.0	136.7	61.5	11.4
61	579	160.4	139.5	62.8	11.6
62	590	157.7	140.5	63.2	11.7
63	590	159.0	147.4	66.5	12.3
64	590	159.6	145.0	62.2	12.0
*65					
*66					
*67					

*Cell broke.

AM0-25°C CHARACTERISTICS FOR
TYPE II, IMPLANTED/FURNACE ANNEALED JUNCTIONS
10 ohm-cm SILICON WITH BSF

Cell No.	V _{oc} (mV)	I _{sc} (mA)	I ₄₅₀ (mA)	P ₄₅₀ (mW)	η (%)
1	570	159.5	152.4	68.6	12.7
2	575	157.4	150.3	67.6	12.5
3	566	155.2	149.3	67.2	12.4
4	564	157.2	149.7	67.4	12.4
5	571	162.9	147.0	66.1	12.2
6	564	158.7	150.9	67.9	12.5
7	561	157.3	149.3	67.2	12.4
8	576	157.7	147.0	66.1	12.2
9	561	157.3	150.6	67.8	12.5
10	567	153.8	149.4	67.2	12.4
11	561	155.5	138.9	62.5	11.5
*12					
13	559	158.6	137.2	61.7	11.4
14	563	155.7	145.0	65.2	12.0
15	567	154.7	147.8	66.5	12.3
16	563	155.6	139.0	62.5	11.5
17	563	156.6	149.3	67.2	12.4
18	575	157.3	151.3	68.1	12.6
19	566	156.9	149.8	67.4	12.4
20	562	158.2	143.8	64.7	11.9
21	563	158.4	146.9	66.1	12.2
22	579	157.0	145.4	65.4	12.1
23	560	155.2	139.8	62.9	11.6
24	578	158.7	159.7	71.9	13.3
25	558	159.4	140.8	63.4	11.7
26	567	155.8	146.2	65.8	12.1
27	570	158.2	148.2	66.7	12.3
28	574	159.3	153.7	69.2	12.8
29	569	156.0	147.0	66.1	12.2
*30					
31	560	158.2	149.9	67.4	12.5
*32					
33	564	154.4	147.7	66.5	12.3
34	564	159.0	149.2	67.1	12.4
*35					
36	564	152.9	141.0	63.4	11.7
37	568	155.9	146.6	66.0	12.2
38	565	153.6	145.0	65.2	12.0
39	563	155.7	139.6	62.8	11.6
40	557	155.7	143.0	64.3	11.9
41	566	157.2	150.7	67.8	12.5
42	569	155.8	144.7	65.1	12.0

*Cell broke.

TYPE II (Continued)

Cell No.	V _{oc} (mV)	I _{sc} (mA)	I ₄₅₀ (mA)	P ₄₅₀ (mW)	η (%)
43	560	158.6	146.4	65.9	12.2
*44					
45	566	154.6	146.6	66.0	12.2
46	563	154.5	139.5	62.8	11.6
47	566	160.5	150.3	67.6	12.5
48	570	157.8	146.0	65.7	12.1
49	570	158.2	143.5	64.6	11.9
50	563	153.9	140.6	63.6	11.7
51	563	157.6	149.2	67.1	12.4
52	559	156.2	146.0	65.7	12.1
53	561	156.0	139.7	62.9	11.6
54	557	158.7	141.1	63.5	11.7
55	564	157.0	148.4	66.8	12.3
56	556	156.9	139.9	62.9	11.6
57	561	157.5	147.7	66.5	12.3
*58					
59	564	158.0	149.8	67.4	12.4
60	578	159.9	152.3	68.5	12.7
61	564	154.7	137.3	61.8	11.4
62	563	154.7	139.4	62.7	11.6
63	561	159.5	148.7	66.9	12.4
*64					
65	556	157.4	144.4	65.0	12.0
*66					
67	560	156.2	145.5	65.5	12.1
68	565	156.6	149.6	67.3	12.4
*69					
*70					
71	571	164.7	158.7	71.4	13.2
72	559	154.8	142.7	64.2	11.9
73	571	155.0	149.0	67.0	12.4
74	570	157.9	145.8	65.6	12.1
*75					
76	566	154.9	143.4	64.7	12.0
77	577	160.0	149.9	67.4	12.5
78	582	163.2	156.1	70.2	13.0
*79					
80	563	154.4	137.0	61.6	11.4

*Cell broke.

9

**AM0-25°C CHARACTERISTICS FOR
TYPE III, IMPLANTED/PULSE ANNEALED JUNCTIONS
10 ohm-cm SILICON WITH BSF**

Cell No.	V _{oc} (mV)	I _{sc} (mA)	I ₄₅₀ (mA)	P ₄₅₀ (mW)	η (%)
1	560	154.9	146.1	65.8	12.1
2	564	154.8	139.1	62.6	11.6
3				37.1	6.9
4	564	153.7	143.2	64.4	11.9
5	569	156.6	136.2	61.3	11.3
6	564	152.6	137.6	61.9	11.4
*7					
8	567	154.1	147.0	66.2	12.2
9	564	154.5	145.1	65.3	12.1
10	563	155.1	138.2	62.2	11.5
11	561	153.4	143.9	64.8	12.0
12	564	155.2	135.3	60.9	11.2
13	561	154.8	141.4	63.6	11.7
14	560	153.8	144.7	65.1	12.0
15	564	157.1	144.5	65.0	12.0
16	561	152.2	144.3	64.9	12.0
17	570	154.3	146.6	66.0	12.2
18	567	158.8	144.4	65.0	12.0
19	563	153.8	140.6	63.3	11.7
20	563	153.5	119.2	53.6	9.9
21	562	153.6	132.8	59.8	11.0
22	565	153.2	146.7	66.0	12.2
23	561	154.5	142.2	64.0	11.8
*24					
25	562	152.3	124.6	56.0	10.3
26	565	156.6	140.1	63.0	11.6
27	561	154.5	148.1	66.6	12.3
28	563	154.5	142.6	64.2	11.8
29	563	152.7	115.4	51.9	9.6
*30					
31	562	154.3	145.8	65.6	12.1
*32					
33	560	156.0	141.8	63.8	11.8
34	559	153.7	147.9	66.1	12.1
35	567	154.3	143.0	64.3	11.9
36	563	153.6	145.6	65.5	12.1
37	559	151.8	138.5	62.3	11.5
38	564	155.4	136.8	61.6	11.4
39	562	154.7	144.7	65.1	12.0
*40					
41	553	152.1	106.3	47.8	8.8
42	563	156.0	148.7	66.9	12.4

*Cell broke.

TYPE III (Continued)

Cell No.	V _{oc} (mV)	I _{sc} (mA)	I ₄₅₀ (mA)	P ₄₅₀ (mW)	η (%)
43	566	155.8	128.7	57.9	10.7
44	564	154.1	129.7	58.4	10.8
45	562	155.0	143.1	64.4	11.9
46	562	154.0	113.7	51.2	9.4
47	562	155.0	143.4	64.5	11.9
48	563	155.6	143.3	64.5	11.9
49	553	152.6	129.2	58.1	10.7
50	567	153.5	143.6	64.6	11.9
51	562	158.1	92.4	41.6	7.7
52	564	150.4	142.2	64.0	11.8
53	562	155.5	135.7	61.1	11.3
54	568	154.1	149.4	67.2	12.4
55	558	154.3	144.6	65.1	12.0
56	562	153.8	123.4	55.5	10.3
57	565	152.1	146.3	65.8	12.2
*58					
59	562	156.3	146.3	65.8	12.2
*60					
61	568	154.0	147.9	66.5	12.3
62	557	153.2	139.6	62.8	11.6
63	559	155.2	138.4	62.3	11.5
64	563	156.2	100.6	45.3	8.4
*65					
66	567	155.1	147.8	66.5	12.3
67	560	153.8	135.2	60.8	11.2
68	564	152.2	138.9	62.5	11.5
69	562	151.8	140.0	63.0	11.6
70	566	126.0	50.5	22.7	4.2
*71					
72	556	155.2	130.5	58.7	10.8
73	560	153.4	144.2	64.9	12.0
74	561	154.5	133.0	59.8	11.0
*75					
76	570	153.8	148.2	66.7	12.3
77	571	156.4	149.2	67.1	12.4
78	561	153.7	147.7	66.5	12.3
79	565	157.6	136.2	61.3	11.3

*Cell broke.